



저작자표시-비영리-변경금지 2.0 대한민국

이용자는 아래의 조건을 따르는 경우에 한하여 자유롭게

- 이 저작물을 복제, 배포, 전송, 전시, 공연 및 방송할 수 있습니다.

다음과 같은 조건을 따라야 합니다:



저작자표시. 귀하는 원저작자를 표시하여야 합니다.



비영리. 귀하는 이 저작물을 영리 목적으로 이용할 수 없습니다.



변경금지. 귀하는 이 저작물을 개작, 변형 또는 가공할 수 없습니다.

- 귀하는, 이 저작물의 재이용이나 배포의 경우, 이 저작물에 적용된 이용허락조건을 명확하게 나타내어야 합니다.
- 저작권자로부터 별도의 허가를 받으면 이러한 조건들은 적용되지 않습니다.

저작권법에 따른 이용자의 권리는 위의 내용에 의하여 영향을 받지 않습니다.

이것은 [이용허락규약\(Legal Code\)](#)을 이해하기 쉽게 요약한 것입니다.

[Disclaimer](#)

이학박사 학위논문

Evolution of deformation microstructures  
of mantle xenolith and epidote blueschist:  
Implications for seismic properties in the  
lithosphere and subduction zones

맨틀 포획암과 녹렴석 청색편암의 변형미구조  
진화: 암석권 및 섭입대에서의 지진파 특성에  
대한 의의

2021 년 8 월

서울대학교 대학원

지구환경과학부

박 용

**Evolution of deformation microstructures  
of mantle xenolith and epidote blueschist:  
Implications for seismic properties in the  
lithosphere and subduction zones**

지도 교수 정 해 명

이 논문을 이학박사 학위논문으로 제출함  
2021 년 7 월

서울대학교 대학원  
지구환경과학부  
박 용

박 용의 이학박사 학위논문을 인준함  
2021 년 7 월

위 원 장 \_\_\_\_\_ 이 인 성 \_\_\_\_\_

부위원장 \_\_\_\_\_ 정 해 명 \_\_\_\_\_

위 원 \_\_\_\_\_ 길 영 우 \_\_\_\_\_

위 원 \_\_\_\_\_ 이 준 기 \_\_\_\_\_

위 원 \_\_\_\_\_ 박 문 재 \_\_\_\_\_

**Doctoral Thesis**

Evolution of deformation microstructures  
of mantle xenolith and epidote blueschist:  
Implications for seismic properties in the  
lithosphere and subduction zones

**Yong Park**

A dissertation submitted in partial fulfillment of the  
requirements for the degree of Doctor of Philosophy

**School of Earth and Environmental Sciences**

**Seoul National University**

**August 2021**

# ABSTRACT

## **Evolution of deformation microstructures of mantle xenolith and epidote blueschist: Implications for seismic properties in the lithosphere and subduction zones**

Yong Park

School of Earth and Environmental Sciences

The Graduate School

Seoul National University

To understand the deformation environments and mechanisms of rocks and seismic properties in the lithospheric mantle and convergent plate margins, the deformation microstructures of mantle peridotite xenoliths and epidote blueschists were studied. First, the deformation environments and lattice preferred orientations (LPOs) of olivine in mantle peridotite xenoliths from lithospheric mantle in Shanwang, eastern China were investigated. Two types of LPOs of olivine were found: type-B LPO in spinel lherzolites and type-E LPO in spinel wehrlites. Paleostress of sample was estimated to be 18–74 MPa using a free dislocation density and recrystallized grain-size piezometer of olivine. Water content was measured using FTIR: 50–200 ppm H/Si for olivine, 120–760 ppm H/Si for enstatite, and 1060–7690 ppm H/Si for diopside. These data suggest that the type-B LPO of olivine was developed in the presence of water at high stress, and type-E LPO of olivine was most likely developed in the presence of water at relatively low stress. Using the two different types of olivine LPOs, our data suggest that seismic anisotropy under the study area can be explained by two deformation modes in different times. Second, to understand the deformation microstructures and LPO development of glaucophane and epidote at the top of a subducting slab in a warm subduction zone,

deformation experiments of epidote blueschist were conducted for the first time in simple shear under the pressures of  $P = 0.9\text{--}1.5$  GPa and temperatures of  $T = 400\text{--}500$  °C. Experimental results showed that type-1 and -2 LPOs of glaucophane and epidote were developed with increasing shear strain. These experimental results suggest that the magnitude of shear strain, grain size, and rheological contrast between constituent minerals are important factors affecting the development of LPO of glaucophane and epidote at the top of a subducting slab in a warm subduction zone. The 8–9 % reduction of  $V_p$  and 6–7 % reduction of  $V_s$  of experimentally deformed epidote blueschist, compared to the seismic velocity of the lithospheric mantle surrounding the subducting slab, indicate that deformed epidote blueschist can contribute to the seismic low velocity layer observed on the top of the subducting slab. The calculation of seismic anisotropy for the oceanic crust composed of epidote blueschist suggests that the volume proportion and LPO types of glaucophane and epidote, and the subducting angle of the slab can be important factors to control seismic velocity and anisotropy observed in subduction zones. Third, to understand deformation mechanisms and LPO developments of minerals in naturally deformed rocks, epidote blueschists from a subducted oceanic crust in serpentinite mélangé of Río San Juan metamorphic complex, Dominican Republic were studied. Most LPOs of amphiboles corresponded to the type-2 LPO of glaucophane, and some LPOs of zoisites and epidotes corresponded to the type-1 LPO of epidote. Observations of the high density of subgrain boundaries and strong fabric strength of amphibole and zoisite porphyroclast suggest that their LPOs were developed by dislocation creep. The calculations of delay time of S-wave and anisotropic layer thickness in the study area suggest that the subducted oceanic crust metamorphosed in blueschist-facies condition can highly contribute to the seismic anisotropy depending on the LPO of the constituent minerals.

**Keyword:** Deformation microstructures, lattice preferred orientation, epidote blueschist, mantle xenolith, deformation experiment, seismic anisotropy

**Student Number:** 2012-20341

# TABLE OF CONTENTS

<b>ABSTRACT .....</b>	<b>i</b>
<b>TABLE OF CONTENTS .....</b>	<b>iv</b>
<b>LIST OF FIGURES .....</b>	<b>ix</b>
<b>LIST OF TABLES .....</b>	<b>xvii</b>
<b>LIST OF PUBLICATIONS.....</b>	<b>xix</b>
<b>CHAPTER 1. Introduction .....</b>	<b>1</b>
<b>CHAPTER 2. Deformation microstructures of olivine and pyroxene in mantle xenoliths in Shanwang, eastern China, near the convergent plate margin, and implications for seismic anisotropy .....</b>	<b>7</b>
<b>Abstract.....</b>	<b>8</b>
<b>2.1. Introduction .....</b>	<b>10</b>
<b>2.2. Geological background .....</b>	<b>14</b>
<b>2.3. Methods.....</b>	<b>18</b>
2.3.1. Sample description .....	18
2.3.2. Determination of lattice preferred orientation (LPO).....	22
2.3.3. Calculation of the seismic velocity and anisotropy .....	25
2.3.4. Estimation of paleostress.....	26
2.3.5. Measurement of water content .....	28
<b>2.4. Results .....</b>	<b>29</b>
2.4.1. LPOs of olivine, enstatite, and diopside.....	29
2.4.2. Seismic anisotropy of minerals and whole rocks .....	35
2.4.3. Paleostress estimation of sample.....	42
2.4.4. Water content of minerals in the sample .....	45
<b>2.5. Discussions and implications .....</b>	<b>47</b>
2.5.1. LPOs of olivine .....	47
2.5.1.1. <i>Type-B LPO of olivine</i> .....	47
2.5.1.2. <i>Type-E LPO of olivine</i> .....	48

2.5.2. LPOs of pyroxene.....	50
2.5.3. Relationship between fabric strength of minerals and seismic anisotropy .....	52
2.5.4. Thickness of anisotropic layer under the study area.....	55
2.5.5. Implications for seismic anisotropy in eastern China.....	61
<b>2.6. Conclusion.....</b>	<b>65</b>

**CHAPTER 3. Lattice preferred orientation and deformation microstructures of glaucophane and epidote in experimentally deformed epidote blueschist at high pressure .....66**

<b>Abstract.....</b>	<b>67</b>
<b>3.1. Introduction .....</b>	<b>69</b>
<b>3.2. Methods .....</b>	<b>72</b>
3.2.1. Starting material .....	72
3.2.2. Deformation experiment in simple shear .....	76
3.2.3. Determination of LPOs of minerals .....	80
3.2.4. Observation of the deformation microstructures in minerals .....	81
<b>3.3. Results .....</b>	<b>82</b>
3.3.1. Deformation microstructures after experiments.....	82
3.3.2. LPOs of glaucophane and epidote.....	87
3.3.3. Observations of intracrystalline deformation microstructures in deformed glaucophane .....	90
3.3.4. Observations of dislocation microstructures in deformed glaucophane and epidote using TEM .....	92
<b>3.4. Discussions .....</b>	<b>96</b>
3.4.1. LPO formation and deformation mechanisms of glaucophane .....	96
3.4.2. LPO formation and deformation mechanisms of epidote.....	101
3.4.3. Implications for deformation mechanisms of epidote blueschist in a warm subduction zone.....	105
3.4.4. Implications for seismic anisotropy of subducting slab in a subduction zone .....	108
<b>3.5. Conclusion.....</b>	<b>110</b>

<b>CHAPTER 4. Seismic velocity and anisotropy of glaucophane and epidote in epidote blueschists and implications for seismic properties in a warm subduction zone.....</b>	<b>112</b>
<b>Abstract.....</b>	<b>113</b>
<b>4.1. Introduction .....</b>	<b>115</b>
<b>4.2. Methods .....</b>	<b>119</b>
4.2.1. Sample description .....	119
4.2.2. Measurement of LPOs.....	120
4.2.3. Calculation of the seismic velocity and anisotropy .....	123
<b>4.3. Results .....</b>	<b>125</b>
4.3.1. Seismic velocity and anisotropy for deformed glaucophanes .....	125
4.3.2. Seismic velocity and anisotropy for deformed epidotes.....	131
4.3.3. Seismic velocity and anisotropy for deformed epidote blueschist (whole rock) .....	133
<b>4.4. Discussions and implications .....</b>	<b>136</b>
4.4.1. Seismic velocity of epidote blueschist induced by LPO of minerals ..	136
4.4.2. Relationship between seismic properties of epidote blueschist and deformation of minerals .....	141
4.4.2.1. <i>Seismic velocity of epidote blueschist versus shear strain</i> .....	141
4.4.2.2. <i>Seismic velocity of epidote blueschist versus fabric strength</i> .....	146
4.4.2.3. <i>Seismic anisotropy of epidote blueschist versus shear strain</i> .....	154
4.4.2.4. <i>Seismic anisotropy of epidote blueschist versus fabric strength</i> ..	157
4.4.3. Relationship between LPOs of minerals in epidote blueschist and seismic properties of subducting slab.....	161
4.4.4. Implications for seismic properties in subduction zone .....	168
4.4.4.1. <i>Low velocity layer (LVL) on top of the subducting slab</i> .....	168
4.4.4.2. <i>Seismic anisotropy of fast shear wave in the forearc region</i> .....	173
<b>4.5. Conclusion.....</b>	<b>188</b>

<b>CHAPTER 5. Deformation microstructures of epidote blueschist from Río San Juan metamorphic complex, Dominican Republic, and implications for seismic anisotropy in the northeastern margin of the Caribbean plate .....</b>	<b>190</b>
<b>Abstract.....</b>	<b>191</b>
<b>5.1. Introduction .....</b>	<b>193</b>
<b>5.2. Geological background .....</b>	<b>196</b>
<b>5.3. Methods .....</b>	<b>200</b>
5.3.1. Sample description .....	200
5.3.1.1. <i>Zoisite eclogite–epidote blueschist facies metamorphic rock .....</i>	202
5.3.1.2. <i>Epidote eclogite–epidote blueschist facies metamorphic rock.....</i>	203
5.3.1.3. <i>Lawsonite–epidote blueschist facies metamorphic rock.....</i>	208
5.3.1.4. <i>Felsic blueschist facies metamorphic rock.....</i>	208
5.3.1.5. <i>Epidote blueschist–upper greenschist facies metamorphic rock..</i>	209
5.3.2. Determination of LPOs of minerals .....	214
5.3.3. Calculation of seismic velocity and anisotropy.....	216
<b>5.4. Results .....</b>	<b>218</b>
5.4.1. LPOs of minerals.....	218
5.4.1.1. <i>LPOs of amphibole group minerals .....</i>	218
5.4.1.2. <i>LPOs of epidote group minerals.....</i>	224
5.4.1.3. <i>LPOs of omphacite .....</i>	230
5.4.1.4. <i>LPOs of phengite .....</i>	232
5.4.1.5. <i>LPOs of garnet .....</i>	236
5.4.1.6. <i>LPOs of quartz, chlorite, titanite, and albite.....</i>	238
5.4.2. Seismic velocity and anisotropy of minerals.....	246
5.4.2.1. <i>Polycrystalline amphibole group minerals.....</i>	246
5.4.2.2. <i>Polycrystalline epidote group minerals.....</i>	252
5.4.2.3. <i>Polycrystalline omphacites .....</i>	255
5.4.2.4. <i>Polycrystalline phengites .....</i>	257
5.4.2.5. <i>Polycrystalline garnets.....</i>	259
5.4.2.6. <i>Polycrystalline quartzs, chlorites, titanites, and albites.....</i>	261
5.4.3. Seismic velocity and anisotropy of whole rocks .....	269

<b>5.5. Discussions .....</b>	<b>272</b>
5.5.1. The development of LPOs of minerals in high pressure metabasites..	272
5.5.1.1. <i>LPO development of amphiboles</i> .....	272
5.5.1.2. <i>LPO development of epidote group minerals</i> .....	277
5.5.1.3. <i>LPO development of omphacites</i> .....	286
5.5.2. Estimation of metamorphic pressure (P) and temperature (T) of epidote blueschist facies rocks .....	289
5.5.3. Implications for seismic anisotropy in the northeastern margin of the Caribbean plate.....	291
<b>5.6. Conclusion.....</b>	<b>295</b>
<b>CHAPTER 6. Summary &amp; Conclusion .....</b>	<b>297</b>
<b>REFERENCES .....</b>	<b>303</b>
<b>ABSTRACT (in Korean).....</b>	<b>326</b>

# LIST OF FIGURES

<b>Figure 2.1.</b> Simplified geologic map showing the major tectonic setting and study area of Shanwang in eastern China .....	17
<b>Figure 2.2.</b> Optical photomicrograph of representative samples of lherzolite and wehrlite .....	20
<b>Figure 2.3.</b> Optical photomicrograph of wehrlite showing metasomatic textures and lherzolite without metasomatic textures.....	21
<b>Figure 2.4.</b> The details of grain shape analysis to determine lineation in sample .....	24
<b>Figure 2.5.</b> Pole figures of olivine in lherzolite and wehrlite samples .....	30
<b>Figure 2.6.</b> Pole figures of enstatite (orthopyroxene, Opx) in lherzolite samples .....	33
<b>Figure 2.7.</b> Pole figures of diopside (clinopyroxene, Cpx) in lherzolite and wehrlite samples .....	34
<b>Figure 2.8.</b> Seismic anisotropy of olivine in lherzolite samples and wehrlite samples .....	36
<b>Figure 2.9.</b> Seismic anisotropy of enstatite (Opx) in lherzolite samples .....	37
<b>Figure 2.10.</b> Seismic anisotropy of diopside (Cpx) in lherzolite and wehrlite samples .....	38
<b>Figure 2.11.</b> Seismic anisotropy of whole rock for lherzolite samples and wehrlite samples .....	40

<b>Figure 2.12.</b> Backscattered electron (BSE) images showing dislocation microstructures of samples for type-E LPO and type-B LPO of olivine .....	43
<b>Figure 2.13.</b> Seismic anisotropy compared to the fabric strength (M-index) of minerals .....	54
<b>Figure 2.14.</b> Four different geodynamic models for the origin of seismic anisotropy .....	58
<b>Figure 2.15.</b> The relationship between olivine volume fraction and the required thickness of the anisotropic layer (log scale) needed to explain seismic anisotropy for lherzolite and wehrlite .....	59
<b>Figure 2.16.</b> Schematic diagram for the evolution of the lithosphere beneath the Eastern Block of the Sino-Korean craton .....	64
<b>Figure 3.1.</b> Optical photomicrograph (XPL) with retardation plate and backscattered electron (BSE) image of the starting material.....	74
<b>Figure 3.2.</b> Photograph of a modified Griggs apparatus, high pressure and high temperature solid-medium apparatus.....	77
<b>Figure 3.3.</b> Photographs of a starting material and parts of the sample assembly .....	78
<b>Figure 3.4.</b> Schematic of sample assembly for the deformation experiment in simple shear .....	79
<b>Figure 3.5.</b> BSE images of deformed samples after simple shear experiments under different shear strains .....	85
<b>Figure 3.6.</b> BSE images of sample deformed with high shear strain.....	86

<b>Figure 3.7.</b> Pole figures of glaucophane and epidote in starting material and deformed samples .....	89
<b>Figure 3.8.</b> BSE image, GROD angle map (mis2mean), and KAM map showing the intracrystalline deformation microstructure of glaucophane deformed under different shear strains .....	91
<b>Figure 3.9.</b> Weak-beam dark field (WBDF) images of glaucophane experimentally deformed under low ( $\gamma = 0.6$ ) and high ( $\gamma = 4.5$ ) shear strain .....	93
<b>Figure 3.10.</b> WBDF and bright field (BF) images of epidote experimentally deformed under a shear strain of $\gamma = 2.4$ and $\gamma = 4.5$ .....	95
<b>Figure 3.11.</b> Simplified glaucophane crystal structure projected onto the (001) plane, and schematic of the glaucophane crystal form with different dominant slip systems in glaucophane.....	100
<b>Figure 3.12.</b> Simplified epidote crystal structure, and schematic of the epidote crystal form with different behavior by shear deformation.....	104
<b>Figure 3.13.</b> Schematic of the development of LPOs of glaucophane and epidote with increasing shear strain.....	107
<b>Figure 4.1.</b> Pole figures of glaucophane and epidote in deformed samples showing representative LPOs of each mineral .....	122
<b>Figure 4.2.</b> Seismic velocity and seismic anisotropy of polycrystalline glaucophanes.....	129
<b>Figure 4.3.</b> Seismic velocity and seismic anisotropy of polycrystalline epidotes .....	132

<b>Figure 4.4.</b> Seismic velocity and seismic anisotropy of epidote blueschist (whole rock).....	135
<b>Figure 4.5.</b> Seismic velocity and seismic anisotropy for single crystal of glaucophane and a schematic of glaucophane crystal form.....	138
<b>Figure 4.6.</b> Seismic velocity and seismic anisotropy for single crystal of epidote and a schematic of epidote crystal form .....	140
<b>Figure 4.7.</b> Seismic velocity of polycrystalline glaucophanes compared to the magnitude of shear strain.....	143
<b>Figure 4.8.</b> Seismic velocity of polycrystalline epidotes compared to the magnitude of shear strain.....	144
<b>Figure 4.9.</b> Seismic velocity of epidote blueschist (whole rock) compared to the magnitude of shear strain.....	145
<b>Figure 4.10.</b> Seismic velocity of polycrystalline glaucophanes compared to the fabric strength (M-index and J-index) .....	148
<b>Figure 4.11.</b> Seismic velocity of polycrystalline epidotes compared to the fabric strength (M-index and J-index) .....	150
<b>Figure 4.12.</b> Seismic velocity of epidote blueschist (whole rock) compared to the fabric strength (M-index and J-index) .....	152
<b>Figure 4.13.</b> Seismic anisotropy of polycrystalline minerals and whole rock compared to the magnitude of shear strain .....	156
<b>Figure 4.14.</b> Seismic anisotropy of polycrystalline minerals and whole rock compared to the fabric strength (M-index and J-index).....	159
<b>Figure 4.15.</b> The delay time of oceanic crust composed of epidote blueschist .....	164

<b>Figure 4.16.</b> The $V_p/V_s$ ratios of oceanic crust composed of epidote blueschist .....	166
<b>Figure 4.17.</b> The comparison between seismic velocity calculated for deformed rocks and those calculated for the lithospheric mantle surrounding the subducting slab .....	171
<b>Figure 4.18.</b> Schematic diagrams for the fast shear wave ( $V_{s1}$ ) polarization direction in the forearc region of the subduction zone induced by the subducting oceanic crust composed mainly of epidote blueschist .....	178
<b>Figure 4.19.</b> Seismic velocity and anisotropy of epidote blueschist (whole rock) composed of glaucophane showing the type-1 LPO and epidote showing the type-1 LPO by different volume ratios...	180
<b>Figure 4.20.</b> Seismic velocity and anisotropy of epidote blueschist (whole rock) composed of glaucophane showing the type-1 LPO and epidote showing the type-2 LPO by different volume ratios...	182
<b>Figure 4.21.</b> Seismic velocity and anisotropy of epidote blueschist (whole rock) composed of glaucophane showing the type-2 LPO and epidote showing the type-1 LPO by different volume ratios...	184
<b>Figure 4.22.</b> Seismic velocity and anisotropy of epidote blueschist (whole rock) composed of glaucophane showing the type-2 LPO and epidote showing the type-2 LPO by different volume ratios...	186
<b>Figure 5.1.</b> Simplified geotectonic map of the northeastern margin of the Caribbean plate and geological map of the northern Río San Fuan metamorphic complex, Dominican Republic .....	198

<b>Figure 5.2.</b> Optical photomicrographs of zoisite eclogite-epidote blueschist, zoisite bearing epidote blueschist, and epidote eclogite-epidote blueschist facies metamorphic rocks .....	204
<b>Figure 5.3.</b> Optical photomicrographs of lawsonite bearing epidote blueschist, felsic blueschist, and epidote blueschist-upper greenschist facies metamorphic rocks .....	210
<b>Figure 5.4.</b> EBSD phase maps of analyzed areas in each sample.....	220
<b>Figure 5.5.</b> Pole figures of amphibole group minerals in each sample.....	222
<b>Figure 5.6.</b> Pole figures of zoisite in each sample .....	227
<b>Figure 5.7.</b> Pole figures of epidote in each sample.....	228
<b>Figure 5.8.</b> Pole figures of omphacite in each sample.....	231
<b>Figure 5.9.</b> Pole figures of phengite in each sample.....	234
<b>Figure 5.10.</b> Pole figures of garnet in each sample.....	237
<b>Figure 5.11.</b> Pole figures of quartz in each sample.....	240
<b>Figure 5.12.</b> Pole figures of chlorite in each sample .....	241
<b>Figure 5.13.</b> Pole figures of titanite in each sample .....	243
<b>Figure 5.14.</b> Pole figures of albite in each sample.....	245
<b>Figure 5.15.</b> Seismic velocity and anisotropy of amphiboles.....	251
<b>Figure 5.16.</b> Seismic velocity and anisotropy of zoisites .....	253
<b>Figure 5.17.</b> Seismic velocity and anisotropy of epidotes.....	254
<b>Figure 5.18.</b> Seismic velocity and anisotropy of omphacites .....	256

<b>Figure 5.19.</b> Seismic velocity and anisotropy of phengites .....	258
<b>Figure 5.20.</b> Seismic velocity and anisotropy of garnets .....	260
<b>Figure 5.21.</b> Seismic velocity and anisotropy of quartzes .....	262
<b>Figure 5.22.</b> Seismic velocity and anisotropy of chlorites.....	264
<b>Figure 5.23.</b> Seismic velocity and anisotropy of titanites.....	266
<b>Figure 5.24.</b> Seismic velocity and anisotropy of albites .....	268
<b>Figure 5.25.</b> Seismic velocity and anisotropy of whole rocks .....	271
<b>Figure 5.26.</b> BSE image and high-resolution EBSD mapping images showing the intracrystalline deformation microstructure of glaucophane grain .....	274
<b>Figure 5.27.</b> BSE image and high-resolution EBSD mapping images showing the intracrystalline deformation microstructure of zoisite porphyroclast grain.....	278
<b>Figure 5.28.</b> BSE image and high-resolution EBSD mapping images showing the intracrystalline deformation microstructure of zoisite-epidote grains .....	281
<b>Figure 5.29.</b> BSE image and high-resolution EBSD mapping images showing the intracrystalline deformation microstructure of epidote aggregate (lawsonite pseudomorph) grains .....	284
<b>Figure 5.30.</b> BSE image and high-resolution EBSD mapping images showing the intracrystalline deformation microstructure of omphacite grain .....	288

**Figure 5.31.** The delay time of S-wave for 7 km-thick oceanic crust  
underthrust tilted  $\sim 20^\circ$  beneath the Caribbean plate.....293

**Figure 5.32.** The required thickness of the anisotropic layer (log scale)  
beneath the Hispaniola to derive the delay time of  $\delta t \sim 1.3$  s  
observed near the study area.....294

# LIST OF TABLES

<b>Table 2.1.</b> Results of modal composition, lattice preferred orientations (LPOs), and fabric strength (M-index) .....	31
<b>Table 2.2.</b> Seismic anisotropies of P- and S-waves for olivine, enstatite (Opx), diopside (Cpx), and whole rock .....	41
<b>Table 2.3.</b> Estimated stress ( $\sigma$ ) from: free dislocation density ( $\rho$ ); and recrystallized grain-size piezometer .....	44
<b>Table 2.4.</b> Water contents measured by FTIR spectroscopy for olivine, Opx, and Cpx in each sample .....	46
<b>Table 2.5.</b> Thickness of anisotropic layer in eastern China calculated using four different geodynamic models .....	60
<b>Table 3.1.</b> The representative composition of glaucophane and epidote in the starting material .....	75
<b>Table 3.2.</b> Experimental conditions and results for the deformation experiment on epidote blueschist.....	84
<b>Table 4.1.</b> Experimental conditions, LPOs, and seismic anisotropy of deformed polycrystalline glaucophanes, epidotes, and epidote blueschist (whole rock).....	127
<b>Table 4.2.</b> Seismic velocity of deformed polycrystalline glaucophanes, epidotes, and epidote blueschist (whole rock).....	128

<b>Table 5.1.</b> Modal composition (in volume %) of the area analyzed by EBSD and whole area of samples .....	201
<b>Table 5.2.</b> Representative mineral compositions of zoisite eclogite-epidote blueschist facies rock (sample 2449) .....	205
<b>Table 5.3.</b> Representative mineral compositions of zoisite bearing epidote blueschist facies rock (sample 2461) .....	206
<b>Table 5.4.</b> Representative mineral compositions of epidote eclogite-epidote blueschist facies rock (sample 1017Y) .....	207
<b>Table 5.5.</b> Representative mineral compositions of lawsonite bearing epidote blueschist facies rock (sample 2462) .....	211
<b>Table 5.6.</b> Representative mineral compositions of felsic blueschist facies rock (sample 2444) .....	212
<b>Table 5.7.</b> Representative mineral compositions of epidote blueschist-upper greenschist facies rock (sample 1015Y) .....	213
<b>Table 5.8.</b> Average P-wave velocity (km/s) of the constituent minerals of the area analyzed in the samples.....	247
<b>Table 5.9.</b> Average S-wave velocity (km/s) of the constituent minerals of the area analyzed in the samples.....	248
<b>Table 5.10.</b> The azimuthal anisotropy of P-wave (%) of the constituent minerals of the area analyzed in the samples.....	249
<b>Table 5.11.</b> The maximum polarization anisotropy of S-wave (%) of the constituent minerals of the area analyzed in the samples .....	250

## LIST OF PUBLICATIONS

- Park, Y.**, Jung, S., and Jung, H., 2020. Lattice preferred orientation and deformation microstructures of glaucophane and epidote in experimentally deformed epidote blueschist at high pressure. *Minerals* **10**(9), 803, 1–19. DOI: 10.3390/min10090803
- Park, Y.**, and Jung, H., 2015. Deformation microstructures of olivine and pyroxene in mantle xenoliths in Shanwang, eastern China, near the convergent plate margin, and implications for seismic anisotropy. *International Geology Review* **57**(5–8), 629–649. DOI: 10.1080/00206814.2014.928240
- Bang, Y., Hwang, H., Kim, T., Cynn, H., **Park, Y.**, Jung, H., Park, C., Popov, D., Prakapenka, V. B., Wang, L., Liermann, H., Irifune, T., Mao, H., and Lee, Y., 2021. The stability of subducted glaucophane with the Earth's secular cooling. *Nature communications* **12**(1), 1496, 1–7. DOI: 10.1038/s41467-021-21746-8
- Hwang, G. C., Hwang, H., Bang, Y., Choi, J., **Park, Y.**, Jeon, T., Chae, B., Jung, H., and Lee, Y., 2021. A role for subducted albite in the water cycle and alkalinity of subduction fluids. *Nature communications* **12**(1), 1155, 1-7. DOI: 10.1038/s41467-021-21419-6
- Choi, S., **Park, Y.**, Kweon, J. J., Kim, S., Jung, H., Lee, S. K., and Lee, Y., 2021. Fossil eggshells of amniotes as a paleothermometry tool. *Palaeogeography, Palaeoclimatology, Palaeoecology* **571**(1), 110376, 1–18. DOI: 10.1016/j.palaeo.2021.110376
- Cao, Y., Du, J., Park, M., Jung, S., **Park, Y.**, Kim, D., Choi, S., Jung, H., and Austrheim, H., 2020. Metastability and nondislocation-based deformation mechanisms of the Flem eclogite in the Western Gneiss Region, Norway. *Journal of Geophysical Research: Solid Earth*, **125**(5), e2020JB019375, 1–33. DOI: 10.1029/2020JB019375

# CHAPTER 1

## Introduction

Since the rocks within the tectonic blocks undergo a variety of thermodynamic environments depending on their location and the timing of the tectonic situation, they are deformed by various mechanisms such as dislocation creep, diffusion creep, dissolution-precipitation creep, cataclastic flow, and rigid body rotation. Thus, the deformation microstructures recorded in naturally deformed rock can provide a great deal of information for understanding the deformation processes and mechanisms in large-scale tectonic systems, such as continental orogenic collision belt or oceanic subduction zone. Especially, lattice preferred orientation (LPO) of deformed minerals is one of the keys to interpret the deformation environment because the crystallographic axis of minerals can distribute to specific orientation by given physical or chemical conditions (Karato et al., 2008).

The seismic anisotropy observed in the Earth's interior can also provide the information of the geodynamic processes in large scale, such as lithospheric mantle flow and tectonics (Long and Becker, 2010; Park and Levin, 2002; Savage, 1999). Specifically, the source for the splitting of S-wave has been regarded as multiple

anisotropic mediums including continental lithospheric mantle wedge and subducting oceanic slab in the forearc region of the subduction zone (Long, 2013). There are several suggestions that seismic anisotropy of the shear wave was caused by the flow direction of lithospheric mantle (Abt et al., 2009; Long and Silver, 2008; 2009a; 2009b), hydration of sub-vertical fault zones (Faccenda et al., 2008) and/or fluid-filled cracks in subducting slabs (Healy et al., 2009), LPOs of minerals consisting of the lithospheric mantle (Jung and Karato, 2001b; Jung et al., 2009b; Jung et al., 2020; Karato et al., 2008; Kneller et al., 2005; Lee and Jung, 2015; Nakajima and Hasegawa, 2004; Nicolas and Christensen, 1987; Ohuchi et al., 2011; Park and Levin, 2002; Park and Jung, 2015; Park et al., 2014; Savage, 1999; Skemer et al., 2012) and consisting of the subducting oceanic crust and the slab-mantle boundary (Bezacier et al., 2010a; 2010b; Cao and Jung, 2016; Cao et al., 2013; 2014; Jung, 2011; Ha et al., 2018; Kim and Jung, 2015; Kim et al., 2013a; 2013b; 2016; 2018; Lee et al., 2020; 2021; Park and Jung, 2019; Park et al., 2020a).

As mentioned above, the studies on the deformation microstructures and seismic properties of major constituent minerals of the lithospheric mantle and subducting slab are very important to understand the deformation environments and mechanisms of rocks and to interpret the seismic anisotropy of subduction zones. To this end, olivine and pyroxenes in mantle peridotite xenoliths provide well-preserved information on the deformation and metamorphic processes of the upper mantle lithosphere (Mercier and Nicolas, 1975). On the other hand, many hydrous and elastically anisotropic minerals that exist in the subducted oceanic crust and the slab-mantle boundary depending on temperatures and depths can provide information on the deformation and metamorphic processes in the subduction zone (Hacker et al.,

2003; Poli and Schmidt, 2002; Schmidt and Poli, 1998). Specifically, glaucophane and epidote in blueschist-facies metamorphic rocks provide microstructural and petrological information under the pressures of 0.8–2.2 GPa and temperatures of 300–550 °C condition (Evans, 1990; Forneris and Holloway, 2003; Peacock, 1992; 1993). However, unlike olivine and pyroxene, studies on the deformation mechanisms of glaucophane and epidote are relatively limited to naturally deformed rocks (Brunsmann et al., 2000; Cao et al., 2014; Franz and Liebscher, 2004; Ildefonse et al., 1990; Kim et al., 2013a; Müller and Franz, 2004; 2008; Reynard et al., 1989; Wassmann and Stöckhert, 2013; Zucali et al., 2002), and the debate continues for the dominant mechanism that influences their LPO development under the pressure and temperature conditions of subducting slab (Cao et al., 2014; Kim et al., 2015; Park et al., 2020a). In addition, there was no experimental study on the deformation of epidote blueschist before Park *et al.* (2020a). Therefore, this dissertation focuses on the deformation microstructures and seismic properties of naturally deformed mantle peridotite xenoliths, blueschist-facies metamorphic rocks, and experimentally deformed epidote blueschist in the following four chapters.

In Chapter 2, deformation microstructures and LPOs of minerals and dislocation microstructures of olivine in mantle peridotite xenoliths from Shanwang in eastern China were studied to understand the deformation mechanism and seismic anisotropy in the upper mantle. LPO of minerals were determined by electron backscattered diffraction (EBSD) technique with scanning electron microscope (SEM). To understand the deformation environment of olivine, paleostress was estimated using free dislocation density observed by the oxidation decoration technique and using recrystallized grain-size piezometer, and water content was

measured by using Fourier transformation infrared (FTIR) spectroscopy. The seismic anisotropy of each mineral was calculated, and the thickness of the anisotropic layer under the study area was estimated for four geodynamic models using the delay time from shear wave splitting in eastern China and S-wave velocity and anisotropy from the LPOs of minerals in the mantle xenoliths. Consequently, two deformation modes of the upper mantle below the study area were proposed to explain seismic anisotropy in eastern China (near Shanwang) by using the petrofabrics of olivine found in this study.

In Chapter 3, deformation experiments of epidote blueschist in simple shear were conducted to understand the deformation microstructures and LPO development of glaucophane and epidote at the top of a subducting slab in a warm subduction zone. Deformation experiments were performed using a high-pressure, high-temperature solid medium apparatus (modified Griggs apparatus) under the epidote blueschist-facies condition at pressures of  $P = 0.9\text{--}1.5$  GPa and temperatures of  $T = 400\text{--}500$  °C. Deformation microstructures of experimentally deformed samples were observed using field-emission SEM (FE-SEM), and LPOs of minerals in the samples were determined by EBSD technique. To understand the deformation mechanisms and LPO development of glaucophane and epidote, intracrystalline microstructures were observed through high-resolution EBSD mapping, and dislocation microstructures were observed by using transmission electron microscopy (TEM). As a result, with increasing shear strain, two different LPOs of glaucophane and epidote were determined, and deformation mechanisms that predominantly developed the LPO of glaucophane and epidote and important factors influencing these mechanisms were proposed in this study.

In Chapter 4, seismic properties of glaucophane and epidote in experimentally deformed epidote blueschist were studied to understand the seismic low velocity layer and seismic anisotropy induced by LPOs of glaucophane and epidote in subduction zones. Seismic velocity and anisotropy of glaucophane and epidote were calculated using LPO data determined in Chapter 3 and elastic constants of each minerals, and those of epidote blueschist (whole rock) were calculated according to the volume proportions of constituent minerals. These seismic velocity and anisotropy were compared with the shear strain and fabric strength of minerals to find the relationship between these factors. The delay time of S-wave and  $V_p/V_s$  ratio of oceanic crust composed of epidote blueschist were calculated by considering the subducting angle of the slab and the volume proportion of glaucophanes and epidotes with different LPO types. In addition, seismic velocity of experimentally deformed epidote blueschist in this study and that of naturally deformed rocks reported in previous studies were compared with the seismic velocity of lithospheric mantle surrounding the slab. According to the results, important factors to control seismic velocity and anisotropy observed in subduction zones are suggested in this study.

In chapter 5, deformation microstructures of naturally deformed epidote blueschists from Río San Juan metamorphic complex in Dominican Republic were studied to understand deformation mechanisms and LPO developments of minerals and seismic anisotropy induced by their LPOs in the study area. Chemical compositions of minerals were analyzed by using the field-emission electron probe microanalyzer (FE-EPMA), and the LPOs of minerals in high pressure metabasites were determined by the EBSD technique. The high-resolution EBSD mapping was

performed on the representative minerals in each sample to understand their deformation and LPO development mechanisms. Seismic anisotropy of minerals was calculated using the orientation data obtained through EBSD analysis and elastic constants of each minerals. Seismic anisotropy of whole rocks was calculated by using whole orientation data of the constituent minerals and the average density weighted by the volume proportion of each sample. Then, to understand the seismic anisotropy in the northeastern margin of the Caribbean plate, the delay time from shear wave splitting was calculated by considering the sample orientation aligned in different directions due to the transition of tectonic setting from subduction to oblique underthrust and/or lateral shear in the study area. In addition, the anisotropic layer thickness was estimated for detached oceanic crust, which was regarded as an oceanic slab segregated from subducted North American plate, by considering orientation of constituting minerals. Consequently, it is suggested to what extent the anisotropic layer that may exist beneath the study area can contribute to the seismic anisotropy in the northeastern margin of the Caribbean plate, depending on the constituent minerals and their orientations.

## CHAPTER 2

# **Deformation microstructures of olivine and pyroxene in mantle xenoliths in Shanwang, eastern China, near the convergent plate margin, and implications for seismic anisotropy**

*\* This chapter has been modified from a published paper:*

Park, Y., and Jung, H., 2015. Deformation microstructures of olivine and pyroxene in mantle xenoliths in Shanwang, eastern China, near the convergent plate margin, and implications for seismic anisotropy. *International Geology Review* 57(5–8), 629–649. DOI: 10.1080/00206814.2014.928240

## Abstract

Deformation microstructures, including lattice preferred orientations (LPOs) of olivine, enstatite, and diopside, in mantle xenoliths at Shanwang, eastern China, were studied to understand the deformation mechanism and seismic anisotropy of the upper lithospheric mantle. The Shanwang is located across the Tan-Lu fault zone, which was formed due to the collision between the Sino-Korean and South China cratons. All samples are spinel lherzolites and spinel wehrlites. LPOs of minerals were determined using the electron backscattered diffraction (EBSD) technique. There were two types of olivine LPO: type-B in spinel lherzolites, and type-E in spinel wehrlites. Enstatite showed two types of LPO (type-BC and type-AC), and diopside showed four different types of LPO. Observations of strong LPOs and numerous dislocations in olivine suggest that samples showing both type-B and -E LPOs were deformed in dislocation creep. The azimuthal anisotropy of P-wave was in the range of 2.2–11.6 % for olivine, 1.2–2.3 % for enstatite, and 2.1–6.4 % for diopside. The maximum polarization anisotropy of S-wave was in the range of 1.93–7.53 % for olivine, 1.53–2.46 % for enstatite, and 1.81–6.57% for diopside. Furthermore, the thickness of the anisotropic layer was calculated for four geodynamic models to understand the origin of seismic anisotropy under the study area by using delay time from shear wave splitting, and S-wave velocity and anisotropy from LPOs of minerals. As a result, it is suggested that the seismic anisotropy under the study area can be most likely explained by two deformation modes that might have occurred at different times: one mode of deformed lherzolites

with a type-B LPO of olivine by lateral shear during/after the period of the Mesozoic continental collision between the Sino-Korean and South China cratons; and the other mode of deformed wehrlites with a type-E LPO of olivine by horizontal extension during the period of change in absolute plate motion in relation to the westward-subducting Pacific plate.

## 2.1. Introduction

Since mantle peridotite xenoliths provide information about the deformation and metamorphic processes of the upper mantle lithosphere (Mercier and Nicolas, 1975), these rocks have been perceived as being crucial in interpreting both the geophysical and geochemical environments and the deformation mechanisms in the upper mantle. In particular, the seismic anisotropic layer is considered to be related to the presence of mainly olivine and orthopyroxene in the mantle, and therefore an understanding of the lattice preferred orientations (LPOs) of these minerals in nature is important in distinguishing the deformation processes of the upper mantle (Jung and Karato, 2001b; Park and Levin, 2002; Park et al., 2020b; Nakajima and Hasegawa, 2004; Karato et al., 2008; Kneller et al., 2005; Long and Silver, 2008; 2009a; 2009b; Long, 2013; Mainprice, 2007; Nicolas and Christensen, 1987; Savage, 1999; Silver, 1996; Skemer et al., 2012; Vinnik et al., 1989). From the seismic anisotropy calculated using the LPOs of olivine and pyroxenes in mantle xenoliths, Pera *et al.* (2003) presented the first petrophysical results of upper mantle structure constraints beneath the Torre Alfina area in central Italy, by considering four geodynamic models: upwelling, lateral shear, horizontal extension, and tilted slab. Subsequently, similar studies were conducted to constrain the structures beneath the Sanbagawa belt in southwest Japan (Tasaka et al., 2008), the Rio Grande rift in the New Mexico, USA (Satsukawa et al., 2011), and northeast Tasmania in southwest Australia (Michibayashi et al., 2012).

The LPO and seismic anisotropy of olivine are well known in both “dry” and “wet” conditions in experimental studies (Bystricky et al., 2000; Carter and Ave'Lallemant, 1970; Jung and Karato, 2001b; Jung et al., 2006; 2009b; Karato et al., 2008; Katayama et al., 2004; Katayama and Karato, 2006; Ohuchi et al., 2011; 2012; Zhang and Karato, 1995; Zhang et al., 2000) and within many natural rocks (Ben Ismail and Mainprice, 1998; Jung, 2009; Jung et al., 2009a; 2013; 2014; Kamei et al., 2010; Katayama et al., 2005; Michibayashi et al., 2006; 2009; Mizukami et al., 2004; Nicolas and Christensen, 1987; Sawaguchi, 2004; Skemer et al., 2006; 2010; Tommasi et al., 2008; Vauchez et al., 2005). According to previous experimental studies, the type-E LPO of olivine (defined as the crystallographic [100] axis of olivine aligned subparallel to the shear direction and the [001] axis aligned subnormal to the shear plane) is found under low stress and moderate water content. In contrast, the type-B LPO of olivine (defined as the crystallographic [001] axis of olivine aligned subparallel to the shear direction and the [010] axis aligned subnormal to the shear plane) is found under high stress and/or moderate to high water content. It is considered that finding the type-B olivine LPO in nature is important because trench-parallel seismic anisotropy of fast shear waves found in many subduction zones can be attributed to type-B LPO (Jung and Karato, 2001b; Karato et al., 2008; Kneller et al., 2005; Long and van der Hilst, 2005; 2006; Nakajima and Hasegawa, 2004; Nakajima et al., 2006). However, previous studies related to the LPO and seismic anisotropy of orthopyroxene are limited (Christensen and Lundquist, 1982; Hidas et al., 2007; Skemer et al., 2006; Soustelle et al., 2010; Vauchez et al., 2005), and Jung *et al.* (2010) recently classified the LPOs of enstatite into one typical type-AC and three newly defined types: type-AB, -BC and -ABC (in this nomenclature, the initial letter represents the slip plane and the second

indicates the slip direction, and the letters of A, B, and C correspond to the direction of [100], [010], and [001], respectively).

The Sino-Korean craton (or North China craton) is one of the major eastern Eurasian Archaean cratons on Earth, and it is considered that refractory ancient mantle roots are depleted beneath this craton, with significant buoyancy and high viscosity (Griffin et al., 1998b; Kelemen et al., 1998). Many analytical geochemical studies have revealed that the refractory lithosphere can be changed to more fertile materials by the interaction between the asthenosphere and lithosphere, or cratonic upper mantle (Griffin et al., 1998a; Kelemen et al., 1998; O'Reilly et al., 2001). According to several studies, such mantle metasomatism is considered to occur beneath the Sino-Korean craton (Chu et al., 2009; Zhang and Sun, 2002; Zhang, 2005; Zhang et al., 2007; Zheng et al., 2005a; 2005b; 2006; Xiao et al., 2010; Xiao and Zhang, 2011), and previous studies have calculated the seismic anisotropy of shear waves therein using SKS splitting measurements (Chang et al., 2009; Huang et al., 2008; Iidaka and Niu, 2001; Liu et al., 2008; Zhao and Zheng, 2005; Zhao and Xue, 2010; Zhao et al., 2007b; 2008; 2009; 2011; 2013). These studies reveal an E–W to WNW–ESE-trending polarization direction of fast shear waves in eastern China (near the Shanwang area), with a direction subparallel to the average absolute plate motion direction of the Sino-Korean craton (Gripp and Gordon, 2002). However, the origin of such seismic anisotropy is not yet well understood.

In this chapter, deformation microstructures including the LPOs of olivine (forsterite), orthopyroxene (enstatite), and clinopyroxene (diopside) in mantle xenoliths from Shanwang, in eastern China were studied to understand the

deformation mechanism and seismic anisotropy in the upper mantle. The seismic anisotropy of each mineral was calculated, and the thickness of the anisotropic layer under the study area was estimated for four geodynamic models (Pera et al., 2003) using both the delay time from shear wave splitting in eastern China, and S-wave velocity and anisotropy from the LPOs of minerals in the mantle xenoliths. Then, to explain seismic anisotropy in eastern China (near Shanwang), the deformation modes of the upper mantle under the study area were proposed by using the petrofabrics of olivine found in the samples.

## 2.2. Geological background

The Sino-Korean craton is divided into three regions, the Western and Eastern Blocks, and the Trans-North China Orogen (Central Zone in Fig. 2.1). The eastern boundary of the Trans-North China Orogen nearly coincides with the North-South Gravity Lineament (NSGL), which is a major geophysical feature in the central Sino-Korean craton that separates the Archean Liaolu and the Archean Ordos cratonic nuclei (Zhao et al., 2000; 2001; Zheng et al., 2001; 2005a). To the west of the NSGL, in an area that includes the Western Block and the Central Zone, the Archean Ordos nucleus is found as a thick lithosphere (~200 km), with a relatively low heat flow (40–60 mW/m<sup>2</sup>) and strong negative Bouguer gravity anomalies. In contrast, to the east of the NSGL, within the Eastern Block, the Archean Liaolu nucleus is characterized by a thin lithosphere (~80–110 km), high heat flow (60–80 mW/m<sup>2</sup>), and weak negative to positive regional Bouguer anomalies (Chen et al., 2006; 2008; Griffin et al., 1998a; Hu et al., 2000; Lysak, 2009; Sodoudi et al., 2006; Yuan, 1996; Zhao et al., 2009). In particular, geochemical studies have been conducted on mantle xenoliths from the Paleozoic diamond-bearing kimberlites in Mengyin and Fuxian counties (Griffin et al., 1998a; Zhang et al., 2008; Zheng and Lu, 1999), and from Cenozoic basalts found in the Shanwang, Hebi and Qixia areas (Fan et al., 2000; Gao et al., 2002; Xiao et al., 2010; Xiao and Zhang, 2011; Ying et al., 2006; Zhang, 2005; Zhang et al., 2007; 2010; 2011; Zheng et al., 1998; 2001; 2005a; 2006). Such studies have indicated that the newly accreted fertile lithospheric mantle underplated in the late Mesozoic–Cenozoic lithosphere beneath the Eastern Block; and it has therefore

been proposed that a thick cratonic lithosphere (~200 km) with a cold geotherm (~40 mW/m<sup>2</sup>) was replaced by a thin lithosphere (~80–110 km) with a hot geotherm in the Cenozoic by asthenospheric upwelling.

The study area (in Shanwang, Eastern China) is located within the Tan-Lu fault zone in the Archean Liaolu nucleus. Three episodes of volcanism have occurred, the first eruption occurring in 16.8–18.2 Ma (K-Ar method; Jin, 1985). In the study area, Sr-Nd isotopic analyses of Neogene basalts showed values of  $^{143}\text{Nd}/^{144}\text{Nd} = 0.512744\text{--}0.512967$  and  $^{87}\text{Sr}/^{86}\text{Sr} = 0.70349\text{--}0.70450$  (Zhi et al., 1994). In addition, Sr-Nd isotopic analyses of spinel peridotite xenoliths in eastern China reported the values from a depleted mantle composition ( $^{143}\text{Nd}/^{144}\text{Nd} = 0.5135$ ,  $^{87}\text{Sr}/^{86}\text{Sr} = 0.7035$ ) to an enriched mantle composition ( $^{143}\text{Nd}/^{144}\text{Nd} < 0.51265$  and  $^{87}\text{Sr}/^{86}\text{Sr} > 0.7045$ ; Fan et al., 2000). These results indicate that a depleted mantle source related to asthenospheric upwelling exists beneath this area. Recently, the  $^{187}\text{Re}/^{188}\text{Os}$  values of wehrlite xenoliths had higher values than the lherzolite xenoliths in Shanwang and other Cenozoic basalts, and high  $^{187}\text{Os}/^{188}\text{Os}$  ratios in peridotite xenoliths within the Tan-Lu fault zone were observed (Xiao and Zhang, 2011). As a result, they interpreted that the lherzolite was replaced as wehrlite by a progressive metasomatic change between a lherzolite mantle and an infiltrating metasomatic melt, and that the Tan-Lu fault zone might play an important role as a major melt infiltrating channel for asthenospheric upwelling in the lithospheric mantle beneath the eastern Sino-Korean craton (Xiao et al., 2010; Xiao and Zhang, 2011).

In the Shanwang area, garnet-bearing peridotite xenoliths were found in the lavas of episode 1 volcanism (16.8–18.2 Ma; Jin, 1985), and the equilibrium P-T

condition was estimated to be a pressure of 16–24 kbar and a temperature of 1000–1180 °C by using a combination of a Grt-Opx barometer (Brey and Köhler, 1990) based on Al partitioning, and both the Grt-Cpx (Ravna, 2000b) and the Grt-Opx (O'Neill and Wood, 1979) Fe-Mg exchange thermometers (Zheng et al., 2006). This P-T condition was overlapped the range of values derived for garnet peridotite xenoliths from different Cenozoic basalts in the Nushan area (Xu et al., 1998; 2000), and corresponded well to the surface heat flow (80 mW/m<sup>2</sup>) of the conductive model geotherm in eastern China (Zheng et al., 2006).

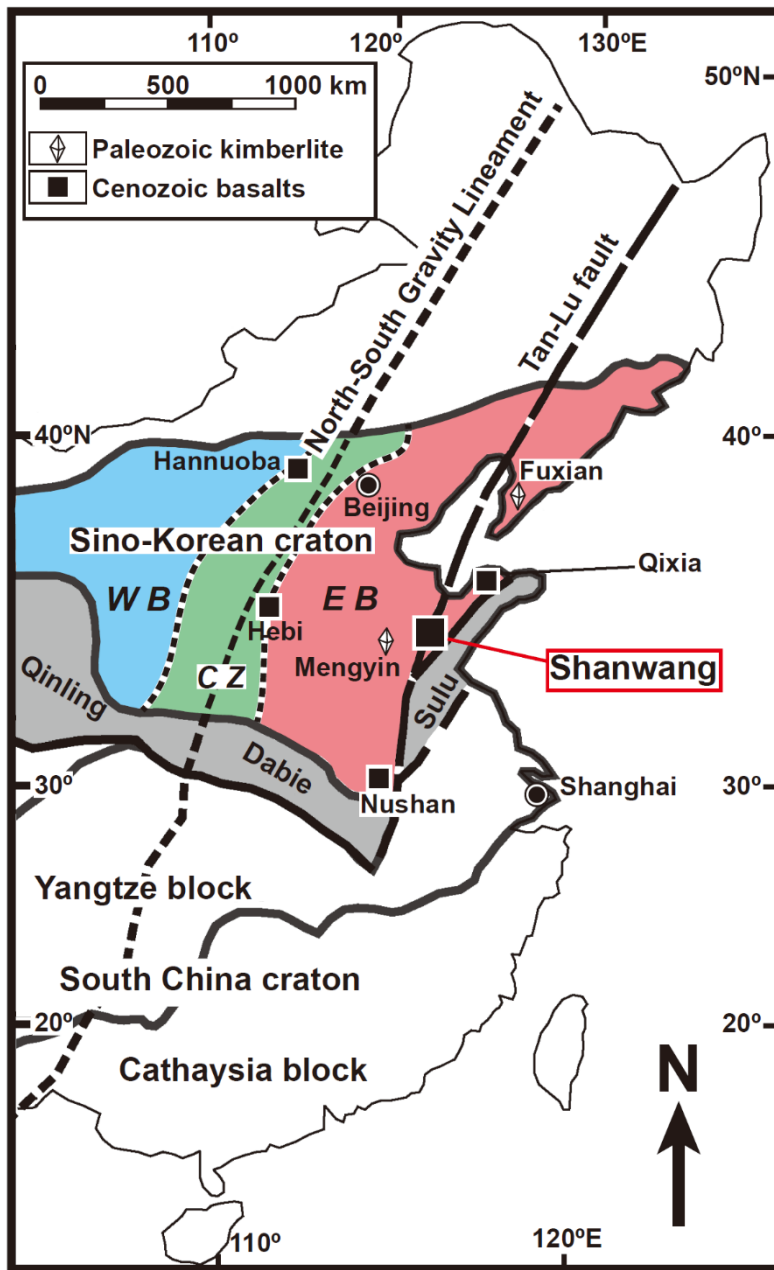


**Figure 2.1.** Simplified geologic map showing the major tectonic setting and study area of Shanwang in eastern China. EB (red area) and WB (blue area) represent the Eastern and Western Blocks of the Sino-Korean craton, respectively. CZ (green area) is the Central Zone and indicates the Trans-North China Orogen (modified after Zheng et al., 2005a; 2005b).

## 2.3. Methods

### 2.3.1. Sample descriptions

Six mantle xenoliths were collected from the lavas of episode 1 volcanism erupted at ~16 Ma in the Shanwang area, eastern China. Petrologically, all samples are spinel lherzolites (samples 565-1, 565-2, and 568) or wehrlites (samples 561, 569, and 570) based on the IUGS scheme (Le Maitre, 2002), and the size of these xenoliths is in the range of 5–13 cm. In the case of lherzolite, samples consist mainly of olivine (58–70 %), clinopyroxene (Cpx, 13–18 %), and orthopyroxene (Opx, 16–27 %), whereas the wehrlite samples consist mainly of olivine (63–83 %) and Cpx (17–37 %), and both include minor minerals such as magnetite and spinel. The optical photomicrographs of representative samples for wehrlite (561) and lherzolite (568) were taken under crossed polarized light, and both samples showed a porphyroclastic texture, elongated grains of olivine and pyroxene, and undulose extinction of olivine (Fig. 2.2a and b). The optical photomicrograph (Fig. 2.2c) and backscattered electron (BSE) image (Fig. 2.2d) show well-developed subgrain boundaries in olivine. Exsolution lamellae of Opx in Cpx porphyroclasts of the wehrlite (Fig. 2.2e and f) suggested a slow cooling event in the lithospheric mantle from originally high temperature of ~1000 °C or above (Kil and Wendlandt, 2004; Robinson et al., 1977; Song and Cao, 2021). Previous studies suggested that the wehrlite prevailing in the Cenozoic basalts in eastern China was replaced from the lherzolite by a progressive metasomatic change between lherzolitic mantle and an infiltrating melt (Xiao et al., 2010; Xiao and Zhang, 2011). The wehrlite samples in

this study also showed metasomatic textures such as sieve-textured clinopyroxene, fluid inclusion trails trapped in healed cracks of olivine, and reaction zones between olivine and clinopyroxene, and showed a few metasomatic minerals such as amphibole (Fig. 2.3a–d). In contrast, the lherzolite samples hardly showed metasomatic textures and showed clear olivine grains without fluid inclusion trails and pyroxene grains without cleavage (Fig. 2.3e and f). Although the lack of garnet in the xenoliths indicates that samples came from below 60 km depth, Zheng *et al.* (2006) reported the garnet-bearing lherzolites and the garnet coexisting with spinel in the peridotite xenoliths, suggesting that samples were derived from the garnet-spinel transition zone (~60–80 km) beneath the Shanwang area. This range of depth is within the lithosphere in the eastern Sino-Korean craton. There are many geochemical studies indicating that the Shanwang xenoliths were derived from the newly accreted lithospheric mantle underplated in the late Mesozoic–Cenozoic lithosphere (Xiao *et al.*, 2010; Xiao and Zhang, 2011; Zhang *et al.*, 2007; Zheng *et al.*, 1998; 2005a; 2005b; 2006).

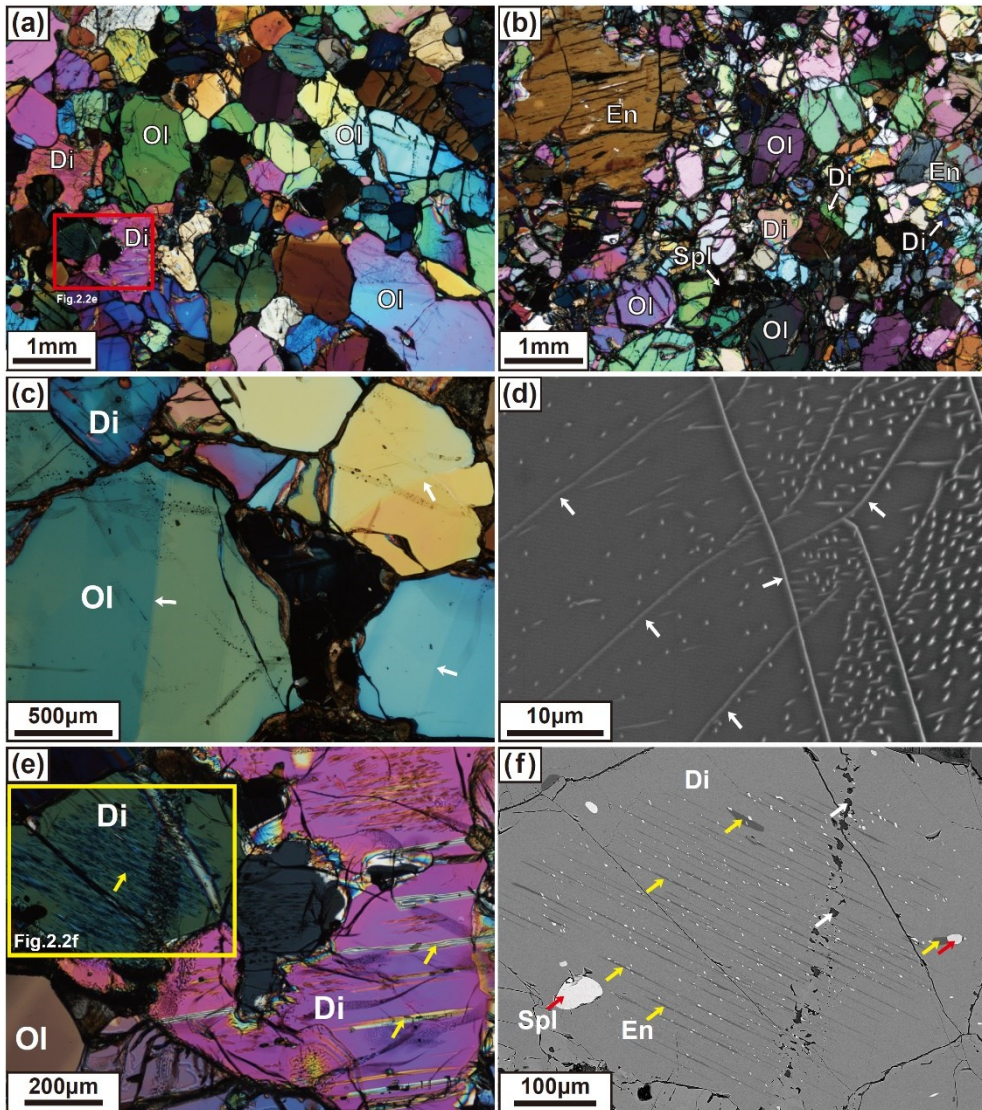


**Figure 2.2.** Optical photomicrograph of representative samples of lherzolite and wehrlite. **(a)** and **(b)** Optical photomicrograph of XZ plane using cross-polarized light showing a porphyroclastic texture for **(a)** wehrlite (sample 561) and **(b)** lherzolite (sample 568). Ol: olivine, Di: diopside, En: enstatite, and Spl: spinel. **(c)** Optical photomicrograph showing undulose extinctions (white arrows) of olivine (sample 561). **(d)** Backscattered electron (BSE) image showing dislocation microstructures within olivine (sample 561). The white arrows indicate subgrain boundaries. **(e)** Optical photomicrograph showing exsolution lamellae of Opx (yellow arrows) in Cpx porphyroclasts (sample 561). **(f)** BSE image showing exsolution lamellae of Opx (yellow arrows) and spinels (red arrows) in Cpx (sample 561). The white arrows indicate the holes where the fluid inclusions existed.

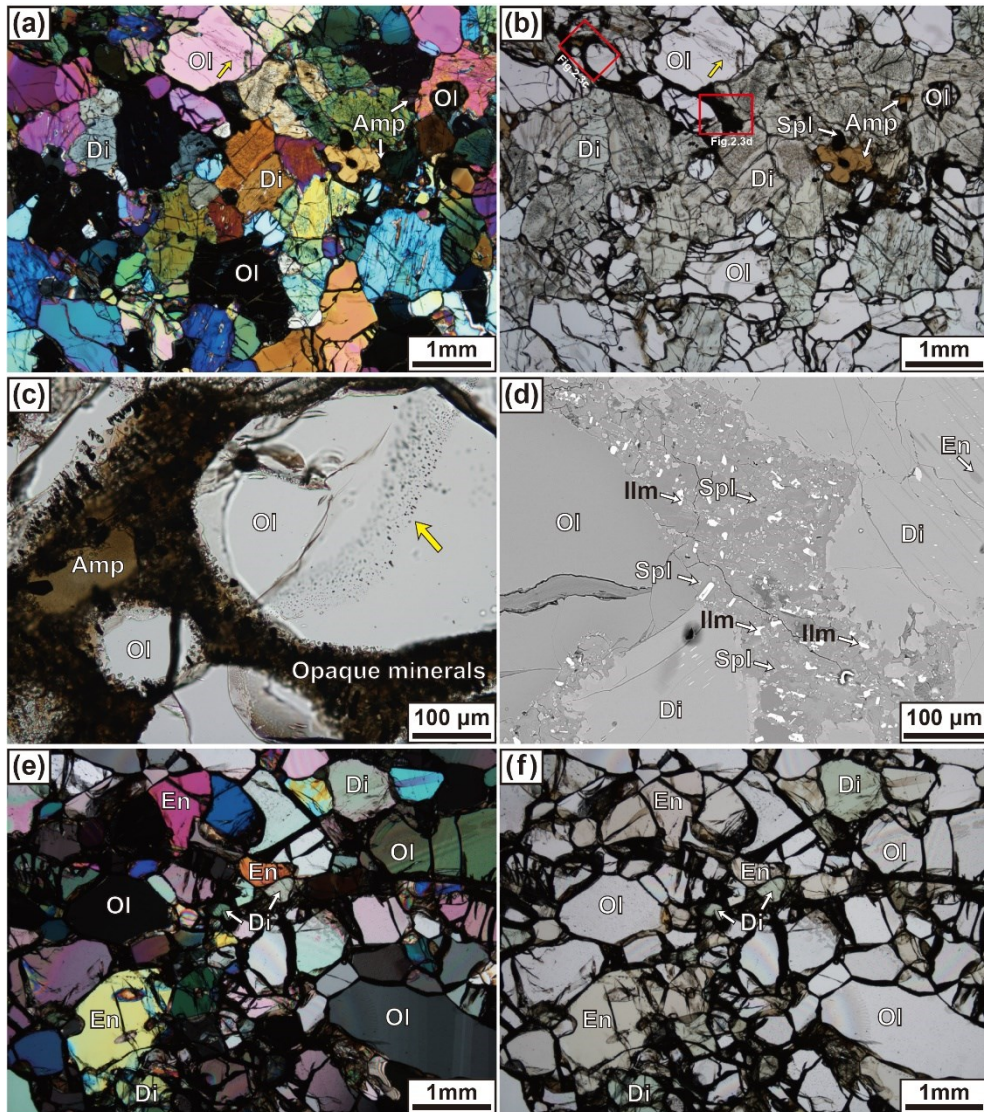


**Figure 2.3.** Optical photomicrograph of wehrlite showing metasomatic textures and lherzolite without metasomatic textures. **(a)** Cross-polarized and **(b)** plane-polarized optical photomicrographs of wehrlite (sample 561) showing sieve-textured clinopyroxene (diopside). **(c)** Plane-polarized optical photomicrograph of wehrlite (sample 561) showing fluid inclusion trail in olivine, and reaction zone around grain boundary. In **(a)** to **(c)**, yellow arrow indicates fluid inclusion trail trapped in healed crack of olivine. **(d)** BSE image of wehrlite (sample 561) showing reaction zone between olivine and diopside. **(e)** Cross-polarized and **(f)** plane-polarized optical photomicrographs of lherzolite (sample 565-1) showing clear olivine grains without fluid inclusion trails and pyroxene grains without cleavage. Ol: olivine, Di: diopside, En: enstatite, Spl: spinel, Amp: amphibole, and Ilm: ilmenite.

### 2.3.2. Determination of lattice preferred orientation (LPO)

Electron backscattered diffraction (EBSD) patterns were used to determine the LPOs of olivine, Opx, and Cpx from a thin section of sample (Jung et al., 2006; 2010; Prior et al., 1999). HKL's EBSD system with a Nordlys II detector attached to the scanning electron microscope (SEM, JEOL JSM 6380) was used in this study, and the analysis was performed at the School of Earth and Environmental Sciences (SEES), Seoul National University (SNU), South Korea. Foliation of the samples was determined by both compositional layering of pyroxene and the shape-preferred orientation of deformed grains, such as elongated grains of pyroxene (Passchier and Trouw, 1996). Lineation of the samples was determined by grain shape analysis of digitized lines from the elongated olivine and pyroxene grain boundaries in the foliation plane, using the method of Panozzo (1983; 1984). According to the grain shape analysis method, digitized lines were transformed into ellipsoidal shapes, and the angle ( $\alpha$ ) of major axis for each ellipsoid was measured by counterclockwise from the horizontal reference frame ( $0^\circ \leq \alpha < 180^\circ$ ; Fig. 2.4b). Then, the angle was applied as a coefficient to an equation ( $A(\alpha)$ ) for total length of the two-dimensional outline projection ( $0 < A(\alpha) \leq 1$ ). In this method, the angle where total length has a maximum value ( $A(\alpha) = 1$ ) indicates the direction of lineation (Fig. 2.4c).

The LPO of the mineral was measured in the XZ plane of thin section, where the X- and Z-directions coincide with the lineation and the direction normal to the foliation, respectively. Thin sections of samples were polished using 600-, 3000-,

and 6000-mesh polishing powders, and 1  $\mu\text{m}$  diamond paste. The sections were then polished using Syton (0.06- $\mu\text{m}$  colloidal silica slurry) to remove mechanical surface damage using a chemical/mechanical polishing technique (Lloyd, 1987). To prevent charging in the SEM, the thin sections were coated with  $\sim 3$  nm carbon after polishing. The section surface was tilted at  $70^\circ$  to the incident electronic beam in the chamber, and the conditions of EBSD analysis were as follows: 20 kV accelerating voltage, 15 mm working distance, and 60 spot size. All EBSD patterns were manually indexed for accuracy using HKL's Channel 5 software at the Tectonophysics Laboratory, SEES, at SNU.

After EBSD analysis, the uncorrelated grain pairs were determined from the data and the fabric strength of the sample was estimated by calculating the misorientation index (M-index; Skemer et al., 2005). The M-index is defined as:

$$M = 0.5 \int |R^T(\varphi) - R^O(\varphi)| d\varphi \quad (2.1)$$

where  $R^T(\varphi)$  is the theoretical distribution of uncorrelated misorientation angles for a random fabric,  $R^O(\varphi)$  is the observed distribution of uncorrelated misorientation angles for a real fabric from EBSD data, and  $\varphi$  is the misorientation angle of uncorrelated grain pair (Skemer et al., 2005). This M-index ranges from 0 (a random fabric) to 1 (a single crystal fabric).

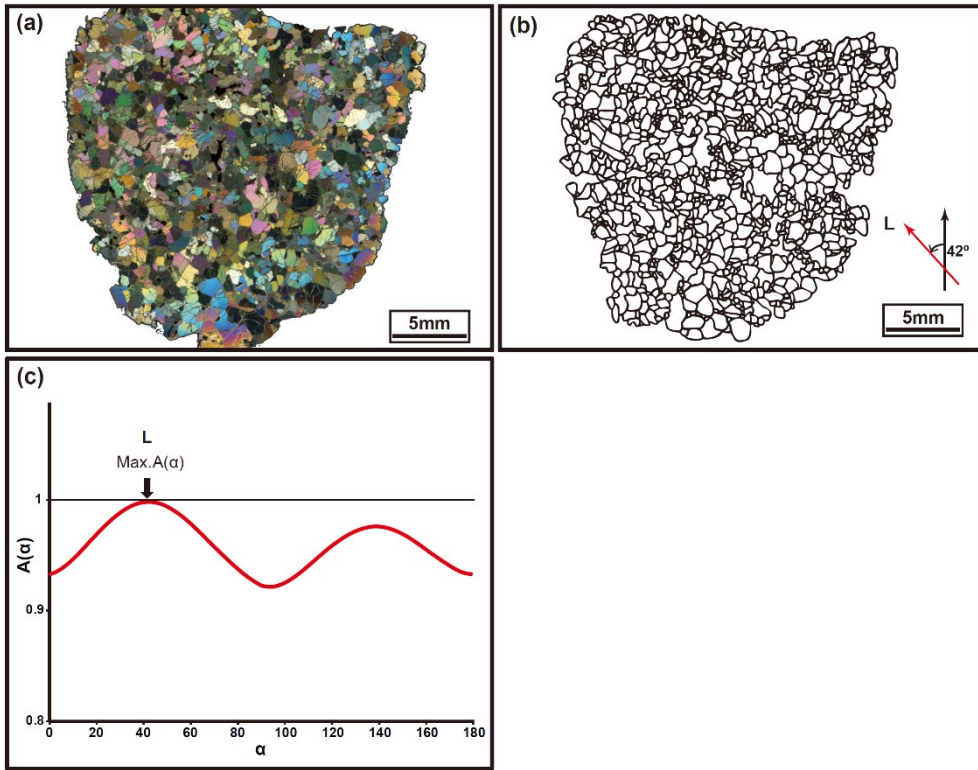


**Figure 2.4.** The details of grain shape analysis to determine lineation in sample. **(a)** Optical photomicrograph of sample (565-2) under cross-polarized light. The thin section was made in the foliation which was determined by compositional layering. **(b)** The grain boundaries for elongated olivine and pyroxene in the foliation were drawn on the OHP film, then the film was scanned to obtain the digitized lines of grain boundaries. The red arrow indicates the lineation determined by the grain shape analysis in (c). The black arrow indicates the original reference frame. L: lineation. **(c)** The method how to determine the lineation following grain shape analysis (Panozzo, 1984; 1983).  $\alpha$ : angle of the rotated line or set of lines, which is measured counterclockwise from the original reference frame indicated by black arrow in (b) ( $0^\circ \leq \alpha < 180^\circ$ ),  $A(\alpha)$ : total length of the projection of two-dimensional outline of shape ( $0 < A(\alpha) \leq 1$ ). The angle  $\alpha$  where  $A(\alpha)$  has a maximum ( $A(\alpha) = 1$ ) indicates the direction of lineation (L).

### 2.3.3. Calculation of the seismic velocity and anisotropy

The seismic velocity and anisotropy of each mineral were calculated using both the LPO data from the EBSD analysis and the petrophysics software (Mainprice, 1990) with the Voigh-Reuss-Hill (VRH) averaging scheme. The software solves the Christoffel equation to calculate the seismic velocity and anisotropy using both the macroscopic elastic tensor  $\langle C_{ij} \rangle$  and the density of whole rock. The macroscopic elastic tensor was calculated by integrating elastic stiffness coefficients ( $C_{ij}$ ) of all single-crystal minerals for all orientations of grains which were obtained as triplet of Euler angle in the EBSD analysis. In this chapter, elastic coefficients of single-crystal for olivine (Abramson et al., 1997), enstatite (Chai et al., 1997), and diopside (Collins and Brown, 1998) were used. The density of bulk rock can average from densities and volume proportions of constituent minerals. The azimuthal anisotropy of P-wave ( $AV_p$ ) was calculated as:

$$AV_p = 200 \times [(V_{p_{\max}} - V_{p_{\min}}) / (V_{p_{\max}} + V_{p_{\min}})] (\%) \quad (2.2)$$

where  $V_{p_{\max}}$  and  $V_{p_{\min}}$  are the maximum and minimum P-wave velocity, respectively.

The polarization anisotropy of shear wave ( $AV_s$ ) was calculated as:

$$AV_s = 200 \times [(V_{s1} - V_{s2}) / (V_{s1} + V_{s2})] (\%) \quad (2.3)$$

where  $V_{s1}$  and  $V_{s2}$  are the fast and slow S-wave velocity, respectively (Birch, 1960; Ji and Xia, 2002).

### 2.3.4. Estimation of paleostress

To estimate stress magnitude, the free dislocation density of olivine in samples was observed using the oxidation decoration technique (Jung and Karato, 2001b; Karato, 1987; Karato and Lee, 1999; Karato and Jung, 2003). The samples were decorated with oxygen for 1 hour at 800 °C (Kohlstedt et al., 1976b) to observe the dislocation microstructure using a SEM, and polished using Syton to remove the thin oxide layer on the surface. The decorated samples were coated with carbon after polishing, and the dislocations in olivine were imaged as a BSE image using the SEM (JEOL JSM 6380) in SEES, SNU, with the following conditions of 15 kV accelerating voltage, 10 mm working distance, 20 nA beam current, and 60 spot size. The relationship between dislocation density and stress is now shown as:

$$\sigma_1 - \sigma_3 = \alpha \cdot \mu \cdot b \cdot \rho^{(1/2)} \quad (2.4)$$

where  $\sigma_1$  is the maximum principal stress,  $\sigma_3$  is the minimum principal stress,  $\alpha$  is a numerical parameter,  $\mu$  is the shear modulus,  $b$  is the length of the Burgers vector of dislocation, and  $\rho$  is the free dislocation density (Kohlstedt and Goetze, 1974; Kohlstedt et al., 1976a). In this chapter, the values of  $\alpha$ ,  $\mu$ , and  $b$  were referred from those presented in several papers, to ensure the validity of estimated results (Bai and Kohlstedt, 1992; Goetze and Kohlstedt, 1973; Jung and Karato, 2001b; Karato and Jung, 2003; Kohlstedt and Goetze, 1974; Kohlstedt et al., 1976a). Dislocation densities were measured from 30 grains of each sample using a “first principle” method as:

$$\rho = \sum l / V \quad (2.5)$$

where  $\sum l$  is the total length of dislocations in a volume  $V$ , which were then averaged to obtain the stress of the samples (Karato and Lee, 1999).

Stress magnitudes in the samples were also estimated from the relationship between stress and recrystallized olivine grain size. To use the recrystallized grain size piezometer (Jung and Karato, 2001a; Karato et al., 1980; Van der Wal et al., 1993), the average recrystallized grain size in olivine were measured using the linear intercept method in two dimensions, and were then multiplied by the same correction factor of 1.5 for three-dimensional grain sizes (Gifkins, 1970; Russ and Dehoff, 2000).

### **2.3.5. Measurement of water content**

The water content (or hydroxyl concentration) of olivine, Opx, and Cpx for each sample was measured using Fourier transformation infrared (FTIR) spectroscopy. In this chapter, a Nicolet 6700 FTIR spectrometer with a Continuum IR microscope at the Tectonophysics Laboratory, SEES in SNU was used. All samples were polished on both sides down to a thickness of 83–275  $\mu\text{m}$ , and they were dried in an oven at 120  $^{\circ}\text{C}$  for more than 24 hours before measurement of water content. The water content within a single crystal was measured by focusing the IR beam (aperture size of 50 $\times$ 50  $\mu\text{m}$ ) on clean areas without cracks and grain boundaries using unpolarized transmitted light, and a KBr beam-splitter and a mercury cadmium telluride (MCT) detector with OMNIC software were used.  $\text{N}_2$  gas was flushed to eliminate moisture from the atmosphere by purging the sample chamber during FTIR measurements. A series of 128 scans were accumulated for each FTIR spectrum, with a resolution of 4  $\text{cm}^{-1}$ . The water content was calculated using the Peterson's calibration (1982) for the range of wave numbers 3100–4000  $\text{cm}^{-1}$ , because the range is dominated by the O-H bonds stretching vibrations (Paterson, 1982). The water content was determined by averaging the values of 10–15 grains for each sample.

## 2.4. Results

### 2.4.1. LPOs of olivine, enstatite, and diopside

The LPOs of olivine, enstatite, and diopside are shown in the pole figure (Figs. 2.5 to 2.7), and LPO types of olivine and enstatite are summarized in Table 2.1. In lherzolite samples (565-1, 565-2, and 568), the crystallographic [001] axes of olivine were aligned subparallel to the lineation, and the [010] axes were strongly aligned subnormal to the foliation (Fig. 2.5a). This fabric is similar to the type-B LPO of olivine, which is found under high stress and/or a moderate–high water content (Jung and Karato, 2001b; Jung et al., 2006; Katayama et al., 2004). On the other hand, in wehrlite samples (561, 569, and 570), the crystallographic [100] axes of olivine were aligned subparallel to the lineation, and the [001] axes were aligned subnormal to the foliation (Fig. 2.5b). This fabric is similar to type-E LPO of olivine, which is found at low stress and moderate water content (Jung and Karato, 2001b; Jung et al., 2006; Katayama et al., 2004).

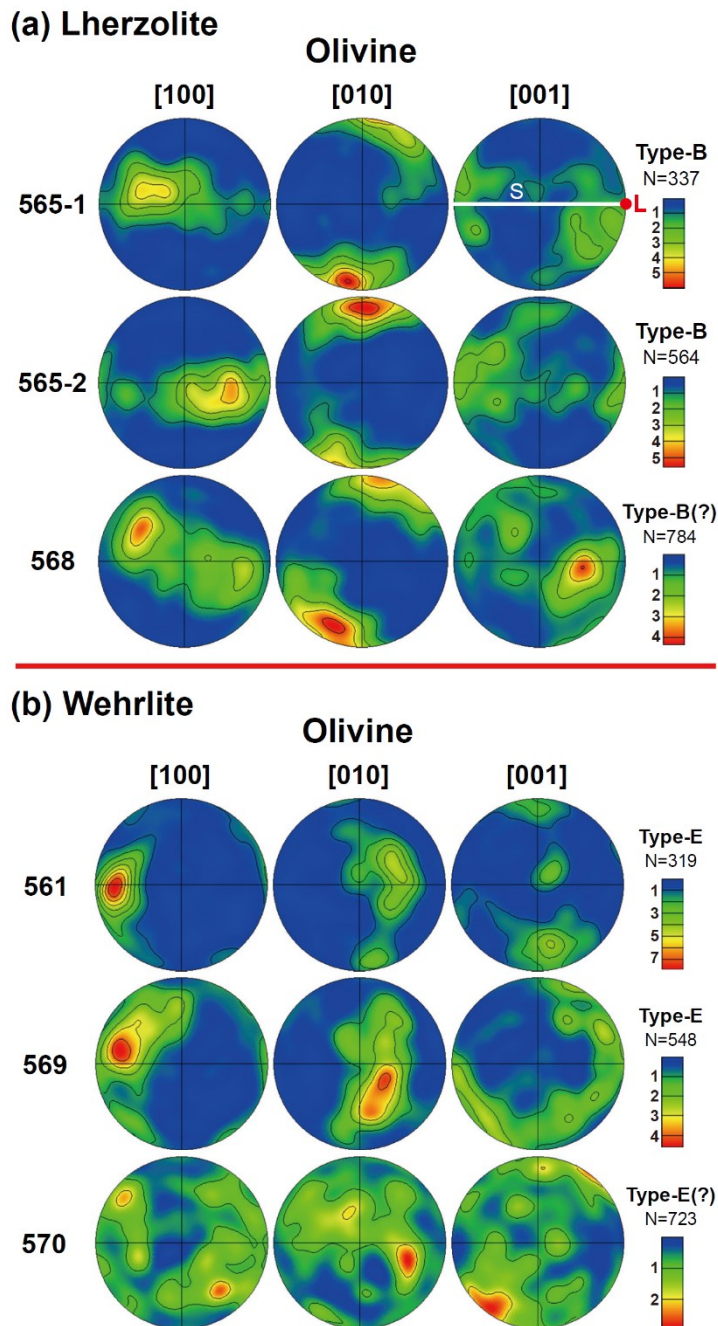


**Figure 2.5.** Pole figures of olivine in **(a)** lherzolite samples (565-1, 565-2, and 568) and **(b)** wehrlite samples (561, 569, and 570). Pole figures are presented in the lower hemisphere using an equal-area projection. A half-scatter width of  $20^\circ$  was used. The color coding refers to the density of data points (contours in the pole figures correspond to the multiples of uniform distribution). S: foliation, L: lineation, and N: number of grains.

**Table 2.1.** Results of modal composition, LPOs, and fabric strength (M-index).

Sample	Analyzed modal composition			Type of LPOs <sup>1</sup>			M-index <sup>2</sup>		
	OI (%)	Opx (%)	Cpx (%)	OI	Opx		OI	Opx	Cpx
561	62.9	-	37.1	E	-		0.157	-	0.057
565-1	58.4	27.0	14.6	B	BC		0.156	0.053	0.103
565-2	69.7	17.8	12.5	B	~BC		0.165	0.055	0.109
568	66.7	15.8	17.5	~B	AC		0.117	0.057	0.056
569	79.2	-	20.8	~E	-		0.134	-	0.083
570	82.9	-	17.1	~E	-		0.037	-	0.229

<sup>1</sup> LPO types of olivine (OI) and enstatite (Opx) were classified by Jung *et al.* (2006) and Jung *et al.* (2010), respectively.

<sup>2</sup> The M-index was calculated using the uncorrelated grain pairs determined from LPO data (Figs. 2.4 to 2.6) showing the fabric strength of minerals (Skemer *et al.*, 2005).

The LPO of enstatite was classified into two different types: type-AC and type-BC (Fig. 2.6). The LPO of enstatite for sample 568 is type-AC, which is characterized as the crystallographic [001] axes of enstatite aligned subparallel to the lineation and the [100] axes aligned subnormal to the foliation (Fig. 2.6). This fabric has frequently been reported (Christensen and Lundquist, 1982; Jung et al., 2010). On the other hand, the LPO of enstatite for samples 565-1 and 565-2 is type-BC, which is characterized as the crystallographic [001] axes of enstatite aligned subparallel to the lineation and the [010] axes aligned subnormal to the foliation (Fig. 2.6). This fabric has rarely been reported (Jung et al., 2010).

The diopside in the samples showed four different types of LPOs (Figs. 2.7). In the sample 565-1, the crystallographic (010) poles of diopside were aligned subparallel to the lineation and the [001] axes were aligned subnormal to the foliation (Fig. 2.7a). In the sample 565-2, the [001] axes of diopside were aligned subparallel to the lineation and the (010) poles were aligned subnormal to the foliation (Fig. 2.7a). In the samples 568 and 569, the [100] axes of diopside were aligned subparallel to the lineation and the [001] axes were strongly aligned subnormal to the foliation (Fig. 2.7). In the sample 561, the [001] axes of diopside were strongly aligned subparallel to the lineation of the rock, and the [100] axes weakly aligned subnormal to the foliation (Fig. 2.7b). Although diopside in the sample 570 unexpectedly showed the strongest LPO of all samples, this was attributed to the large porphyroclasts (3 to 5 mm in diameter) of the diopside (Fig. 2.7b).

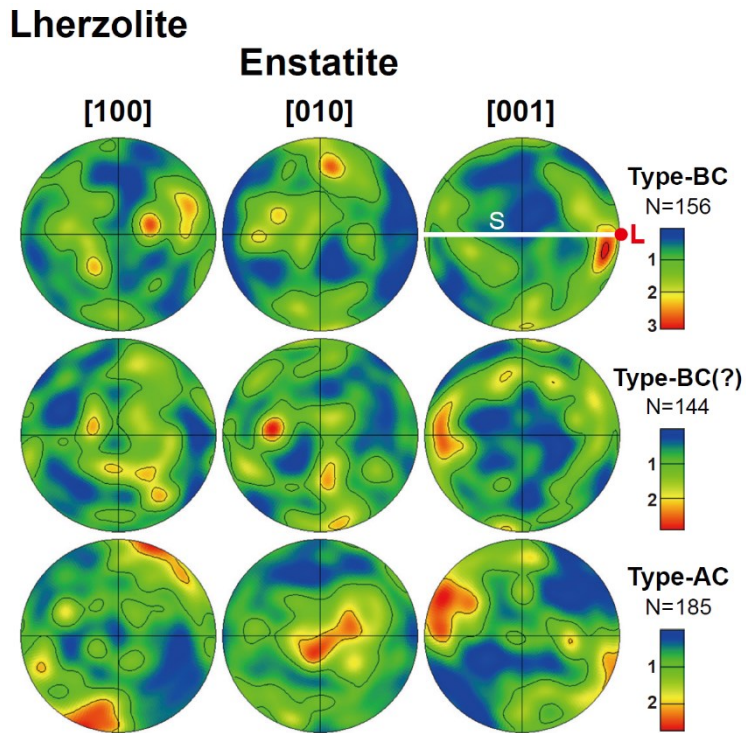


**Figure 2.6.** Pole figures of enstatite (orthopyroxene, Opx) in lherzolite samples (565-1, 565-2, and 568). Pole figures are presented in the lower hemisphere using an equal-area projection. A half-scatter width of  $20^\circ$  was used. The color coding refers to the density of data points (contours in the pole figures correspond to the multiples of uniform distribution). S: foliation, L: lineation, and N: number of grains.

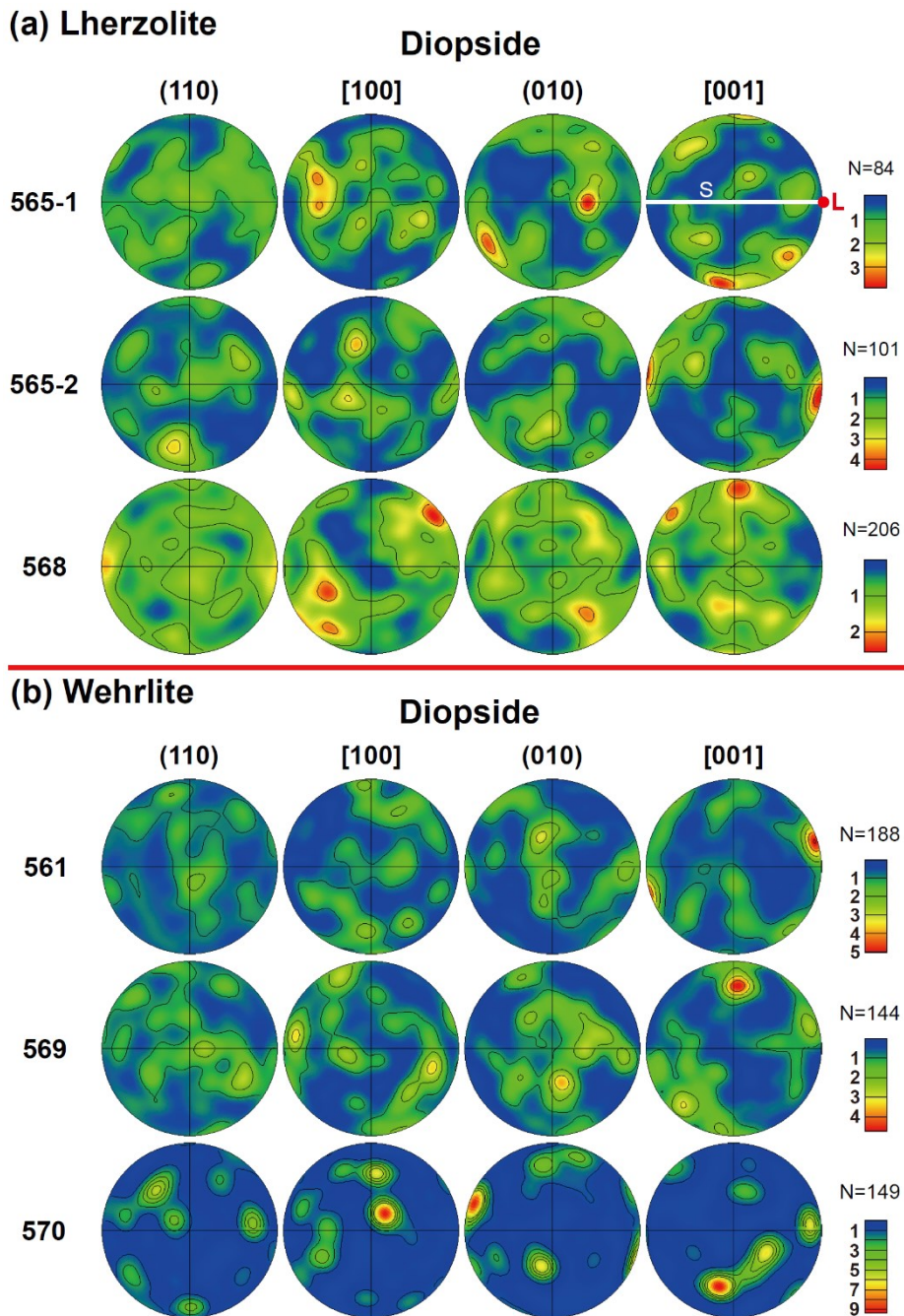


**Figure 2.7.** Pole figures of diopside (clinopyroxene, Cpx) in **(a)** lherzolite samples (565-1, 565-2, and 568) and **(b)** wehrlite samples (561, 569, and 570). Pole figures are presented in the lower hemisphere using an equal-area projection. A half-scatter width of  $20^\circ$  was used. The color coding refers to the density of data points (contours in the pole figures correspond to the multiples of uniform distribution). S: foliation, L: lineation, and N: number of grains.

## 2.4.2. Seismic anisotropy of minerals and whole rocks

The seismic anisotropies of P- and S-waves ( $AV_p$  and  $AV_s$ ) for olivine, enstatite, and diopside are shown in Figs. 2.8 to 2.10, and summarized in Table 2.2. The azimuthal anisotropy of P-wave ( $AV_p$ ) was in the range of 2.2–11.6 % for olivine, 1.2–2.3 % for enstatite, and 2.1–6.4 % for diopside. The maximum polarization anisotropy of the shear wave (Max.  $AV_s$ ) was in the range of 1.93–7.53 % for olivine, 1.53–2.46 % for enstatite, and 1.81–6.57 % for diopside (Table 2.2). In the samples of olivine showing a type-B LPO (lherzolites for 565-1, 565-2, and 568), the polarization direction of the fast S-wave ( $V_{s1}$ ) was subnormal to the lineation for the vertically propagating S-waves (Fig. 2.8a). In contrast, the polarization direction of  $V_{s1}$  for olivine with a type-E LPO (wehrlites for 561, 569, and 570) was subparallel to lineation (Fig. 2.8b). For enstatite, all  $V_{s1}$  polarization directions were subparallel to lineation (Fig. 2.9). The diopside in the lherzolites was subnormal to lineation for the vertically propagating S-wave which was the same in the case of olivine (Fig. 2.10a), whereas that of diopside in the wehrlites ensured that the polarization direction of  $V_{s1}$  was subparallel to lineation (Fig. 2.10b).

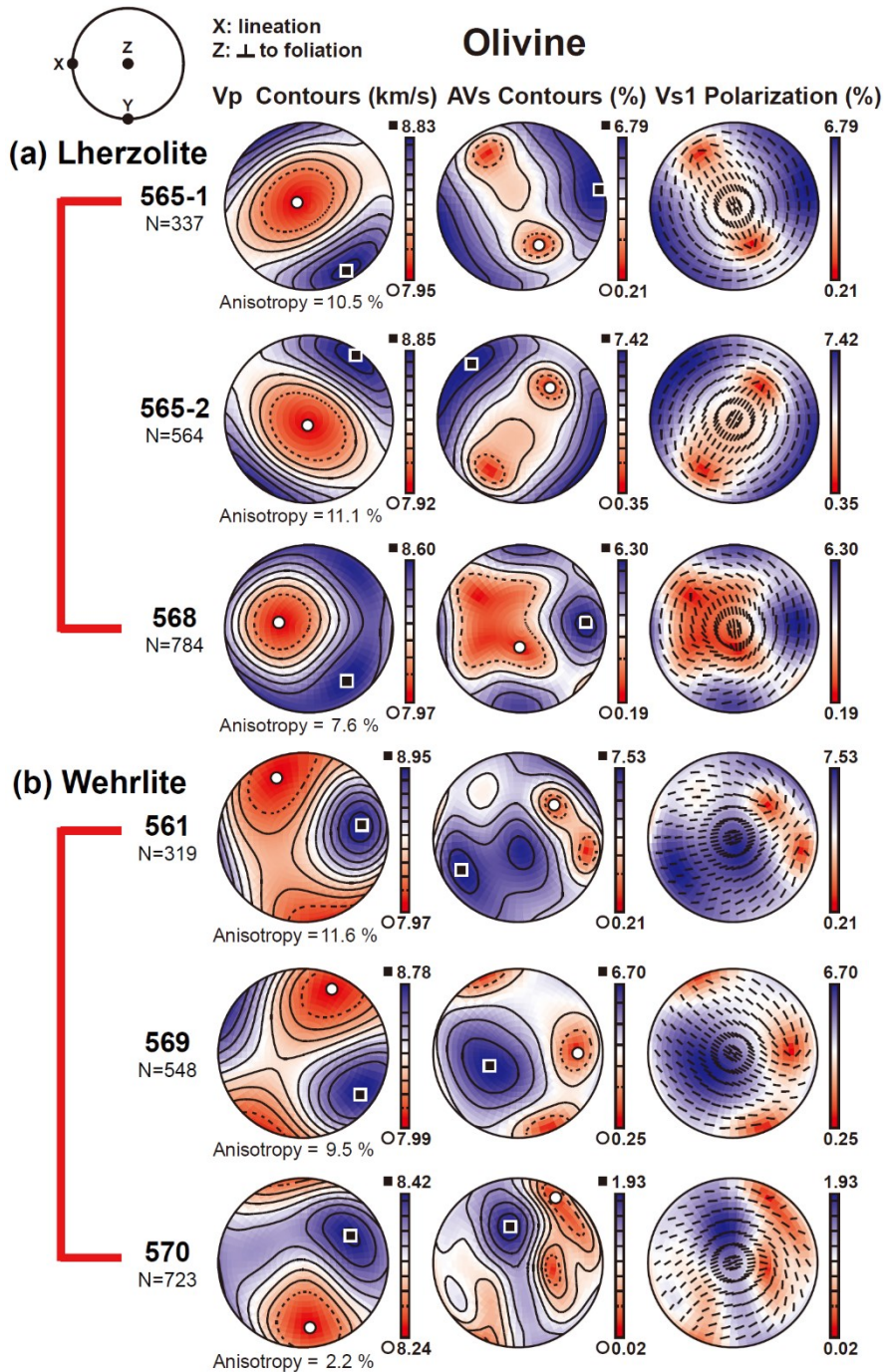


**Figure 2.8.** Seismic anisotropy of olivine in **(a)** lherzolite samples (565-1, 565-2, and 568) and **(b)** wehrlite samples (561, 569, and 570). The E-W direction and the center of the stereographic projection correspond to the lineation (X) and the direction normal to the foliation (Z), respectively. Black square: the maximum values in each contour, open circle: the minimum value in each contour.

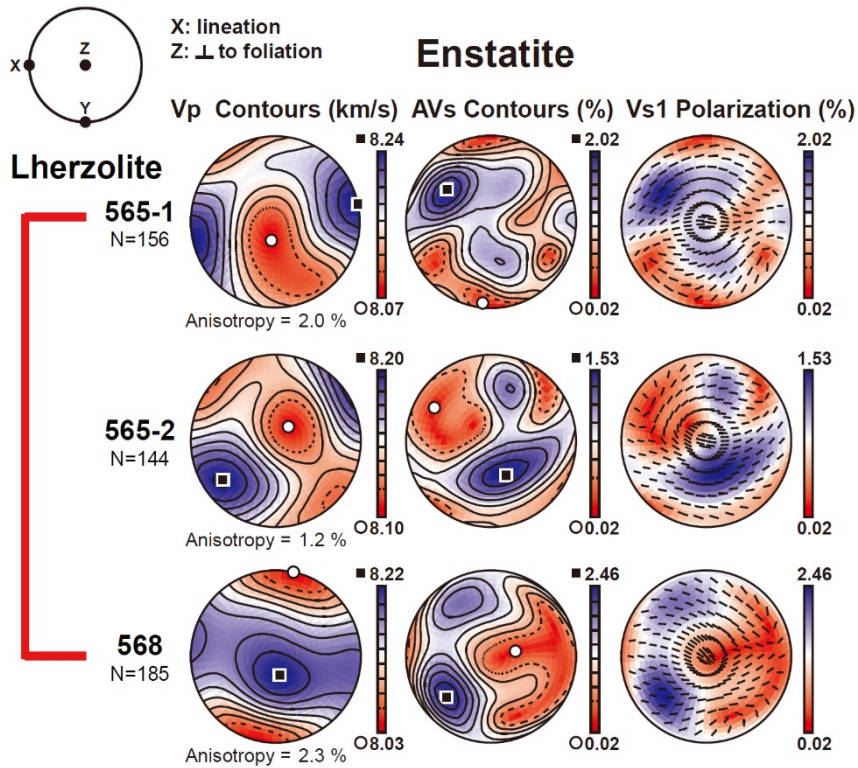


**Figure 2.9.** Seismic anisotropy of enstatite (Opx) in lherzolite samples (565-1, 565-2, and 568). The E-W direction and the center of the stereographic projection correspond to the lineation (X) and the direction normal to the foliation (Z), respectively. Black square: the maximum values in each contour, open circle: the minimum value in each contour.

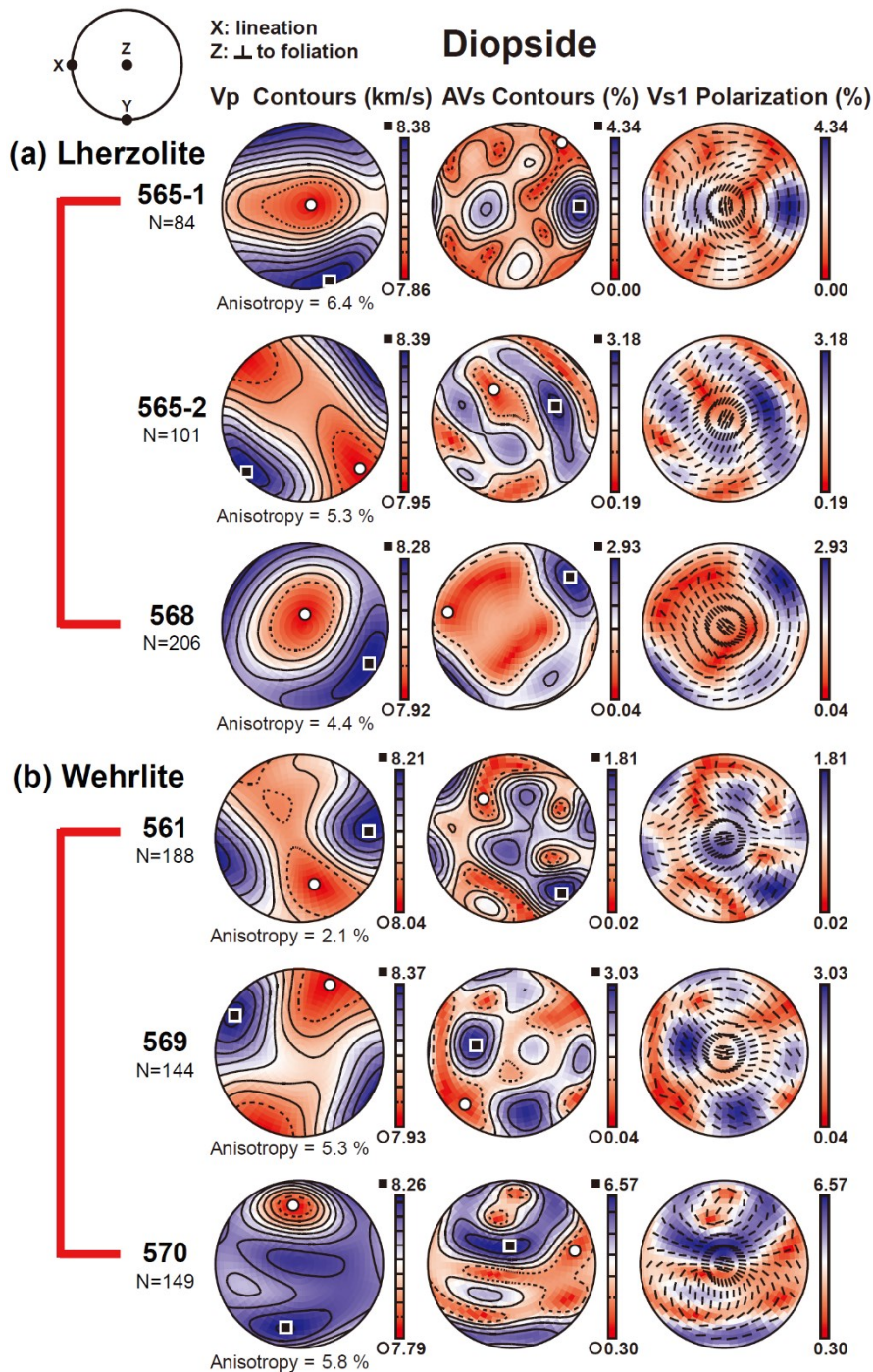


**Figure 2.10.** Seismic anisotropy of diopside (Cpx) in **(a)** lherzolite samples (565-1, 565-2, and 568) and **(b)** wehrlite samples (561, 569, and 570). The E-W direction and the center of the stereographic projection correspond to the lineation (X) and the direction normal to the foliation (Z), respectively. Black square: the maximum values in each contour, open circle: the minimum value in each contour.

After combining the seismic anisotropy of all minerals for each sample based on the analyzed modal composition in Table 2.1, all contours and polarization directions of the fast S-wave ( $V_{s1}$ ) were found to be similar to those of olivine (Fig. 2.11). However, the anisotropy of P-wave and the maximum anisotropy of S-wave were reduced to 1.9–8.4 % and 2.48–5.70 %, respectively (Table 2.2). As a result, the seismic anisotropies of the whole rocks for each sample were lower than that of olivine because of the additional orientation data of enstatite and diopside, except for those in sample 570, where the seismic anisotropy of diopside was unexpectedly stronger than that of olivine.

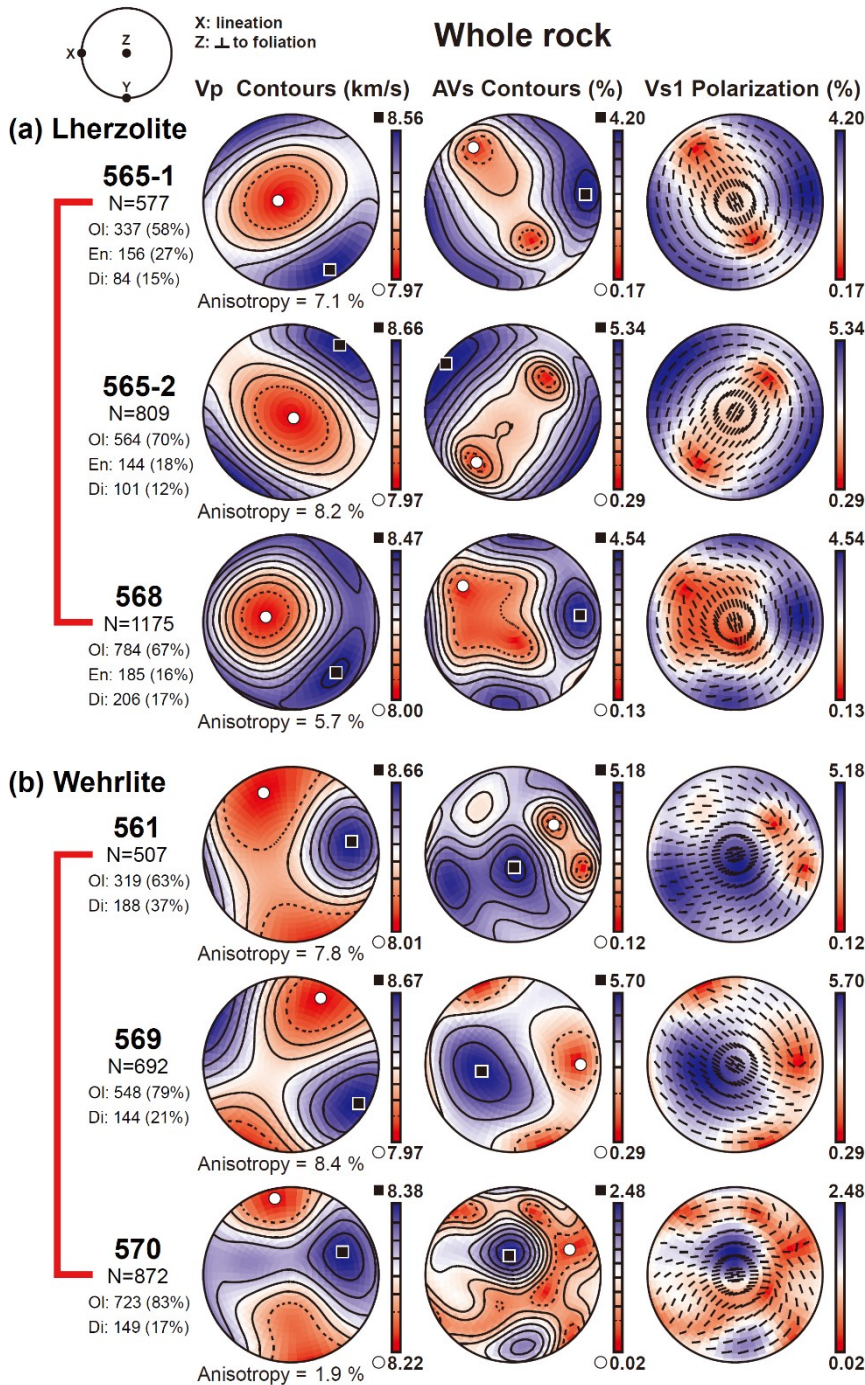


**Figure 2.11.** Seismic anisotropy of whole rock for **(a)** lherzolite samples (565-1, 565-2, and 568) and **(b)** wehrlite samples (561, 569, and 570). The E-W direction and the center of the stereographic projection correspond to the lineation (X) and the direction normal to the foliation (Z), respectively. Black square: the maximum values in each contour, open circle: the minimum value in each contour.

**Table 2.2.** Seismic anisotropies of P- and S-waves for olivine, enstatite (Opx), diopside (Cpx), and whole rock.

Sample	Olivine		Opx		Cpx		Whole rock <sup>1</sup>	
	AVp (%)	Max. AVs (%)	AVp (%)	Max. AVs (%)	AVp (%)	Max. AVs (%)	AVp (%)	Max. AVs (%)
561	11.6	7.53	-	-	2.1	1.81	7.8	5.18
565-1	10.5	6.79	2.0	2.02	6.4	4.34	7.1	4.20
565-2	11.1	7.42	1.2	1.53	5.3	3.18	8.2	5.34
568	7.6	6.30	2.3	2.46	4.4	2.93	5.7	4.54
569	9.5	6.70	-	-	5.3	3.03	8.4	5.70
570	2.2	1.93	-	-	5.8	6.57	1.9	2.48

<sup>1</sup> The seismic anisotropy of whole rock was calculated following the analyzed modal compositions of each sample in Table 2.1.

AVp: the azimuthal seismic anisotropy of P-wave, Max. AVs: the maximum polarization seismic anisotropy of S-wave.

### 2.4.3. Paleostress estimation of sample

The stress of samples was estimated using the relationship between the free dislocation density and stress and using the recrystallized grain-size piezometer (as demonstrated in Chapter 2.3.4). Dislocation microstructures in olivine are shown in Fig. 2.12. In the samples showing olivine type-E LPO, well-developed subgrain boundaries were observed in a large fraction of the grains. In contrast, few subgrain boundaries and mostly straight dislocations were observed in samples with type-B olivine LPO. Using Equation 2.4 and different constants from several papers, the stress of each sample was estimated and then those of samples were compared to each other (Table 2.3). Using Equation 2.5, the free dislocation density ( $\rho$ ) of the samples was calculated to be between  $0.270 \times 10^{12} \text{ m}^{-2}$  and  $0.384 \times 10^{12} \text{ m}^{-2}$ . This result led us to calculate the stress of samples as being in the range  $62\text{--}74 \pm 20 \text{ MPa}$  by following the values of Goetze and Kohlstedt (1973),  $51\text{--}60 \pm 20 \text{ MPa}$  by Kohlstedt and Goetze (1974),  $39\text{--}51 \pm 20 \text{ MPa}$  by Bai and Kohlstedt (1992), and  $50\text{--}64 \pm 20 \text{ MPa}$  by Jung and Karato (2001b). In addition, the stresses obtained from the recrystallized grain-size piezometer (Jung and Karato, 2001a) were estimated to be  $\sigma = 18 \pm 6 \text{ MPa}$  and  $\sigma = 44 \pm 13 \text{ MPa}$  for samples with an olivine type-E LPO (561) and olivine type-B LPO (565-1), respectively. These results show that the sample with an olivine type-B LPO deformed at relatively higher stress than that with an olivine type-E LPO.

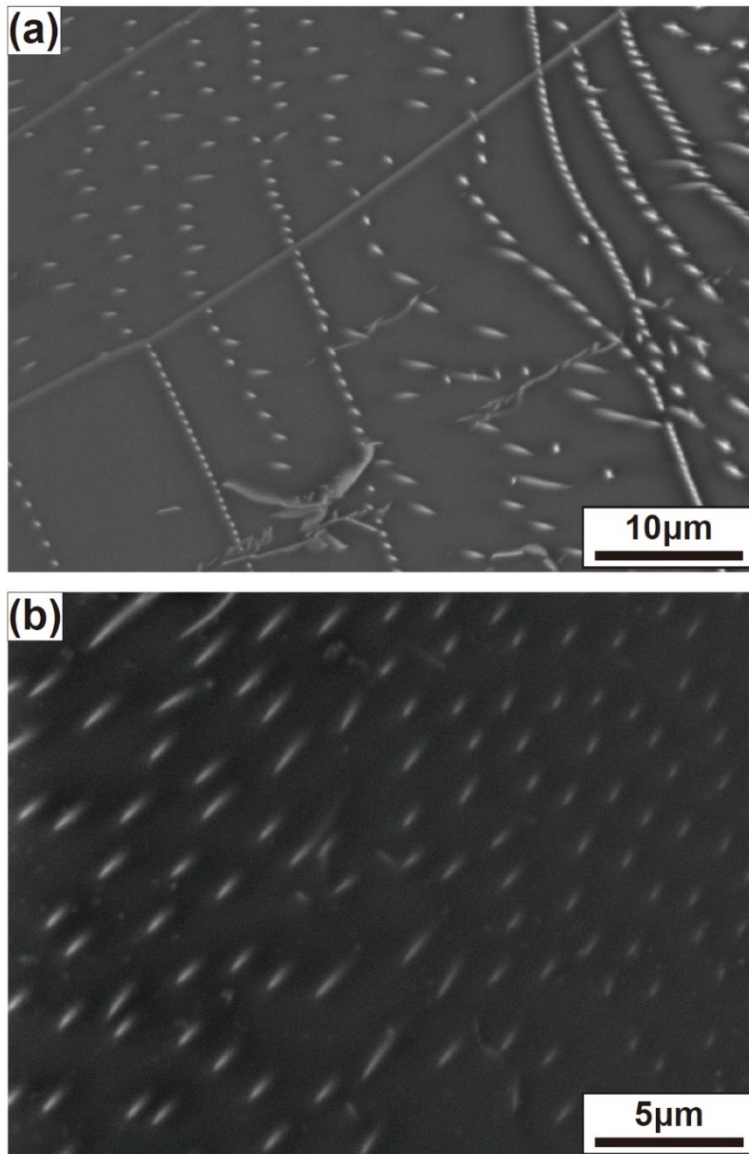


**Figure 2.12.** Backscattered electron (BSE) images showing dislocation microstructures of samples for **(a)** type-E LPO (sample 561) and **(b)** type-B LPO (sample 565-1) of olivine. **(a)** Well-developed subgrain boundaries were observed in a large fraction of the grains. **(b)** Straight dislocations and few subgrain boundaries were observed.

**Table 2.3.** Estimated stress ( $\sigma$ ) from: free dislocation density ( $\rho$ ); and recrystallized grain-size piezometer.

sample	$\rho$ ( $10^{12} \text{ m}^{-2}$ ) <sup>1</sup>	$\sigma$ (MPa) <sup>2</sup> by equation (1)				d ( $\mu\text{m}$ ) <sup>3</sup>	$\sigma$ (MPa) <sup>4</sup>
		G&K, 1973 <sup>5</sup>	K&G, 1974 <sup>6</sup>	B&K, 1992 <sup>7</sup>	J&K, 2001 <sup>8</sup>		
561	0.384	74 $\pm$ 20	60 $\pm$ 20	51 $\pm$ 20	64 $\pm$ 20	495	18 $\pm$ 6
565-1	0.306	66 $\pm$ 20	54 $\pm$ 20	43 $\pm$ 20	54 $\pm$ 20	388	44 $\pm$ 13
565-2	-	-	-	-	-	454	41 $\pm$ 13
568	-	-	-	-	-	298	51 $\pm$ 13
569	0.270	62 $\pm$ 20	51 $\pm$ 20	39 $\pm$ 20	50 $\pm$ 20	-	-
570	0.345	70 $\pm$ 20	57 $\pm$ 20	47 $\pm$ 20	59 $\pm$ 20	-	-

<sup>1</sup>  $\rho$ : free dislocation density measured using Equation 2.5:  $\rho = \sum l/V$  (Karato and Lee, 1999).

<sup>2</sup>  $\sigma$ : estimated stress by Equation 2.4:  $\sigma_1\text{-}\sigma_3 = \alpha\cdot\mu\cdot b\cdot\rho^{1/2}$  (Kohlstedt *et al.*, 1976a).

<sup>3</sup> d: recrystallized grain size measured by linear intercept method (Gifkins, 1970; Russ and Dehoff, 2000).

<sup>4</sup>  $\sigma$ : estimated stress using recrystallized grain-size piezometer (Jung and Karato, 2001b).

<sup>5</sup> Estimated stress using the values of constants from Goetze and Kohlstedt (1973).

<sup>6</sup> Estimated stress using the values of constants from Kohlstedt and Goetze (1974) and Kohlstedt *et al.* (1976a).

<sup>7</sup> Estimated stress using the values of constants from Bai and Kohlstedt (1992).

<sup>8</sup> Estimated stress using the values of constants from Jung and Karato (2001a) and Karato and Jung (2003).

#### **2.4.4. Water content of minerals in the sample**

Water content was determined for minerals in samples (Table 2.4). FTIR spectroscopy showed that most samples were dry in olivine ( $50\text{--}120 \pm 30$  ppm H/Si), except for one sample (561) containing a moderate amount of water ( $200 \pm 30$  ppm H/Si). However, the coexisting enstatites and diopside contained much more water than olivine ( $120\text{--}760 \pm 100$  ppm H/Si and  $1320\text{--}7690 \pm 100$  ppm H/Si, respectively) in the lherzolites (samples 565-1, 565-2, and 568). In addition, the coexisting diopside in the wehrlites (samples 561, 569, and 570) also contained much more water than olivine ( $1060\text{--}3970 \pm 100$  ppm H/Si).

**Table 2.4.** Water contents measured by FTIR spectroscopy for olivine, Opx, and Cpx in each sample.

Sample	Thickness ( $\mu\text{m}$ )	Water content (ppm H/Si) <sup>1</sup>		
		Ol	Opx	Cpx
561	83	200 $\pm$ 30	-	3970 $\pm$ 100
565-1	192	60 $\pm$ 30	760 $\pm$ 30	3920 $\pm$ 100
565-2	275	90 $\pm$ 30	240 $\pm$ 30	7690 $\pm$ 100
568	187	80 $\pm$ 30	120 $\pm$ 30	1320 $\pm$ 100
569	230	120 $\pm$ 30	-	1290 $\pm$ 100
570	168	50 $\pm$ 30	-	1060 $\pm$ 100

<sup>1</sup> To estimate water contents, Paterson's calibration (1982) was used. The water content was determined as an average value of at least 10 grains for olivine (Ol), enstatite (Opx), and diopside (Cpx).

## 2.5. Discussions and implications

### 2.5.1. LPOs of olivine

#### 2.5.1.1. *Type-B LPO of olivine*

The type-B LPO of olivine was found in the lherzolites from mantle xenoliths in Shanwang (eastern China). The proposed mechanisms for producing type-B olivine LPO are water-induced fabric transition (Jung and Karato, 2001b; Jung et al., 2006; Katayama et al., 2004), melt-induced slip change (Holtzman et al., 2003), and the pressure effect on the deformation of olivine at high pressure ( $> 3$  GPa; Jung et al., 2009b; Ohuchi et al., 2011; Raterron et al., 2011). However, the lherzolite samples with type-B olivine LPOs in this study showed no melt. In addition, previous study reported that the equilibrium condition of garnet-bearing peridotite xenolith was estimated to be a pressure of 16–24 kbar (Zheng et al., 2006). As a result, lack of the garnet in the samples suggests that spinel lherzolites were originated from a shallow depth of less than about 60 km. Therefore, the possibility of melt segregation and a pressure effect can be ruled out for the production of type-B olivine LPOs. On the other hand, the water content of olivine in the lherzolites (samples 565-1, 565-2, and 568) was  $60\text{--}80 \pm 30$  ppm H/Si but that of coexisting pyroxenes (Opx and Cpx) in the samples was much larger than that of olivine:  $120\text{--}760 \pm 100$  ppm H/Si for Opx and  $1320\text{--}7690 \pm 100$  ppm H/Si for Cpx (Table 2.4). This discrepancy between the water content of olivine and pyroxene is considered to be due to a markedly

higher OH diffusion rate for olivine than for pyroxene (Peslier and Luhr, 2006). The high water content of coexisting pyroxenes in the Shanwang xenoliths indicates that olivine originally contained much more water than the current estimation, considering partition coefficient ( $D_{\text{Cpx/Ol}}$ ) of water between olivine and Cpx in previous experimental studies (Aubaud et al., 2004; Hauri et al., 2006). The FTIR data are consistent with a study of Nushan peridotite xenoliths in Eastern Block (Yang et al., 2008), in which olivine contained 0–10 wt ppm H<sub>2</sub>O (0–170 ppm H/Si), and both Opx and Cpx contained much more water: 2–40 wt ppm H<sub>2</sub>O (30–670 ppm H/Si) and 2–100 wt ppm H<sub>2</sub>O (30–1670 ppm H/Si), respectively. Since Yang *et al.* (2008) used the calibration of Bell *et al.* (2003), the water content above had already been converted to Paterson's calibration by dividing by 3.5 to compare with the data in this study. In addition, the estimated stresses for lherzolites with type-B fabric in this study are relatively high (~50 MPa) in nature (Jung, 2009; Katayama et al., 2005; Skemer et al., 2006). Consequently, it was considered that the formation of type-B olivine LPO is most likely due to water at high stress.

#### 2.5.1.2. Type-E LPO of olivine

In this study the type-E LPO of olivine was also found in the wehrlite from mantle xenoliths in Shanwang (eastern China). The proposed mechanisms for producing type-E olivine LPO are a pre-existing mechanical anisotropy on the mantle lithosphere (Michibayashi and Mainprice, 2004) and the deformation of olivine in the presence of a moderate amount of water at low stress (Harigane et al., 2013; Jung et al., 2006; Katayama et al., 2004; Mehl et al., 2003). Michibayashi and

Mainprice (2004) showed that type-A olivine LPO (the crystallographic [100] axes of olivine are aligned subparallel to the lineation, and the [010] axes are aligned subnormal to the foliation), which was formed by E-W mantle flow, was transformed to type-E olivine LPO due to the NW-SE strike-slip shear. Therefore, they emphasized the importance of initial mechanical anisotropy, which can control later structural behavior of the lithosphere. LPO of olivine in this study is thought to have been changed from type-B in the early to late Mesozoic to type-E in the late Mesozoic to Cenozoic. However, this change cannot be explained by the simple rotation of initial mechanical anisotropy due to late extension in the E-W direction. According to a previous experimental study (Jung et al., 2006; Katayama et al., 2004), type-E fabric was found under low stress ( $< 400$  MPa) and moderate water content ( $200 < C_{OH} < 1000$  ppm H/Si). The olivine showing type-E LPO in the wehrlites (samples 561, 569, and 570) contained  $50\text{--}200 \pm 30$  ppm H/Si of water (Table 2.4). This value ( $\sim 200$  ppm H/Si) has been considered as the minimum amount of water required for producing type-E olivine LPO (Jung et al., 2006; Katayama et al., 2004). In addition, because the coexisting pyroxene (Cpx) in the samples also contained much more water than olivine ( $1060\text{--}3970 \pm 100$  ppm H/Si; Table 2.4), olivine in the wehrlites is considered to contain much more water than given by the current estimation, and likewise for olivine in the lherzolites. Furthermore, the estimated stresses for wehrlites with type-E fabric in this study are relatively low ( $\sim 20$  MPa), similar to the results from other studies (Jung, 2009; Katayama et al., 2005; Michibayashi et al., 2006; Skemer et al., 2010). Consequently, it was considered that the formation of type-E olivine LPO is most likely due to the presence of water at relatively low stress.

## 2.5.2. LPOs of pyroxene

Jung *et al.* (2010) recently classified the LPOs of enstatite into four types: one typical type and three newly defined types, as mentioned above (in Chapter 2.1). According to this classification, enstatite in the samples showed one typical (type-AC) and another LPO type (type-BC), and these LPO patterns of enstatite were considered to be related to the proportion of minerals in the sample (Jung *et al.*, 2010). Their study indicated that the type-AC fabric of enstatite was found in samples containing a small portion of enstatite with a large portion of olivine, whereas the type-AB and -BC fabrics of enstatite were found in samples containing large portions of enstatite. A similar trend was found in this study, with type-BC and -AC LPOs of enstatite containing a large portion (18–27 %) and a small portion (16 %) of enstatite, respectively. At present, however, how the proportion of minerals affects the formation of different enstatite LPOs in rock cannot be hypothesized yet, and further study is required to understand this. Recently, other possible mechanisms for producing LPO of Opx were reported in an experimental study with  $P = 1.5$  GPa and  $T = 1100$  °C (Manthilake *et al.*, 2013). Both hydrous aluminous enstatite and  $\text{MgSiO}_3$ -enstatite showed type-AC LPO with a slip system of (100)[001], and anhydrous aluminous enstatite showed type-BC LPO with a slip system of (010)[001]. However, the enstatite in the Shanwang xenoliths has been reported as a  $\text{MgSiO}_3$ -enstatite by geochemical analysis (Chu *et al.*, 2009; Xiao *et al.*, 2010; Xiao and Zhang, 2011; Zhang *et al.*, 2007; Zheng *et al.*, 1998; 2005a; 2005b; 2006), and one sample (568) with type-AC enstatite LPO and two other samples (565-1 and

565-2) with type-BC LPO observed here are inconsistent with the experimental results of Manthilake *et al.* (2013). As a result, further study is needed to understand the mechanism for producing enstatite LPO.

Historically, the LPOs of diopside have not yet been defined as a specific type; however, the LPO types of another clinopyroxene, omphacite, have previously been classified as type-S, -L, and -SL (Brenker *et al.*, 2002; Godard and van Roermund, 1995; Helmstaedt *et al.*, 1972; Mauler *et al.*, 2001; Zhang *et al.*, 2006). In this study, four different types of diopside LPO were classified to understand the mechanism for producing diopside LPOs, and one sample (568) showed a diopside LPO similar to the type-L omphacite LPO. However, no specific relationship was found between the diopside fabric and the various geological components such as stress, water content, and modal composition of the rock. Therefore, further study is required to understand the LPO formation of diopside.

### **2.5.3. Relationship between fabric strength of minerals and seismic anisotropy**

The correlation between seismic anisotropy and fabric (LPO) strength (J- or M-index) has been reported in previous studies for olivine (Ben Ismail and Mainprice, 1998; Jung et al., 2009a; Mainprice et al., 2000; Skemer et al., 2005) and enstatite (Jung et al., 2010). These previous results indicate that the azimuthal anisotropy of P-wave (AV<sub>p</sub>) and the maximum polarization anisotropy of S-wave (Max. AV<sub>s</sub>) increase with an increase in the fabric strength (J- or M-index) of minerals. The increasing trends of seismic anisotropy *versus* J-index of olivine, however, are not linear, with different rates of increase for different axes ([100], [010], and [001] in olivine; Ben Ismail and Mainprice, 1998). In contrast, the increasing trend of seismic anisotropy *versus* M-index of olivine is linear, with an almost identical increasing rate for any axes and all LPO types of olivine in experimentally deformed samples (Skemer et al., 2005).

In this study, the seismic anisotropy of P- and S-wave was compared with the M-index for each mineral in the samples and plotted against the previous data of olivine (Jung et al., 2009a) and enstatite (Jung et al., 2010) in naturally deformed samples (Fig. 2.13). In case of the olivine of different LPO types, seismic anisotropy of P- and S-wave increased with increasing M-index. However, the increasing rate was shown as curvilinear rather than linear (Fig. 2.13), similar to finding from a previous report (Mainprice et al., 2000) where the J-index was used. In case of

enstatite and diopside, there are also tendencies for increase in both P- and S-wave anisotropy with an increase in the M-index, but increasing rates were lower than that of olivine (Fig. 2.13). As a result, these data suggest that the seismic anisotropy of whole rock composed of olivine, enstatite, and diopside would be lower than that of olivine only, as mentioned in Chapter 2.4.2.

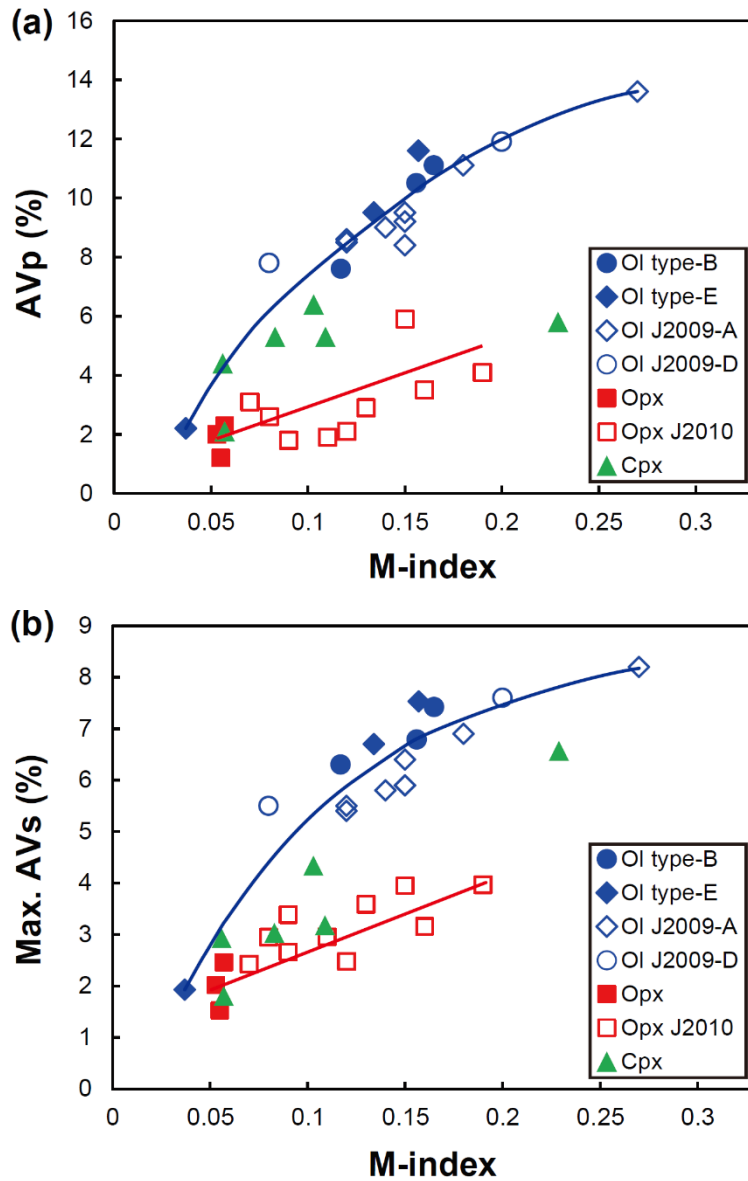


**Figure 2.13.** Seismic anisotropy compared to the fabric (LPO) strength (M-index) of minerals. **(a)** The azimuthal anisotropy of P-wave (AVp) for each mineral. **(b)** The maximum polarization anisotropy of S-wave (Max. AVs) for each mineral. Ol: olivine, Opx: enstatite, Cpx: diopside. J2009-A: data for type-A olivine LPO from Jung *et al.* (2009a), J2009-D: data for type-D olivine LPO from Jung *et al.* (2009a), and J2010: data from Jung *et al.* (2010).

#### **2.5.4. Thickness of anisotropic layer under the study area**

The seismic anisotropy of shear wave is measured by the seismic wave passing through multiple anisotropic mediums in the Earth. Because of the large volume proportions in the lithosphere, the upper mantle have been considered as the main anisotropic mediums (Long and Becker, 2010). Lower mantle can also contribute to the Vs1 polarization direction, but the magnitude of seismic anisotropy in the lower mantle is small. Therefore, the mantle peridotite xenolith can be used to interpret these anisotropic structures when it is considered that the seismic anisotropy of shear waves is mostly related to the lithospheric mantle. Zhao and Xue (2010) suggested that the observed seismic anisotropy beneath the Sino-Korean craton is primarily caused by shear wave splitting from the lithospheric mantle because the seismic anisotropy of shear wave within the crust is weak ( $\sim 0.2\text{--}2.3\%$ ) and Vs1 polarization directions are not parallel to the asthenospheric flow beneath the study area.

Following a previous study that considered four different geodynamic models (upwelling, lateral shear, horizontal extension, and tilted slab) for the origin of seismic anisotropy in central Italy (Pera et al., 2003; Fig. 2.14), the thickness of the anisotropic layer under the study area was calculated for each model using the delay time from shear wave splitting beneath the Eastern Block of the Sino-Korean craton (delay time of  $0.8 \pm 0.26$  s; Zhao and Xue, 2010) and the seismic velocity and anisotropy of S-wave from the LPOs of minerals in the samples (Fig. 2.15 and Table 2.5). The thickness (T) of the anisotropic layers can be described as follows:

$$T = (100 \times \delta t \times \langle V_s \rangle) / AV_s \text{ (km)} \quad (2.6)$$

where  $\delta t$  is the delay time of the S-wave,  $\langle V_s \rangle$  is the average velocity of fast and slow shear wave velocities ( $V_{s1}$  and  $V_{s2}$ ), and  $AV_s$  is the seismic anisotropy of the S-wave expressed as a percentage (Pera et al., 2003). As indicated by Equation 2.6, the thickness of the anisotropic layer can increase with increasing the average velocity of  $V_{s1}$  and  $V_{s2}$  when the delay time and  $AV_s$  are fixed. In addition, because the lherzolite and wehrlite samples showed different types of olivine LPO and it was considered that the lherzolite had become wehrlite via metasomatism of the upper mantle lithosphere (Xiao et al., 2010; Xiao and Zhang, 2011), the required thickness of the anisotropic layer was calculated separately for lherzolite samples (565-1, 565-2, and 568) and wehrlite samples (561, 569, and 570) based on the volume fraction of olivine.

As a result, the thicknesses of the anisotropic layer from the LPOs of lherzolite samples were estimated to be in the range of 80–125 km, 90–125 km, 310–680 km, and 160–290 km for the upwelling, lateral shear, horizontal extension, and tilted slab models, respectively; while those from the LPOs of wehrlite samples were estimated to be in the range of 230–415 km, 180–190 km, 125–140 km, and 140–190 km, respectively (Table 2.5). Owing to the thin lithospheric thickness of the Eastern Block (~80–110 km currently; Chen et al., 2006; 2008; Griffin et al., 1998a; Sodoudi et al., 2006; Zhao et al., 2009), it can most likely be interpreted that the lherzolite samples have been deformed by either upwelling or a lateral shear mode, but the wehrlite samples have been deformed by a horizontal extension mode.

Because many studies have indicated that lithospheric thinning by metasomatic melts occurred during the late Mesozoic to the Cenozoic (Fan et al., 2000; Gao et al., 2002; Griffin et al., 1998a; Xiao et al., 2010; Xiao and Zhang, 2011; Ying et al., 2006; Zhang, 2005; Zhang et al., 2007; 2008; 2010; J. Zhang et al., 2011; Zheng et al., 1998; 2001; 2005a; 2006; Zheng and Lu, 1999), it is possible that the mantle lherzolite xenoliths may have recorded the previous deformation fabric (i.e., the subduction of the South China craton beneath the Sino-Korean craton during the Mesozoic). To consider the geodynamic mechanism of mantle flow during the Mesozoic E-W trend collision, an attempt was made to calculate the required anisotropic layer thickness for lherzolite samples (565-1, 565-2, and 568). The delay time from shear wave splitting was used beneath the Western Block of the Sino-Korean craton (delay time of  $1.5 \pm 0.17$  s; Zhao and Xue, 2010), because this block has a thick Archaean or Proterozoic lithosphere (~200 km) which is considered to be equivalent to the previous thickness of the Eastern Block before the occurrence of lithospheric thinning (Chen et al., 2006; 2008; Griffin et al., 1998a; Sodoudi et al., 2006; Zhang et al., 2008; Zhao et al., 2009; Zhao and Xue, 2010; Zheng et al., 1998; 2001). Consequently, the anisotropic layer thickness was estimated to be in the range of 145–240 km, 165–235 km, 535–1270 km, and 290–545 km for the upwelling, lateral shear, horizontal extension, and tilted slab models, respectively (Table 2.5). This result indicates that the lherzolite samples might have been deformed by lateral shear mode, because the required thickness of this model is in accord with the thickness of the thick lithosphere.

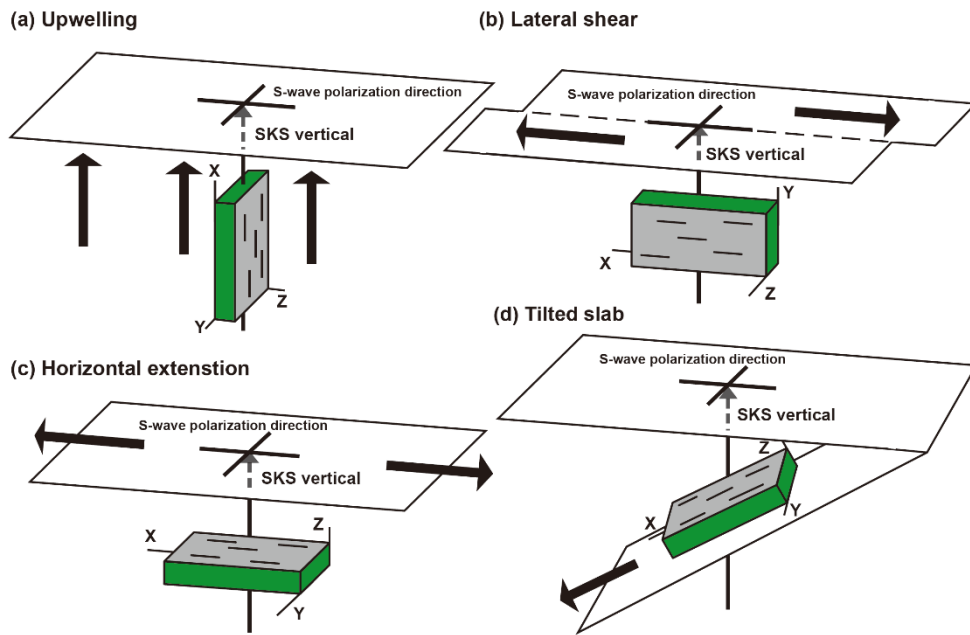


**Figure 2.14.** Four different geodynamic models for the origin of seismic anisotropy (modified after Pera *et al.*, 2003): **(a)** upwelling, **(b)** lateral shear, **(c)** horizontal extension, and **(d)** tilted slab. The plane with gray color represents the foliation.

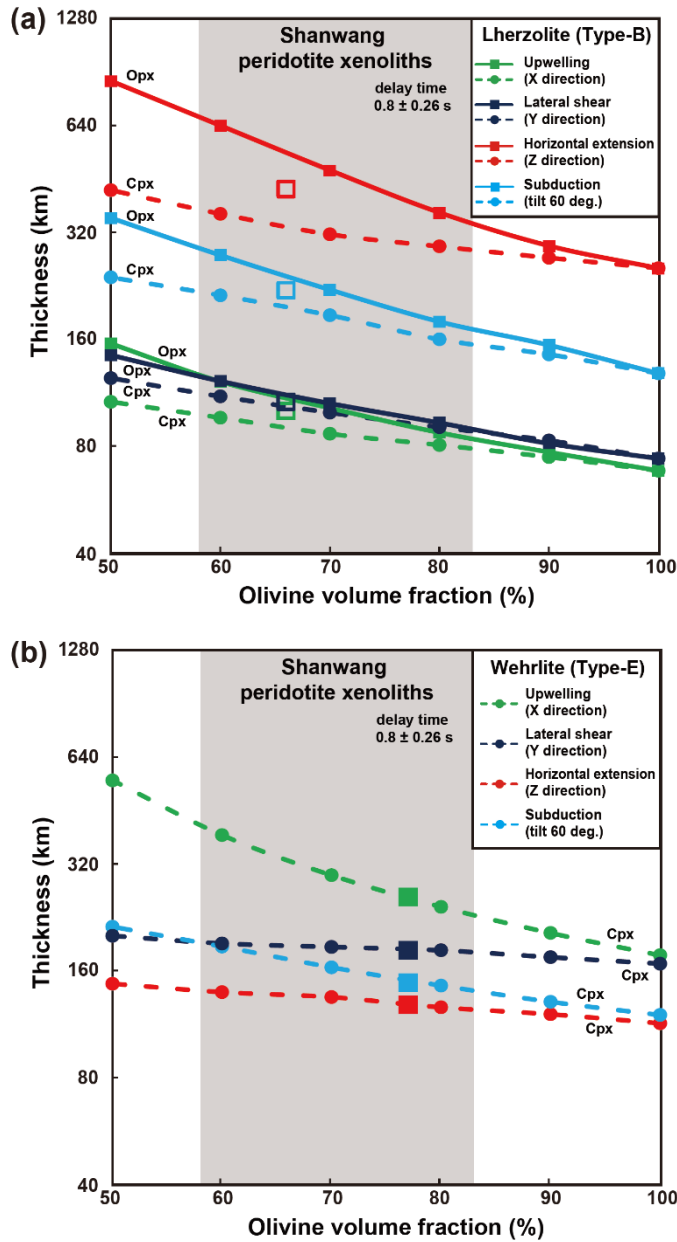


**Figure 2.15.** The relationship between olivine volume fraction and the required thickness of the anisotropic layer (log scale) needed to explain seismic anisotropy for **(a)** lherzolite and **(b)** wehrlite. The large open and solid squares represent the mean composition of lherzolite and wehrlite, respectively. The gray shaded area represents the range of the modal composition of Shanwang peridotite xenoliths from this study.

**Table 2.5.** Thickness of anisotropic layer in eastern China calculated using four different geodynamic models: upwelling, lateral shear, horizontal extension, and tilted slab.

Geodynamic models	Thickness of anisotropic layer (km) <sup>1</sup>		Thickness of anisotropic layer (km) <sup>2</sup>	
	Lherzolite (Type-B Ol)	Wehrlite (Type-E Ol)	Lherzolite (Type-B Ol)	Wehrlite (Type-E Ol)
Upwelling	80–125 (±30)	230–415 (±100)	145–240 (±20)	430–775 (±70)
Lateral shear	90–125 (±30)	180–190 (±60)	165–235 (±20)	335–360 (±40)
Horizontal extension	310–680 (±120)	125–140 (±40)	535–1270 (±80)	235–265 (±30)
Tilted slab	160–290 (±60)	140–190 (±50)	290–545 (±40)	265–360 (±30)
Lithospheric thickness of eastern China	~ <b>80–110 km</b> for current		~ <b>200 km</b> for Archean or Proterozoic	

<sup>1</sup> The thickness of the anisotropic layer was calculated using the delay time of S-wave beneath the Eastern Block of the Sino-Korean craton (delay time =  $0.80 \pm 0.26$  s; Zhao and Xue, 2010).

<sup>2</sup> The thickness of the anisotropic layer was calculated using the delay time of S-wave beneath the Western Block of the Sino-Korean craton (delay time =  $1.50 \pm 0.17$  s; Zhao and Xue, 2010).

### **2.5.5. Implications for seismic anisotropy in eastern China**

In previous studies, type-B olivine LPO in nature has generally been found in subduction zones (Jung, 2009; Skemer et al., 2006; Tasaka et al., 2008), and the trench-parallel seismic anisotropy of the fast shear wave in the mantle wedge has been attributed to type-B LPO (Jung and Karato, 2001b; Karato et al., 2008; Kneller et al., 2005; Long and van der Hilst, 2005; 2006; Nakajima and Hasegawa, 2004; Nakajima et al., 2006). On the other hand, type-E olivine LPO shows similar seismic signatures to that of type-A olivine LPO, which has a  $V_{s1}$  polarization direction parallel to the mantle flow (Jung et al., 2006). Therefore, type-E olivine LPO can be also considered to demonstrate seismic anisotropy in the upper mantle, as can type-A LPO (Jung et al., 2006; Jung, 2009; Karato et al., 2008; Katayama et al., 2004; Montagner and Tanimoto, 1990; 1991).

The study area, Shanwang, has located at the front of the continental-collisional subduction zone between the Sino-Korean craton and the South China craton, and has simultaneously lain astride the Tan-Lu fault zone. Since the Tan-Lu fault zone is considered to be a syn-orogenic sinistral strike-slip fault (Fletcher et al., 1995; Gilder et al., 1999; Li, 1994; Xu and Zhu, 1994; Yin and Nie, 1993; Zhang et al., 2012; Zhu et al., 2004), many studies have indicated that this syn-orogenic fault zone might play an important role as a major melt-infiltrating channel from the asthenosphere into the lithospheric mantle beneath the eastern Sino-Korean craton during the Mesozoic and Cenozoic (Fan et al., 2000; Gao et al., 2002; Xiao et al., 2010; Xiao

and Zhang, 2011; Ying et al., 2006; Zhang, 2005; Zhang et al., 2007; 2010; J. Zhang et al., 2011; Zheng et al., 1998; 2001; 2005a; 2006). There is a possibility that the lithospheric mantle was deformed under wet conditions, as suggested by the high water content of constituent minerals (Opx and Cpx) in xenoliths (in Chapter 2.5.1.1) beneath Shanwang area. Because the Tan-Lu fault zone was a strike-slip fault until late Mesozoic (Zhang et al., 2012; Zhu et al., 2004), the formation of type-B olivine LPO in the lherzolite can most likely be interpreted to have been formed by lateral shear due to syn-orogenic strike-slip fault during/after the continental-collisional subduction between the Sino-Korean craton and the South China craton (i.e., movement in the N–S to NNE–SSW direction). This interpretation is consistent with the result of calculation in Chapter 2.5.4. This type-B LPO can be used to explain the trench-parallel E–W- to WNW–ESE-trending polarization directions of the fast shear wave in the Eastern Block of the Sino-Korean craton, near the Shanwang area (Fig. 2.16a and b).

After the continental-collisional subduction event between the Sino-Korean craton and the South China craton, the subduction of the western Pacific plate beneath the eastern Sino-Korean craton was initiated although the exact time and process of the initiation of subduction remains controversial (Zhu and Xu, 2019). This subduction caused the lithospheric thinning by thermal erosion from the rise of the asthenosphere (Griffin et al., 1998a; Zheng et al., 2007; Zheng and Dai, 2018). In addition, the lherzolitic mantle went through the metasomatism and changed to wehrlite because the Tan-Lu fault zone might have acted as a major channel for the infiltrating-melt from the asthenosphere (Xiao and Zhang, 2011; Xiao et al., 2010). Simultaneously, it is suggested that the direction of absolute plate motion (APM)

was changed from a N–S to an E–W trend by the westward-subducting Pacific plate beneath the Eurasian plate during the late Mesozoic to Cenozoic, and by movement of the stagnant slab of the subducted Pacific plate, which is considered to reach the boundary between the Central Zone and the Eastern Block of the Sino-Korean craton (Ai and Zheng, 2003; Chen, 2010; Huang and Zhao, 2006; Zhao et al., 2007a; Zhu and Zheng, 2009). Because the Tan-Lu fault zone also changed from strike-slip to extensional fault at that time due to the trench rollback (Zhang et al., 2012; Zheng and Dai, 2018), the formation of type-E olivine LPO in the wehrlites can most likely be interpreted to have been formed in the horizontal extension mode. This type-E olivine LPO can be used to interpret a  $V_{s1}$  polarization direction subparallel to the current average APM of the Sino-Korean craton (Gripp and Gordon, 2002; Fig. 2.16c and d). This model is consistent with a previous hybrid model of mantle flow where the subduction of the Pacific plate causes a mantle wedge flow and an extension in the Eastern Block (Zhao and Xue, 2010; Zhao et al., 2011; 2013). The latter authors also proposed the relatively huge upwelling at the Central Zone. However, our study is limited to the Eastern Block in Shanwang region. As a result, further study on the LPO of minerals in mantle xenoliths derived from beneath the Central Zone is needed.

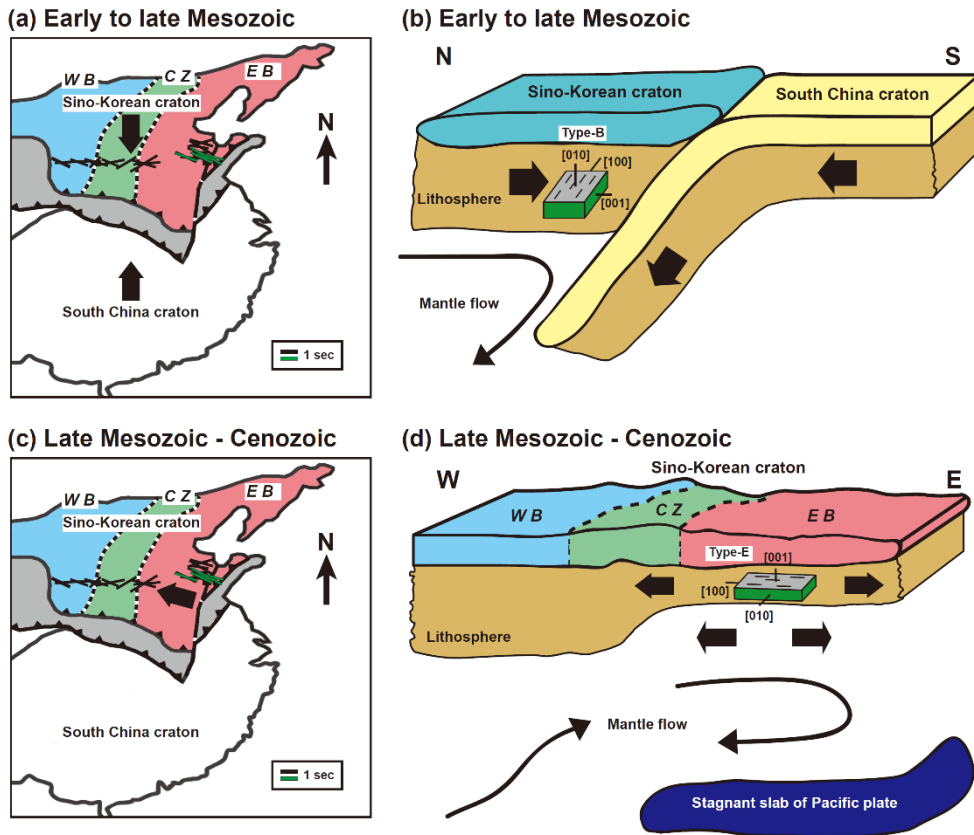


**Figure 2.16.** Schematic diagram for the evolution of the lithosphere beneath the Eastern Block of the Sino-Korean craton. **(a)** and **(b)** Early to late Mesozoic; **(c)** and **(d)** late Mesozoic to Cenozoic. In **(a)** and **(c)**, the polarization directions of fast shear waves are indicated by black bars (modified after Zhao and Xue, 2010) and green bars (modified after Zhao and Zheng, 2005). The thick black arrows indicate directions of plate motion. Absolute plate motion in **(c)** is after Gripp and Gordon (2002).

## 2.6. Conclusion

Deformation microstructures, including the LPOs of olivine, enstatite, and diopside in mantle xenoliths (in Shanwang, eastern China), were studied to further understand the deformation mechanism and seismic anisotropy of the upper mantle. In this study, two types of olivine LPOs were found: type-E in wehrlites and type-B in spinel lherzolites. In addition, two types of enstatite LPO (type-BC and type-AC) and four different types of diopside LPO were found. Observations of strong LPOs, and the numerous dislocations in olivine, suggest that samples showing both type-B and -E olivine LPOs were deformed in dislocation creep. Seismic anisotropy calculated using the LPO of minerals showed that the seismic anisotropy of olivine was stronger than that of both enstatite and diopside. Furthermore, the thickness of the anisotropic layer was calculated for four different geodynamic end models to understand the origin of seismic anisotropy beneath the study area. As a result, it is suggested that seismic anisotropy under the study area can most likely be explained by two deformation modes that might have occurred at different times: one mode deformed lherzolites with a type-B olivine LPO by lateral shear during/after the period of Mesozoic continental collision between the Sino-Korean and South China cratons, while the other deformed the wehrlites with a type-E olivine LPO by horizontal extension during the period of change in APM in relation to the westward-subducting Pacific plate.

## CHAPTER 3

# Lattice preferred orientation and deformation microstructures of glaucophane and epidote in experimentally deformed epidote blueschist at high pressure

*\* This chapter has been modified from a published paper:*

Park, Y., Jung, S., and Jung, H., 2020. Lattice preferred orientation and deformation microstructures of glaucophane and epidote in experimentally deformed epidote blueschist at high pressure. *Minerals* **10**(9), 803, 1–19.  
DOI: 10.3390/min10090803

## Abstract

To understand the lattice preferred orientation (LPO) of glaucophane and epidote and deformation microstructures at the top of a subducting slab in a warm subduction zone, deformation experiments of epidote blueschist were conducted in simple shear by using a modified Griggs apparatus. Deformation experiments were performed under high pressure (0.9–1.5 GPa), temperature (400–500 °C) and shear strain ( $\gamma$ ) in the range of 0.4–4.5. At low shear strain ( $\gamma \leq 1$ ), the [001] axes of glaucophane were in subparallel alignment with the shear direction, and the (010) poles were subnormally aligned with the shear plane. At high shear strain ( $\gamma > 2$ ), the [001] axes of glaucophane were in subparallel alignment with the shear direction, and the [100] axes were subnormally aligned with the shear plane. At a shear strain between  $2 < \gamma < 4$ , the (010) poles of epidote were in subparallel alignment with the shear direction, and the [100] axes were subnormally aligned with the shear plane. At a shear strain where  $\gamma > 4$ , the alignment of the (010) epidote poles had altered from subparallel to subnormal to the shear plane, while the [001] axes were in subparallel alignment with the shear direction. The microstructure of glaucophane observed by transmission electron microscopy (TEM) and mapped by electron back-scattered diffraction (EBSD) technique suggests that the LPO of glaucophane was developed by dislocation creep, somewhat affected by the cataclastic flow at high shear strain. The LPO development of epidote is considered to have been affected by dislocation creep under a shear strain of  $2 < \gamma < 4$ , but it is highly affected by cataclastic flow with rigid body rotation under a high shear strain ( $\gamma > 4$ ). The

experimental results indicate that the magnitude of shear strain and rheological contrast between component minerals plays an important role in the formation of LPOs for glaucophane and epidote.

### 3.1. Introduction

Several previous studies have recognized blueschist as one of the representative rocks in the subduction zone at increased depths. This is because the subducting oceanic crust is considered to transform to blueschist-facies metamorphic rock under high pressure (0.5–2.5 GPa) and relatively low temperature (150–550 °C) conditions (Evans, 1990; Peacock, 1993; Schmidt and Poli, 1998). The blueschist has been reported worldwide in the paleo-subduction zone or active subduction zone (Agaard et al., 2009; Ernst, 1988; Tsujimori and Ernst, 2014). Previous geophysical studies have reported that the low-velocity layer of the subduction zone almost coincides with the upper plane of the double seismic zone at the top of the subducting oceanic crust (Hasegawa et al., 2007; Kawakatsu and Watada, 2007; Tsuji et al., 2008). Glaucophane and lawsonite or epidote in blueschist is considered to potentially affect seismic velocity at the top of the subducting ocean crust (Abers et al., 2013; Hirose et al., 2008), as these minerals contain a high H<sub>2</sub>O content (as hydroxyl) in their molecular structure (Hacker et al., 2003; Peacock, 1993). Other studies have reported that the tremors and low-frequency earthquakes (LFEs) occur near the top of the low-velocity layers (Audet and Kim, 2016; Audet et al., 2010). In addition, researchers have suggested that the lattice preferred orientation (LPO) of glaucophane, one of the elastically anisotropic minerals in blueschist, may affect the trench-parallel seismic anisotropy of the forearc region where the subducting slab has a high dip angle (Cao and Jung, 2016; Cao et al., 2013; 2014; Kim et al., 2013a).

To better understand the characteristics of this subduction zone, it is necessary to understand the deformation behavior of the constituent minerals in blueschist. Among these minerals, glaucophane and epidote, recognized as the principal minerals of epidote blueschist, are important at the top of the slab in warm subduction zones. Previous studies on the deformation of natural rocks have suggested several deformation mechanisms for glaucophane; (1) the rigid behavior of glaucophane in eclogitic micaschist (Ildefonse et al., 1990), (2) rigid body rotation and dynamic recrystallization by dislocation creep in glaucophanite (Zucali et al., 2002), (3) dislocation glide (or slip) in eclogitic micaschist and glaucophane schist (Reynard et al., 1989), (4) dynamic recrystallization by dislocation creep in natural blueschist (Cao et al., 2014; Kim et al., 2013a), and (5) dissolution-precipitation creep in rocks deformed at high P/T conditions with aqueous fluids (Wassmann and Stöckhert, 2013). For epidote, five deformation mechanisms have been proposed; (1) rigid body rotation for epidote (zoisite) in metabasite rock (Brunsmann et al., 2000), (2) dislocation glide for epidote (clinozoisite) in eclogite (Müller and Franz, 2004; 2008), (3) either dislocation glide or sliding on the cleavage by fracturing in naturally deformed rocks (Franz and Liebscher, 2004), (4) rigid body rotation at relatively low shear strain ( $\gamma = 2$ ) and (5) granular flow with a diffusion-assisted grain boundary sliding at relatively high shear strain ( $\gamma = 4.5$  and  $7.5$ ) for epidote (zoisite) product in an experimentally deformed plagioclase matrix (Stünitz and Tullis, 2001). Thus, glaucophane and epidote are likely to be deformed through brittle and ductile behavior based on the results from these previous studies. However, the dominant mechanism in the subducting slab of the subduction zone continues to be debated in the literature.

It is possible to develop the LPOs of glaucophane and epidote in blueschist through these deformation mechanisms. Previous studies have reported several LPOs or slip systems of glaucophane. Dislocation slip systems of glaucophane were first reported by a transmission electron microscopy (TEM)/high-resolution electron microscopy (HREM) study (Reynard et al., 1989). Recent studies on natural blueschists have reported three LPO types of glaucophane; (1) LPO indicating a (100)[001] slip system, or point/SL-type LPO (Bezacier et al., 2010a; Cao and Jung, 2016; Cao et al., 2013; 2014; Choi et al., 2021; Fujimoto et al., 2010; Ha et al., 2018; Kim et al., 2013b; 2013a; Teyssier et al., 2010), (2) LPO indicating a {110}[001] slip system, or girdle/L-type LPO (Bezacier et al., 2010a; Cao and Jung, 2016; Cao et al., 2013; 2014; Kim et al., 2013b), and (3) LPO indicating a (010)[001] slip system (Cossette et al., 2015). Although there has been little description on the slip systems of epidote, certain TEM/HREM studies have suggested the easiest slip plane (e.g., Müller and Franz, 2004; Ray et al., 1986). There are two LPO types of epidote that have recently been reported: one is the LPO indicating a (001)[010] slip system (Bezacier et al., 2010a; Cao et al., 2011; 2013; Ha et al., 2018; Kim et al., 2013a), and the other is the LPO indicating a {101}[010] slip system (Cao et al., 2011; 2013; Cossette et al., 2015; Fujimoto et al., 2010). Although LPOs of glaucophane and epidote have been reported, there is little clarity as to the deformation mechanisms that developed their LPOs.

In this chapter, deformation experiments for epidote blueschist were conducted in simple shear under high pressure (0.9–1.5 GPa) and temperature (400–500 °C) to understand the development of LPOs and deformation mechanisms of glaucophane and epidote in the conditions prevailing over the subducting slab in a warm subduction zone.

## 3.2. Methods

### 3.2.1. Starting material

The starting material was a natural epidote blueschist-facies rock collected from the Voltri massif in the western Alps, Italy. This was a massive fine-grained rock with a small grain size (average  $\sim 30 \mu\text{m}$ ; Fig. 3.1a). There was no clear foliation and lineation in the hand specimen and thin section. The blueschist was composed mainly of Na-amphibole (glaucothane,  $\sim 55\%$ ), epidote ( $\sim 15\%$ ), albite ( $\sim 15\%$ ), titanite ( $\sim 5\%$ ), chlorite ( $\sim 5\%$ ) and garnet (almandine,  $\sim 5\%$ ). The starting material underwent peak metamorphic conditions at a pressure of 22–28 kbar and a temperature of 460–500 °C and was re-equilibrated at a pressure of 10–15 kbar and a temperature of 450–500 °C (Malatesta et al., 2012). The mineral composition of the starting material was measured with a JEOL JXA-8100 electron probe X-ray microanalyzer at the Center for Research Facilities at Gyeongsang National University (GNU), South Korea. The measurement conditions included an accelerating voltage of 15 kV, a current of 10 nA, and a  $5 \times 5 \mu\text{m}^2$  beam size. The Na-amphibole was classified as pure glaucothane, represented by the formula  $\text{Na}_{2.0}[(\text{Mg}_{1.7}\text{Fe}^{2+}_{1.3})(\text{Ca}_{0.04}\text{Mn}_{0.01})\text{Al}_{1.8}\text{Fe}^{3+}_{0.09}]\text{Si}_{8.1}\text{O}_{22}(\text{OH})_2$ . The epidote was classified as  $\text{Ep}_{50.4}\text{Czo}_{49.6}$ , represented by the formula  $\text{Ca}_{2.0}\text{Al}_{2.0}(\text{Fe}^{3+}_{0.50}\text{Al}^{\text{VI}}_{0.49})(\text{Si}_{1.0}\text{O}_4)(\text{Si}_{2.0}\text{O}_7)\text{O}(\text{OH})$  (Table 3.1). The backscattered electron (BSE) image of the starting material illustrates the subhedral shape of the constituent minerals with an absence of fractures and few cleavages (Fig. 3.1b). Most grain boundaries of glaucothane are irregular and curved, whilst some glaucothane grains represent the

retrograded rim from Na-rich to NaCa/Ca-rich, after having undergone somewhat retrograde metamorphism (Vignaroli et al., 2005). Epidote minerals also possess irregular grain boundaries and are relatively larger than glaucophane minerals.

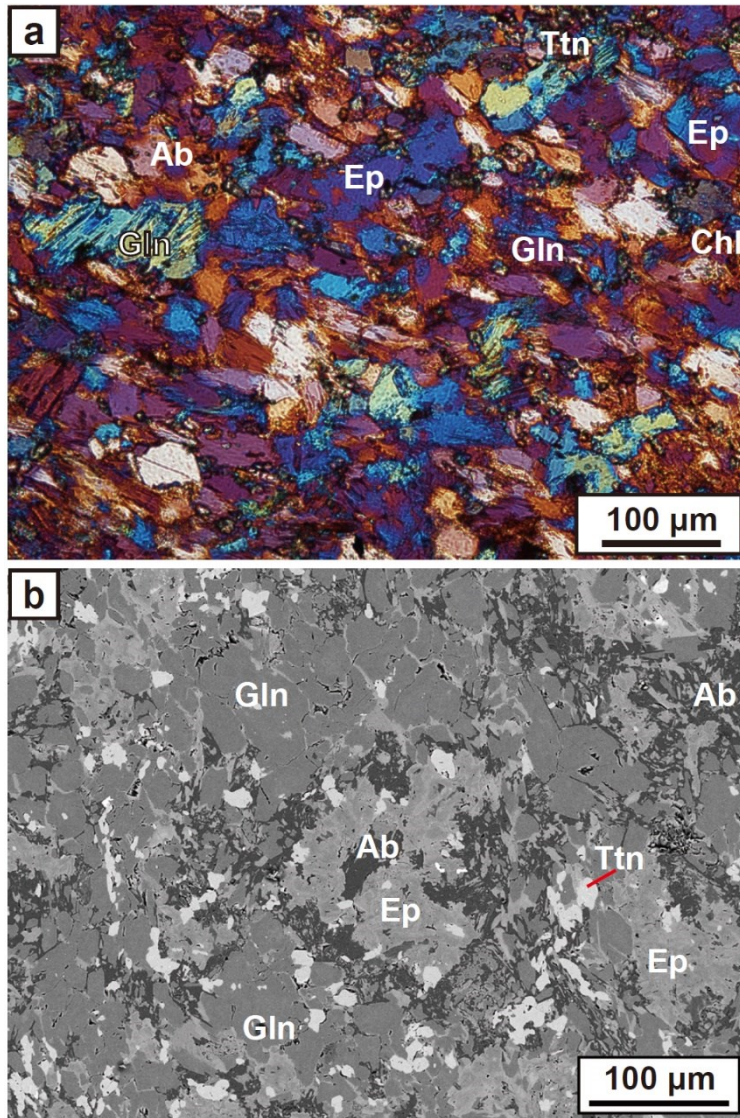


**Figure 3.1.** (a) Optical photomicrograph (XPL) with retardation plate ( $\lambda = 530$  nm) and (b) backscattered electron (BSE) image of the starting material (massive fine-grained epidote blueschist-facies rock). The average grain size of constituent minerals was  $\sim 30$   $\mu\text{m}$ . Gln: glaucophane, Ep: epidote, Ttn: titanite, Ab: albite, and Chl: chlorite.

**Table 3.1.** The representative composition of glaucophane and epidote in the starting material.

Element	SiO <sub>2</sub>	TiO <sub>2</sub>	Al <sub>2</sub> O <sub>3</sub>	Cr <sub>2</sub> O <sub>3</sub>	FeO	MgO	CaO	MnO	Na <sub>2</sub> O	K <sub>2</sub> O	NiO	Total
Gln	57.31	0.03	10.68	0.03	11.92	8.22	0.26	0.08	7.30	n.d.	n.d.	95.84
Ep	38.02	0.00	26.76	n.d.	7.61	0.03	23.37	0.07	0.03	0.01	n.d.	95.90
Cation	Si	Ti	Al	Cr	Fe <sup>2+</sup>	Fe <sup>3+</sup>	Mg	Ca	Mn	Na	K	Sum
Gln	8.06	0.00	1.77	0.00	1.31	0.09	1.73	0.04	0.01	1.99	-	15.01
Ep	3.01	0.00	2.49	-	0.00	0.50	0.00	1.98	0.00	0.00	0.00	7.99
Gln	Si [T]	Ti [T]	Al [T]	Ti [C]	Al [C]	Cr [C]	Fe <sup>2+</sup> [C]	Fe <sup>3+</sup> [C]	Mg [C]	Ca [C]	Mn [C]	
Cal. #	8.06	0.00	0.00	0.00	1.77	0.00	1.31	0.09	1.72	0.04	0.01	
Gln	Fe <sup>2+</sup> [B]	Mg [B]	Ca [B]	Mn [B]	Na [B]	Na [A]	Ca [A]	K [A]				
Cal. #	0.00	0.00	0.00	0.00	1.99	0.00	0.00	0.00				
Ep	Si [T]	Al <sup>IV</sup> [T]	Ti [M]	Cr [M]	Al <sup>VI</sup> [M]	Fe <sup>3+</sup> [M]	Mg [M]	Mn [M]	Na [M]	K [M]	Ca [A]	
Cal. #	3.01	0.00	0.00	0.00	2.49	0.50	0.00	0.00	0.00	0.00	1.98	

Gln: glaucophane, Ep: epidote, n.d.: not detected, Cal. #: the calculated cation values occupying each site in the crystal structure, [T] and [A]: T-site and A-site in amphibole (glaucophane) and epidote crystal structures, [C] and [B]: C-site and B-site in amphibole (glaucophane) structure, and [M]: M-site in epidote structure.

### 3.2.2. Deformation experiment in simple shear

Deformation experiments of epidote blueschist were conducted using a modified Griggs apparatus at the Tectonophysics laboratory, SEES at SNU, Seoul, South Korea (Fig. 3.2). As there was no clear foliation and lineation in the starting material, the sample was core-drilled in an arbitrary orientation in the same direction (Fig. 3.3a) as a cylindrical rod with a 3.15 mm diameter (Fig. 3.3b) and cut at 45° to ~400 μm thick (Fig. 3.3c), for the simple shear experiment. Figures 3.3d and 3.4 presents parts and schematic diagram of sample assembly designed for the deformation experiment in simple shear, respectively. The sample was sandwiched between alumina pistons cut at 45° in the maximum principal stress ( $\sigma_1$ ) direction, keeping the same orientation for all experiments (Fig. 3.4). Weak CsCl or NaCl was used as a pressure medium. A thin Ni foil, a strain marker, was inserted in the middle of the sample perpendicular to the shear plane. Temperature was monitored using two thermocouples (Pt<sub>70</sub>-Rh<sub>30</sub> and Pt<sub>94</sub>-Rh<sub>6</sub>) near the top and bottom of the specimen. The confining pressure and temperature were raised to the target pressure (0.9–1.5 GPa) and temperature (400–500 °C) within ~10 h and ~30 min, respectively. The sample was deformed by moving the tungsten carbide (WC) and alumina (Al<sub>2</sub>O<sub>3</sub>) pistons at a constant speed ( $\sim 8.7 \times 10^{-5}$  mm·s<sup>-1</sup>). Following the deformation experiment, the sample was quenched to room temperature by shutting off the power to preserve microstructures developed during experiments. The confining pressure was decreased to room pressure in the same length of time that it took to increase and reach the target pressure.

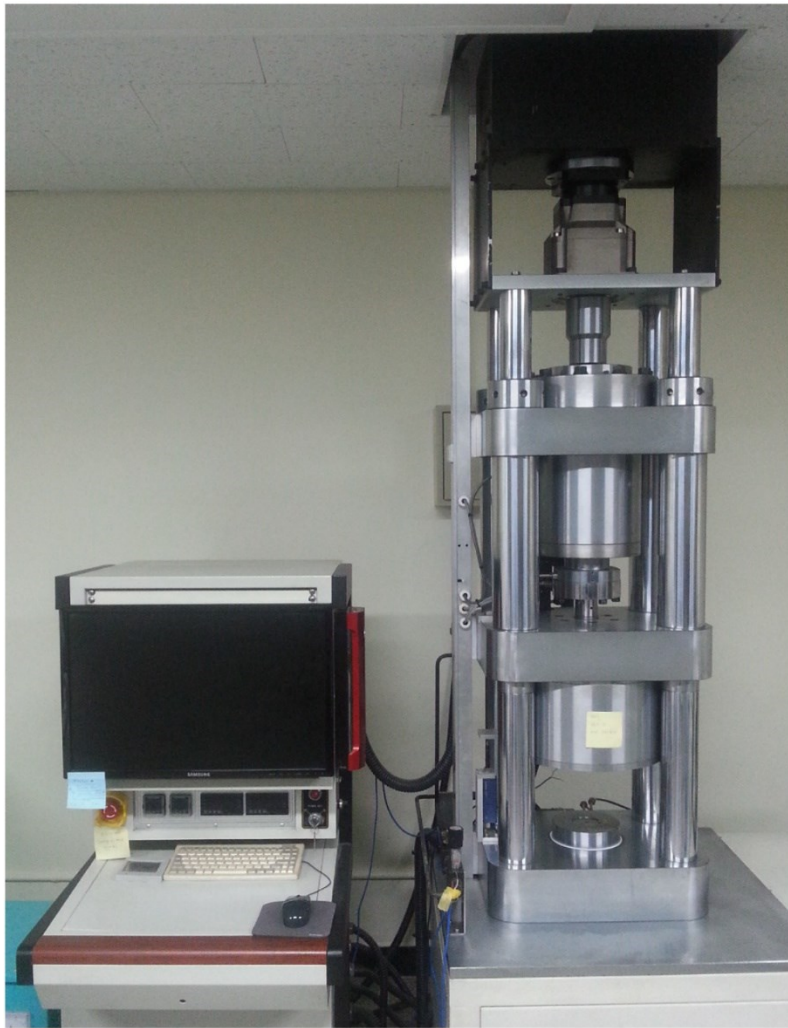


**Figure 3.2.** Photograph of a modified Griggs apparatus, high pressure and high temperature solid-medium apparatus housed at Tectonophysics laboratory, School of Earth and Environmental Sciences (SEES) in Seoul National University (SNU), Seoul, South Korea. This apparatus has a capability of deformation of rock at high pressure and high temperature up to  $P = 5 \text{ GPa}$  and  $T = 1500 \text{ }^\circ\text{C}$ , respectively.

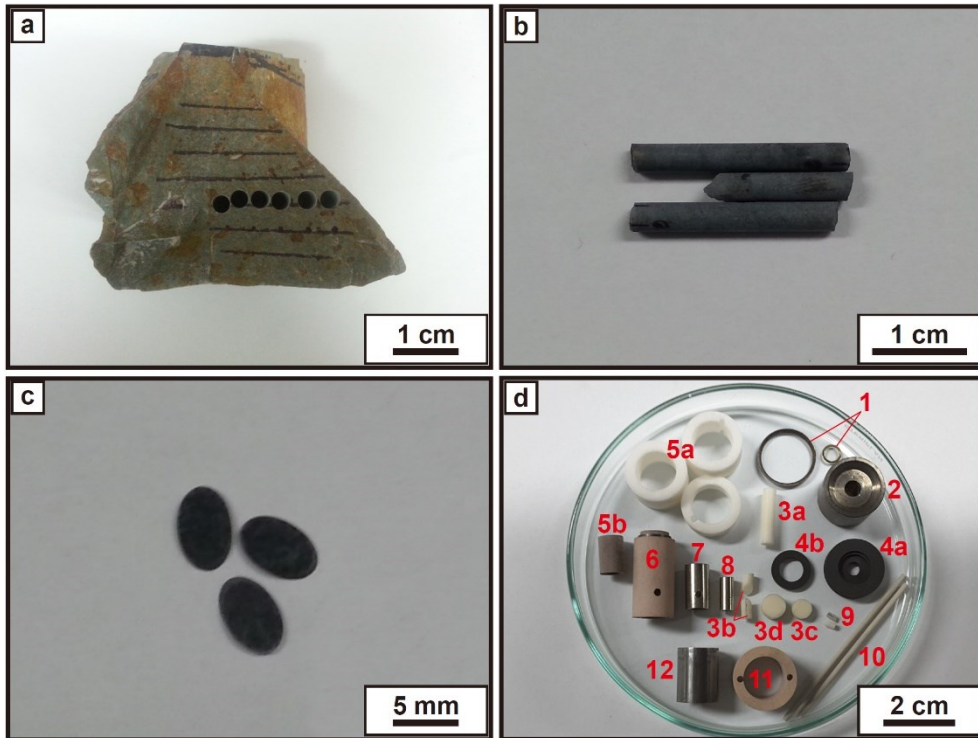


**Figure 3.3.** Photographs of a starting material and parts of the sample assembly **(a)** Starting material core-drilled in an arbitrary orientation in the same direction along the drawn line. **(b)** Sample core drilled in the form of a cylindrical rod. **(c)** Sample disk cut to  $\sim 400 \mu\text{m}$  thick at a  $45^\circ$  angle. **(d)** Parts of the sample assembly used for the deformation experiment in simple shear. 1: Cu seal-ring, 2: Pb plug, 3a: Alumina piston (16.0 mm long), 3b: Alumina pistons cut by  $45^\circ$ , 3c: Alumina piston in Ni sleeve (2.54 mm long), 3d: Alumina piston in furnace set (3.81 mm long), 4a: Graphite top lid, 4b: Graphite bottom ring, 5a: CsCl or NaCl outer pressure medium, 5b: CsCl or NaCl inner pressure medium, 6: Furnace set (outer pyrophyllite sleeve-graphite furnace-inner pyrophyllite sleeve), 7: Ni sleeve, 8: Ni jacket/capsule, 9: Alumina tubes for thermocouples, 10: Mullite tubes for thermocouples, 11: Hard-fired pyrophyllite sleeve, and 12: Tungsten Carbide bottom rod (14.88 mm long).

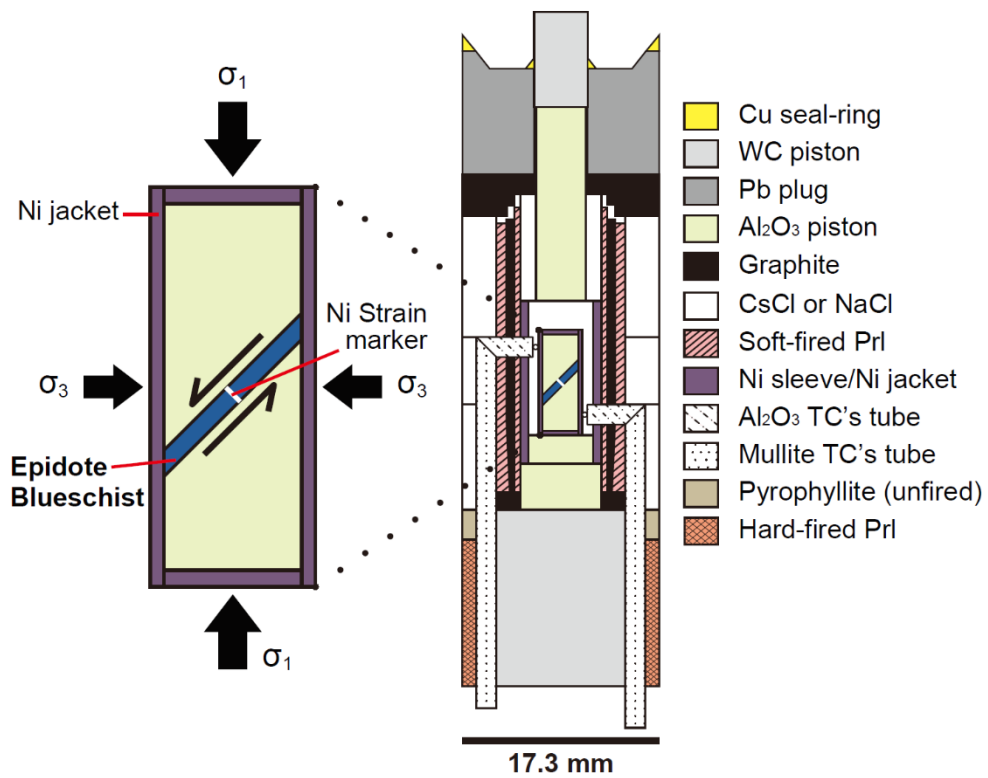


**Figure 3.4.** Schematic of sample assembly for the deformation experiment in simple shear. The sample was positioned at 45° to the maximum principal stress ( $\sigma_1$ ). A strain marker was placed perpendicular to the shear plane in the middle of the sample.

### **3.2.3. Determination of LPOs of minerals**

The LPOs of minerals in epidote blueschist were determined using the EBSD technique (Prior et al., 1999), prior to and after the deformation experiment. To determine the LPOs, HKL Technology's EBSD system (Channel 5 software) with a Nordlys II detector attached to the SEM (JEOL JSM 6380) at the SEES in SNU was used. The LPOs of glaucophane and epidote were measured in the XZ plane of the deformed samples; the X and Z-directions represent the shear direction and direction normal to the shear plane, respectively. Samples were polished using alumina powders, diamond paste of 1  $\mu\text{m}$ , and Syton (0.06  $\mu\text{m}$  colloidal silica slurry) because the measurement of the LPO of minerals using SEM involved removing the mechanical surface damage using a chemical-mechanical polishing technique (Lloyd, 1987). The polished plane was coated with a  $\sim 3$  nm thick carbon to prevent charging in the SEM, and the surface was tilted  $70^\circ$  to the incident electron beam in the chamber. EBSD analysis was conducted under a 20 kV accelerating voltage, a 15 mm working distance, and a spot size of 60. For each grain, all EBSD patterns were manually indexed point by point to determine the LPO of the mineral accurately.

### **3.2.4. Observation of the deformation microstructures in minerals**

The observation of deformed samples following the experiments was conducted using field-emission SEM (FE-SEM; JEOL JSM 7100F) at the SEES in SNU. To observe the intracrystalline deformation microstructures in samples, EBSD mapping of deformed grains was conducted using the Oxford Instruments' EBSD system (AZtec v.3.4 software), with a Symmetry detector attached to the FE-SEM at the SEES in SNU. EBSD analysis was conducted under a 15 kV accelerating voltage, a 25 mm working distance, a ~3 nA probe current, and a 0.1–0.2  $\mu\text{m}$  step size. Data was subsequently processed using MTEX, a MATLAB toolbox (Bachmann et al., 2011), to calculate the local misorientations for textural analysis. This chapter used the grain reference orientation deviation (GROD) angle map and the kernel angle misorientation (KAM) map. The former is a map generated based on the deviation between mean orientation of a reference point and those of other points. The KAM map is the misorientation less than the predefined threshold value calculated by the mean orientation between a point and its neighbors. The TEM technique was also used to observe dislocation structures in deformed grains. TEM observations under a 300 kV accelerating voltage were carried out using a JEOL JEM-3010 at the National Center for Inter-university Research Facilities (NCIRF) in SNU. Focused ion beam (FIB) foils for TEM investigations were prepared using the FEI Helios 650 at the NCIRF in SNU. The FIB mineral foils were extracted subparallel to the shear direction and shear plane.

## 3.3. Results

### 3.3.1. Deformation microstructures after experiments

Table 3.2 summarizes the experimental conditions and results for the deformation experiments on the epidote blueschist. The deformation microstructures of representative samples are shown in Figure 3.5. Even though the sample assembly designed for simple shear was used (Fig. 3.4), there was a small proportion of the pure shear component ( $\sim 5\text{--}9\%$ ) for all experiments depending on the shear strain magnitude. The magnitude of shear strain ( $\gamma$ ) was quantified by the rotational angle of the thin Ni strain marker and/or elongated shapes of grains. In the sample deformed with low shear strain ( $\gamma \leq 1$ ), most minerals exhibited a similar shape to that of the starting material (Fig. 3.5a and b). Glaucophane grains had slightly elongated obliquely to the shear direction, with some fractures present subparallel to the shear plane inside a grain. In contrast, epidote grains exhibited kink bands and book shelf gliding textures (Franz and Liebscher, 2004; Fig. 3.5b). In the sample deformed with an intermediate shear strain ( $1 < \gamma \leq 2$ ), glaucophane grains had elongated, demonstrating cataclastic mosaic fragmented texture. Their rotation was also more oblique to shear direction than those deformed with low shear strain. However, epidote grains had reduced elongation than glaucophane, exhibiting shear band type fragmented texture in this region (Fig. 3.5c and d). In the sample deformed with high shear strain ( $\gamma > 2$ ), all minerals appeared to be elongated and/or flowed subparallel to the shear direction (Fig. 3.5e and f). Relatively large glaucophanes ( $\sim 30\text{--}50\ \mu\text{m}$ ) were highly elongated, consisting of many small-size grains from 0.5

to 5  $\mu\text{m}$ . They were in subparallel alignment with the shear direction, exhibiting a cataclastic/granular flow texture. The microstructure of epidote and titanite also presented with similar cataclastic/granular flow textures.

In contrast, small grains, originally less than 5  $\mu\text{m}$  in size prior to the experiment, appeared to flow exhibiting a thin ductile banded shape (Fig. 3.6). In this region, the ductile shear band representing the C-C' structure and the cataclastic flow textures coexist (Fig. 3.6a). The brittle microfault, indicated by a small offset of the thin banded titanite in the glaucophane, and the ductile elongated shear band of small glaucophane minerals were also observed to coexist (Fig. 3.6b).

**Table 3.2.** Experimental conditions and results for the deformation experiment on epidote blueschist.

Run #	P (GPa)	T (°C)	Peak $\sigma_d$ (MPa)	Shear strain ( $\gamma$ )	Shear strain rate ( $s^{-1}$ )	LPO of Gln	LPO of Ep
JH148	1.2	430 $\pm$ 10	700 $\pm$ 20	0.4 $\pm$ 0.02	1.5 $\times$ 10 <sup>-5</sup>	Type-1	Weak fabric
JH98b	1.5	500 $\pm$ 10	710 $\pm$ 20	0.6 $\pm$ 0.03	3.4 $\times$ 10 <sup>-5</sup>	Type-1	Weak fabric
JH88b	1.5	400 $\pm$ 10	800 $\pm$ 20	0.8 $\pm$ 0.03	4.4 $\times$ 10 <sup>-5</sup>	Type-1	Weak fabric
JH112b	0.9	430 $\pm$ 10	720 $\pm$ 20	0.9 $\pm$ 0.03	4.2 $\times$ 10 <sup>-5</sup>	Type-1	Weak fabric
JH94b	1.5	400 $\pm$ 10	900 $\pm$ 20	1.5 $\pm$ 0.06	6.0 $\times$ 10 <sup>-5</sup>	Transitional fabric	Weak fabric
JH88a	1.5	400 $\pm$ 10	800 $\pm$ 20	2.1 $\pm$ 0.12	1.2 $\times$ 10 <sup>-4</sup>	Type-2	Type-1
JH98a	1.5	500 $\pm$ 10	710 $\pm$ 20	2.4 $\pm$ 0.12	1.4 $\times$ 10 <sup>-4</sup>	Type-2	Type-1
JH150	1.2	480 $\pm$ 10	680 $\pm$ 20	2.7 $\pm$ 0.15	1.2 $\times$ 10 <sup>-4</sup>	Type-2	Type-1
JH112a	0.9	430 $\pm$ 10	720 $\pm$ 20	2.9 $\pm$ 0.20	1.4 $\times$ 10 <sup>-4</sup>	Type-2	Type-1
JH94a	1.5	400 $\pm$ 10	900 $\pm$ 20	4.5 $\pm$ 0.38	1.8 $\times$ 10 <sup>-4</sup>	Type-2	Type-2

$\sigma_d$  : differential stress, Gln: glaucophane, and Ep: epidote

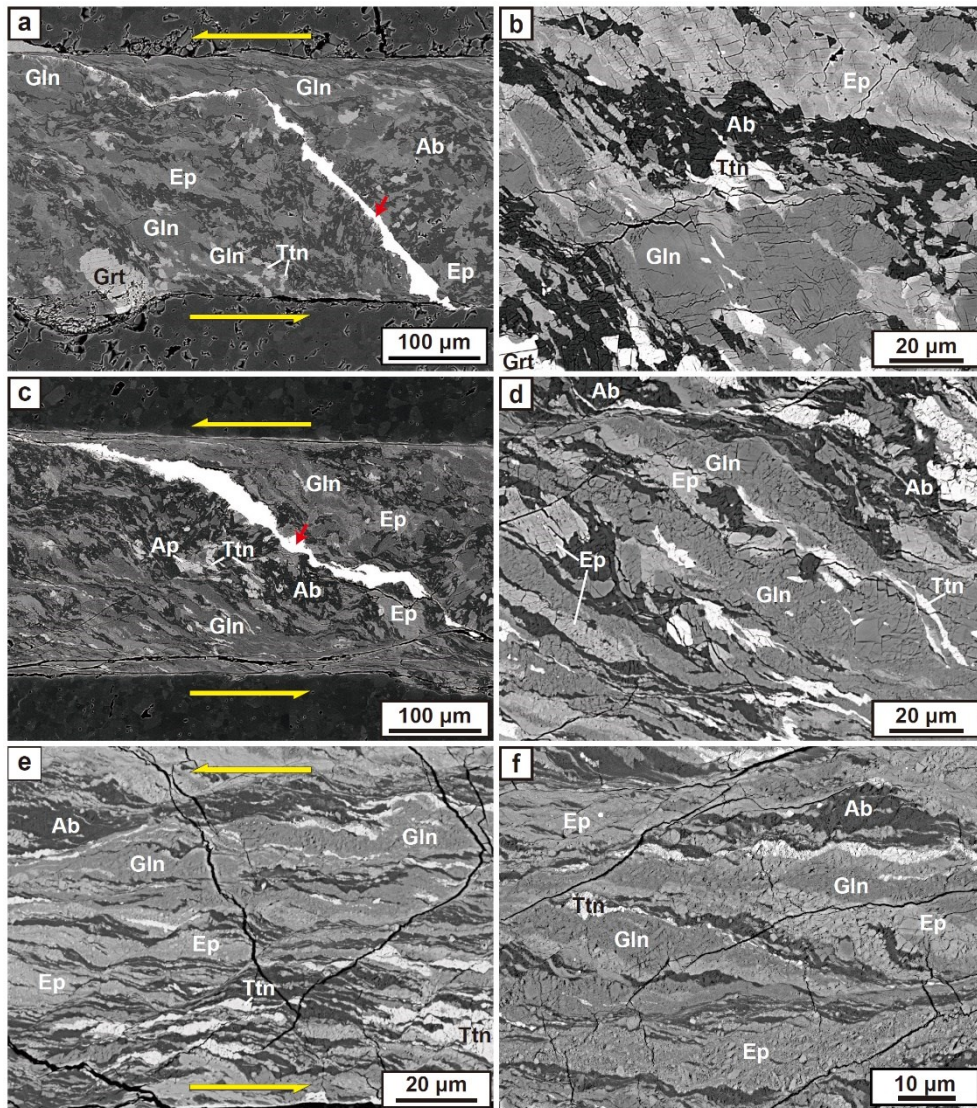


**Figure 3.5.** BSE images of deformed samples after simple shear experiments. **(a)** and **(b)** Sample deformed with low shear strain (JH88b,  $\gamma = 0.8$ ); **(c)** and **(d)** sample deformed with intermediate shear strain (JH94b,  $\gamma = 1.5$ ); **(e)** and **(f)** sample deformed with high shear strain (JH94a,  $\gamma = 4.5$ ). Long yellow arrows indicate the left-lateral (sinistral) shear sense, and red arrows indicate the Ni strain marker. All samples in the images show the left-lateral (sinistral) shear sense. Gln: glaucophane, Ep: epidote, Ttn: titanite, Ab: albite, Chl: chlorite, Grt: garnet, and Ap: apatite.

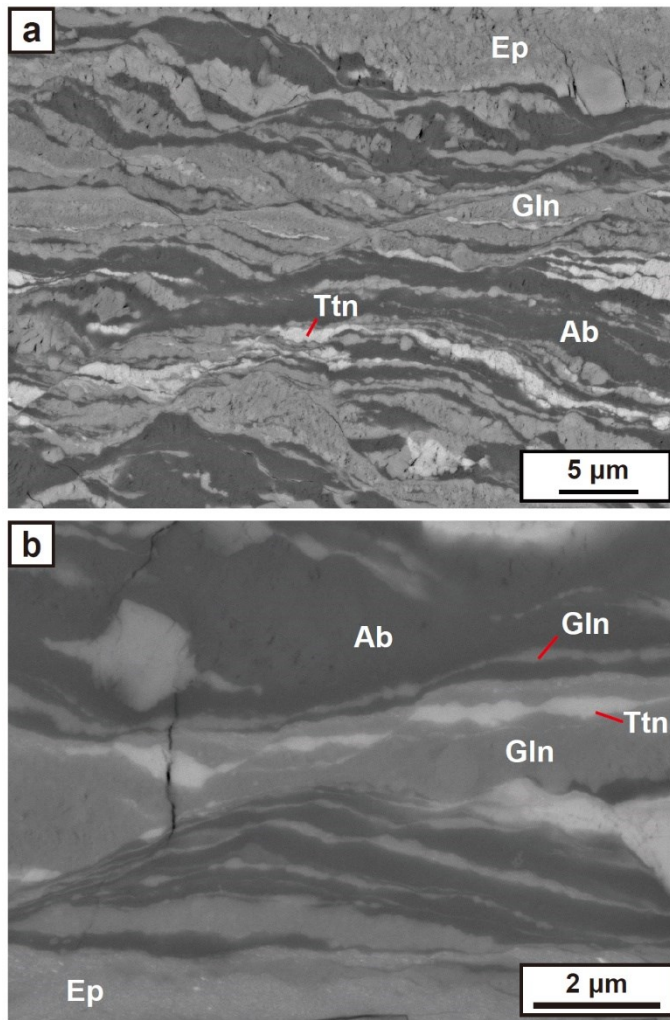


**Figure 3.6.** BSE images of sample deformed with high shear strain (JH94a,  $\gamma = 4.5$ ).  
 (a) Ductile shear band showing C-C' structure with cataclastic flow texture; (b)  
 brittle microfault indicated by the titanite offset and ductile elongated shear band of  
 small glaucophane. All images show the left-lateral (sinistral) shear sense. Gln:  
 glaucophane, Ep: epidote, Ttn: titanite, and Ab: albite.

### 3.3.2. LPOs of glaucophane and epidote

Figure 3.7 illustrates the LPOs of glaucophane and epidote. The starting material was set up in the same orientation for all experiments. The initial fabric of glaucophane in the starting material is shown in Figure 3.7a. It exhibited a weak girdle distribution of the crystallographic [100] axes and the (110) and (010) poles, subnormally aligned with the direction becoming a shear direction, and the [001] axes aligned obliquely to that direction. Based on the pole figures of glaucophane deformed after the experiments (Fig. 3.7b–3.7k), the LPO of glaucophane had altered with increasing shear strain ( $\gamma$ ). In samples deformed under low shear strain ( $\gamma \leq 1$ ), the (010) poles of glaucophane had subnormally aligned with the shear plane and the [001] axes were in subparallel alignment with the shear direction; this is defined here as type-1 LPO for glaucophane (Fig. 3.7b–3.7e). With increasing shear strain between  $1 < \gamma \leq 2$ , the [100] axes and (010) poles were in subparallel alignment with the shear plane and subnormal to shear direction, appearing to be a transitional fabric (Fig. 3.7f). In samples deformed under high shear strain ( $\gamma > 2$ ), the [100] axes were subnormally aligned with the shear plane and the [001] axes were in subparallel alignment with the shear direction; this is defined here as type-2 LPO for glaucophane (Fig. 3.7g–3.7k).

The initial fabric of epidote in the starting material showed that the crystallographic [100] axes were subnormally aligned in the direction becoming a shear direction forming a girdle shape, and the (010) poles were in subparallel

alignment with that direction (Fig. 3.7a). After deformation experiments, the LPO of epidote had also altered with increasing shear strain ( $\gamma$ ). The LPOs of epidote in deformed samples that had undergone low shear strain ( $\gamma < 2$ ) exhibited a weak nonsystematic fabric (Fig. 3.7b–3.7f). However, in samples deformed under a shear strain between  $2 < \gamma < 4$ , the [100] axes of epidote were subnormally aligned with the shear plane, and the (010) poles were in subparallel alignment with the shear direction; this is defined here as type-1 LPO for epidote (Fig. 3.7g–3.7j). In the sample deformed under a high shear strain of  $\gamma = 4.5$ , the (010) poles of epidote were subnormally aligned with the shear plane, and the [001] axes were in subparallel alignment with the shear direction; this is defined here as type-2 LPO for epidote (Fig. 3.7k).

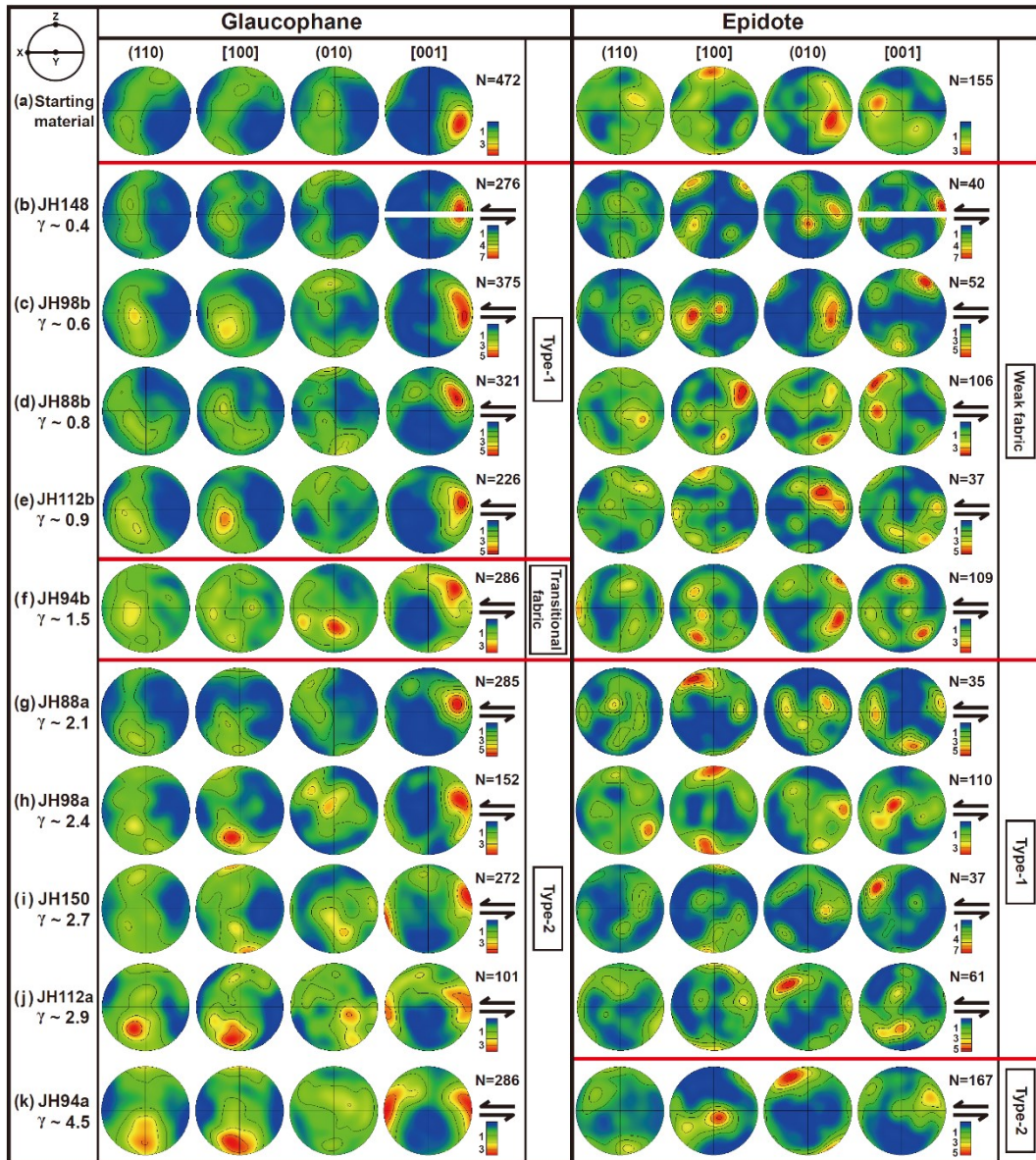


**Figure 3.7.** Pole figures of glaucophane and epidote in (a) starting material and (b)–(k) deformed samples showing LPO presented in the lower hemisphere using an equal-area projection. A half-scatter width of  $30^\circ$  was used. The X- and Z- directions correspond to the shear direction and the direction normal to the shear plane in the experiment, respectively. White line in pole figure: shear plane; black arrows: shear direction; and N: the number of grains.

### **3.3.3. Observations of intracrystalline deformation microstructures in deformed glaucophane**

EBSD mapping in single glaucophane was undertaken for samples deformed under different shear strains (Fig. 3.8), to observe the intracrystalline deformation microstructures of glaucophane. In glaucophane deformed under a low shear strain of  $\gamma = 0.8$  at a pressure of 1.5 GPa and a temperature of 400 °C (JH88b), the GROD angle map showed that the local misorientation had gradually increased toward the edge of the grain (Fig. 3.8b). In contrast, the KAM map indicated that intracrystalline misorientations were present on the inside and edge of the grain (black arrows in Fig. 3.8c). In glaucophane deformed under a low shear strain of  $\gamma = 0.6$  at a pressure of 1.5 GPa and high temperature of 500 °C (JH98b), the GROD angle map illustrated that the high misorientation focused on the fracture in the grain (Fig. 3.8e). However, the KAM map presented well-preserved misorientation lines, irrelevant to the fractures (Fig. 3.8f). For glaucophane deformed under a high shear strain of  $\gamma = 4.5$  at a pressure of 1.5 GPa and temperature of 400 °C (JH94a), regardless of the cataclastically comminuted grain, the KAM map showed that several misorientation lines were present in the remaining relatively large grains (Fig. 3.8i).

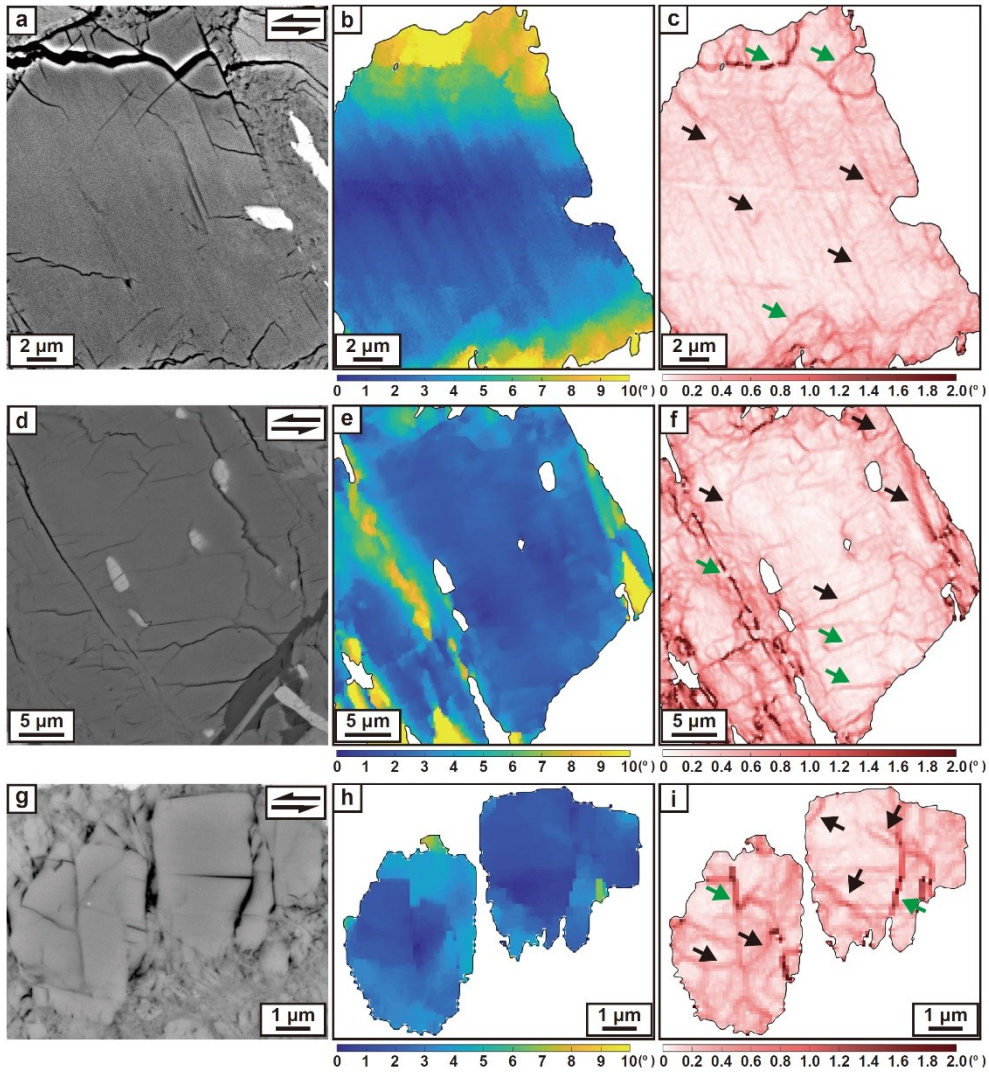


**Figure 3.8.** BSE image, GROD angle map (mis2mean), and KAM map showing the intracrystalline deformation microstructure of glaucophane deformed under different shear strains of **(a)–(c)**  $\gamma = 0.8$  (in JH88b), **(d)–(f)**  $\gamma = 0.6$  (in JH98b), and **(g)–(i)**  $\gamma = 4.5$  (in JH94a). Black arrows in the BSE images indicate the left-lateral (sinistral) shear sense. Black and green arrows in KAM map indicate the local plastic strain (i.e., dislocation density or rotation of the lattice) and the tilted crystal orientation by brittle fracture, respectively. Step size of mapping: **(b)** and **(c)**  $0.15 \mu\text{m}$ ; **(e)** and **(f)**  $0.2 \mu\text{m}$ ; **(h)** and **(i)**  $0.1 \mu\text{m}$ .

### **3.3.4. Observations of dislocation microstructures in deformed glaucophane and epidote using TEM**

Weak-beam dark field (WBDF) and bright field (BF) images were captured using TEM to observe dislocation microstructures in glaucophane and epidote following the experiments (Figs. 3.9 and 3.10). In glaucophane deformed under a low shear strain ( $\gamma \leq 1$ ;  $\gamma = 0.6$ , in JH98b), WBDF images showed the presence of several dislocation structures. Stacking faults aligned perpendicular to the shear direction (yellow arrow) were observed, in addition to a dislocation loop with a curve toward the shear direction for diffraction vector of  $\mathbf{g} = 101$  (Fig. 3.9a). Straight dislocations aligned perpendicular or oblique to the shear direction were also observed for  $\mathbf{g} = 101$  (Fig. 3.9b). In the glaucophane deformed under a high shear strain ( $\gamma > 2$ ;  $\gamma = 4.5$ , in JH94a), WBDF images of relatively large grains showed the presence of several distorted lattice structures (moiré fringe textures) and straight dislocations aligned obliquely to the shear direction (yellow arrow) (Fig. 3.9c and d).

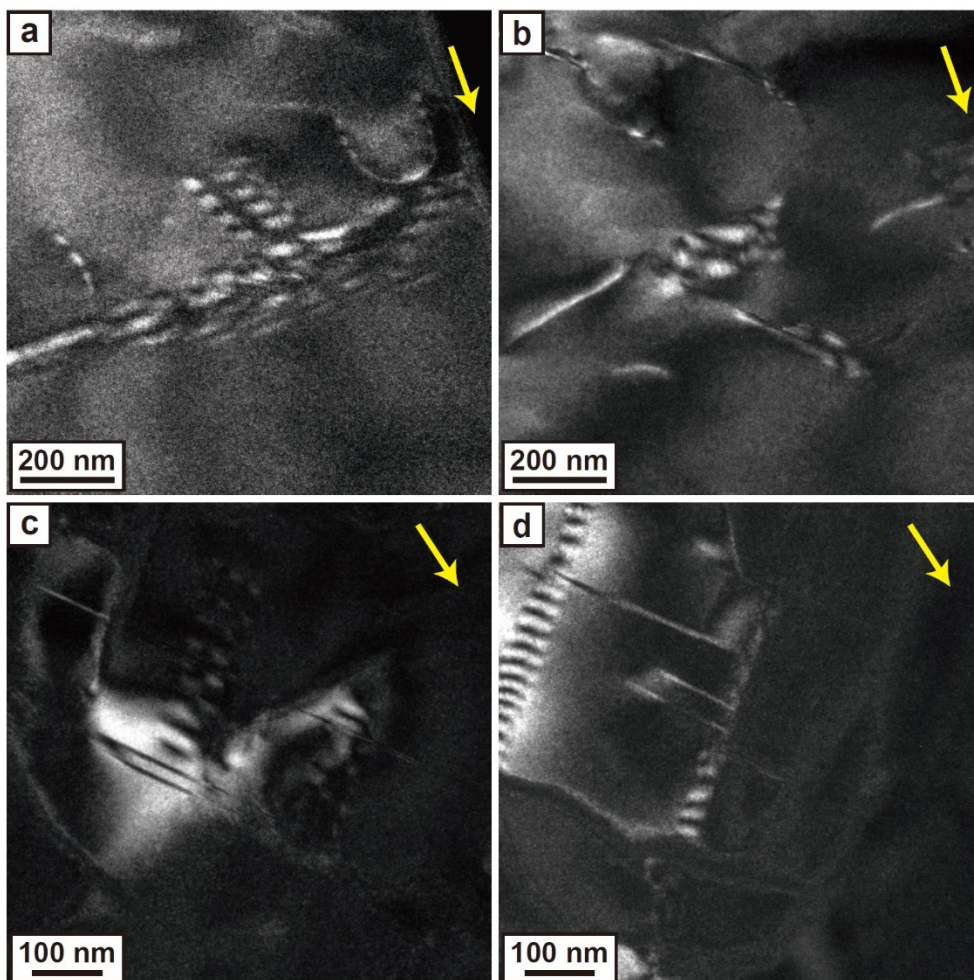


**Figure 3.9.** Weak-beam dark field (WBDF) images of glaucophane experimentally deformed with **(a) and (b)** low shear strain ( $\gamma = 0.6$ ) at  $P = 1.5$  GPa and  $T = 500$  °C (JH98b) and with **(c) and (d)** high shear strain ( $\gamma = 4.5$ ) at  $P = 1.5$  GPa and  $T = 400$  °C (JH94a). Yellow arrows indicate shear direction in the images. P: pressure; and T: temperature.

In epidote deformed under a shear strain between  $2 < \gamma < 4$  ( $\gamma = 2.4$ , in JH98a), WBDF images illustrated the presence of several twin boundaries as well as subgrain boundaries aligned parallel or perpendicular to the shear direction (yellow arrow) (Fig. 3.10a and b). The free dislocations observed in the epidote were scattered and/or aligned to form a line (Fig. 3.10b). The BF image of epidote deformed under a high shear strain of  $\gamma = 4.5$  (JH94a) showed the presence of many distorted lattice structures with brittle failures, similar in texture to glaucophane deformed with a high shear strain (Fig. 3.10c). In addition, a relatively large grain of epidote conserving deformation twins aligned obliquely to the shear direction (yellow arrow) was surrounded by grains that were of tens of nanometers size (Fig. 3.10d).

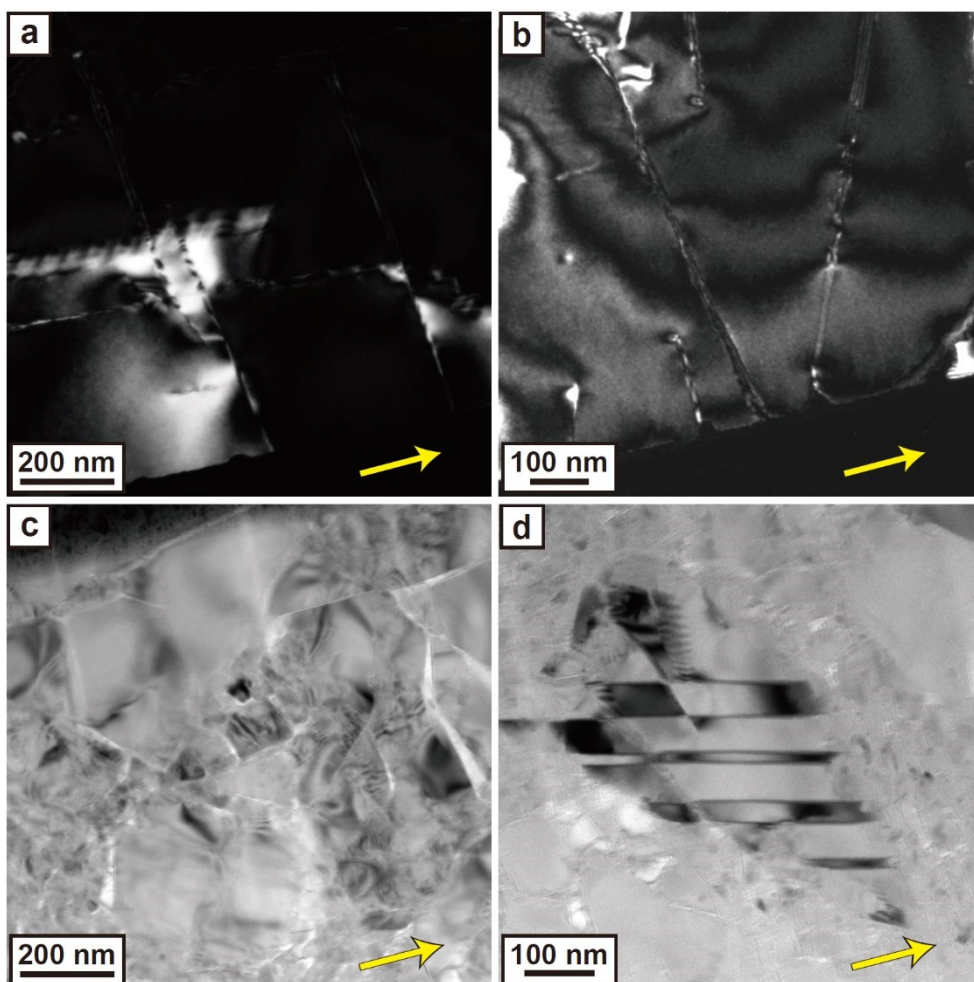


**Figure 3.10.** (a) and (b) Weak-beam dark field (WBDF) images of epidote experimentally deformed under a shear strain of  $\gamma = 2.4$  at  $P = 1.5$  GPa and  $T = 500$  °C (JH98a); (c) and (d) bright field (BF) images of epidote experimentally deformed under a high shear strain of  $\gamma = 4.5$  at  $P = 1.5$  GPa and  $T = 400$  °C (JH94a). Yellow arrows indicate the shear direction in the images. P: pressure; and T: temperature.

## 3.4. Discussions

### 3.4.1. LPO formation and deformation mechanisms of glaucophane

Although the starting material did not show a clear foliation and lineation in the hand specimen, there was an initial fabric, as shown in Figure 3.7a. However, the initial LPO of minerals in the starting material was obviously altered with increasing shear strain (Fig. 3.7b–3.7k). Type-1 LPOs for glaucophane in samples deformed under a low shear strain ( $\gamma \leq 1$ ) exhibited (010) poles subnormally aligned with the shear plane and the [001] axes in subparallel alignment with the shear direction (Fig. 3.7b–3.7e); this is rarely observed in natural blueschist. A recent study reported this type-1 LPO for glaucophane in weakly deformed (folded) blueschist-facies rock (Cossette et al., 2015). Previous TEM/HREM study also reported a dislocation slip system of (010)[001] in glaucophane from a blueschist-facies micaschist at a pressure  $< 1.0$  GPa and temperature between 350 and 450 °C (Reynard et al., 1989). They suggested that the dislocation glide (or slip) may operate at relatively low temperatures as the Na occupying the *M4*-site is able to jump into the neighboring empty *A*-site in glaucophane (Reynard et al., 1989). As the easiest slip systems in chain-silicate structures tend to avoid breaking the Si-O bond (Nicolas and Poirier, 1976; van Duysen and Doukhan, 1984), they concluded that the dislocation glide needs to operate between the Si-O tetrahedral chains; this means the (010) in glaucophane (Fig. 3.11a and b) (Reynard et al., 1989). This suggestion coincides

with the observed dislocation in a single crystal of glaucophane deformed under a low shear strain ( $\gamma=0.6$ ) in this study (Fig. 3.9a and b). Various dislocations observed with different diffraction vectors indicate that differing dislocation slip systems were activated by shear deformation. Although this glaucophane was deformed at a relatively high pressure and temperature (i.e., 1.5 GPa and 500 °C, JH98b), the KAM map for glaucophane deformed at a pressure of 1.5 GPa and temperature of 400 °C showed that intracrystalline deformation (i.e., dislocation glide) also occurs at relatively lower temperature (Fig. 3.8c). The glaucophane shape slightly elongated oblique to the shear direction is considered a result of the rigid body rotation in a weak plagioclase matrix (Fig. 3.5b). Thus, these results suggest that glaucophane was deformed by the simultaneous rotation of a relatively rigid body with intracrystalline dislocation glide (or slip) forming a strong type-1 LPO under a pressure between 0.9–1.5 GPa and a temperature between 400–500 °C. This result is consistent with the suggestion from a previous study that rigid body rotation and dynamic recrystallization by dislocation creep are the deformation mechanisms for glaucophane (Zucali et al., 2002). The glaucophane that had deformed under a shear strain between  $1 < \gamma \leq 2$ , was elongated showing cataclastic and mosaic fragmented texture (Fig. 3.5d). This microstructure may indicate that the predominant deformation of glaucophane had converted to brittle behavior as cataclastic flow and rigid body rotation, exhibiting a transitional LPO with a decrease in the fabric strength of glaucophane (Fig. 3.7f).

For deformed samples under a high shear strain ( $\gamma > 2$ ), type-2 LPOs of glaucophane exhibited the [100] axes subnormally aligned with the shear plane and the [001] axes in subparallel alignment with the shear direction (Fig 3.7g–3.7k),

which have been reported in many natural blueschists (Bezacier et al., 2010a; Cao and Jung, 2016; Cao et al., 2013; 2014; Choi et al., 2021; Fujimoto et al., 2010; Ha et al., 2018; Kim et al., 2013a; 2013b; Teyssier et al., 2010). This type-2 LPO of glaucophane is also similar to the type-1 LPO of hornblende (Jung, 2017; Ko and Jung, 2015). A previous TEM/HREM study reported major dislocation glides for (100)[001] and {110}[001] in glaucophane from an eclogitic micaschist (at 1.5–1.8 GPa and 550–600 °C). These are sufficiently active independent slip systems that ensure its ductile behavior during progressive deformation (Reynard et al., 1989). Other previous studies on natural blueschist have also suggested that dislocation creep was a dominant mechanism in the formation of type-2 glaucophane LPO (Cao et al., 2014; Kim et al., 2013a). Based on the TEM investigation in this study, many dislocations and distorted lattice structures were present in a single crystal of glaucophane deformed under a high shear strain ( $\gamma = 4.5$ ) under a pressure of 1.5 GPa and temperature of 400 °C (JH94a; Fig. 3.9c and d). The KAM map of the deformed grain illustrated many intracrystalline misorientations, irrelevant to the fracture, indicating the activation of dislocations (Fig. 3.8i). High shear strain energy is likely to form an (100) slip plane by breaking the octahedral Mg-O bond, weak *M4*-site (occupied by Na), and empty *A*-site (Fig. 3.11a and c). As such, these results suggest that the magnitude of shear strain may be a major cause for changes to dominant slip systems and the formation of different LPOs of glaucophane in the blueschist-facies metamorphic condition. In addition, elongated aggregates of small-size grains with cataclastic/granular flow texture for glaucophane deformed under a strain of  $\gamma > 2$  (Fig. 3.5e and f), suggest that the type-2 LPO formation may be influenced by simultaneous cataclastic flow deformation of glaucophane. However, originally small grains of glaucophane ( $\sim 5 \mu\text{m}$ ) prior to deformation, appear to flow exhibiting

a ductile thin banded shape (Fig. 3.6). These microstructures imply that high shear strain has a different influence on relatively large grains ( $\geq 30 \mu\text{m}$ ) and very fine-grains of glaucophane, causing cataclastic flow deformation and a crystal plastic deformation via dynamic recrystallization (Drury and Urai, 1990), respectively. As a result, the rheological contrast between component minerals, shear strain, and grain size may be important factors influencing the deformation mechanisms of glaucophane.

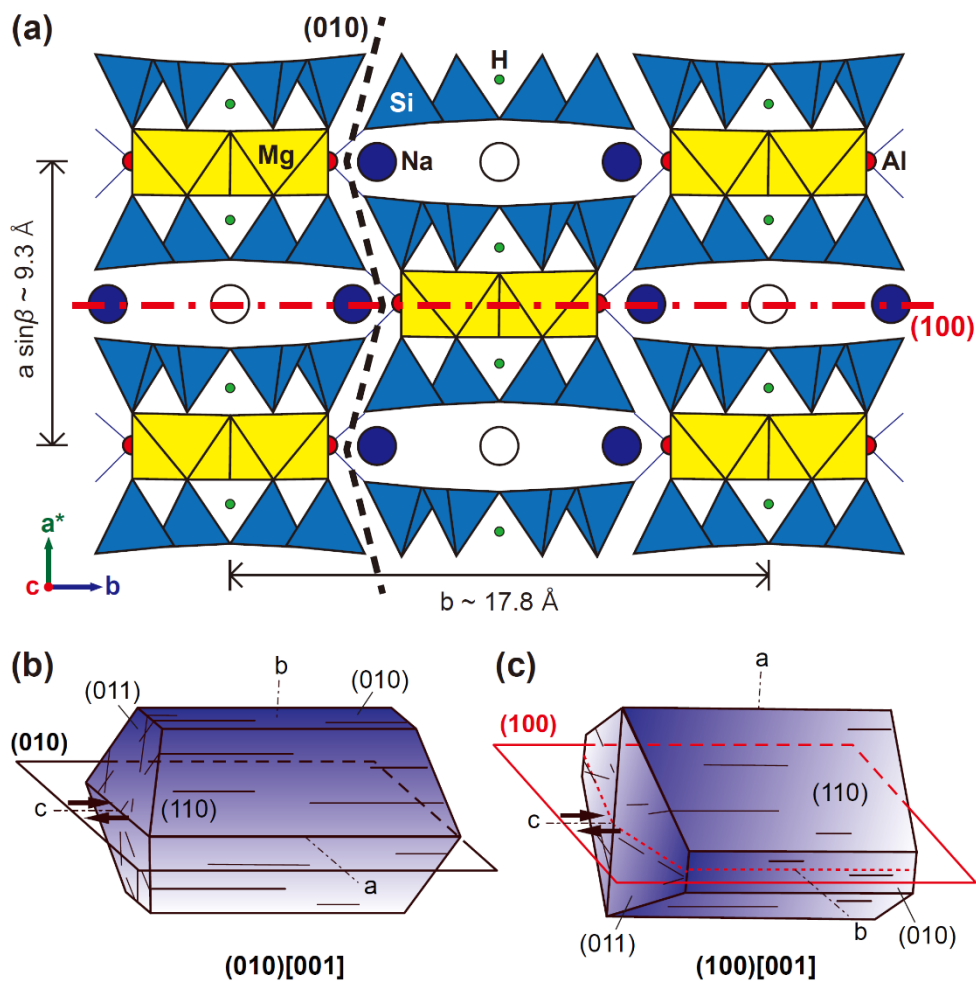


**Figure 3.11.** (a) Simplified glaucophane crystal structure projected onto the (001) plane. Black dashed and red dot-dashed lines indicate the tracks of the easiest slip system planes at low and high shear strain, respectively. Blue tetrahedron: Si-O structure, yellow octahedron: Mg-O structure (*M1*-site), red circle: Al (*M2*-site), green circle: H, blue circle: Na (*M4*-site), and white circle: empty space (*A*-site). The Mg-O octahedron in *M3*-site has been omitted; (b) and (c) schematic of the glaucophane crystal form and different dominant slip systems in glaucophane. The transparent truncate sheet and black arrows indicate a dominant slip plane and a dominant slip direction, respectively.

### 3.4.2. LPO formation and deformation mechanisms of epidote

The experimental results showed that epidote in samples deformed under a low shear strain of  $\gamma \leq 2$  exhibited mostly weak and nonsystematic LPOs (Fig. 3.7b–3.7f). This may be due to insufficient strain developing an intracrystalline deformation in epidote as a rigid material. A previous study also reported similar results, revealing that low shear strain ( $\gamma = 2$ ) was insufficient to produce a strong preferred orientation of experimentally deformed epidote mineral as a relatively rigid particle in a deformed plagioclase matrix at a pressure of 1.5 GPa and a temperature of 750 °C (Stünitz and Tullis, 2001). In contrast, the type-1 LPO of epidote in samples deformed under a shear strain between  $2 < \gamma < 4$  (Fig. 3.7g–3.7j) and type-2 LPO of epidote deformed under a shear strain of  $\gamma = 4.5$  (Fig. 3.7k) were different from previously reported LPOs (Bezacier et al., 2010a; Cao et al., 2011; 2013; Cossette et al., 2015; Fujimoto et al., 2010; Ha et al., 2018; Kim et al., 2013a). However, a previous TEM and HREM investigation reported stacking faults on (100) and lamellar twins on (100) as easiest shearing planes of epidote mineral (clinozoisite and zoisite) (Ray et al., 1986). Other studies have also observed deformation twin lamellae on (100) of clinozoisite in eclogite (Müller and Franz, 2004; 2008). This plane was consistent with a relatively weak bond for the *A*-site (occupied by Ca) and *M3*-site (occupied by Al-Fe<sup>3+</sup>; Fig. 3.12a and b) (Deer et al., 1986). On TEM observations of the epidote crystal deformed under a shear strain between  $2 < \gamma < 4$  ( $\gamma = 2.4$ , JH98a), several aligned dislocations, subgrain boundaries, and deformation twins were present (Fig. 3.10a and b). This suggests that dislocation glide or slip may

play a major role in the formation of type-1 LPO for epidote. This result is consistent with deformation processes of epidote group minerals as suggested by Franz and Liebscher (2004); these are either dislocation glide or sliding on the cleavage by fracturing in naturally deformed rocks. On the contrary, another previous study suggested a rigid body rotation as an LPO formation mechanism for epidote group minerals in metabasite rocks through two potential processes. Firstly, where zoisite minerals are deformed by shearing parallel to the (100) cleavage planes and rotated to align with the (100) plane subparallel to foliation. Secondly, where they are deformed by stretching in the [010] axes, resulting in boudinaged crystals in subparallel alignment with lineation, and the (100) plane is simultaneously aligned, subparallel to foliation (Brunsmann et al., 2000). As the epidote is a relatively rigid mineral in this blueschist sample, a rigid body rotation may also be a major process for the development of type-1 LPO.

The type-2 LPO of epidote has not yet been reported. A previous experimental study has suggested that epidote minerals are deformed by granular flow and diffusion-assisted grain boundary sliding at relatively high shear strain ( $\gamma = 4.5$  and  $7.5$ ), thereby developing shear band textures at a pressure of 1.5 GPa and temperature of 750 °C (Stünitz and Tullis, 2001). Based on the TEM investigation in this study, relatively large grains of epidote conserving deformation twins surrounded by nanocrystalline grains were observed in the sample deformed under a shear strain of  $\gamma > 4$  ( $\gamma = 4.5$ , JH94a; Fig. 3.10c and d). These microstructures indicate that cataclastic/granular flow with rigid body rotation may play an important role in the formation of type-2 LPO of epidote (Fig. 3.12c). In contrast, a previous study on naturally bent and kinked epidote crystal suggested that all  $\{100\}$ ,  $\{010\}$ ,  $\{001\}$

planes play a major role in the deformation of epidote group minerals, either as dislocation slip planes or as cleavage planes (Franz and Liebscher, 2004). Thus, type-1 and type-2 LPOs of epidote were likely to have been developed by dislocation creep and cataclastic flow with rigid body rotation due to rheological contrasts with other minerals. Further studies on the slip system of epidote are required at various pressure and temperature conditions to better understand the epidote LPOs/slip systems transition.

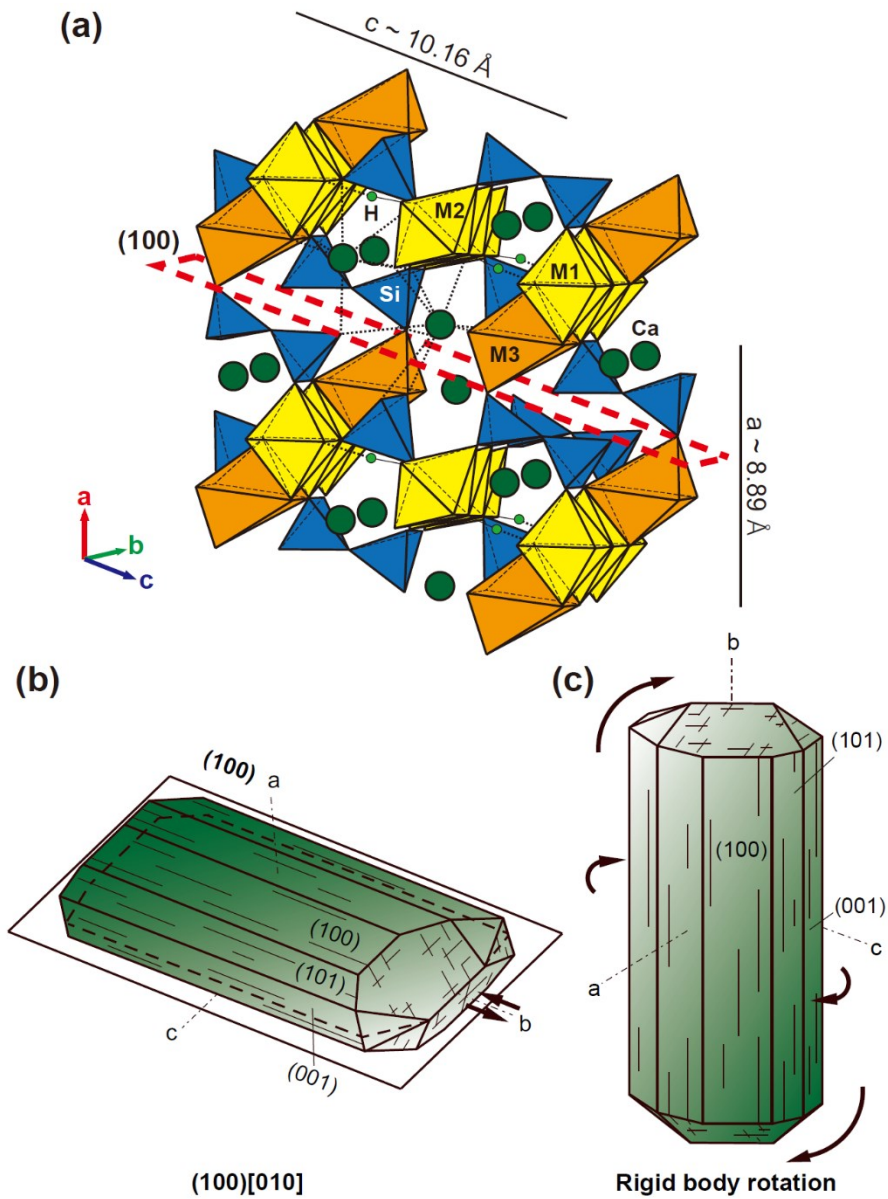


**Figure 3.12.** (a) Simplified epidote crystal structure. Red dashed rectangular indicate the tracks of the easiest (100) slip plane. Blue tetrahedron: Si-O structure, yellow octahedron: Al-O structure (*M1*- and *M2*-site), orange octahedron: Al-Fe<sup>3+</sup> substitution-O (*M3*-site), blue circle: H, and green circle: Ca (*A1*- and *A2*-site); (b) and (c) schematic of the epidote crystal form with different behavior by shear deformation. The transparent truncate sheet and black arrows in (b) indicate a dominant slip plane and a dominant slip direction, respectively. Black arrows in (c) indicate a direction of rigid body rotation by shear strain.

### **3.4.3. Implications for deformation mechanisms of epidote blueschist in a warm subduction zone**

The EBSD analysis and TEM investigation of experimental specimens revealed that glaucophane and epidote, major constituent minerals of epidote blueschist, had deformed simultaneously through brittle and ductile behavior at a pressure of 0.9–1.5 GPa and a temperature of 400–500 °C. These results indicate that epidote blueschist is likely to undergo deformation in the brittle–ductile regime. The nonlocalized cataclastic flow in the deformed sample may be attributed to the deformation microstructures in the semi-brittle regime following the brittle–ductile transition (Karato, 2008; Kohlstedt et al., 1995). Thus, a brittle–ductile transition of glaucophane is likely to occur under a pressure of 1.0–1.5 GPa at 400–500 °C in epidote blueschist. This result is relatively consistent with previous suggestions that glaucophane may be deformed under a ductile regime (i.e., dislocation creep), in natural epidote blueschist at the pressures of ~0.5–2.0 GPa (Cao et al., 2011; 2013; Kim et al., 2013a). A previous experimental study on lawsonite blueschist also suggested that the brittle–ductile transition of glaucophane is likely to occur at a pressure of ~2 GPa and temperatures between 400 and 500 °C (Kim et al., 2015). One may argue that the cataclastic deformation microstructure in this study was produced by the deformation of the sample at a fast strain rate. However, there are also examples showing cataclastic deformation microstructures in natural blueschists and blueschist-facies metamorphic rocks that were deformed at low strain rates (Balestro et al., 2014; Ukar and Cloos, 2019).

The deformation microstructures of epidote under low shear strain showed kink bands or bookshelf gliding textures (Fig. 3.5a–d) indicating that the epidote was a rigid material and cleaved (Passchier and Trouw, 2005). In contrast, glaucophanes under low shear strain was elongated to the shear direction and their LPOs were developed. These experimental results have suggested that the shear strain required to change the LPO of epidote appears to be larger than glaucophane (Fig. 3.13). This is likely a result of the strength contrast between glaucophane and epidote, as deformation is concentrated and strain is localized on relatively weaker minerals (Ebert et al., 2007; Gardner et al., 2017; Holyoke and Tullis, 2006; Kim et al., 2013b). As a result, epidote blueschist that exists in a warm subduction zone may be deformed under the coexistence of brittle and ductile regimes due to the rheological contrast between constituent minerals under stable pressure and temperature conditions.

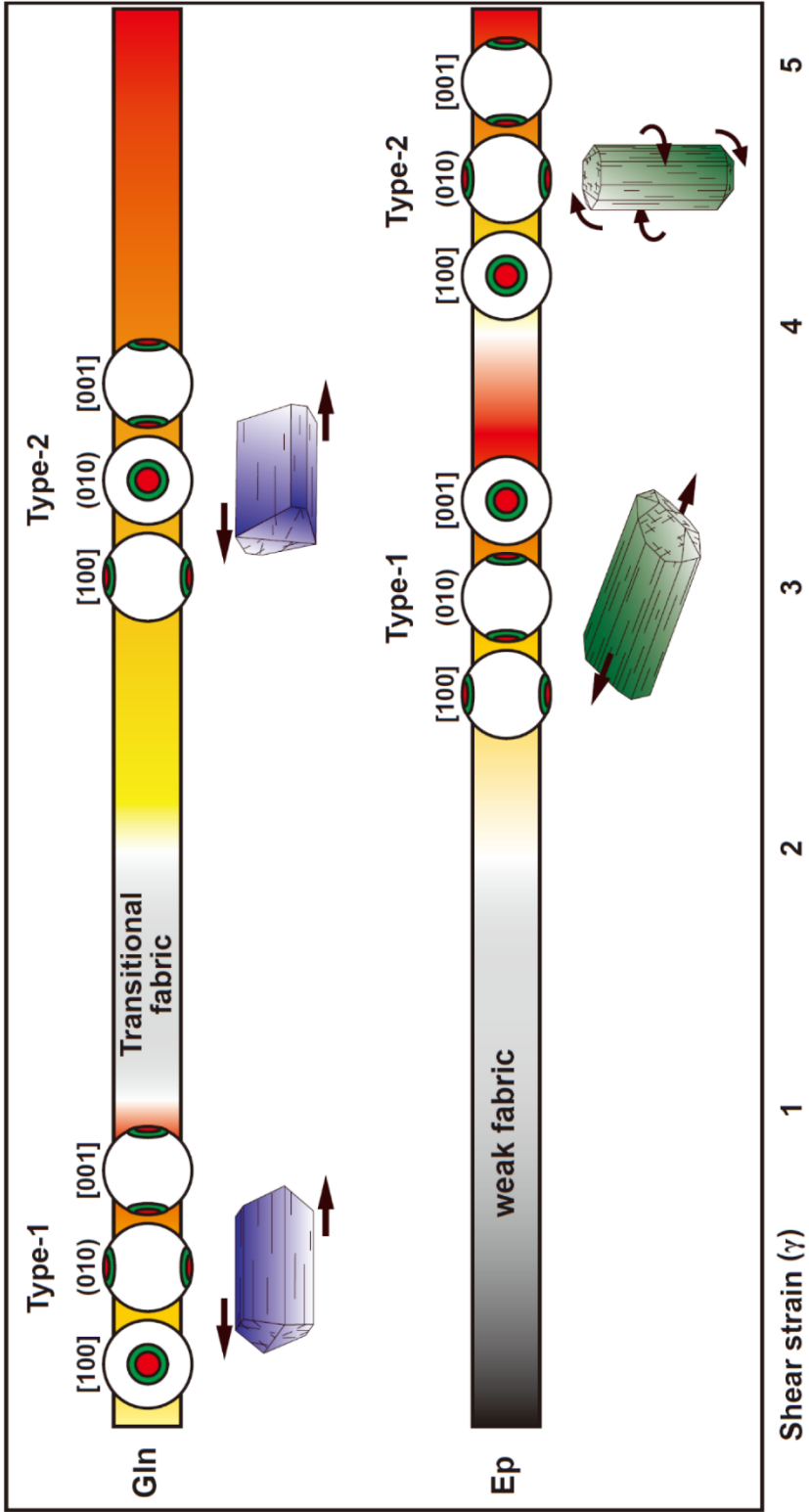


**Figure 3.13.** Schematic of the development of LPOs of glaucophane and epidote with increasing shear strain. Gln: glaucophane; and Ep: epidote.

### **3.4.4. Implications for seismic anisotropy of subducting slab in a subduction zone**

The seismic anisotropy of shear waves in the forearc region of the subduction zone has been mainly observed by SKS wave propagating through the anisotropic mediums and throughout the area subperpendicular to the Earth's surface (Long, 2013). As SKS anisotropic data are measured by path integration, the source for the splitting of S-waves has been regarded as multiple anisotropic layers. Among these layers, the mantle wedge and sub-slab mantle have been considered as the main anisotropic mediums because of the large volume proportions in the lithosphere (Long and Becker, 2010). Specifically, the B-type LPO of olivine in the mantle wedge has been suggested as a cause for the change from the trench-normal to trench-parallel polarization direction of the fast shear wave in the forearc region (Jung and Karato, 2001b; Karato et al., 2008). However, subducting oceanic crust is also a potential anisotropic layer where many elastically anisotropic minerals are stable (Hacker et al., 2003; Schmidt and Poli, 1998). Therefore, recent studies have suggested that type-2 LPO of glaucophane may affect the trench-parallel seismic anisotropy of the forearc region, where the subducting slab has a high dip angle (Cao and Jung, 2016; Cao et al., 2013; 2014; Kim et al., 2013a). This is because the propagation velocity of the fast S-wave ( $V_{s1}$ ) through the b- and c-axes of the glaucophane is much faster than that through an a-axis in glaucophane. In contrast, the type-1 LPO of glaucophane may contribute to the trench-normal polarization direction regardless of the subducting angle because the b- and c-axes are

continuously aligned parallel to the shear direction in the subducting slab with different dip angles. The type-1 and type-2 LPOs of epidote in this chapter have not yet been reported in natural samples. However, if epidote with type-1 LPO exists in the subducting slab, this LPO may also influence the trench-normal seismic anisotropy regardless of whether the subducting angle due to the  $V_{s1}$  through the a- and b-axes of the epidote is much faster than that through the c-axis. In contrast, if epidote with type-2 LPO exists in the subducting slab, this LPO may contribute to the trench-parallel seismic anisotropy where the subducting slab has a low dip angle. However, further research is needed to determine whether these LPO types of epidote could exist in natural blueschist. Consequently, different types of LPOs for glaucophane and epidote may contribute to the different seismic anisotropies of the forearc region in the subduction zone: type-1 LPOs of glaucophane and epidote can contribute to the trench-normal seismic anisotropy in the subducting slab, and type-2 LPOs of glaucophane and epidote may affect the trench-parallel seismic anisotropy of the forearc region, where the subducting slab has a high dip angle and a low dip angle, respectively.

### 3.5. Conclusion

In this chapter, deformation experiments of epidote blueschist in simple shear were conducted using the modified Griggs apparatus to understand deformation microstructures, the development of LPOs, and deformation mechanisms of glaucophane and epidote over a warm subducting slab. After the experiments, two different types of glaucophane and epidote LPOs were developed by different mechanisms depending on the magnitude of shear strain and grain size. TEM observations and EBSD mapping of glaucophane suggest that the LPO of glaucophane was developed by dislocation creep under a shear strain of  $0.4 \leq \gamma \leq 4.5$ . At a shear strain of  $\gamma > 2$ , cataclastic/granular flow microstructures were observed in large grains. At a high shear strain of  $\gamma = 4.5$ , thin ductile shear bands were observed in the small grains. These experimental results suggest that the brittle–ductile transition of glaucophane likely occurs at epidote blueschist-facies metamorphic conditions. On the other hand, intracrystalline microstructures in epidote such as subgrain boundaries and twins revealed by TEM observations suggest that the LPO of epidote was developed by dislocation creep under a shear strain of  $2 < \gamma < 4$ . However, the development of the LPO of epidote under a high shear strain ( $\gamma > 4$ ) is considered to be influenced by cataclastic flow with rigid body rotation because epidote is more rigid than other minerals in the matrix. Therefore, these data suggest that the magnitude of shear strain, grain size, and rheological contrast between component minerals are important factors influencing the deformation mechanisms and development of LPOs of glaucophane and epidote. However, there is a need for

further studies on the fabric transition of epidote under various pressure and temperature conditions.

## **CHAPTER 4**

**Seismic velocity and anisotropy of  
glaucophane and epidote in epidote  
blueschists and implications for seismic  
properties in a warm subduction zone**

## Abstract

To understand the cause of seismic low velocity layer and seismic anisotropy in a warm subduction zone, seismic properties of glaucophane and epidote in epidote blueschist were studied. The epidote blueschists were experimentally deformed in simple shear at high pressure (0.9–1.5 GPa) and temperature (400–500 °C) conditions, and seismic velocity and anisotropy of glaucophane and epidote were calculated using the lattice preferred orientation (LPO) and elastic constants of each minerals. The average P- and S-wave velocity ( $V_{p_{aver}}$  and  $V_{s_{aver}}$ ) of glaucophane were in the range of 7.65–7.80 km/s and 4.54–4.56 km/s, respectively, and the anisotropy of P-wave (AVp) and maximum anisotropy of S-wave (Max. AVs) were in the range of 6.9–15.2 % and 3.73–8.06 %, respectively. The  $V_{p_{aver}}$  and  $V_{s_{aver}}$  of epidote were in the range of 7.31–7.37 km/s and 4.21–4.22 km/s, respectively, and the AVp and Max. AVs were in the range of 3.0–5.6 % and 5.31–7.23 %, respectively. The  $V_{p_{aver}}$  and  $V_{s_{aver}}$  of whole rock (epidote blueschist) were in the range of 7.55–7.59 km/s and 4.40–4.48 km/s, respectively, and the AVp and Max. AVs were in the range of 5.7–8.5 % and 3.80–4.93 %, respectively. The AVp and Max. AVs of glaucophane were increased with increasing the magnitude of shear strain ( $\gamma$ ), but those of epidote were decreased with increasing the shear strain. The delay time of S-wave which was calculated from subducting oceanic crust composed of epidote blueschist was generally increased with increasing the subducting angle of the slab and increasing volume proportion of glaucophane. The  $V_p/V_s$  ratio was generally increased with increasing volume proportion of epidote at low subducting angle and

increased with increasing volume proportion of glaucophane at high subducting angle. The  $V_{p_{aver}}$  and  $V_{s_{aver}}$  of experimentally deformed epidote blueschist were reduced about 8–9 % and 6–7 %, respectively, compared to the seismic velocities of lithospheric mantle surrounding the slab. The trench-normal seismic anisotropy can be caused by the type-1 LPO of glaucophane and epidote. On the other hand, the trench-parallel seismic anisotropy can be caused by the type-2 LPO of epidote in the subduction zone with low subducting angle and by the type-2 LPO of glaucophane in the subduction zone with high subducting angle. These results suggest that volume proportion, LPO types of glaucophane and epidote, and subducting angle of the slab are important factors to control seismic velocity and anisotropy observed in subduction zones.

## 4.1. Introduction

The seismic low velocity layer (LVL) is an 1–7 km-thick layer that slow P- and S-wave velocities are observed at depth of 30–250 km, compared to the surrounding lithospheric mantle (Abers, 2000; Abers et al., 2013). The LVL has been reported at the top of the subducting slab in both cold and warm subduction zones, but the depth of LVL observed in the cold subduction zone was deeper than that in the warm subduction zone (Abers, 2000; Abers et al., 2013; Hasegawa et al., 2007; Hirose et al., 2008; Kawakatsu and Watada, 2007; Tsuji et al., 2008). Many previous studies have suggested that the LVL is due to the basaltic hydrous phases metamorphic rock in the top of the subducting oceanic crust (Abers et al., 2013; Hasegawa et al., 2007; Hirose et al., 2008; Kawakatsu and Watada, 2007; Tsuji et al., 2008). However, direct evidence that LVL is due to the basaltic hydrous phases is limited, and the reason why LVLs are observed in these areas is still unknown.

Seismic anisotropy of S-wave is also widely observed in the forearc region of subduction zones (Long and Becker, 2010; Long and Silver, 2008). The source of the S-wave splitting has been regarded as multiple anisotropic layers, and the mantle wedge and sub-slab mantle have been considered the main anisotropic mediums due to the large volume proportion of the lithosphere (Long and Becker, 2010; Long and Silver, 2008). Previous studies suggested several causes for trench-parallel polarization direction of fast shear wave ( $V_{s1}$ ) such as 3-D mantle flow parallel to the trench due to the trench roll-back (Long and Silver, 2008), the type-B LPO of olivine under wet condition in the mantle wedge (Jung and Karato, 2001b; Karato et

al., 2008; Kneller et al., 2005; Nakajima and Hasegawa, 2004) and/or high pressure in the upper mantle (Jung et al., 2009b; Lee and Jung, 2015; Ohuchi et al., 2011), hydration of sub-vertical fault zones in subducting oceanic plates (Faccenda et al., 2008), and fluid-filled cracks in subducting slabs (Healy et al., 2009). On the other hand, the trench-normal  $V_{s1}$  polarization direction in the forearc region is observed in central Alaska (Christensen and Abers, 2010), South Sandwich trench in eastern Scotia plate (Müller, 2001), Kamchatka (Levin et al., 2004) and Nicaragua (Abt et al., 2009). Although the arc-parallel mantle flow was suggested as a cause of this trench-normal  $V_{s1}$  polarization direction (Abt et al., 2009), the trench-normal seismic anisotropy in the forearc region is still an enigma.

Although its volume proportion is relatively smaller than that of the lithospheric mantle, subducting oceanic crust could be a high potential anisotropic layer to decipher this enigmatic trench-normal seismic anisotropy in the forearc region of subduction zones. There are many elastically anisotropic minerals in the subducted oceanic crust (e.g., glaucophane, epidote, lawsonite, and phengite) and the slab–mantle interphase (e.g., serpentine, talc, chlorite, and chloritoid) depending on temperatures and depths (Hacker et al., 2003). In particular, glaucophane (Bezacier et al., 2010a) and epidote (Aleksandrov et al., 1974) are representative elastically anisotropic minerals in the subducting oceanic crust of the warm subduction zone. These glaucophane and epidote can affect the seismic anisotropy of warm subduction zones when they are aligned in a specific direction by the LPO. The LPOs of glaucophane and epidote can also contribute to the seismic velocity of subducting crust because the fastest seismic propagation axes of mineral are aligned in different directions depending on the LPO type (Cao et al., 2013; Park et al., 2020a).

As mentioned in Chapter 3.1, previous studies on the deformation microstructures of natural blueschist reported three LPO types of glaucophane: (1) LPO indicating (100)[001] slip system (Bezacier et al., 2010a; Cao and Jung, 2016; Cao et al., 2013; 2014; Choi et al., 2021; Fujimoto et al., 2010; Ha et al., 2018; Kim et al., 2013a; 2013b); (2) LPO indicating {110}[001] slip system (Bezacier et al., 2010a; Cao and Jung, 2016; Cao et al., 2013; 2014; Kim et al., 2013b); and (3) LPO indicating (010)[001] slip system (Cossette et al., 2015). A recent study on the deformation experiment of epidote blueschist also reported the LPO indicating (010)[001] slip system of glaucophane deformed under low shear strain ( $\gamma \leq 1$ ) and the LPO indicating (100)[001] slip system of glaucophane deformed under high shear strain ( $\gamma > 2$ ) (in Chapter 3; Park et al., 2020a). On the other hand, two LPO types of epidote were reported recently: one is the LPO indicating (001)[010] slip system (Bezacier et al., 2010a; Cao et al., 2011; 2013; Ha et al., 2018; Kim et al., 2013a); the other is the LPO indicating {101}[010] slip system (Cao et al., 2011; 2013; Fujimoto et al., 2010). A recent study on the deformation experiment of epidote blueschist reported the LPO indicating (100)[010] slip system of epidote deformed under a shear strain between  $2 < \gamma < 4$ , and also reported the LPO showing (010)[001] fabric of epidote deformed under high shear strain of  $\gamma = 4.5$  (in Chapter 3; Park et al., 2020a).

Although LPOs of glaucophane and epidote have recently been reported as mentioned above (Bezacier et al., 2010a; Cao and Jung, 2016; Cao et al., 2013; 2014; Choi et al., 2021; Cossette et al., 2015; Fujimoto et al., 2010; Ha et al., 2018; Kim et al., 2013a; 2013b; Park et al., 2020a), the influence of these LPOs on seismic anisotropy in subduction zones has been studied with limited research. Some

researchers suggested that the LPO indicating (100)[001] slip system of glaucophane can affect the trench-parallel seismic anisotropy in the forearc region when the slab has a high subducting angle, and the LPO indicating (001)[010] slip system of epidote may be constructive effect on this seismic anisotropy (i.e., reinforcement of the trench-parallel  $V_{s1}$  polarization direction; Cao and Jung, 2016; Cao et al., 2013; 2014; Kim et al., 2013a). However, the effects of other LPOs of glaucophane and epidote on the seismic anisotropy in subduction zone have not been reported yet. Therefore, seismic velocity and anisotropy of glaucophane and epidote in experimentally deformed epidote blueschist (in Chapter 3; Park et al., 2020a) were calculated to understand the influence of the LPOs of minerals on the seismic properties in subduction zones.

## 4.2. Methods

### 4.2.1. Sample description

Epidote blueschists which were deformed at high pressure and temperature (in Chapter 3; Park et al., 2020a) were used to calculate the seismic velocity and anisotropy of glaucophane and epidote. A natural epidote blueschist collected from Voltri massif in western Alps, Italy, was used as a starting material. The constituent minerals are mainly glaucophane (~55 vol%), epidote (~15 vol%), and plagioclase (~15 vol%) with minor titanite (~5 vol%), chlorite (~5 vol%), and garnet (~5 vol%). Average grain size of minerals was ~30  $\mu\text{m}$ , and sample was hardly deformed showing a massive and no foliated structure (Fig. 3.1). The epidote blueschist was deformed in simple shear under the high pressure (0.9–1.5 GPa) and temperature (400–500 °C) using a modified Griggs apparatus housed at the Tectonophysics laboratory in the School of Earth and Environmental Sciences (SEES), Seoul National University (SNU), South Korea. The experimental procedure was fully described in Chapter 3.2.2. Shear strain ( $\gamma$ ) was measured by the rotational angle of Ni strain marker and/or elongated shapes of grains. All minerals were aligned more parallel to the shear direction with increasing the shear strain (Fig. 3.5). The detail description of the deformation microstructure was referred to Chapter 3.3.1.

## 4.2.2. Measurement of LPOs

The LPOs of minerals in experimentally deformed epidote blueschist were measured by using the HKL's EBSD system (Channel 5 software) with a Nordlys II detector attached to the SEM (JEOL JSM 6380) housed at the SEES in SNU. The detail description for the determination of glaucophane and epidote LPOs was referred to Chapters 3.2.3. The representative LPOs of glaucophane and epidote were plotted in Figure 4.1 using MTEX (version 5.4.0), a MATLAB toolbox (Bachmann et al., 2011). In Chapter 3, two different LPOs of glaucophane and epidote were reported with increasing shear strain (Park et al., 2020a). In the sample deformed under low shear strain ( $\gamma \leq 1$ ), the (010) poles of glaucophane were aligned subnormal to the shear plane and the [001] axes were aligned subparallel to the shear direction (type-1 LPO of glaucophane; Figs. 4.1a and 3.7b–3.7e). Under the shear strain between  $1 < \gamma \leq 2$ , the [100] axes and (010) poles of glaucophane were aligned subnormal to the shear direction within the shear plane, appearing to be a transitional fabric (Figs. 4.1b and 3.7f). In the sample deformed under high shear strain ( $\gamma > 2$ ), the [100] axes of glaucophane were aligned subnormal to the shear plane and the [001] axes were aligned subparallel to the shear direction (type-2 LPO of glaucophane; Figs. 4.1c and 3.7g–3.7k). Epidote in the sample deformed under low shear strain ( $\gamma < 2$ ) exhibited weak nonsystematic fabrics (Figs. 4.1d and 3.7b–3.7f). In the sample deformed under shear strain between  $2 < \gamma < 4$ , however, the [100] axes of epidote were aligned subnormal to the shear plane and the (010) poles were aligned subparallel to the shear direction (type-1 LPO of epidote; Figs. 4.1e and

3.7g–3.7j). In the sample deformed under the shear strain of  $\gamma = 4.5$ , the (010) poles of epidote were aligned subnormal to the shear plane and the [001] axes were aligned subparallel to the shear direction (type-2 LPO of epidote; Figs. 4.1f and 3.7k). The detail description for the LPO development of glaucophane and epidote was referred to Chapters 3.4.1 and 3.4.2, respectively (Park et al., 2020a).

To quantify the fabric strength of minerals, the uncorrelated grain pairs and the orientations of grains as triplet of Euler angle determined from EBSD data were used to calculate the M-index (Skemer et al., 2005) and the J-index (Bunge, 1982), respectively. The M-index is defined by Equation 2.1 as:

$$M = 0.5 \int |R^T(\varphi) - R^0(\varphi)| d\varphi \quad (2.1)$$

where  $R^T(\varphi)$  is the theoretical distribution of uncorrelated misorientation angles for a random fabric,  $R^0(\varphi)$  is the observed distribution of uncorrelated misorientation angles for a real fabric from EBSD data, and  $\varphi$  is the misorientation angle of uncorrelated grain pair (Skemer et al., 2005). This M-index ranges from 0 (random fabric) to 1 (single crystal fabric). In contrast, the J-index is defined as:

$$J = \int [f(\mathbf{g})]^2 d\mathbf{g} \quad (4.1)$$

where  $f(\mathbf{g})$  is the orientation distribution function (ODF),  $\mathbf{g} = (\phi_1, \psi, \phi_2)$  is the orientation data as the Euler angle triplet, and  $d\mathbf{g}$  is a volume element in Euler angle space (Bunge, 1982). This J-index theoretically ranges from 1 (completely random fabric) to infinity (single crystal fabric).

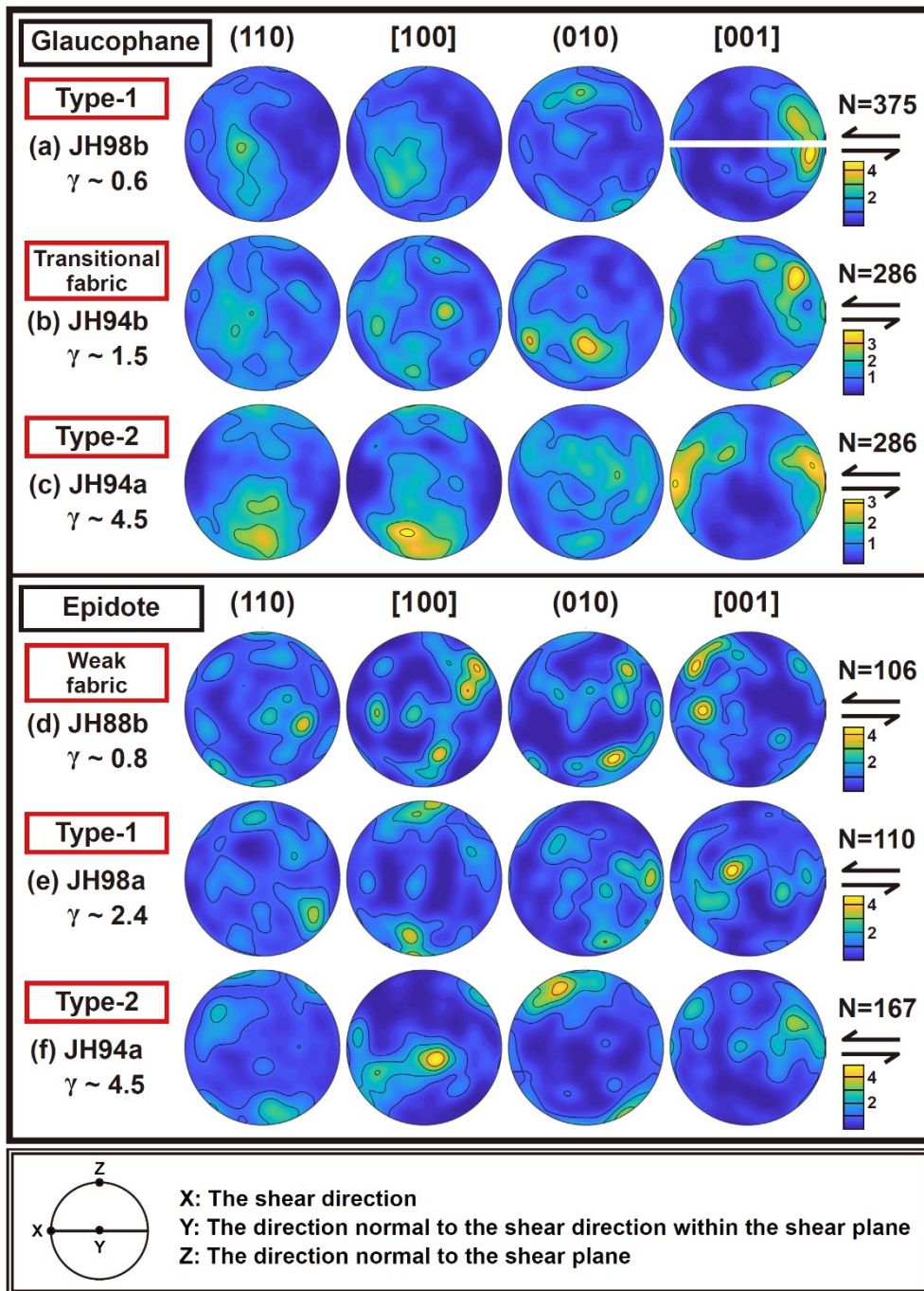


**Figure 4.1.** Pole figures of (a)–(c) glaucophane and (d)–(f) epidote in deformed samples showing representative LPO presented in the lower hemisphere using an equal area projection. White line in pole figure: shear plane, black arrows: shear direction, and N: the number of grains.

### 4.2.3. Calculation of the seismic velocity and anisotropy

The seismic velocity and anisotropy of minerals and whole rock were calculated using both the macroscopic elastic tensor  $\langle C_{ij} \rangle$  and the density by solving the Christoffel equation with the Voigt-Reuss-Hill (VRH) averaging scheme using the MTEX with MSAT toolkits (version 1.1.1) (Walker and Wookey, 2012). The macroscopic elastic tensor was calculated by integrating elastic stiffness coefficients ( $c_{ij}$ ) of all single-crystal minerals for all orientations of grains obtained as triplet of Euler angle in the EBSD analysis. Here, the elastic coefficients of glaucophane (Bezacier et al., 2010a) and epidote (Aleksandrov et al., 1974) were used. The density of whole rock can average from densities and volume proportions of constituent minerals. Here, the density of epidote blueschist was calculated as the average value of the glaucophane and epidote densities according to the modal composition by assuming that the whole rock consists mainly of glaucophane and epidote. The azimuthal anisotropy of P-wave ( $AV_p$ ) was calculated by Equation 2.2 as:

$$AV_p = 200 \times [(V_{p_{\max}} - V_{p_{\min}}) / (V_{p_{\max}} + V_{p_{\min}})] (\%) \quad (2.2)$$

where  $V_{p_{\max}}$  and  $V_{p_{\min}}$  are the maximum and minimum P-wave velocity, respectively. The polarization anisotropy of shear wave ( $AV_s$ ) was calculated by Equation 2.3 as:

$$AV_s = 200 \times [(V_{s1} - V_{s2}) / (V_{s1} + V_{s2})] (\%) \quad (2.3)$$

where  $V_{s1}$  and  $V_{s2}$  are the fast and slow S-wave velocity, respectively.

To observe the relationship between seismic velocity and magnitude of shear strain ( $\gamma$ ), or seismic velocity and fabric strength (i.e., M-index and J-index), isotropic average velocities of P-wave ( $V_{p_{iso,aver}}$ ) and S-wave ( $V_{s_{iso,aver}}$ ) were calculated by averaging the velocity vectors that make up the velocity contours calculated for polycrystals (Walker and Wookey, 2012), and isotropic velocities of P-wave ( $V_{p_{iso}}$ ) and S-wave ( $V_{s_{iso}}$ ) were calculated using the isotropic projected factor by decomposition of the macroscopic elastic tensor ( $C_{iso}$ ) as:

$$V_{p_{iso}} = \sqrt{(C_{33,iso}/\rho)} \text{ (km/s)} \quad (4.2)$$

$$V_{s_{iso}} = \sqrt{(C_{44,iso}/\rho)} \text{ (km/s)} \quad (4.3)$$

where  $\rho$  is density of material,  $C_{33,iso}$  and  $C_{44,iso}$  are principal and shear strain elements in the isotropic elastic tensor matrix, respectively (Browaeys and Chevrot, 2004; Walker and Wookey, 2012).

To compare seismic velocities between deformed rocks and the lithospheric mantle surrounding the slab, the average velocities of P-wave ( $V_{p_{aver}}$ ) and S-wave ( $V_{s_{aver}}$ ) were calculated as:

$$V_{p_{aver}} = (V_{p_{max}} + V_{p_{min}}) / 2 \text{ (km/s)} \quad (4.4)$$

$$V_{s_{aver}} = (V_{s1_{max}} + V_{s2_{max}} + V_{s1_{min}} + V_{s2_{min}}) / 4 \text{ (km/s)} \quad (4.5)$$

where  $V_{s1_{max}}$  and  $V_{s1_{min}}$  are the maximum and minimum velocity of the fast S-wave ( $V_{s1}$ ), and  $V_{s2_{max}}$  and  $V_{s2_{min}}$  are the maximum and minimum velocity of the slow S-wave ( $V_{s2}$ ), respectively.

## 4.3. Results

### 4.3.1. Seismic velocity and anisotropy for deformed glaucophanes

Seismic anisotropy and average velocity calculated for polycrystalline minerals and whole rock (epidote blueschist) are summarized in Tables 4.1 and 4.2, respectively. In the sample deformed under low shear strain ( $\gamma \leq 1$ ), the direction of the  $V_{p_{\max}}$  of polycrystalline glaucophanes was subparallel to the shear direction, and the direction of the  $V_{p_{\min}}$  was subnormal to the shear direction within the shear plane (Fig. 4.2b–4.2e). The low AVs region in AVs contour of glaucophanes was placed in the direction subnormal to the shear direction within the shear plane (Fig. 4.2b–4.2e). The AVp and the maximum AVs (Max. AVs) were 9.4–15.2 % and 5.45–8.06 %, respectively (Table 4.1), and the  $V_{p_{\text{aver}}}$  and  $V_{s_{\text{aver}}}$  were in the range of 7.685–7.715 km/s and 4.545–4.553 km/s, respectively (Table 4.2). In the sample deformed under intermediate shear strain ( $1 < \gamma \leq 2$ ), the Vp and AVs contours of glaucophanes were similar to those of glaucophane in the sample deformed under low shear strain ( $\gamma \leq 1$ ), but AVp and Max. AVs were the lowest values among the samples (AVp = 6.9 % and Max. AVs = 3.73 %; Fig. 4.2f). In the sample deformed under high shear strain ( $\gamma > 2$ ), the direction of the  $V_{p_{\max}}$  of glaucophanes was parallel to the shear direction, and the area/direction of the  $V_{p_{\min}}$  was relocated from the direction subnormal to the shear direction within the shear plane to the direction subnormal to the shear plane with increasing shear strain (Fig. 4.2g–4.2k). The low AVs region in AVs contour of

glaucophanes was placed more in the direction subnormal to the shear plane as a shear strain increased (Fig. 4.2g–4.2k). The AVp and Max. AVs were 10.1–13.1 % and 5.87–8.02 %, respectively (Table 4.1), and the  $V_{p_{aver}}$  and  $V_{s_{aver}}$  were in the range of 7.645–7.800 km/s and 4.543–4.558 km/s, respectively (Table 4.2). The Vs1 polarization direction for deformed glaucophanes at the direction normal to the shear plane was rearranged from subparallel to parallel to the shear direction as increasing a shear strain (Fig. 4.2).

**Table 4.1.** Experimental conditions, LPOs, and seismic anisotropy of deformed polycrystalline minerals and epidote blueschist (whole rock).

Run #	P (GPa)	T (°C)	Shear strain ( $\gamma$ )	Glaucophane		Epidote			Epidote blueschist (whole rock)					
				LPO	AVp (%)	Max.AVs (%)	LPO	AVp (%)	Max.AVs (%)	Gln (vol%)	Ep (vol%)	AVp (%)	Max.AVs (%)	
JH148	1.2	430±10	0.4	Type-1	9.4	5.72	Weak fabric	-	-	-	-	-	-	-
JH98b	1.5	500±10	0.6	Type-1	12.5	6.55	Weak fabric	-	-	-	-	-	-	-
JH88b	1.5	400±10	0.8	Type-1	10.0	5.45	Weak fabric	5.6	5.32	75 %	25 %	8.5	4.69	
JH112b	0.9	430±10	0.9	Type-1	15.2	8.06	Weak fabric	-	-	-	-	-	-	-
JH94b	1.5	400±10	1.5	Transitional fabric	6.9	3.73	Weak fabric	5.0	7.23	72 %	28 %	5.7	3.80	
JH88a	1.5	400±10	2.1	Type-2	12.1	6.41	Type-1	-	-	-	-	-	-	-
JH98a	1.5	500±10	2.4	Type-2	10.8	6.18	Type-1	4.5	5.31	58 %	42 %	6.6	4.50	
JH150	1.2	480±10	2.7	Type-2	10.1	5.87	Type-1	-	-	-	-	-	-	-
JH112a	0.9	430±10	2.9	Type-2	12.6	6.98	Type-1	-	-	-	-	-	-	-
JH94a	1.5	400±10	4.5	Type-2	13.1	8.02	Type-2	3.0	5.32	63 %	37 %	8.0	4.93	

AVp: the azimuthal anisotropy of P-wave, and Max.AVs: the maximum polarization anisotropy of S-wave.

**Table 4.2.** Seismic velocity of deformed polycrystalline minerals and epidote blueschist (whole rock).

Run #	Glaucophane						Epidote						Epidote blueschist (whole rock)							
	V <sub>p</sub> <sup>max</sup> (km/s)	V <sub>p</sub> <sup>min</sup> (km/s)	V <sub>p</sub> <sup>aver</sup> (km/s)	V <sub>s</sub> <sup>l</sup> <sup>max</sup> (km/s)	V <sub>s</sub> <sup>l</sup> <sup>min</sup> (km/s)	V <sub>s</sub> <sup>aver</sup> (km/s)	V <sub>p</sub> <sup>max</sup> (km/s)	V <sub>p</sub> <sup>min</sup> (km/s)	V <sub>p</sub> <sup>aver</sup> (km/s)	V <sub>s</sub> <sup>l</sup> <sup>max</sup> (km/s)	V <sub>s</sub> <sup>l</sup> <sup>min</sup> (km/s)	V <sub>s</sub> <sup>aver</sup> (km/s)	Gln (vol%)(vol%)	Ep (vol%)(vol%)	V <sub>p</sub> <sup>max</sup> (km/s)	V <sub>p</sub> <sup>min</sup> (km/s)	V <sub>p</sub> <sup>aver</sup> (km/s)	V <sub>s</sub> <sup>l</sup> <sup>max</sup> (km/s)	V <sub>s</sub> <sup>l</sup> <sup>min</sup> (km/s)	V <sub>s</sub> <sup>aver</sup> (km/s)
JH148	8.06	7.34	7.700	4.68	4.42	4.553	-	-	-	-	-	-	-	-	-	-	-	-	-	-
JH98b	8.17	7.21	7.690	4.71	4.39	4.545	-	-	-	-	-	-	-	-	-	-	-	-	-	-
JH88b	8.07	7.30	7.685	4.71	4.40	4.553	7.51	7.11	7.310	4.35	4.06	4.205	75 %	25 %	7.91	7.27	7.590	4.60	4.36	4.478
JH112b	8.30	7.13	7.715	4.77	4.37	4.548	-	-	-	-	-	-	-	-	-	-	-	-	-	-
JH94b	7.94	7.41	7.675	4.67	4.45	4.553	7.55	7.18	7.365	4.39	4.08	4.223	72 %	28 %	7.77	7.34	7.555	4.58	4.35	4.453
JH88a	8.11	7.18	7.645	4.72	4.42	4.550	-	-	-	-	-	-	-	-	-	-	-	-	-	-
JH98a	8.14	7.31	7.725	4.68	4.38	4.553	7.51	7.18	7.345	4.31	4.07	4.213	58 %	42 %	7.80	7.30	7.550	4.50	4.29	4.398
JH150	8.19	7.41	7.800	4.70	4.38	4.558	-	-	-	-	-	-	-	-	-	-	-	-	-	-
JH112a	8.18	7.21	7.695	4.74	4.38	4.553	-	-	-	-	-	-	-	-	-	-	-	-	-	-
JH94a	8.19	7.18	7.685	4.73	4.37	4.543	7.44	7.22	7.330	4.33	4.07	4.208	63 %	37 %	7.85	7.25	7.550	4.55	4.30	4.423

V<sub>p</sub><sup>max</sup> : the maximum P-wave velocity, V<sub>p</sub><sup>min</sup> : the minimum P-wave velocity, V<sub>s</sub><sup>l</sup><sup>max</sup> : the maximum fast S-wave velocity,  
V<sub>s</sub><sup>l</sup><sup>min</sup> : the minimum slow S-wave velocity, V<sub>p</sub><sup>aver</sup> : average velocity of P-wave, and V<sub>s</sub><sup>aver</sup> : average velocity of S-wave.

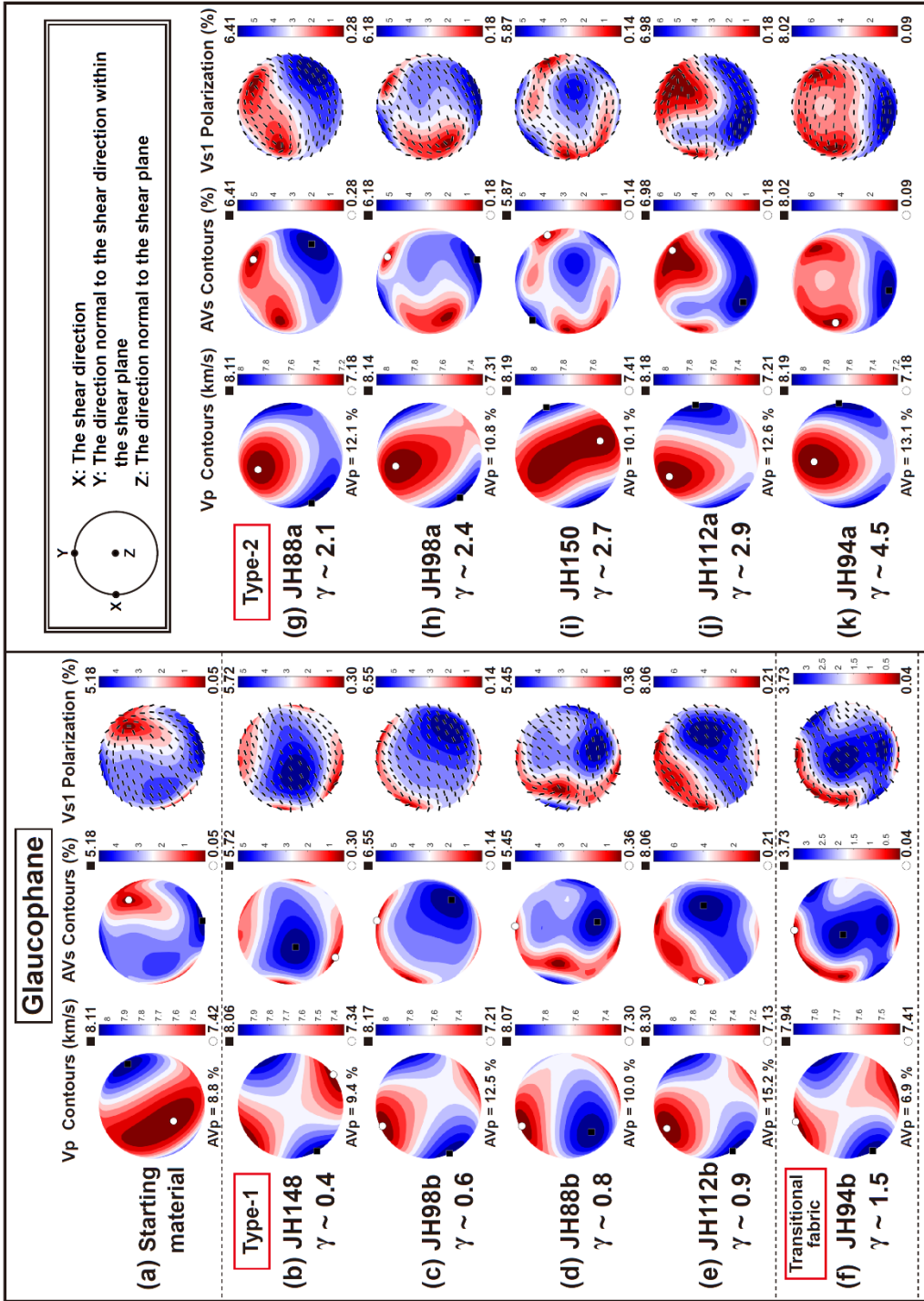


**Figure 4.2.** Seismic velocity and anisotropy of polycrystalline glaucophanes calculated using crystallographic orientation data from EBSD analysis and the elastic stiffness coefficients of glaucophane (Bezacier et al., 2010a). The E-W direction corresponds to the shear direction ( $X$ ), and the center of a stereographic projection circle is the direction normal to the shear plane ( $Z$ ). The contours of P-wave velocity ( $V_p$ ), the contours of S-wave polarization anisotropy ( $AV_s$ ), and polarization directions of the fast shear wave ( $V_{s1}$ ) are shown.

### 4.3.2. Seismic velocity and anisotropy for deformed epidotes

Seismic velocity and anisotropy of polycrystalline epidotes were calculated for four samples due to the limited number of epidote grains in deformed samples (Fig. 4.3). The  $V_p$  and AVs contours of epidotes deformed under a shear strain of  $\gamma < 2$  were similar to the contours for the starting material due to the insufficient strain to develop a systematic LPO of epidote (Fig. 4.3b and c). In the sample deformed under a shear strain between  $2 < \gamma < 4$ , the fast  $V_p$  region in  $V_p$  contour of epidotes was in the direction subnormal to the shear plane and oblique to the shear direction, forming a weak girdle distribution (Fig. 4.3d). The high AVs region in AVs contour of epidotes was in the direction oblique to the shear direction following the position of the fast  $V_p$  region in  $V_p$  contour (Fig. 4.3d). On the contrary, the fast  $V_p$  region in  $V_p$  contour of epidotes deformed under a shear strain of  $\gamma = 4.5$  formed an oblique girdle distribution for both shear direction and direction normal to the shear plane (Fig. 4.3e). The high AVs region in AVs contour of epidotes was subnormal to the shear direction forming a girdle distribution, which is the similar position of the fast  $V_p$  region in  $V_p$  contour (Fig. 4.3e). The  $V_{s1}$  polarization direction for deformed epidotes at the direction normal to the shear plane was rearranged from subparallel to subnormal to the shear direction as increasing shear strain (Fig. 4.3). The AVp and Max. AVs for deformed epidotes were 3.0–5.6 % and 5.31–7.23 %, respectively (Table 4.1), and the  $V_{p\text{aver}}$  and  $V_{s\text{aver}}$  were in the range of 7.310–7.365 km/s and 4.205–4.223 km/s, respectively (Table 4.2).

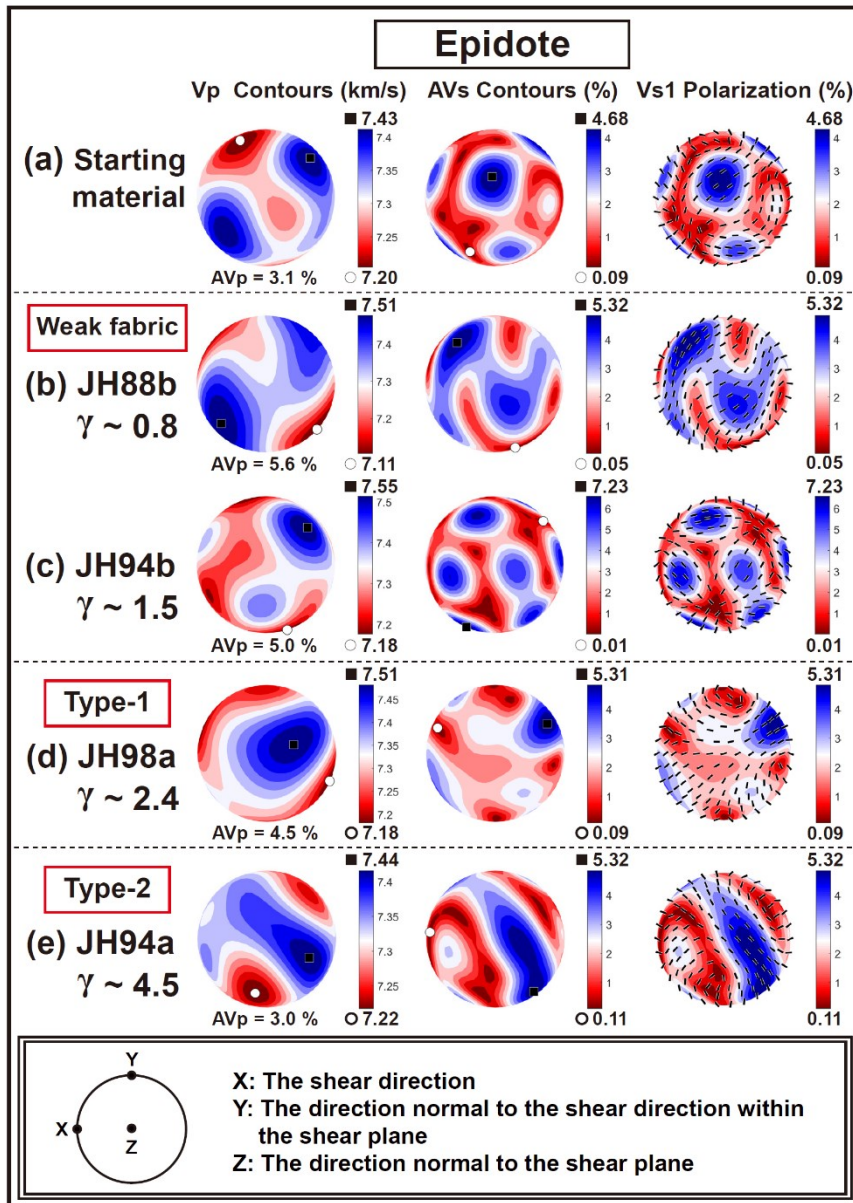


**Figure 4.3.** Seismic velocity and anisotropy of polycrystalline epidotes calculated using crystallographic orientation data from EBSD analysis and the elastic stiffness coefficients of epidote (Aleksandrov et al., 1974). The E-W direction corresponds to the shear direction (X), and the center of a stereographic projection circle is the direction normal to the shear plane (Z). The contours of P-wave velocity (Vp), the contours of S-wave polarization anisotropy (AVs), and polarization directions of the fast shear wave (Vs1) are shown.

### **4.3.3. Seismic velocity and anisotropy for deformed epidote blueschist (whole rock)**

Seismic velocity and anisotropy of epidote blueschist (whole rock) are shown in Figure 4.4. It was assumed that the epidote blueschist consists mainly of glaucophane and epidote, which are the dominant minerals in the sample. Because of the limited number of epidote grains in sample, the seismic velocity and anisotropy of four samples were calculated. With increasing shear strain, the direction of the  $V_{p_{max}}$  of epidote blueschist was aligned more parallel to the shear direction, and the direction of the  $V_{p_{min}}$  was aligned more perpendicular to the shear plane (Fig. 4.4). For the sample deformed under low shear strain ( $\gamma \leq 1$ ), the  $V_{p_{max}}$  direction of epidote blueschist was oblique to the shear direction and the  $V_{p_{min}}$  direction was subnormal to the shear direction within the shear plane (Fig. 4.4a). For the sample deformed under intermediate shear strain ( $1 < \gamma \leq 2$ ), the  $V_{p_{max}}$  direction of epidote blueschist was subparallel to the shear direction and the  $V_{p_{min}}$  direction was subnormal to the shear direction within the shear plane (Fig. 4.4b). For the sample deformed under high shear strain ( $\gamma > 2$ ), the  $V_{p_{max}}$  direction of epidote blueschist was subparallel to the shear direction and the  $V_{p_{min}}$  direction was subnormal to the shear plane (Fig. 4.4c and d). The high AVs regions in AVs contours of epidote blueschists were mostly in the direction subnormal to the shear plane, but in the sample deformed under a shear strain of  $\gamma = 4.5$ , the region of high AVs was in the direction subnormal to the shear direction within the shear plane (Fig. 4.4d). The  $V_s1$  polarization direction for deformed epidote blueschist at the direction normal to

the shear plane was in subparallel alignment with the shear direction (Fig. 4.4). The AVp and Max. AVs of epidote blueschist were 5.7–8.5 % and 3.80–4.93 %, respectively (Table 4.1), and the  $V_{p_{aver}}$  and  $V_{s_{aver}}$  of epidote blueschist were in the range of 7.550–7.590 km/s and 4.398–4.478 km/s, respectively (Table 4.2).

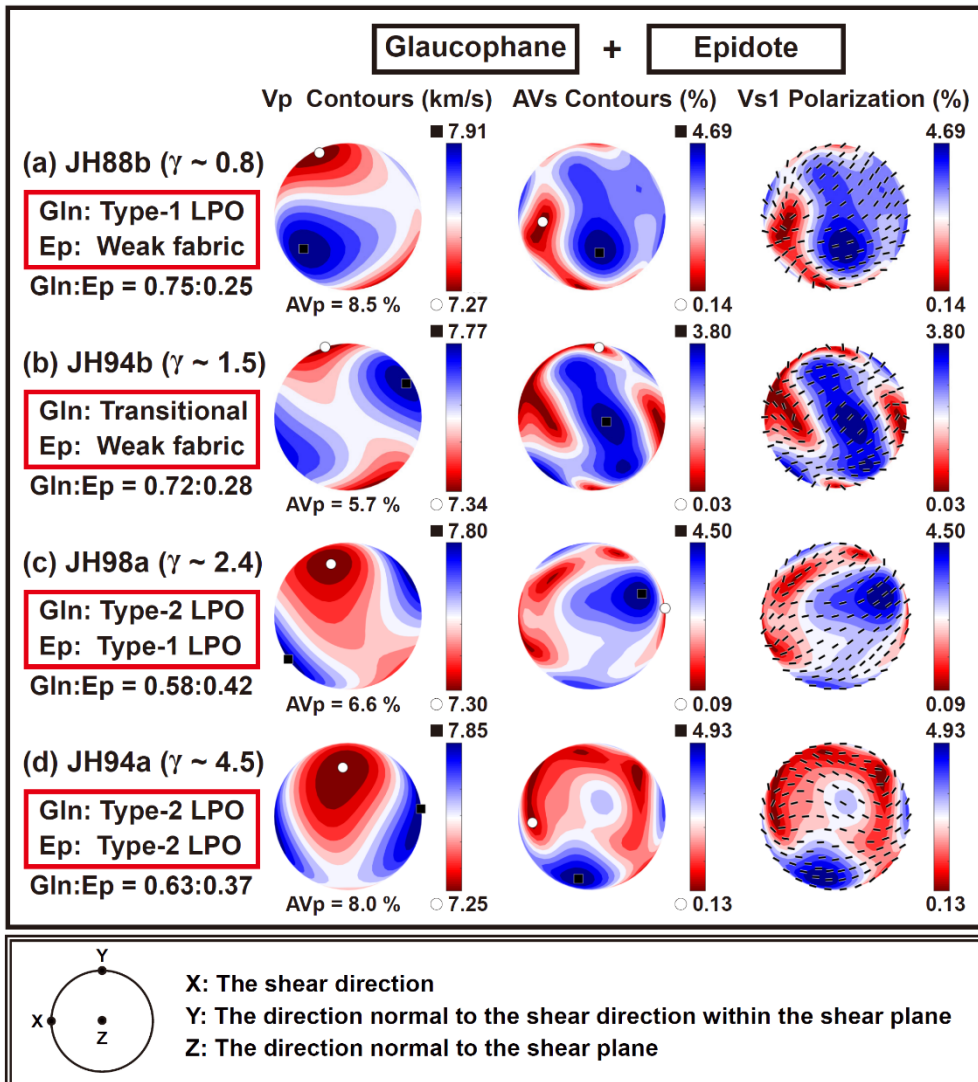


**Figure 4.4.** Seismic velocity and anisotropy of epidote blueschist (whole rock) calculated by assuming that the whole rock consists mainly of glaucophane and epidote as dominant minerals in deformed sample. The ratio of glaucophane to epidote followed the modal composition of deformed samples. The E-W direction corresponds to the shear direction (X), and the center of a stereographic projection circle is the direction normal to the shear plane (Z). The contours of P-wave velocity (Vp), the contours of S-wave polarization anisotropy (AVs), and polarization directions of the fast shear wave (Vs1) are shown.

## 4.4. Discussions and implications

### 4.4.1. Seismic velocity of epidote blueschist induced by LPO of minerals

As the fastest and slowest propagation axes of seismic wave in minerals are aligned in different directions depending on the LPO types, the directions of the maximum and minimum seismic velocity of polycrystalline minerals have been changed to different directions by the LPOs (Figs. 4.2 and 4.3). In the sample deformed under low shear strain ( $\gamma \leq 1$ ), the c-axes of glaucophanes, the orientation of the fastest P-wave propagation in single crystal of glaucophane (Fig. 4.5), were in subparallel alignment with the shear direction (Fig. 4.1a). On the other hand, the a-axes of glaucophanes, the orientation of the slowest P-wave propagation in single crystal of glaucophane (Fig. 4.5), were subnormally aligned with the shear direction within the shear plane (Fig. 4.1a). As a result, the direction of the  $V_{p_{\max}}$  of glaucophanes was subparallel to the shear direction, and the direction of the  $V_{p_{\min}}$  was subnormal to the shear direction within the shear plane (Fig. 4.2b–4.2e). In the sample deformed under high shear strain ( $\gamma > 2$ ), the c-axes of glaucophanes were aligned more parallel to the shear direction, and the a-axes of glaucophanes were subnormally aligned with the shear plane (Fig. 4.1c). According to their alignments, the  $V_{p_{\max}}$  direction of glaucophanes was parallel to the shear direction, and the area/direction of the  $V_{p_{\min}}$  was subnormal to the shear plane (Fig. 4.2g–4.2k). Because the orientation of the fast S-wave propagation in single crystal of

glaucophane is similar to that of the P-wave (Fig. 4.5), the directions of the  $V_{s1_{\max}}$  and  $V_{s1_{\min}}$  of glaucophanes coincide with the directions of  $V_{p_{\max}}$  and  $V_{p_{\min}}$ , respectively. In contrast, the fastest propagation direction of the slow S-wave in single crystal of glaucophane is between the a-axis and c-axis of glaucophane (Fig. 4.5). Although the slowest propagation direction of the slow S-wave is the a-axis of glaucophane, the slow S-wave propagations in the b-axis and c-axis are also similar to the a-axis (Fig. 4.5). As a result, the directions of the  $V_{s2_{\max}}$  and  $V_{s2_{\min}}$  of glaucophanes are difficult to match well with the LPO of glaucophane.

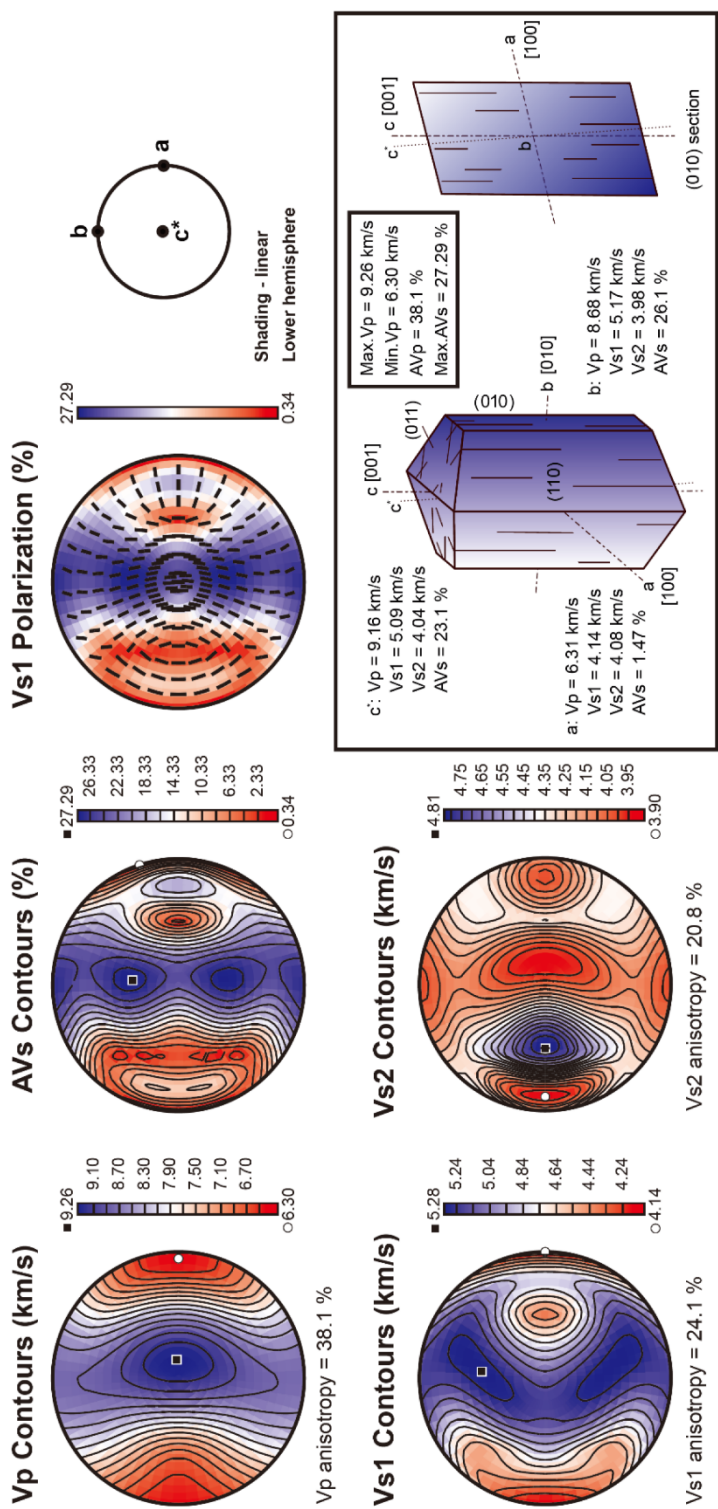


**Figure 4.5.** Seismic velocity and anisotropy for single crystal of glaucophane calculated using the petrophysics software (Mainprice, 1990) and elastic stiffness coefficient from Bezacier *et al.* (2010a). A schematic of glaucophane crystal form is modified after Nesse (2004). a, b, c: crystallographic axes of glaucophane, and c\*: direction perpendicular to both the a- and b-axes of glaucophane.

Epidote has complex orientation of the fastest and slowest propagation axes of P-wave (Fig. 4.6). The orientation of the fastest P-wave propagation is parallel to the b-axis of epidote single crystal, and the orientation of the slowest P-wave propagation is between the a-axis and c-axis in single crystal of epidote, but close to the c-axis (Fig. 4.6). Because of this complex orientation, the direction of  $V_{p_{max}}$  and  $V_{p_{min}}$  of epidotes did not match well with the LPO of epidote (Fig. 4.3). In addition, the orientation of the fast and slow S-wave propagation in single crystal of epidote shows a more complex pattern than that of the P-wave (Fig. 4.6). As a result, it was also difficult to describe the directions of the  $V_{s1}$  and  $V_{s2}$  of epidotes using the LPO of epidote.

The  $V_p$  contours and  $V_{s1}$  polarization direction patterns of epidote blueschists (whole rock) followed those of glaucophanes due to the high proportion of glaucophane in the sample (Fig. 4.4). In contrast, the AVs contours of epidote blueschists followed the complex mixed patterns of AVs contours of glaucophanes and epidotes (Fig. 4.4). These results suggest that  $V_{s1}$  and  $V_{s2}$  of epidote may have a more sensitive influence on the AVs of epidote blueschist than those of glaucophane. The  $V_{p_{aver}}$ ,  $V_{s_{aver}}$  and AVp of epidote blueschist were between those of glaucophanes and epidotes (Tables 1 and 2). However, the Max. AVs of epidote blueschist was lower than both Max. AVs of glaucophanes and epidotes except for a sample (JH94b) which consists of glaucophane exhibiting a transitional LPO (Max. AVs = 3.80 % which is lower than epidotes (7.23 %) but slightly higher than glaucophanes (3.73 %); Table 4.1). These results also suggest that epidote can significantly affect the AVs of epidote blueschist.

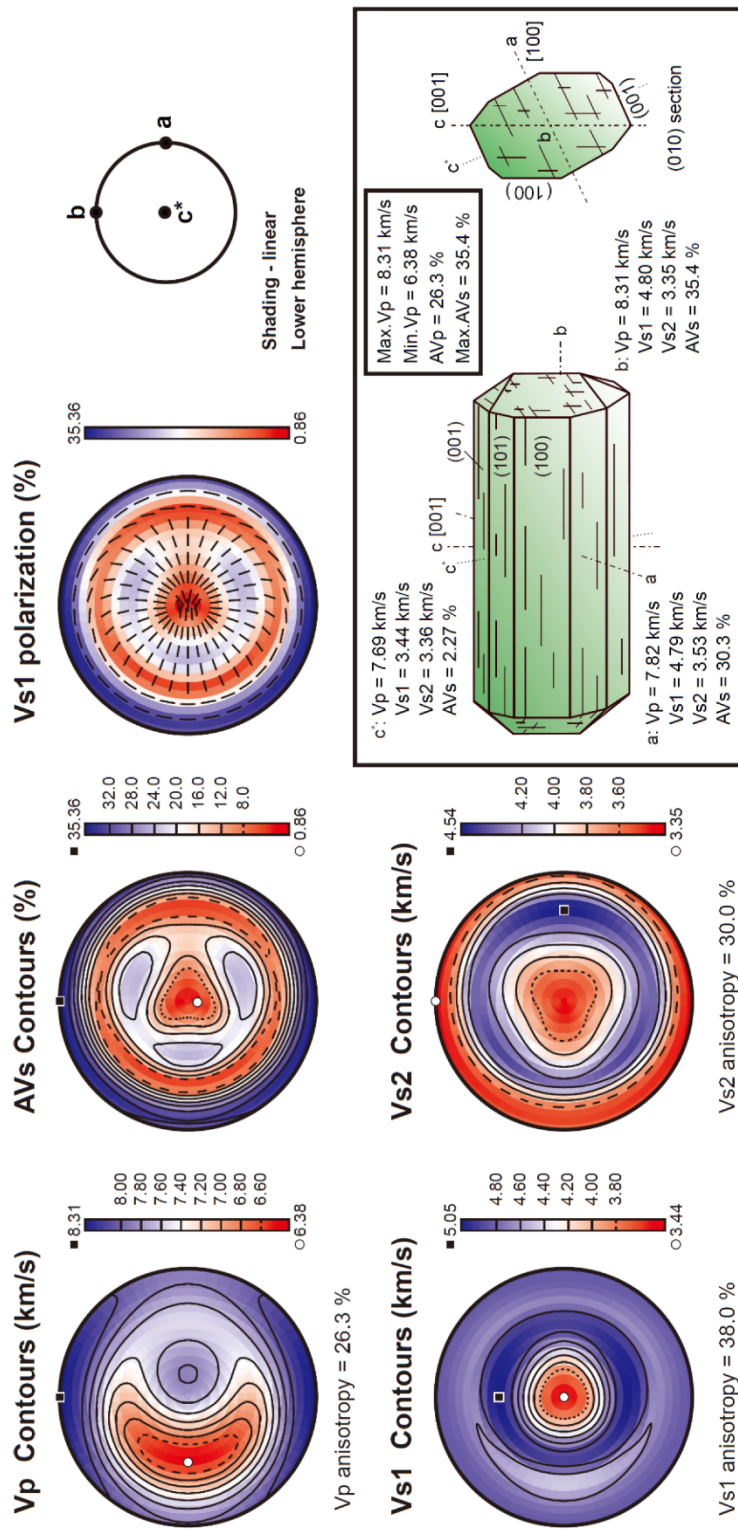


**Figure 4.6.** Seismic velocity and anisotropy for single crystal of epidote calculated using the petrophysics software (Mainprice, 1990) and elastic stiffness coefficient from Aleksandrov *et al.* (1974). A schematic of epidote crystal form is modified after Franz and Liebscher (2004). a, b, c: crystallographic axes of epidote, and c\*: direction perpendicular to both the a- and b-axes of epidote.

## 4.4.2. Relationship between seismic properties of epidote blueschist and deformation of minerals

To understand how the magnitude of shear strain and fabric strength of minerals affect the seismic velocity of polycrystalline minerals, the isotropic velocity ( $V_{p_{iso}}$  and  $V_{s_{iso}}$ ; Equations 4.2 and 4.3) and isotropic average velocity ( $V_{p_{iso,aver}}$  and  $V_{s_{iso,aver}}$ ; Equations 4.4 and 4.5) of deformed glaucophane and epidote polycrystals were calculated in this chapter.

### 4.4.2.1. Seismic velocity of epidote blueschist versus shear strain

The  $V_{p_{iso}}$  and  $V_{s_{iso}}$  of glaucophane polycrystals were increased with increasing shear strain in  $\gamma \leq 1$ , decreased in  $1 < \gamma \leq 2$ , and increased again with increasing shear strain in  $\gamma > 2$  (Fig. 4.7a and b). This trend indicates that glaucophane minerals have independent alignments by shear deformation in low ( $\gamma \leq 1$ ) and in high shear strain zone ( $\gamma > 2$ ) (Park et al., 2020a). In contrast, the  $V_{p_{iso,aver}}$  and  $V_{s_{iso,aver}}$  of glaucophane polycrystals were increased with increasing shear strain in  $\gamma \leq 1$ , and decreased with increasing shear strain after  $\gamma > 1$  (Fig. 4.7c and d). This trend indicates that the low velocity region in velocity contours had shifted in the direction subnormal to the shear plane with increasing shear strain as a transition of the a-axis alignment of glaucophanes.

In case of epidote, only the seismic velocity calculated for four samples were used due to the limited number of epidote grains in deformed samples. Unlike the seismic velocities of glaucophane polycrystals, the  $V_{p_{iso}}$  and  $V_{S_{iso}}$  of epidote polycrystals were decreased with increasing shear strain (Fig. 4.8a and b). In addition, the  $V_{p_{iso,aver}}$  and  $V_{S_{iso,aver}}$  of epidotes were decreased with increasing shear strain after  $\gamma > 2$  (Fig. 4.8c and d). This trend is likely to indicate the high contribution of the cataclastic flow deformation for epidote (Park et al., 2020a). However, more data is needed to get a more accurate trend for the seismic velocity of epidote.

The isotropic velocity and isotropic average velocity calculated for epidote blueschist (whole rock) were in the range between those of the glaucophane and epidote polycrystals (Fig. 4.9). These seismic velocities of epidote blueschist were decreased with increasing shear strain in  $\gamma < 2$  and increased with increasing shear strain after  $\gamma > 2$  (Fig. 4.9). This trend indicates that the seismic velocity of whole rock deformed under  $\gamma < 2$  can be contributed more by epidote than by glaucophane, although the volume proportion of epidote is lower than that of glaucophane. However, the seismic velocity of whole rock deformed under  $\gamma > 2$  is more affected by glaucophane than by epidote.

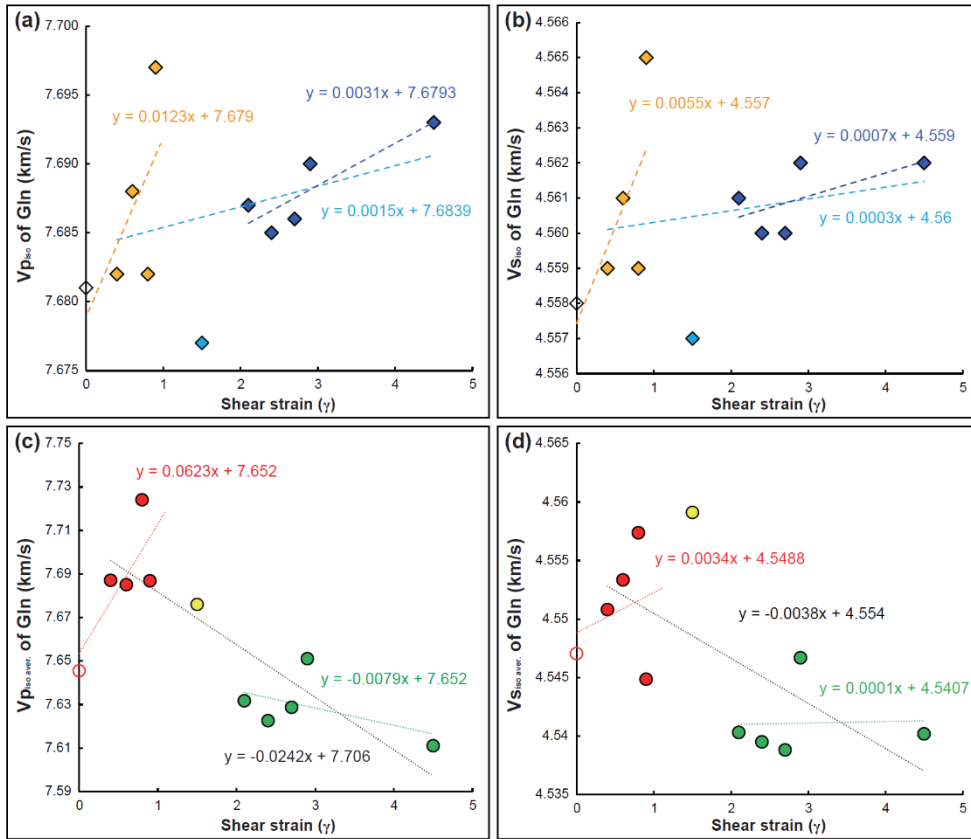


**Figure 4.7.** Seismic velocity of polycrystalline glaucophanes (Gln) compared to the magnitude of shear strain. **(a)** Isotropic velocity of P-wave ( $V_{p,iso}$ ) and **(b)** isotropic velocity of S-wave ( $V_{s,iso}$ ) versus the magnitude of shear strain. Blue open lozenges: polycrystalline glaucophanes in the starting material; orange solid lozenges: glaucophanes deformed under low shear strain ( $\gamma \leq 1$ ); cyan solid lozenges: glaucophanes deformed under intermediate shear strain ( $1 < \gamma < 2$ ); and blue solid lozenges: glaucophanes deformed under high shear strain ( $\gamma \geq 2$ ). **(c)** Isotropic average velocity of P-wave ( $V_{p,iso,aver}$ ) and **(d)** isotropic average velocity of S-wave ( $V_{s,iso,aver}$ ) versus the magnitude of shear strain. Red open circle: polycrystalline glaucophanes in the starting material; red solid circles: glaucophanes deformed under low shear strain ( $\gamma \leq 1$ ); yellow solid circle: glaucophanes deformed under intermediate shear strain ( $1 < \gamma < 2$ ); and green solid circles: glaucophanes deformed under high shear strain ( $\gamma \geq 2$ ).

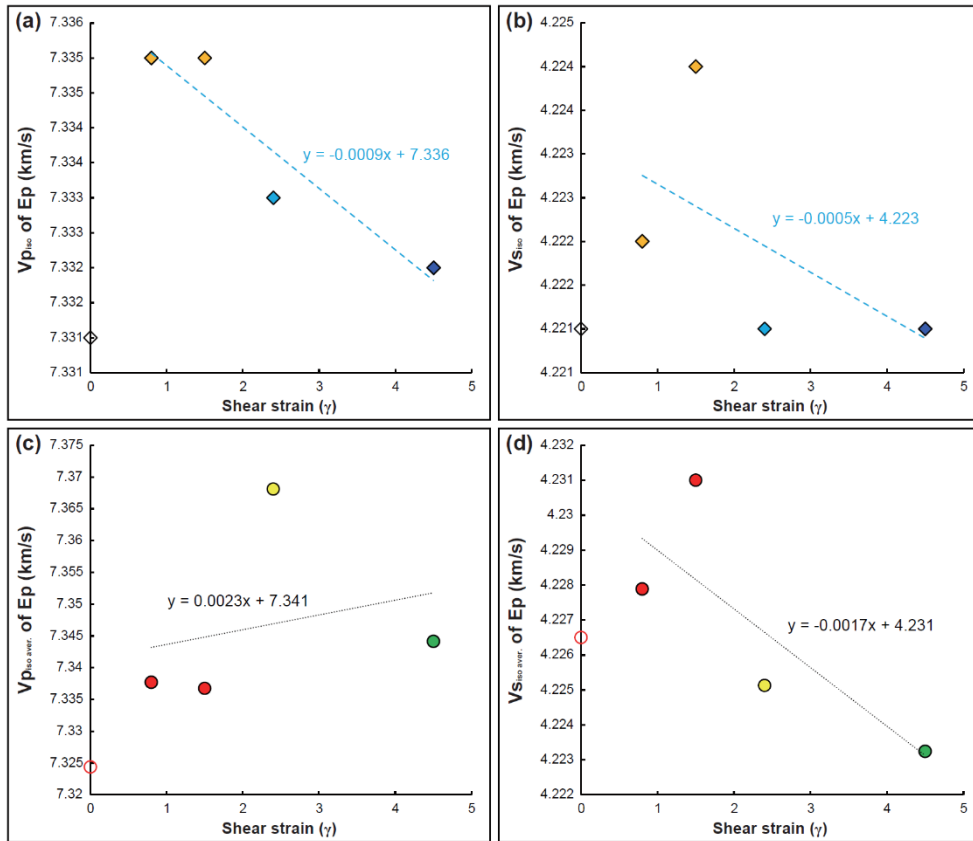


**Figure 4.8.** Seismic velocity of polycrystalline epidotes (Ep) compared to the magnitude of shear strain. **(a)** Isotropic velocity of P-wave ( $V_{p,iso}$ ) and **(b)** isotropic velocity of S-wave ( $V_{s,iso}$ ) versus the magnitude of shear strain. Blue open lozenges: polycrystalline epidotes in the starting material; orange solid lozenges: epidotes deformed under a shear strain of  $\gamma < 2$ ; cyan solid lozenges: epidotes deformed under a shear strain between  $2 < \gamma < 4$ ; and blue solid lozenges: epidotes deformed under a shear strain of  $\gamma > 4$ . **(c)** Isotropic average velocity of P-wave ( $V_{p,iso,aver}$ ) and **(d)** isotropic average velocity of S-wave ( $V_{s,iso,aver}$ ) versus the magnitude of shear strain. Red open circle: polycrystalline epidotes in the starting material; red solid circles: epidotes deformed under a shear strain of  $\gamma < 2$ ; yellow solid circle: epidotes deformed under a shear strain between  $2 < \gamma < 4$ ; and green solid circles: epidotes deformed under a shear strain of  $\gamma > 4$ .

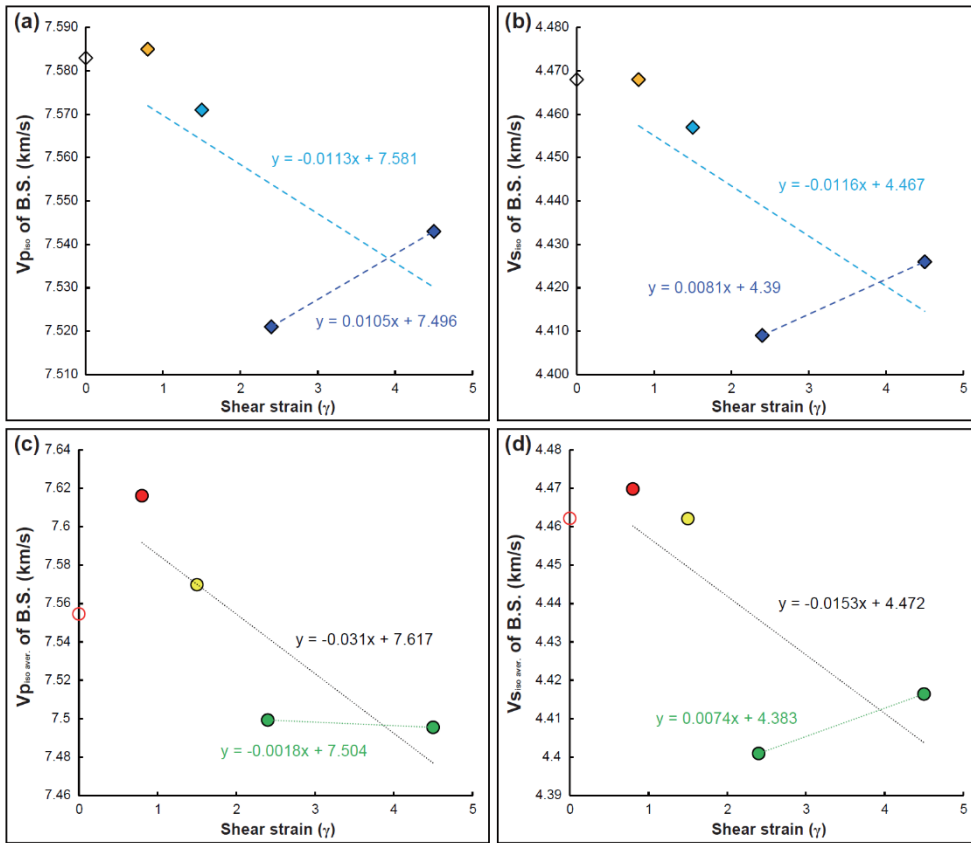


**Figure 4.9.** Seismic velocity of epidote blueschist (whole rock; B.S.) compared to the magnitude of shear strain. **(a)** Isotropic velocity of P-wave ( $V_{p,iso}$ ) and **(b)** isotropic velocity of S-wave ( $V_{s,iso}$ ) versus the magnitude of shear strain. Blue open lozenges: epidote blueschist before experiment (the starting material); orange solid lozenges: epidote blueschist deformed under low shear strain ( $\gamma \leq 1$ ); cyan solid lozenges: epidote blueschist deformed under intermediate shear strain ( $1 < \gamma < 2$ ), and blue solid lozenges: epidote blueschist deformed under high shear strain ( $\gamma \geq 2$ ). **(c)** Isotropic average velocity of P-wave ( $V_{p,iso,aver}$ ) and **(d)** isotropic average velocity of S-wave ( $V_{s,iso,aver}$ ) versus the magnitude of shear strain. Red open circle: epidote blueschist before experiment (the starting material); red solid circles: epidote blueschist deformed under low shear strain ( $\gamma \leq 1$ ); yellow solid circle: epidote blueschist deformed under intermediate shear strain ( $1 < \gamma < 2$ ), and green solid circles: epidote blueschist deformed under high shear strain ( $\gamma \geq 2$ ).

#### 4.4.2.2. Seismic velocity of epidote blueschist versus fabric strength

As a comparison between fabric strength (i.e., M-index and J-index) and seismic velocity of polycrystalline minerals, the  $V_{p_{iso}}$  and  $V_{S_{iso}}$  had high variations with similar fabric strength showing positive slope for glaucophanes deformed under low shear strain ( $\gamma \leq 1$ ) and weak negative slope for glaucophanes deformed under high shear strain ( $\gamma > 2$ ) (Fig. 4.10a–4.10d). The high variations of  $V_{p_{iso}}$  and  $V_{S_{iso}}$  indicate that the degree of deformation by dislocation creep was similar in both the glaucophanes deformed under low and high shear strain, and a weak negative slope suggests that deformation by cataclastic flow simultaneously affected the glaucophanes deformed under high shear strain (Park et al., 2020a). In contrast,  $V_{p_{iso,aver}}$  and  $V_{S_{iso,aver}}$  of glaucophanes deformed under low shear strain ( $\gamma \leq 1$ ) were faster than those deformed under high shear strain ( $\gamma \geq 2$ ) regardless of the fabric strength (Fig. 4.10e–4.10h). This represents the shift of the low velocity region in velocity contour in a direction subnormal to the shear plane due to the transition of the a-axis alignment of glaucophanes deformed under high shear strain (Fig. 4.2).

The isotropic and isotropic average velocity of epidotes exhibited opposite trends for two fabric strength indices (Fig. 4.11). The  $V_{p_{iso}}$  and  $V_{S_{iso}}$  of epidotes were decreased with increasing M-index, but these velocities were increased with increasing J-index (Fig. 4.11a–4.11d). The  $V_{p_{iso,aver}}$  of epidotes was decreased with increasing both M- and J-index (Fig. 4.11e–4.11f), but the  $V_{S_{iso,aver}}$  of epidotes exhibited a similar trend with  $V_{S_{iso}}$  (Fig. 4.11g–4.11h). A negative slope between

seismic velocities and M-index is likely to suggest the high contribution of cataclastic flow deformation for polycrystalline epidotes (Park et al., 2020a). Although seismic velocities of epidote were increased with increasing J-index, they showed lower values for epidotes deformed under higher shear strain. This result may also imply the cataclastic flow deformation of polycrystalline epidote. Due to the limited number of epidote grains in samples, however, it is difficult to get a precise relationship between fabric strength and seismic velocity of epidote. Therefore, more data is needed to get a more accurate trend for the seismic velocity of epidotes.

To compare with the relationship between seismic velocities and fabric strength of whole rock, the M-index and J-index of epidote blueschist were calculated by averaging M-index and J-index of glaucophane and epidote following the modal composition of each sample, respectively. As a result, the isotropic and isotropic average velocity of whole rock were decreased with increasing fabric strength after shear strain of  $\gamma > 2$  (Fig. 4.12). This result is likely to suggest that the seismic velocity of whole rock is more affected by cataclastic flow deformation as the shear strain was increased, but further study is needed due to the limited amount of data.

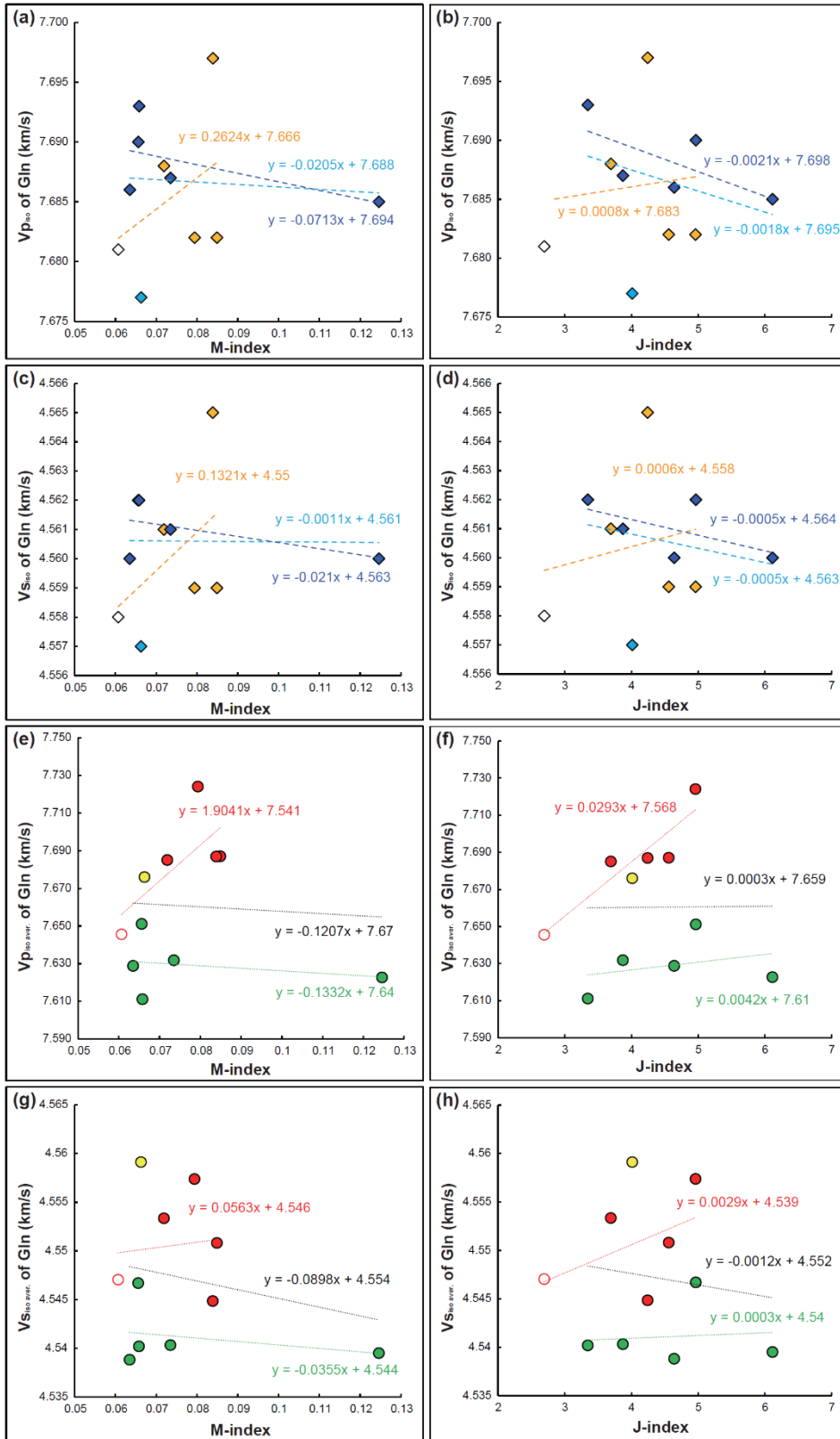


**Figure 4.10.** Seismic velocity of polycrystalline glaucophanes (Gln) compared to the fabric strength (M-index and J-index). **(a)** Isotropic velocity of P-wave ( $V_{p_{iso}}$ ) versus the M-index and **(b)** versus the J-index; **(c)** isotropic velocity of S-wave ( $V_{S_{iso}}$ ) versus the M-index and **(d)** versus the J-index. Blue open lozenges: polycrystalline glaucophanes in the starting material; orange solid lozenges: glaucophanes deformed under low shear strain ( $\gamma \leq 1$ ); cyan solid lozenges: glaucophanes deformed under intermediate shear strain ( $1 < \gamma < 2$ ); and blue solid lozenges: glaucophanes deformed under high shear strain ( $\gamma \geq 2$ ). **(e)** Isotropic average velocity of P-wave ( $V_{p_{iso,aver}}$ ) versus the M-index and **(f)** versus the J-index; **(g)** isotropic average velocity of S-wave ( $V_{S_{iso,aver}}$ ) versus the M-index and **(h)** versus the J-index. Red open circle: polycrystalline glaucophanes in the starting material; red solid circles: glaucophanes deformed under low shear strain ( $\gamma \leq 1$ ); yellow solid circle: glaucophanes deformed under intermediate shear strain ( $1 < \gamma < 2$ ); and green solid circles: glaucophanes deformed under high shear strain ( $\gamma \geq 2$ ).

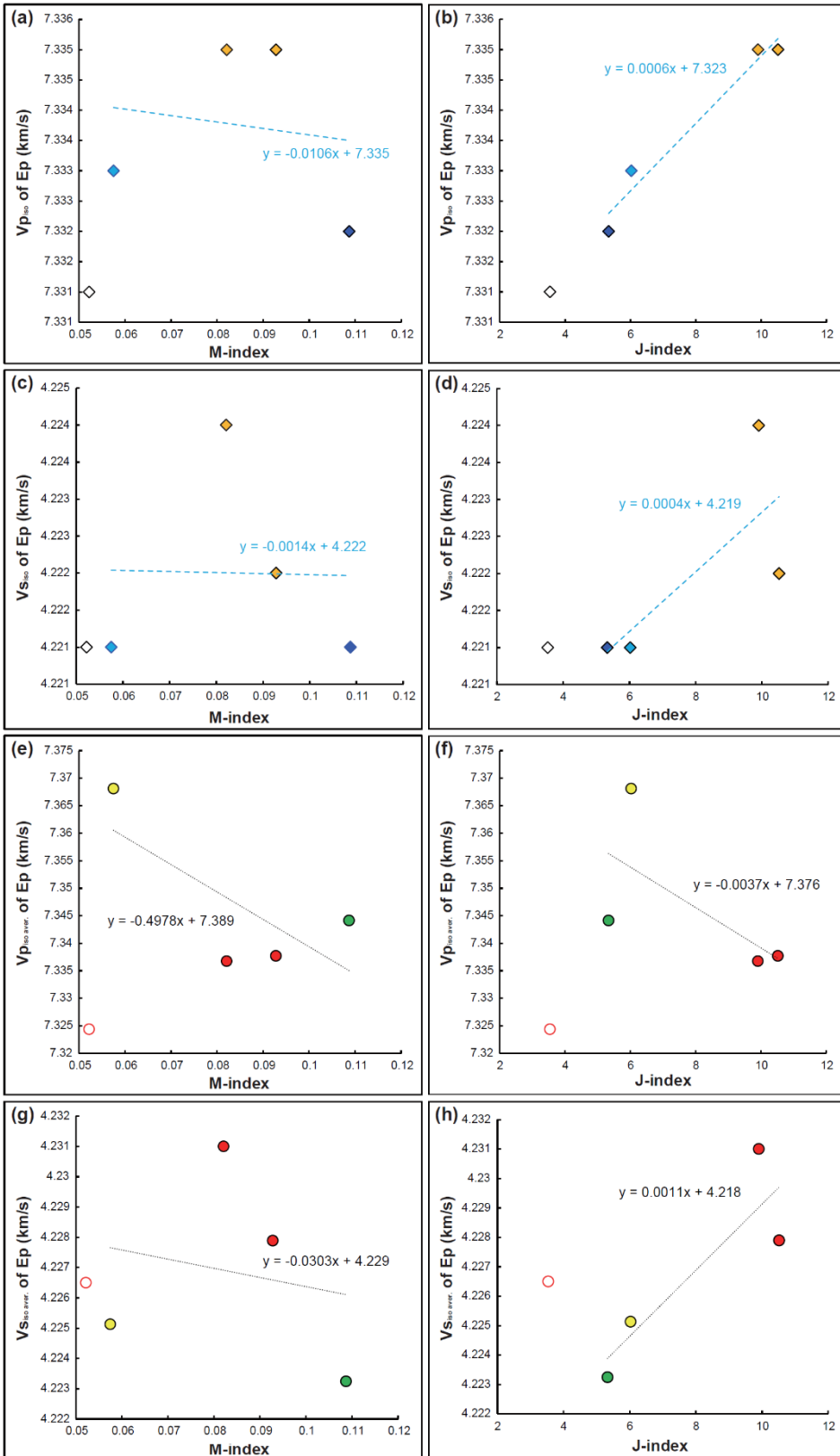


**Figure 4.11.** Seismic velocity of polycrystalline epidotes (Ep) compared to the fabric strength (M-index and J-index). **(a)** Isotropic velocity of P-wave ( $V_{p_{iso}}$ ) versus the M-index and **(b)** versus the J-index; **(c)** isotropic velocity of S-wave ( $V_{S_{iso}}$ ) versus the M-index and **(d)** versus the J-index. Blue open lozenges: polycrystalline epidotes in the starting material; orange solid lozenges: epidotes deformed under a shear strain of  $\gamma < 2$ ; cyan solid lozenges: epidotes deformed under a shear strain between  $2 < \gamma < 4$ ; and blue solid lozenges: epidotes deformed under a shear strain of  $\gamma > 4$ . **(e)** Isotropic average velocity of P-wave ( $V_{p_{iso,aver}}$ ) versus the M-index and **(f)** versus the J-index; **(g)** isotropic average velocity of S-wave ( $V_{S_{iso,aver}}$ ) versus the M-index and **(h)** versus the J-index. Red open circle: polycrystalline epidotes in the starting material; red solid circles: epidotes deformed under a shear strain of  $\gamma < 2$ ; yellow solid circle: epidotes deformed under a shear strain between  $2 < \gamma < 4$ ; and green solid circles: epidotes deformed under a shear strain of  $\gamma > 4$ .

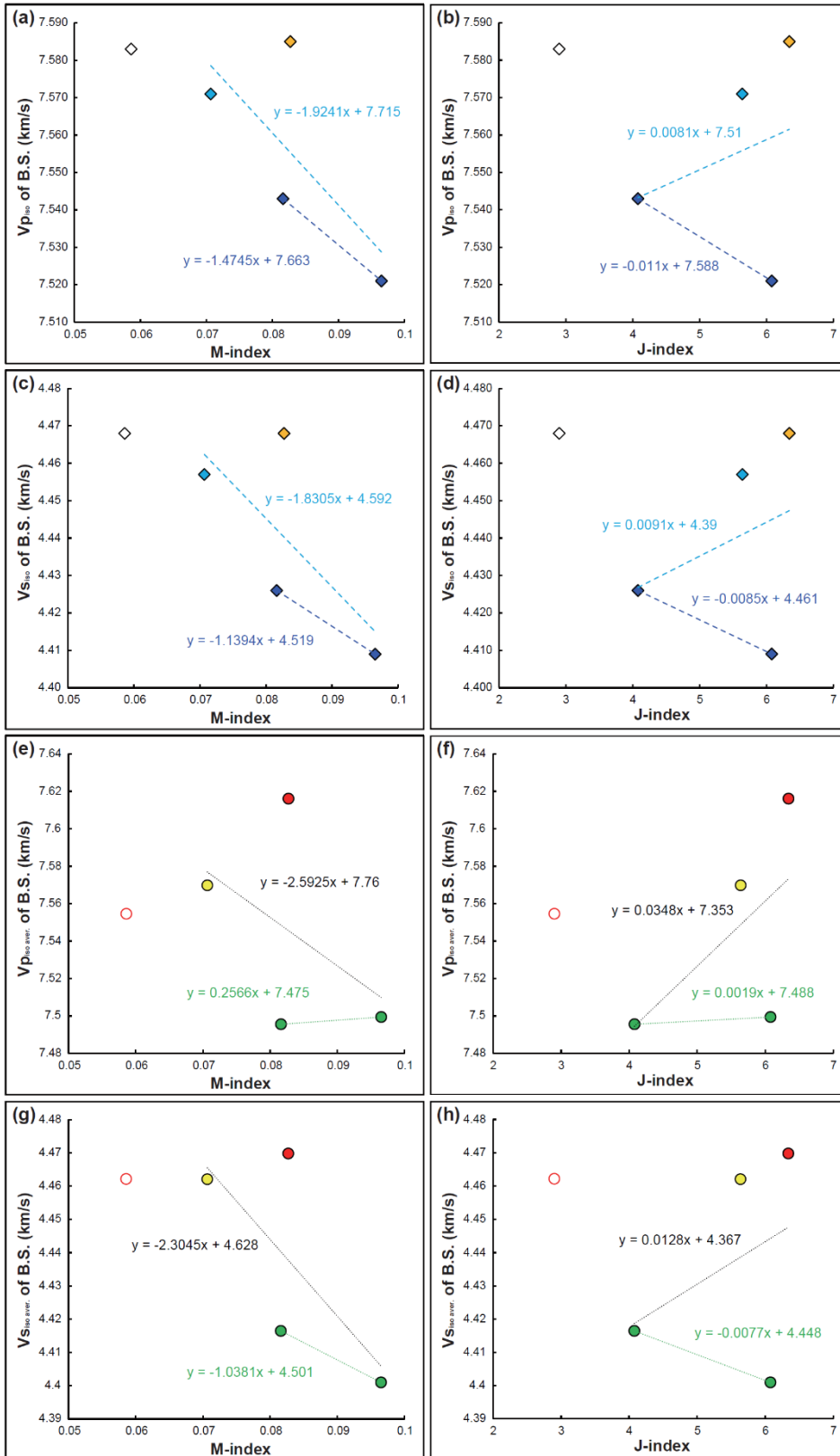


**Figure 4.12.** Seismic velocity of epidote blueschist (whole rock; B.S.) compared to the fabric strength (M-index and J-index). M-index and J-index of epidote blueschist (whole rock) are calculated by averaging M-index and J-index of polycrystalline glaucophanes and epidotes following the modal composition of deformed sample, respectively. **(a)** Isotropic velocity of P-wave ( $V_{p_{iso}}$ ) versus the M-index and **(b)** versus the J-index; **(c)** isotropic velocity of S-wave ( $V_{s_{iso}}$ ) versus the M-index and **(d)** versus the J-index. Blue open lozenges: epidote blueschist before experiment (the starting material); orange solid lozenges: epidote blueschist deformed under low shear strain ( $\gamma \leq 1$ ); cyan solid lozenges: epidote blueschist deformed under intermediate shear strain ( $1 < \gamma < 2$ ), and blue solid lozenges: epidote blueschist deformed under high shear strain ( $\gamma \geq 2$ ). **(e)** Isotropic average velocity of P-wave ( $V_{p_{iso,aver}}$ ) versus the M-index and **(f)** versus the J-index; **(g)** isotropic average velocity of S-wave ( $V_{s_{iso,aver}}$ ) versus the M-index and **(h)** versus the J-index. Red open circle: epidote blueschist before experiment (the starting material); red solid circles: epidote blueschist deformed under low shear strain ( $\gamma \leq 1$ ); yellow solid circle: epidote blueschist deformed under intermediate shear strain ( $1 < \gamma < 2$ ), and green solid circles: epidote blueschist deformed under high shear strain ( $\gamma \geq 2$ ).

#### 4.4.2.3. Seismic anisotropy of epidote blueschist versus shear strain

Seismic anisotropy of P- and S-wave against shear strain of deformed samples are shown in Figure 4.13. The AV<sub>p</sub> and Max. AV<sub>s</sub> values of glaucophanes and epidotes followed the trends of the V<sub>p<sub>iso</sub></sub> and V<sub>S<sub>iso</sub></sub> of each mineral (Fig. 4.13a–4.13b). With increasing shear strain, both AV<sub>p</sub> and Max. AV<sub>s</sub> of polycrystalline glaucophanes were increased up to AV<sub>p</sub> = 15.2 % and Max. AV<sub>s</sub> = 8.06 % in low shear strain ( $\gamma \leq 1$ ), decreased up to AV<sub>p</sub> = 6.9 % and Max. AV<sub>s</sub> = 3.73 % in intermediate shear strain ( $1 < \gamma < 2$ ), and increased again up to AV<sub>p</sub> = 13.1 % and Max. AV<sub>s</sub> = 8.02 % in high shear strain ( $\gamma \geq 2$ ; Fig. 4.13a). This trend suggests that the type-1 and type-2 LPOs of glaucophane have developed independently under low shear strain ( $\gamma \leq 1$ ) and under high shear strain ( $\gamma \geq 2$ ) (Park et al., 2020a). The decrease of AV<sub>p</sub> and Max. AV<sub>s</sub> of glaucophane at the intermediate shear strain is likely to have been caused by transition from type-1 to type-2 glaucophane LPO (Fig. 4.13a).

The AV<sub>p</sub> and Max. AV<sub>s</sub> of epidotes in deformed samples were larger than those of epidote in the starting material, but they exhibited different trends with those of glaucophanes (Fig. 4.13b). The AV<sub>p</sub> of epidotes was decreased with increasing shear strain, but the Max. AV<sub>s</sub> was almost constant with increasing shear strain (Fig. 4.13b). Because the data of epidotes are not as much as those of glaucophanes, however, further studies on the seismic anisotropy for deformed epidotes are needed to get a more accurate tendency. Although the causes of these trends are unclear yet due to

the limited number of data, a negative slope of AVp suggests the high contribution of the cataclastic flow for epidote with increasing shear strain (Park et al., 2020a). These different trends of seismic anisotropy of glaucophanes and epidotes may be caused by the different magnitude of shear strain required to alter the LPOs/slip systems ( $1 < \gamma \leq 2$  for glaucophane, and  $\gamma \sim 4$  for epidote), and/or different dominant mechanisms of LPO development for each mineral with increasing shear strain (Park et al., 2020a).

The AVp and Max. AVs of epidote blueschist (whole rock) were increased with increasing shear strain (Fig. 4.13c). These trends are weakly followed the trends of seismic anisotropy of glaucophanes (Fig. 4.13a). However, more data are needed to surely constrain the relationship between seismic anisotropy of epidote blueschist and those of constituent minerals of rock. Although this limitation, these data indicate that the magnitude of shear strain can highly affect the seismic anisotropy of the upper subducting slab within the epidote blueschist-facies metamorphic condition.

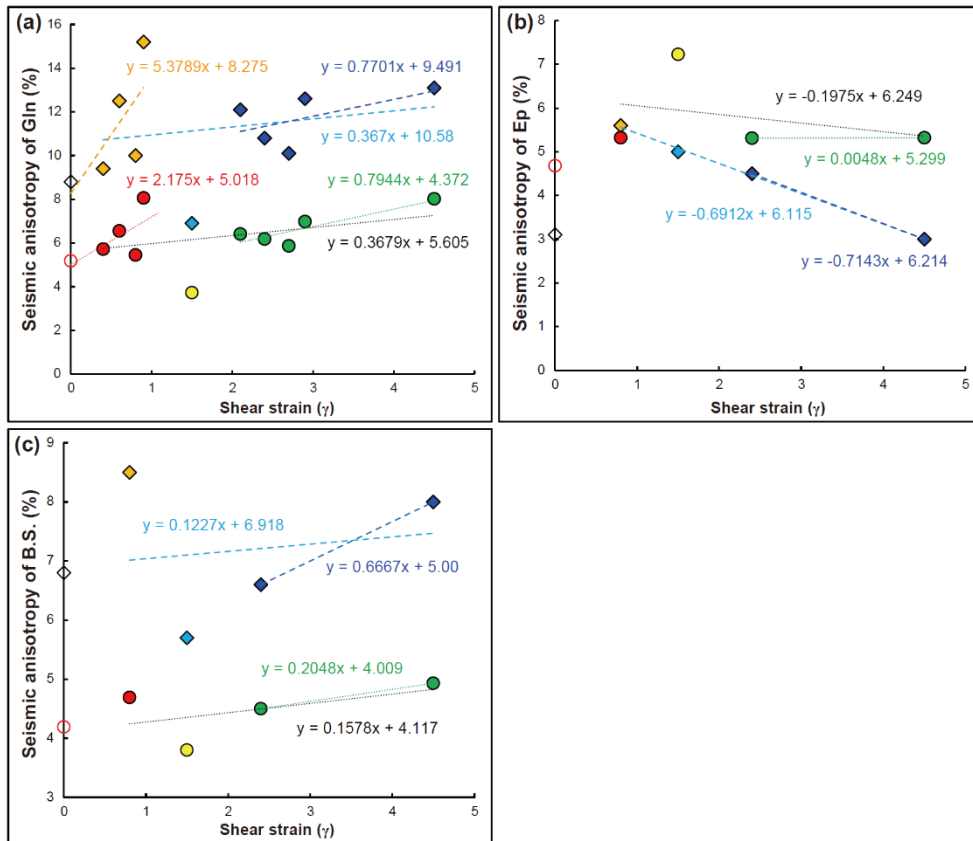


**Figure 4.13.** Seismic anisotropy of polycrystalline minerals and whole rock compared to the magnitude of shear strain for **(a)** Glaucofanite (Gln), **(b)** epidote (Ep), and **(c)** epidote blueschist (whole rock; B.S.). Blue open lozenges: the azimuthal anisotropy of P-wave (AVp) of polycrystalline minerals in the starting material and epidote blueschist before experiment (the starting material); orange solid lozenges: the AVp of minerals and epidote blueschist deformed under low shear strain ( $\gamma \leq 1$ ); cyan solid lozenge: the AVp of minerals and epidote blueschist deformed under intermediate shear strain ( $1 < \gamma < 2$ ); and blue solid lozenges: AVp of minerals and epidote blueschist deformed under high shear strain ( $\gamma \geq 2$ ). Red open circle: the maximum polarization anisotropy of S-wave (Max. AVs) of polycrystalline minerals in the starting material and epidote blueschist before experiment (the starting material); red solid circles: Max. AVs of minerals and epidote blueschist deformed under low shear strain ( $\gamma \leq 1$ ); yellow solid circle: Max. AVs of minerals and epidote blueschist deformed under intermediate shear strain ( $1 < \gamma < 2$ ); and green solid circles: Max. AVs of minerals and epidote blueschist deformed under high shear strain ( $\gamma \geq 2$ ).

#### 4.4.2.4. Seismic anisotropy of epidote blueschist versus fabric strength

Seismic anisotropy of P- and S-wave against fabric strength of deformed samples are shown in Figure 4.14. With increasing fabric strength (i.e., M-index and J-index), the  $AV_p$  and Max. AVs values of polycrystalline glaucophanes deformed under low shear strain ( $\gamma \leq 1$ ) were increased with increasing fabric strength showing a positive slope with high variations, and those of glaucophanes deformed under high shear strain ( $\gamma \geq 2$ ) were decreased with increasing fabric strength showing a weak negative slope (Fig. 4.14a–4.14b). This trend suggests a more contribution of cataclastic flow to glaucophanes deformed under high shear strain ( $\gamma \geq 2$ ) than glaucophanes deformed under low shear strain (Park et al., 2020a). In addition, the similar fabric strength of glaucophanes deformed under low and high shear strain suggests the independent development of glaucophane LPOs with similar degree of deformation by dislocation creep under low and high shear strain (Park et al., 2020a).

The  $AV_p$  of polycrystalline epidotes was decreased with increasing M-index (Fig. 4.14c) but increased with increasing J-index (Fig. 4.14d). In contrast, the Max. AVs of epidotes was almost constant with increasing M-index (Fig. 4.14c), but slightly increased with increasing J-index (Fig. 4.14d). The lower fabric strengths of epidotes deformed under high shear strain ( $\gamma \geq 2$ ) than those of epidotes deformed under low shear strain ( $\gamma < 2$ ) is likely to be caused by the cataclastic flow deformation for epidotes (Park et al., 2020a). Because of the limited number of data, however, further studies on the seismic anisotropy for deformed epidote are needed

to get a more accurate tendency.

The AV<sub>p</sub> and Max. AVs of epidote blueschist (whole rock) were increased with increasing M-index (Fig. 4.14e) but decreased with increasing J-index (Fig. 4.14f). These trends are opposite with isotropic and isotropic average velocities of whole rock (Fig. 4.11), but weakly followed the trends of seismic anisotropies of glaucophane polycrystals (Fig. 4.14a–4.14b). Although more data are needed to surely constrain the relationship between seismic anisotropy of whole rock and those of constituent minerals of rock, these data suggest that fabric strength of deformed glaucophane and epidote can affect the seismic anisotropy of epidote blueschist-facies metamorphic rock.

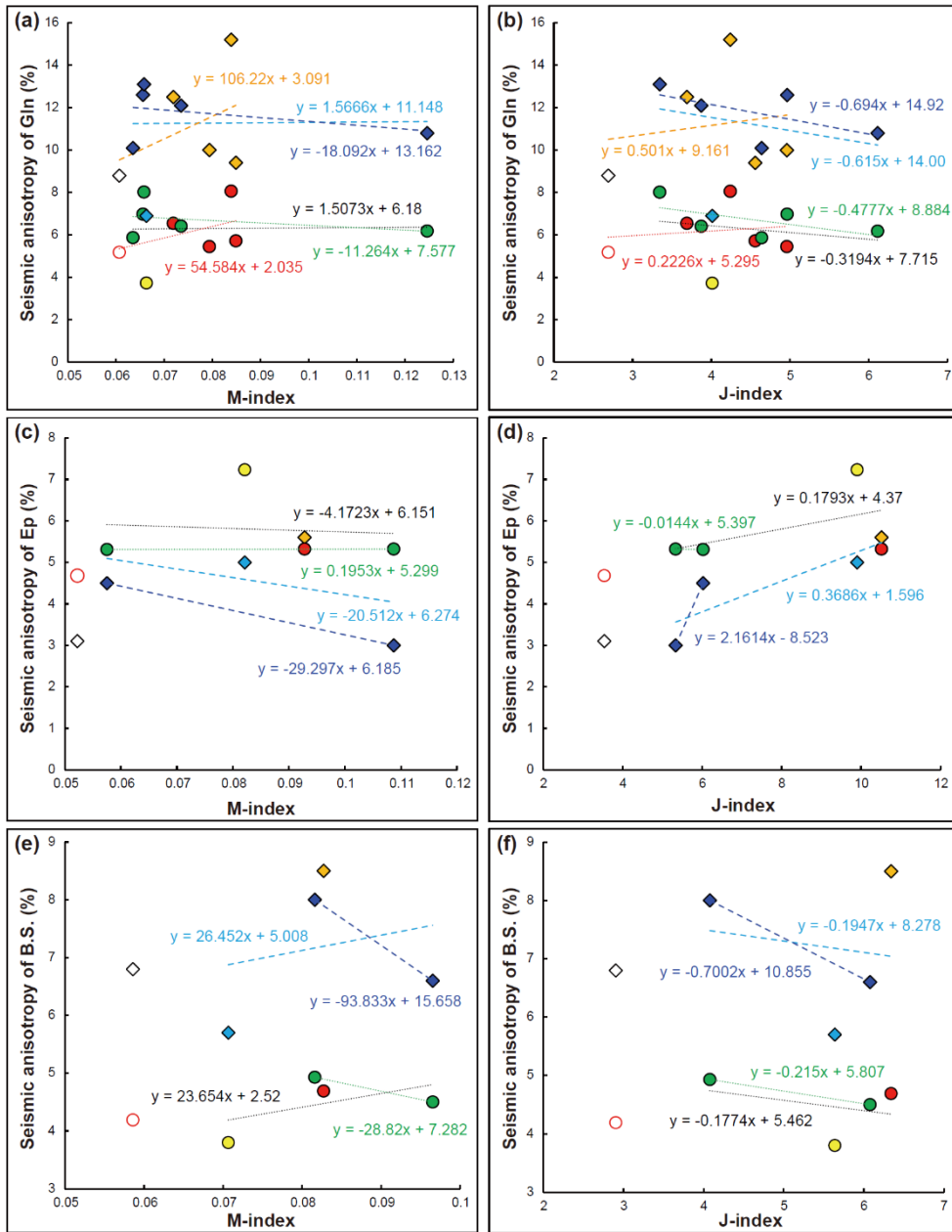


**Figure 4.14.** Seismic anisotropy of polycrystalline minerals and whole rock compared to the fabric strength (M-index and J-index) for **(a)–(b)** glaucophane (Gln), **(c)–(d)** epidote (Ep), and **(e)–(f)** epidote blueschist (whole rock; B.S.). M-index and J-index of epidote blueschist (whole rock) are calculated by averaging M-index and J-index of polycrystalline glaucophanes and epidotes following the modal composition of deformed sample, respectively. Blue open lozenges: the azimuthal anisotropy of P-wave (AV<sub>p</sub>) of polycrystalline minerals in the starting material and epidote blueschist before experiment (the starting material); orange solid lozenges: the AV<sub>p</sub> of minerals and epidote blueschist deformed under low shear strain ( $\gamma \leq 1$ ); cyan solid lozenge: the AV<sub>p</sub> of minerals and epidote blueschist deformed under intermediate shear strain ( $1 < \gamma < 2$ ); and blue solid lozenges: AV<sub>p</sub> of minerals and epidote blueschist deformed under high shear strain ( $\gamma \geq 2$ ). Red open circle: the maximum polarization anisotropy of S-wave (Max. AV<sub>s</sub>) of polycrystalline minerals in the starting material and epidote blueschist before experiment (the starting material); red solid circles: Max. AV<sub>s</sub> of minerals and epidote blueschist deformed under low shear strain ( $\gamma \leq 1$ ); yellow solid circle: Max. AV<sub>s</sub> of minerals and epidote blueschist deformed under intermediate shear strain ( $1 < \gamma < 2$ ); and green solid circles: Max. AV<sub>s</sub> of minerals and epidote blueschist deformed under high shear strain ( $\gamma \geq 2$ ).

### 4.4.3. Relationship between seismic properties of subducting slab and LPOs of minerals

As the seismic anisotropy of shear wave is controlled by the orientation of anisotropic medium passed through the seismic wave, the incidence angle of seismic wave and the subducting angle of the slab are important to understand Vs1 polarization direction in forearc region of the subduction zone (Song and Kawakatsu, 2012). In addition, the LPO of constituent minerals of the subducting crust is important to measure the seismic velocity because the orientation of the fastest seismic wave propagation is altered by LPO type of minerals (in Chapter 4.4.1; Cao et al., 2013; Park et al., 2020a). Because many studies have analyzed the SKS wave splitting data to observe the seismic anisotropy of subduction zone, the incident direction of seismic wave has been regarded as a direction subnormal to the Earth's surface. Therefore, the subducting angle of the slab ( $\theta$ ) and the volume proportion of glaucophanes and epidotes with different LPO types were considered to calculate the seismic properties of the subducting oceanic crust such as delay time of S-wave (Fig. 4.15) and Vp/Vs ratio (Fig. 4.16).

The delay time ( $\delta t$ ) of the subducting oceanic crust was calculated by the equation derived from the form of Equation 2.6 (Pera et al., 2003) as:

$$T = (100 \times \delta t \times \langle V_s \rangle) / AV_s \text{ (km)} \quad (2.6)$$

$$\delta t = (T \times AV_s) / (100 \times \langle V_s \rangle) \text{ (s)} \quad (4.6)$$

where  $T$  is the anisotropic layer thickness,  $\langle V_s \rangle$  is the average velocity of fast and slow shear wave velocities ( $V_{s1}$  and  $V_{s2}$ ), and  $AV_s$  is the seismic anisotropy of the S-wave expressed as a percentage. According to the results, delay time of the subducting crust was generally increased with increasing the subducting angle and volume proportion of glaucophane (Fig. 4.15). The sharp increase in the delay time at  $\theta > 60^\circ$  is due to the increase in the length of seismic wave propagation through the anisotropic medium as well as the passage of seismic wave through the fast propagation direction by the LPOs of glaucophane (Fig. 4.15). However, delay time of the subducting crust with the type-1 LPO of epidote was decreased when the volume proportion of glaucophane is near  $\sim 20\%$  (Fig. 4.15a and 4.15c). This trend indicates that seismic anisotropy of S-wave induced by the type-1 LPO of epidote is counteracting the seismic anisotropy induced by the LPOs of glaucophane. In addition, the delay time of subducting crust with the type-2 LPO of epidote was increased for a dipping subducting slab at  $\theta \leq 30^\circ$ , decreased at  $30^\circ < \theta \leq 60^\circ$ , and increased again at  $\theta > 60^\circ$ . This trend indicates that b-axis of epidote contributes to the seismic anisotropy more than c-axis of epidote (Fig. 4.15b and 4.15d). These results suggest that LPO of glaucophane contributes to the delay time of the subducting slab more than that of epidote, and the seismic anisotropy induced by these LPOs is counteracted (Fig. 4.15).

The  $V_p/V_s$  ratio of the subducting oceanic crust was generally increased with increasing volume proportion of epidote at low subducting angle and with increasing volume proportion of glaucophane at high subducting angle (Fig. 4.16). If the subducting oceanic crust consisted of the glaucophane showing type-1 LPO and the epidote showing type-1 LPO, the  $V_p/V_s$  ratio was low when there was only epidote

in the crust, and the ratio was high when there were 90 % of epidote and 10 % of glaucophane (Fig. 4.16a). If the crust consisted of the glaucophane showing type-1 LPO and the epidote showing type-2 LPO, the  $V_p/V_s$  ratio was low when there was only glaucophane at  $\theta \leq 60^\circ$  and only epidote at  $\theta > 60^\circ$ , and the ratio was high when there was only epidote at  $\theta \leq 60^\circ$  and only glaucophane at  $\theta > 60^\circ$  (Fig. 4.16b). If the crust consisted of the glaucophane showing type-2 LPO and the epidote showing type-1 LPO, the  $V_p/V_s$  ratio was low when there was only glaucophane at  $\theta < 30^\circ$  and only epidote at  $\theta \geq 30^\circ$ , and the ratio was high when there were 90 % of epidote and 10 % of glaucophane at  $\theta \leq 45^\circ$  and only glaucophane at  $\theta > 45^\circ$  (Fig. 4.16c). If the crust consisted of the glaucophane showing type-2 LPO and the epidote showing type-2 LPO, the  $V_p/V_s$  ratio was low when there was only glaucophane at  $\theta \leq 45^\circ$  and only epidote at  $\theta > 45^\circ$ , and the ratio was high when there was only epidote at  $\theta \leq 45^\circ$  and only glaucophane at  $\theta > 45^\circ$  (Fig. 4.16d). The lowest values of  $V_p/V_s$  ratios were  $V_p/V_{s1} = 1.607$ ,  $V_p/V_{s2} = 1.653$ , and  $V_p/V_{s_{\text{mean}}} = 1.630$  when the crust consisted only of the glaucophane showing type-2 LPO at  $\theta = 0^\circ$ . The highest  $V_p/V_{s1}$  of the crust was  $V_p/V_{s1} = 1.744$  when the crust consisted of 90 % of epidote showing type-1 LPO and 10 % of glaucophane showing type-2 LPO at  $\theta = 15^\circ$ , and the highest  $V_p/V_{s2}$  and  $V_p/V_{s_{\text{mean}}}$  of the crust were  $V_p/V_{s2} = 1.819$  and  $V_p/V_{s_{\text{mean}}} = 1.773$  when the crust consisted only of the glaucophane showing type-2 LPO at  $\theta = 85^\circ$  (Fig. 4.16). These data suggest that the volume proportion and LPO types of glaucophane and epidote, and the subducting angle of the slab are important factors for the  $V_p/V_s$  ratio observed at the top of the subducting slab.

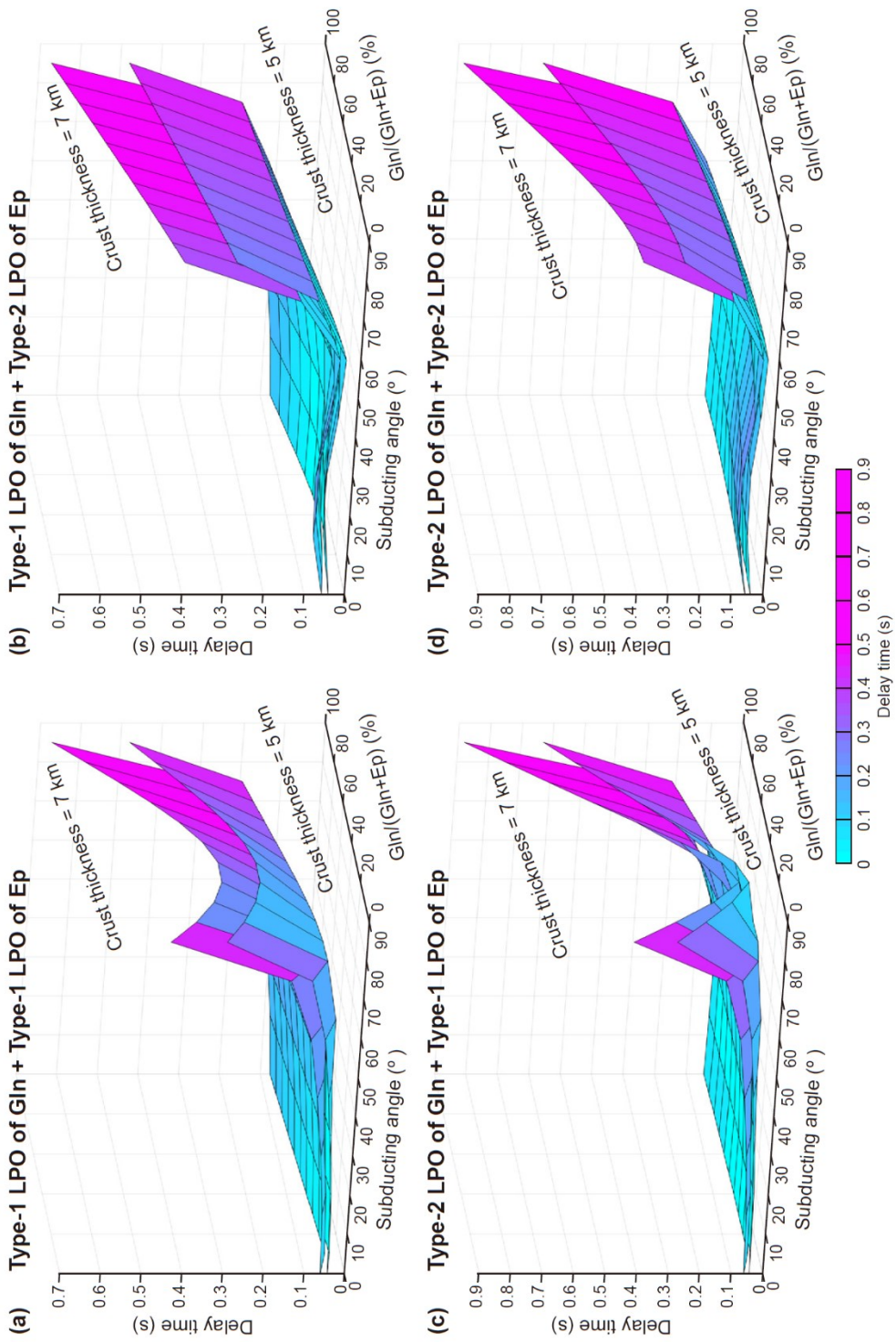


**Figure 4.15.** The delay time of oceanic crust composed of epidote blueschist calculated by different subducting angles of the slab and different volume proportions of two constituent minerals. **(a)** Glaucophane with type-1 LPO (JH98b) and epidote with type-1 LPO (JH98a); **(b)** glaucophane with type-1 LPO (JH98b) and epidote with type-2 LPO (JH94a); **(c)** glaucophane with type-2 LPO (JH94a) and epidote with type-1 LPO (JH98a); and **(d)** glaucophane with type-2 LPO (JH94a) and epidote with type-2 LPO (JH94a).

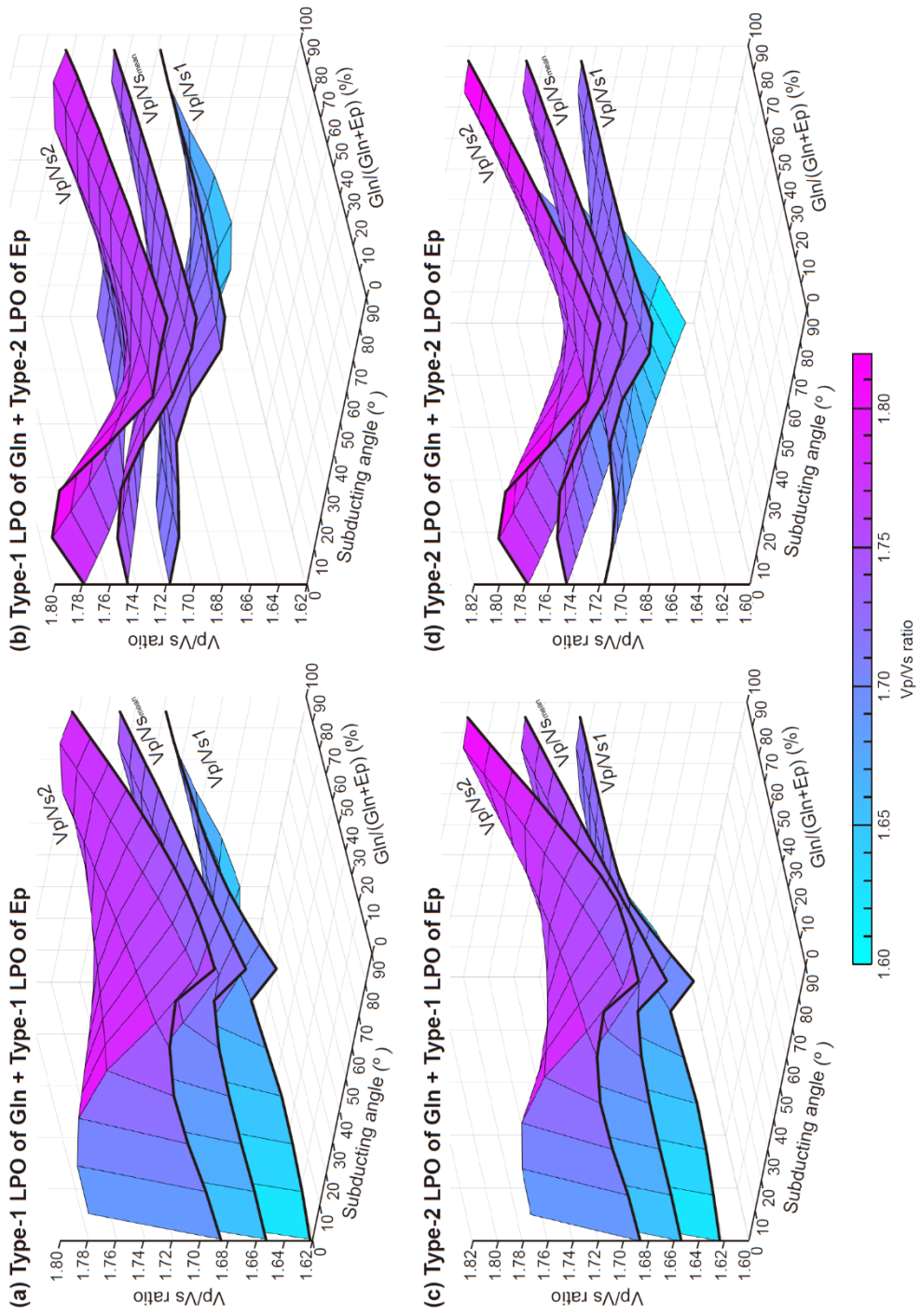


**Figure 4.16.** The  $V_p/V_{s1}$ ,  $V_p/V_{s2}$ , and  $V_p/V_{s_{\text{mean}}}$  ratios of oceanic crust composed of epidote blueschist calculated by different subducting angles of the slab and different volume proportions of two constituent minerals. **(a)** glaucophane with type-1 LPO (JH98b) and epidote with type-1 LPO (JH98a); **(b)** glaucophane with type-1 LPO (JH98b) and epidote with type-2 LPO (JH94a); **(c)** glaucophane with type-2 LPO (JH94a) and epidote with type-1 LPO (JH98a); and **(d)** glaucophane with type-2 LPO (JH94a) and epidote with type-2 LPO (JH94a). The  $V_{s_{\text{mean}}}$  is the averaged velocity of the fast S-wave velocity ( $V_{s1}$ ) and the slow S-wave velocity ( $V_{s2}$ ) at the direction normal to the horizontal plane.

#### **4.4.4. Implications for seismic properties in subduction zone**

##### *4.4.4.1. Low velocity layer (LVL) on top of the subducting slab*

The LVLs on top of the subducting slab (Abers, 2000; Abers et al., 2013) is widely observed in many subduction zones. The velocities in 1–7 km-thick LVLs for five subduction zones located in the boundary of Pacific plate were estimated 5–7 % lower than those of the background lithospheric mantle at depth of 100–250 km (Abers, 2000). It has been suggested that the source of the LVL originates from the hydrated oceanic crust atop of the subducting slabs composed mainly of the metastable blueschist-facies assemblage rocks (Abers, 2000; Abers et al., 2013; Hasegawa et al., 2007; Hirose et al., 2008; Kawakatsu and Watada, 2007; Tsuji et al., 2008). Their suggestions are likely to follow Birch's Law because the densities of minerals constituting the blueschist are lower than those of the minerals constituting the upper mantle (Birch, 1960; Mookherjee and Bezacier, 2012). Previous study had suggested that glaucophane in blueschist facies rock could account for ~17 % and ~7 % reductions of  $V_p$  and  $V_s$ , respectively, in the LVL compared to the surrounding mantle (Mookherjee and Bezacier, 2012). Another study had also suggested that naturally deformed epidote blueschist and foliated eclogite could reduce  $V_p$  by 3–12 % relative to the  $V_p$  of adjacent mantle (Cao et al., 2013). Furthermore, the LVL, which shifted to the mantle wedge above the slab at depth where the dehydration of blueschist facies minerals occurred, was considered a serpentine and/or chlorite layer, and the low velocity zone (LVZ) in the mantle wedge was considered to be due to

significant fluid release from hydrous metamorphic minerals (Hasegawa et al., 2007; Kawakatsu and Watada, 2007; Tsuji et al., 2008).

To compare seismic velocity between experimentally deformed epidote blueschist and the lithospheric mantle surrounding the slab, the seismic velocity of the surrounding lithospheric mantle,  $V_{p0}$  and  $V_{s0}$ , was calculated at  $P = 1.5$  GPa and  $T = 400$  °C by using the computational result ( $V_{p0} = 8.263$  km/s and  $V_{s0} = 4.749$  km/s; Connolly and Kerrick, 2002). The average seismic velocity of experimentally deformed epidote blueschists in this study was  $V_{p_{aver}} = 7.550\text{--}7.590$  km/s and  $V_{s_{aver}} = 4.398\text{--}4.478$  km/s. As a result,  $V_{p_{aver}}$  and  $V_{s_{aver}}$  of deformed epidote blueschist were lower in the range of  $\sim 8\text{--}9\%$  and  $\sim 6\text{--}7\%$ , respectively, compared to  $V_{p0}$  and  $V_{s0}$  (Fig. 4.17a). To confirm the seismic velocity reduction in other naturally deformed rocks, the  $V_{p_{aver}}$  and  $V_{s_{aver}}$  of rocks in previous studies were compared with the  $V_{p0}$  and  $V_{s0}$  (Fig. 4.17a). As a result of comparison,  $V_{p_{aver}}$  and  $V_{s_{aver}}$  of deformed eclogite were reduced when it contained hydrous minerals such as lawsonite and epidote, and  $V_{p_{aver}}$  and  $V_{s_{aver}}$  of naturally deformed blueschists and serpentinites were lower than those of eclogite (Fig. 4.17a). In addition, the average velocity of experimentally deformed epidote blueschists in this study was consistent with that of the mafic epidote blueschists naturally deformed in other studies ( $V_{p_{aver}} = 7.470\text{--}7.890$  km/s and  $V_{s_{aver}} = 4.320\text{--}4.600$  km/s in Bezacier et al., 2010a; Cao et al., 2013; Ha et al., 2018; Kim et al., 2013a). These results suggest that deformed epidote blueschist can contribute to the thin LVLs observed on top of the subducting slab in a warm subduction zone (Abers et al., 2013; Hirose et al., 2008), and deformed serpentinite can also contribute to the LVLs observed in the mantle wedge above the slab at deeper depth where blueschist facies minerals are unstable

(Hasegawa et al., 2007; Kawakatsu and Watada, 2007; Tsuji et al., 2008).

In addition, since constituent minerals of blueschist are elastically anisotropic and the seismic velocity is different depending on the direction of crystal axis through which seismic waves pass, LPOs of the minerals are considered to affect the velocity of the LVL. To understand the role of the subducting angle and LPO types of minerals to the seismic velocity of the subducting crust, the  $V_p$  and  $V_s$  of deformed epidote blueschist were calculated in the direction subnormal to the horizontal plane with different subducting angles (Fig. 4.17b). As a result, the  $V_p$  of the epidote blueschist was increased more than the  $V_s$  by increasing the subducting angle except for a sample deformed under low shear strain (Fig. 4.17b). The increase in  $V_p$  for sample JH94a (from 7.350 to 7.760 km/s) which consists of glaucophane showing the type-2 LPO and epidote showing the type-2 LPO is larger than the increase in  $V_p$  for sample JH98a (from 7.440 to 7.610 km/s) which consists of glaucophane showing the type-2 LPO and epidote showing the type-1 LPO (Fig. 4.17b). This result suggests that despite the decrease in  $V_p$  from the b-axis to the c-axis of epidote, the increase in  $V_p$  from the a-axis to the c-axis of glaucophane is greater than the increase in  $V_p$  from the a-axis to the b-axis of epidote.

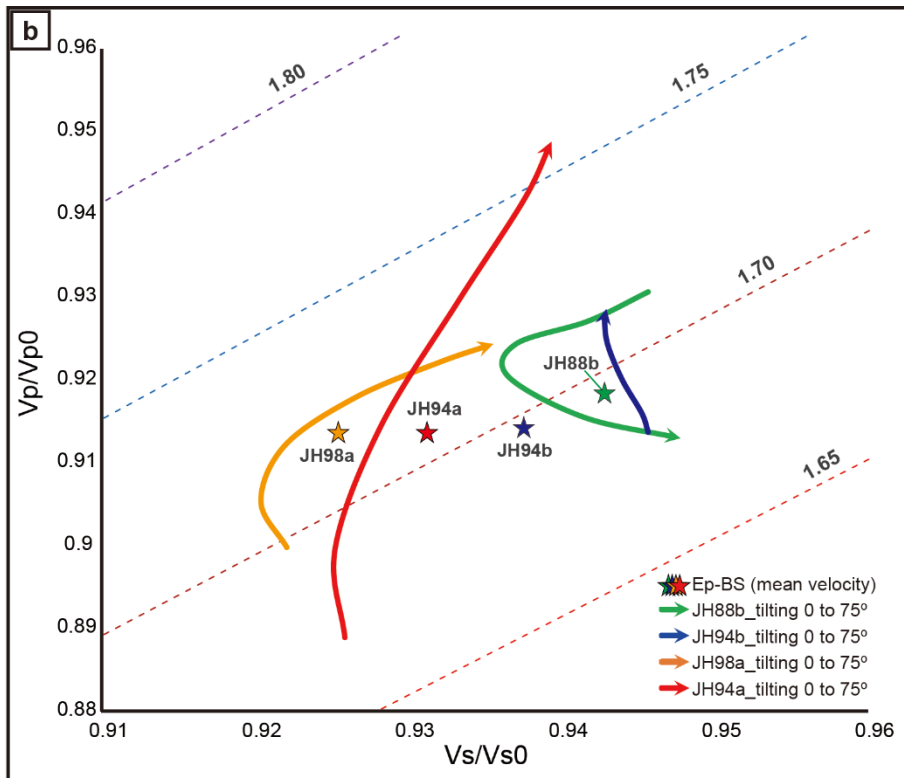
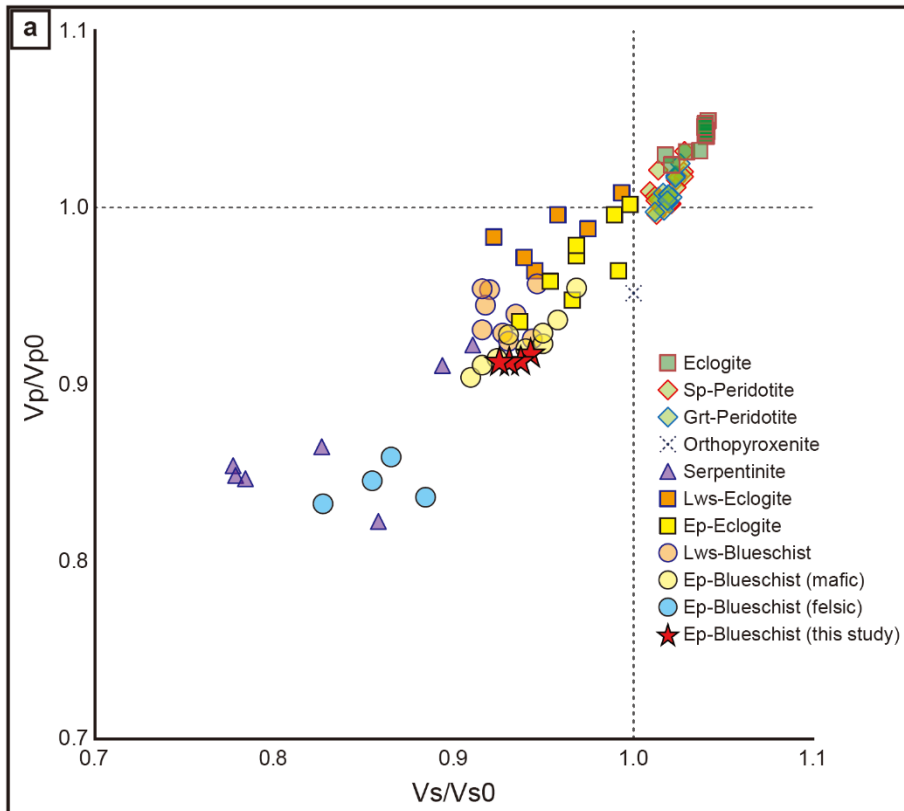


**Figure 4.17. (a)** The comparison between seismic velocity calculated for deformed rocks ( $V_p$  and  $V_s$ ) and those calculated for the lithospheric mantle surrounding the subducting slab ( $V_{p0}$  and  $V_{s0}$ ; Connolly and Kerrick, 2002). Green squares: eclogite (Bascou et al., 2001; 2011; Kim et al., 2018); green lozenges with red line: spinel peridotite (Bascou et al., 2011; Park and Jung, 2015); green lozenges with blue line: garnet peridotite (Bascou et al., 2011); dotted cross: orthopyroxenite (Bascou et al., 2011); purple triangles: serpentinite (Bezacier et al., 2010b; Jung, 2011; Watanabe et al., 2014); orange squares: lawsonite eclogite (Cao and Jung, 2016); yellow squares: epidote eclogite (Bezacier et al., 2010a; Cao et al., 2013; Ha et al., 2018); orange circles: lawsonite blueschist (Cao and Jung, 2016; Cao et al., 2014; Kim et al., 2013a); yellow circles: mafic epidote blueschist (Bezacier et al., 2010a; Cao et al., 2013; Ha et al., 2018; Kim et al., 2013a); blue circles: felsic epidote blueschist (Cao et al., 2013; Ha et al., 2018); and red stars: experimentally deformed epidote blueschist in this study. **(b)** The comparison between seismic velocity calculated for experimentally deformed epidote blueschist in the direction normal to the horizontal plane with different subducting angle ( $V_p$  and  $V_s$ ) and those calculated for the lithospheric mantle surrounding the subducting slab ( $V_{p0}$  and  $V_{s0}$ ).

#### 4.4.4.2. *Seismic anisotropy of fast shear wave in the forearc region*

Seismic anisotropy of fast shear wave in the forearc region of subduction zones has mostly been observed as the trench-parallel Vs1 polarization direction (Long and Becker, 2010; Long and Silver, 2008). As mentioned above in Chapter 4.1, several causes for trench-parallel Vs1 polarization direction were suggested such as 3-D mantle flow (Long and Silver, 2008), LPO of olivine in the mantle wedge (Jung and Karato, 2001b; Karato et al., 2008; Kneller et al., 2005; Nakajima and Hasegawa, 2004) and in the deep upper mantle (Jung et al., 2009b; Lee and Jung, 2015; Ohuchi et al., 2011), and hydration of sub-vertical fault zones (Faccenda et al., 2008) and fluid-filled cracks in subducting oceanic slabs (Healy et al., 2009). However, some exceptional regions showed the trench-normal Vs1 polarization direction (e.g., Abt et al., 2009; Christensen and Abers, 2010; Levin et al., 2004). Although the arc-parallel mantle flow was suggested as a cause of this trench-normal Vs1 polarization direction (Abt et al., 2009), the cause of this phenomenon is still controversial. Because the seismic anisotropy of SKS wave is measured by integrating path through multiple anisotropic layers, the LPO of elastically anisotropic minerals in the subducting oceanic crust (i.e., glaucophane, epidote, lawsonite and phengite) and in the slab-mantle interphase (i.e., serpentine, talc, chlorite, and chloritoid) can influence these exceptional cases. Previous studies suggested that serpentine (Jung, 2011) and chlorite (Kim and Jung, 2015) can contribute to the trench-normal Vs1 polarization direction in the forearc region of the subduction zone with low subducting angle ( $\theta < 60^\circ$ ) and to the trench-parallel Vs1 polarization direction in the

forearc region of the subduction zone with high subducting angle ( $\theta \geq 60^\circ$ ). In addition, other previous studies suggested that chloritoid (Lee et al., 2021) and glaucophane showing type-2 LPO (Cao et al., 2013) can also contribute to the trench-normal Vs1 polarization direction in the forearc region of the subduction zone with low subducting angle ( $\theta < 45^\circ$ ) and to the trench-parallel Vs1 polarization direction in the forearc region of the subduction zone with high subducting angle ( $\theta \geq 45^\circ$ ). In contrast, lawsonite (Choi et al., 2021; Lee et al., 2021) showed opposite trend that the trench-parallel Vs1 polarization direction could occur in the forearc region of the subduction zone with low subducting angle ( $\theta < 45^\circ$ ) and the trench-normal Vs1 polarization direction could occur in the forearc region of the subduction zone with high subducting angle ( $\theta \geq 45^\circ$ ). On the other hand, talc (Lee et al., 2020) and phengite (Lee et al., 2021) can contribute to the trench-parallel Vs1 polarization direction in the forearc region of the subduction zone regardless of the subducting angle.

The seismic anisotropy of deformed epidote blueschist in this study suggests that the trench-normal Vs1 polarization direction could be generated by the type-1 glaucophane LPO in the oceanic crust regardless of the subducting angle (Fig. 4.18a). If the 7 km-thick oceanic crust consists of the type-1 LPO of glaucophane with low subducting angle ( $\theta \leq 30^\circ$ ), a subducting crust can yield delay time ( $\delta t$ ) of  $\delta t = \sim 0.09$ – $0.10$  s in the forearc region of the subduction zone. These characteristics suggest that if the glaucophane with the type-1 LPO dominantly constitutes the subducting oceanic crust, the crust is likely to somewhat contribute to the trench-normal Vs1 polarization direction and  $\sim 14$ – $32$  % of delay time in the forearc region of the subduction zone with low subducting angle ( $\theta \leq 30^\circ$ ), such as the central Alaska

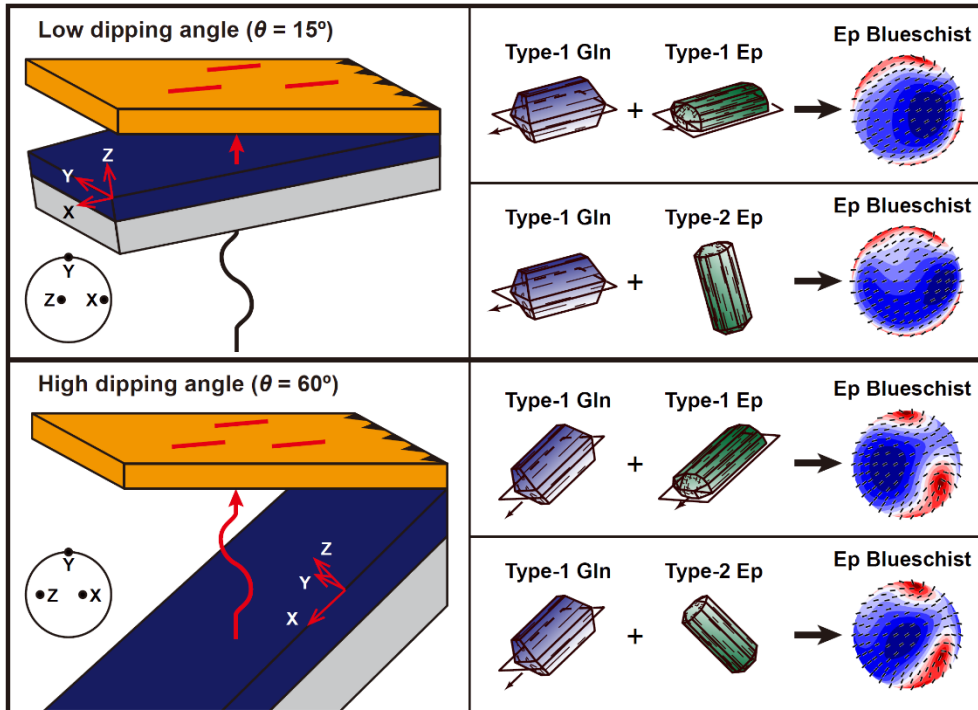
( $\theta = 25^\circ$ ,  $\delta t = \sim 0.8\text{--}1.7$  s in central Alaska; Christensen and Abers, 2010). However, this delay time can be decreased up to  $\sim 55\%$  when the crust consists of 10 % the type-1 glaucophane LPO and 90 % the type-1 epidote LPO (Fig. 4.15a) or decreased up to  $\sim 30\%$  when the crust consists of 50 % the type-1 glaucophane LPO and 50 % the type-2 epidote LPO (Fig. 4.15b). If the 7 km-thick oceanic crust consists of the type-1 glaucophane LPO with high subducting angle ( $\theta \geq 45^\circ$ ), the subducting crust can yield delay time of  $\delta t = \sim 0.13\text{--}0.27$  s in the forearc region of the subduction zone. When this assumption is applied to the subduction zone with high subducting angle ( $\theta \geq 45^\circ$ ), the subducting crust can contribute to the trench-normal Vs1 polarization direction and  $\sim 22\text{--}56\%$  of delay time in the forearc region of the following areas: the South Sandwich trench ( $\theta = 53^\circ$ ,  $\delta t = \sim 0.4$  s in eastern Scotia plate; Müller, 2001), the Kamchatka subduction zone ( $\theta = 55\text{--}60^\circ$ ,  $\delta t = \sim 0.4$  s in Kamchatka; Levin et al., 2004), and the Nicaragua subduction zone ( $\theta = 55^\circ$ ,  $\delta t = \sim 0.3$  s in Nicaragua; Abt et al., 2009). However, these delay times can be decreased up to  $\sim 40\%$  when the crust consists of 30 % the type-1 glaucophane LPO and 70 % the type-1 epidote LPO (Fig. 4.15a) or decreased up to  $\sim 30\%$  as increasing the volume proportion of the type-2 epidote LPO (Fig. 4.15b). The Vs1 polarization direction derived from the type-1 glaucophane LPO is the same as the direction derived from the type-1 epidote LPO. Therefore, when the subducting crust consists of glaucophane showing the type-1 LPO and epidote showing the type-1 LPO, the trench-normal Vs1 polarization direction does not change to the trench-parallel direction (Fig. 4.19). In contrast, the Vs1 polarization direction derived from the type-1 LPO of glaucophane and the type-2 LPO of epidote have a counteracting relationship at low subducting angle. When the subducting crust consists of glaucophane showing the type-1 LPO and epidote showing the type-2 LPO, however, this trench-normal Vs1 polarization direction

does not change to the trench-parallel direction up to the epidote volume ratio of 80 % (Fig. 4.20). These results suggest that type-1 glaucophane LPO may contribute more than LPOs of epidote to the seismic anisotropy in the subduction zone.

The epidote blueschist containing type-2 LPO of glaucophane is also able to induce the trench-normal Vs1 polarization direction in the forearc region of the subduction zone with low subducting angle ( $\theta = 15^\circ$ ; Fig. 4.18b). If 7 km-thick oceanic crust consists of type-2 glaucophane LPO with low subducting angle ( $\theta \leq 30^\circ$ ), the subducting slab can yield delay time of  $\delta t = \sim 0.04$  s in the forearc region of the subduction zone. However, the delay time can be increased up to  $\sim 200$  % ( $\delta t = \sim 0.07\text{--}0.08$  s) with increasing the volume proportion of type-1 epidote LPO (Fig. 4.15c). The delay time can be also increased up to  $\sim 225$  % ( $\delta t = \sim 0.09$  s) with increasing the volume proportion of type-2 epidote LPO (Fig. 4.15d). These results suggest that LPOs of epidote may contribute more than type-2 glaucophane LPO to seismic anisotropy in the subduction zone with low subducting angle ( $\theta \leq 30^\circ$ ). In the subduction zone with high subducting angle ( $\theta \geq 45^\circ$ ), the type-2 glaucophane LPO is considered to induce the trench-parallel Vs1 polarization direction in the forearc region (Fig. 4.18b). When the 7 km-thick oceanic crust consists of type-2 glaucophane LPO with high subducting angle ( $\theta \geq 45^\circ$ ), the subducting slab can yield delay time in the range of  $\delta t = \sim 0.06\text{--}0.30$  s in the forearc region. These results are consistent with the previous suggestion that type-2 glaucophane LPO can contribute to the  $\sim 0.1\text{--}0.3$  s of delay time and the trench-parallel seismic anisotropy in the subduction zone with high subducting angle ( $\theta > 45\text{--}60^\circ$ ) (Cao and Jung, 2016; Cao et al., 2013; 2014; Kim et al., 2013a; Kim et al., 2016). These characteristics suggest that the type-2 LPO of glaucophane existing in the oceanic crust with high

subducting angle is possible to contribute to the trench-parallel Vs1 polarization direction and  $\sim 2\text{--}21\%$  of delay times observed in the Ryukyu arc ( $\theta = 45^\circ$ ,  $\delta t = \sim 0.75\text{--}1.25$  s in Ryukyu; Long and van der Hilst, 2006) and in the SW Hikurangi subduction zone ( $\theta = 58\text{--}60^\circ$ ,  $\delta t = \sim 0.8\text{--}4.5$  s in Hikurangi; Greve et al., 2008). However, the delay time may be decreased up to  $\sim 30\%$  when the crust consists of 30 % of the type-2 glaucophane LPO and 70 % of the type-1 epidote LPO (Fig. 4.15c) or decreased up to  $\sim 50\%$  as increasing the volume proportion of the type-2 epidote LPO (Fig. 4.15d). The Vs1 polarization direction derived from the type-2 glaucophane LPO is similar with the direction derived from the type-1 epidote LPO at the low subducting angle. Therefore, when the subducting crust consists of glaucophane showing the type-2 LPO and epidote showing the type-1 LPO, the trench-normal Vs1 polarization direction does not change to the trench-parallel direction (Fig. 4.21). However, at the high subducting angle, the Vs1 polarization direction changes from trench-parallel to trench-normal when the volume proportion of type-1 epidote LPO is more than 80 % (Fig. 4.21). In contrast, the Vs1 polarization direction derived from the type-2 glaucophane LPO and the type-2 epidote LPO have a counteracting relationship. If the subducting crust consists of glaucophane showing the type-2 LPO and epidote showing the type-2 LPO, the Vs1 polarization direction is changed to the opposite direction when the volume proportion of type-2 epidote LPO is more than 50 % (Fig. 4.22). These results suggest that S-wave seismic anisotropy induced by the LPOs of epidote can offset the seismic anisotropy induced by the type-2 glaucophane LPO.

(a) Epidote blueschist with type-1 LPO of glaucophane in subducting slab



(b) Epidote blueschist with type-2 LPO of glaucophane in subducting slab

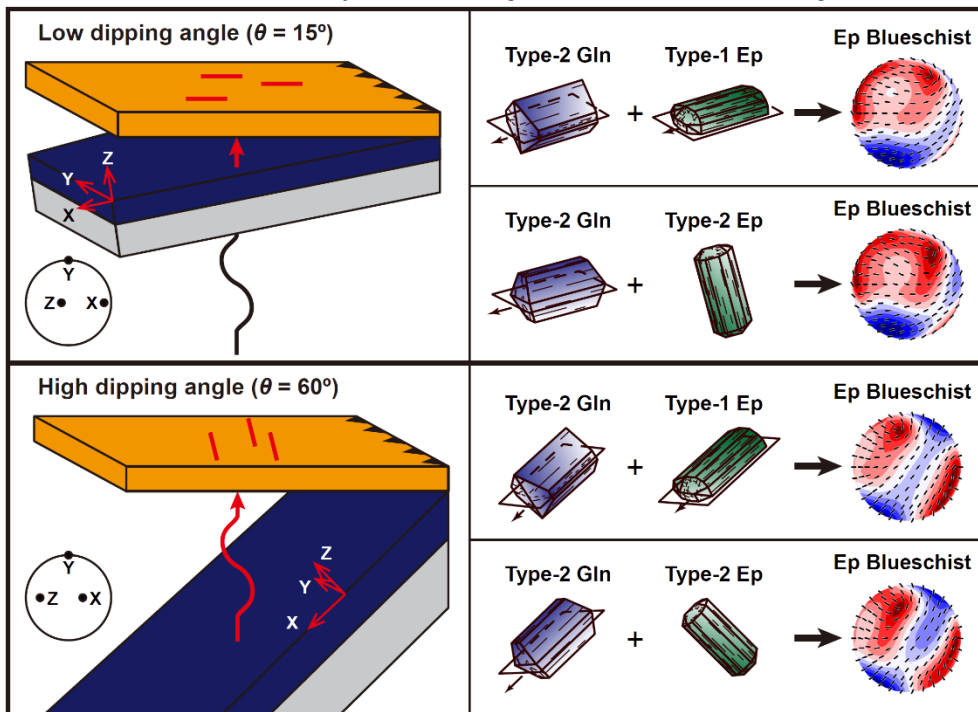


**Figure 4.18.** Schematic diagrams for the fast shear wave ( $V_{s1}$ ) polarization direction in the forearc region of the subduction zone induced by the subducting oceanic crust composed mainly of epidote blueschist. **(a)** Epidote blueschist with type-1 LPO of glaucophane. **(b)** Epidote blueschist with type-2 LPO of glaucophane. X: shear direction (subducting direction of the slab), Z: the direction normal to the shear plane (direction normal to the interface between mantle wedge and subducting slab), and Y: the direction normal to the shear direction within the shear plane (direction normal to the subducting direction within the interface between mantle wedge and subducting slab).

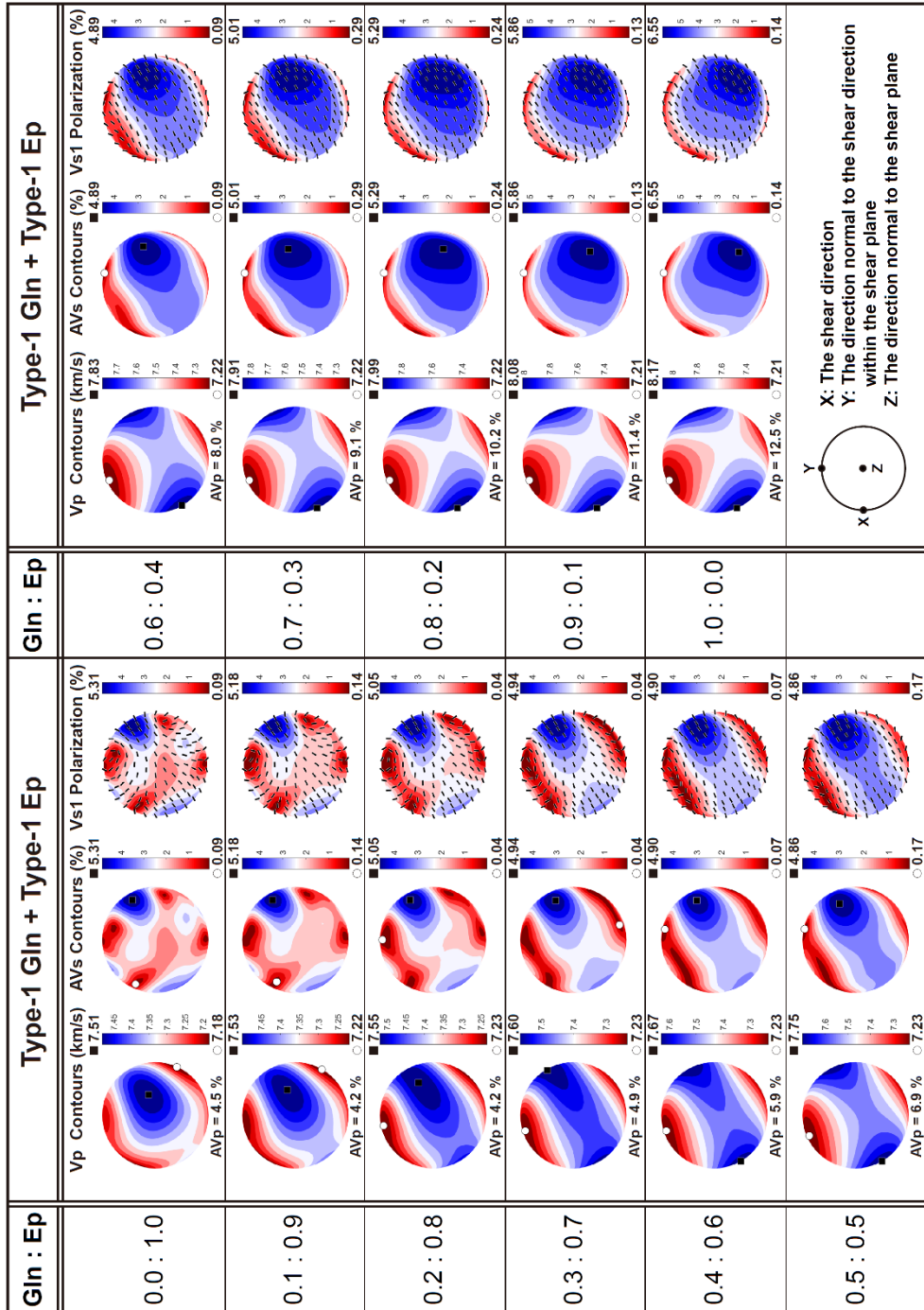


**Figure 4.19.** Seismic velocity and anisotropy of epidote blueschist (whole rock) composed of glaucophane showing the type-1 LPO and epidote showing the type-1 LPO by different volume ratios. The E-W direction corresponds to the shear direction (X), and the center of a stereographic projection circle is the direction normal to the shear plane (Z). The contours of P-wave velocity ( $V_p$ ), the contours of S-wave polarization anisotropy (AVs), and polarization directions of the fast shear wave ( $V_{s1}$ ) are shown.

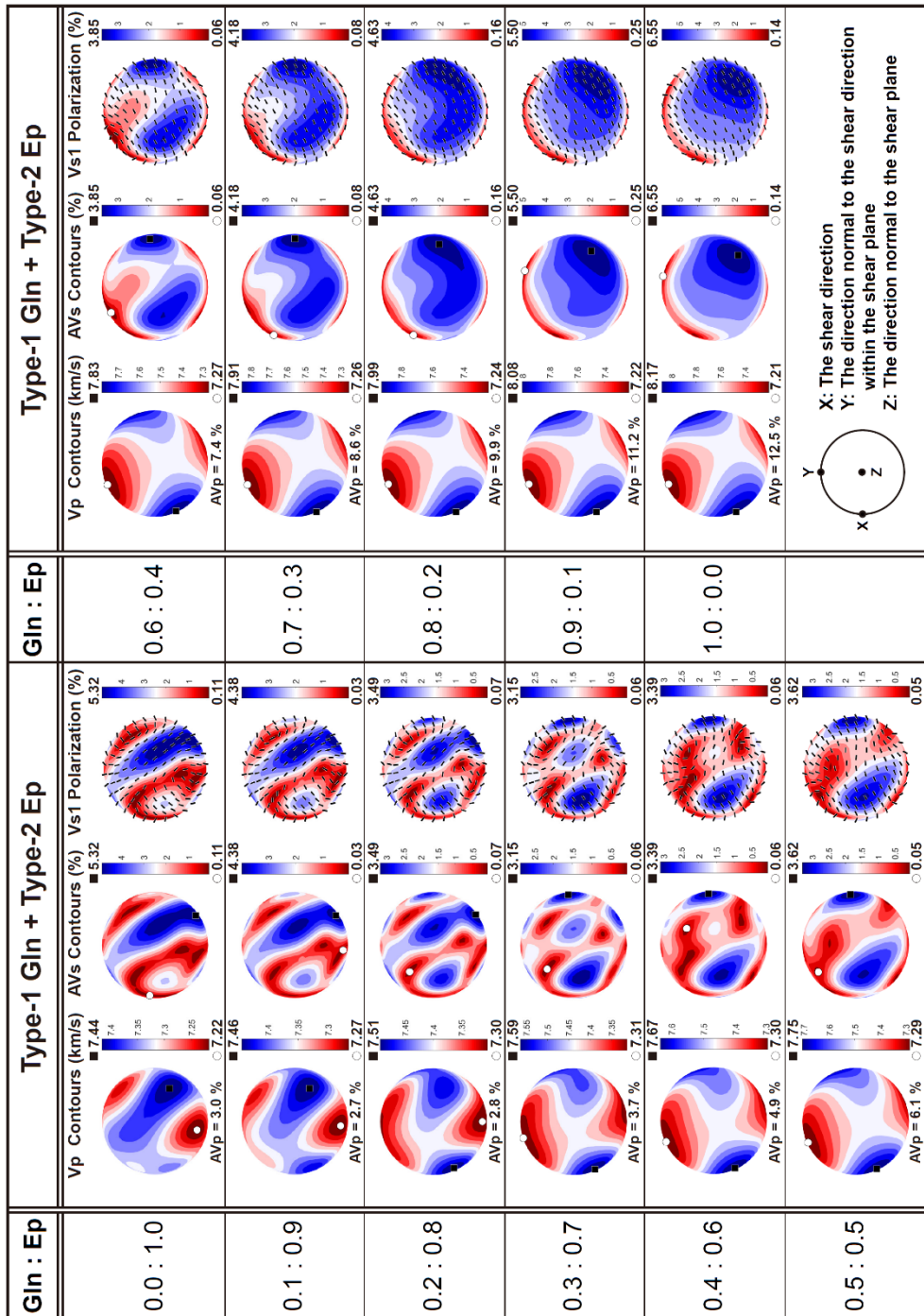


**Figure 4.20.** Seismic velocity and anisotropy of epidote blueschist (whole rock) composed of glaucophane showing the type-1 LPO and epidote showing the type-2 LPO by different volume ratios. The E-W direction corresponds to the shear direction (X), and the center of a stereographic projection circle is the direction normal to the shear plane (Z). The contours of P-wave velocity ( $V_p$ ), the contours of S-wave polarization anisotropy (AVs), and polarization directions of the fast shear wave ( $V_{s1}$ ) are shown.

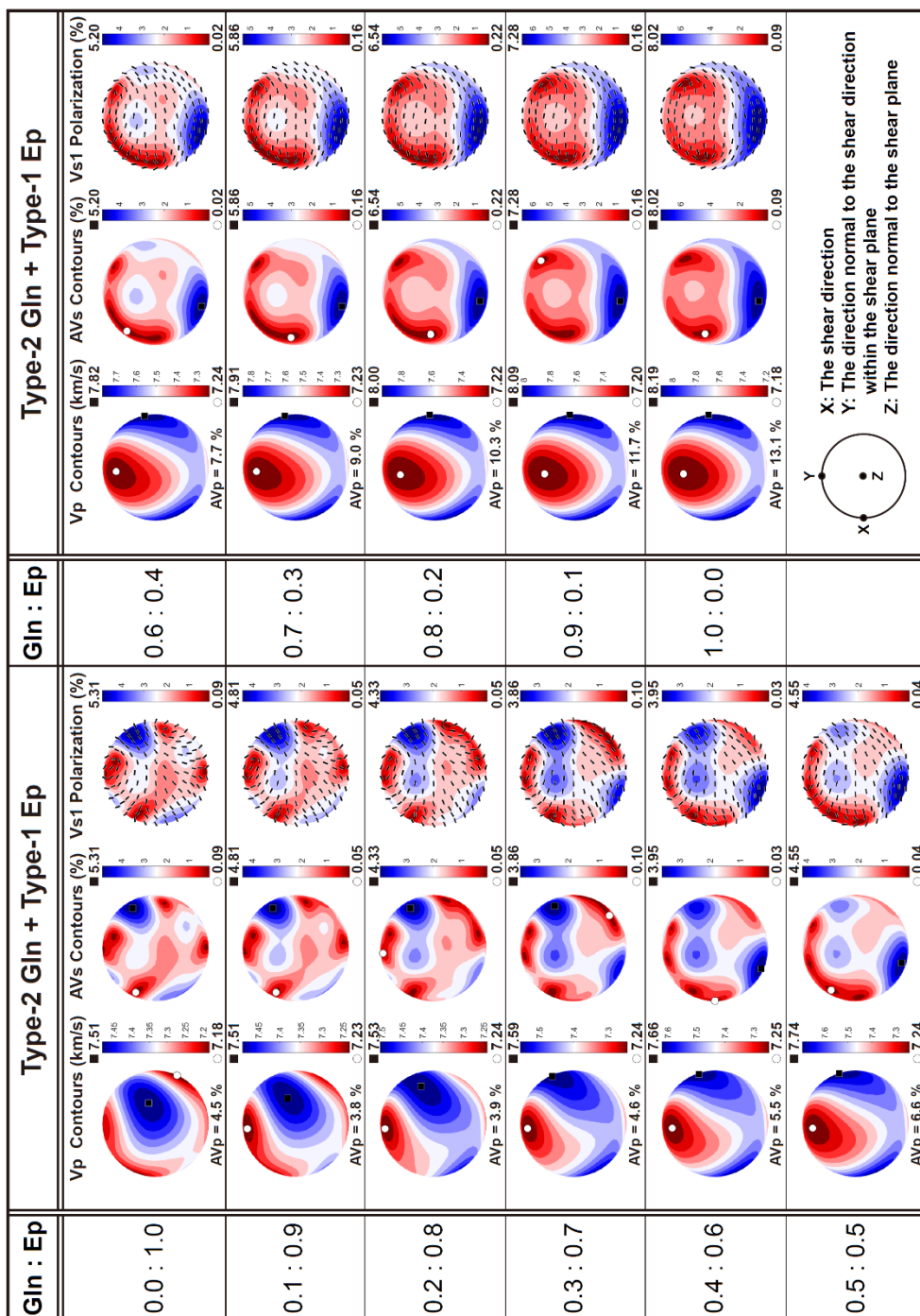


**Figure 4.21.** Seismic velocity and anisotropy of epidote blueschist (whole rock) composed of glaucophane showing the type-2 LPO and epidote showing the type-1 LPO by different volume ratios. The E-W direction corresponds to the shear direction (X), and the center of a stereographic projection circle is the direction normal to the shear plane (Z). The contours of P-wave velocity ( $V_p$ ), the contours of S-wave polarization anisotropy (AVs), and polarization directions of the fast shear wave ( $V_{s1}$ ) are shown.

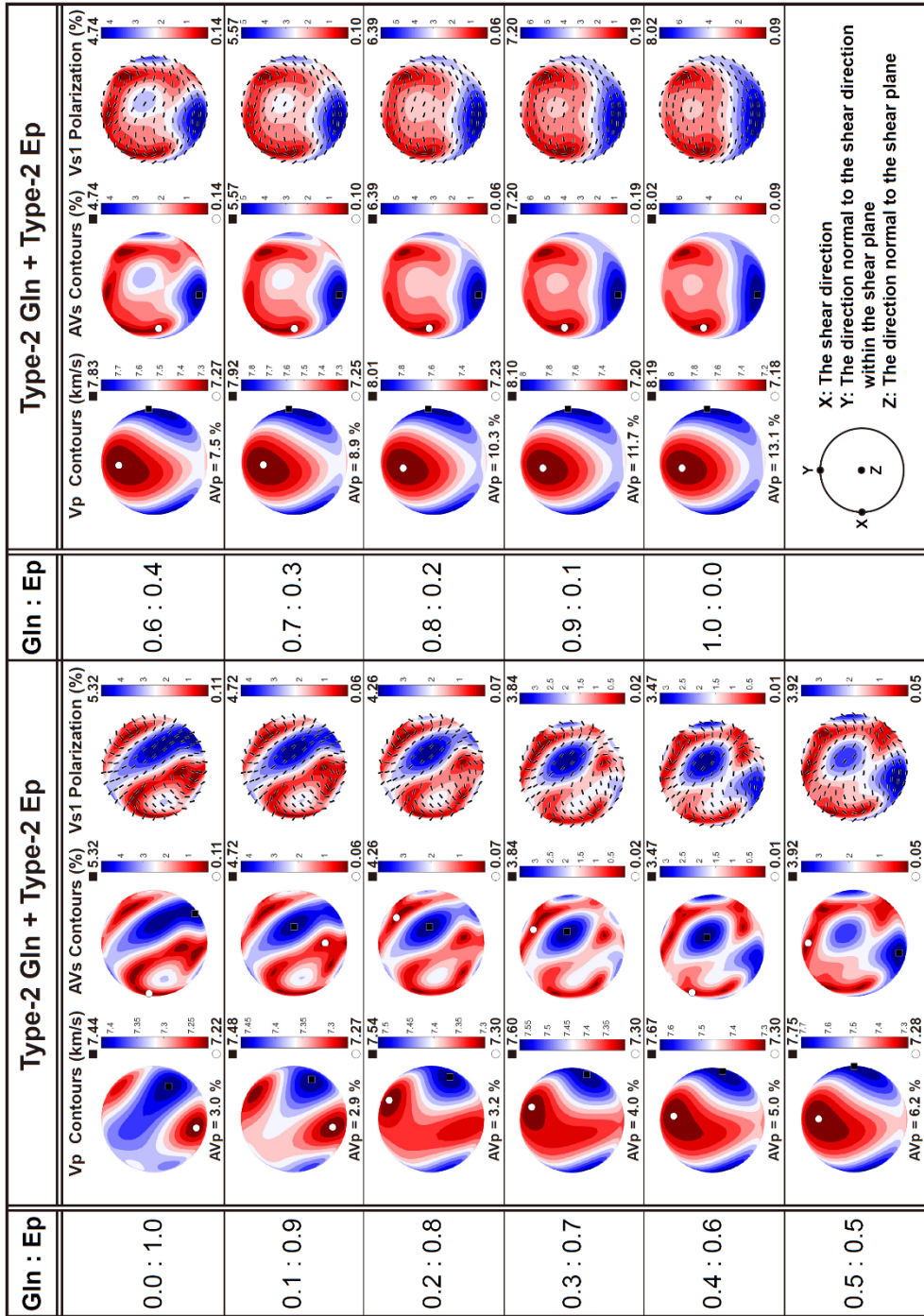


**Figure 4.22.** Seismic velocity and anisotropy of epidote blueschist (whole rock) composed of glaucophane showing the type-2 LPO and epidote showing the type-2 LPO by different volume ratios. The E-W direction corresponds to the shear direction (X), and the center of a stereographic projection circle is the direction normal to the shear plane (Z). The contours of P-wave velocity ( $V_p$ ), the contours of S-wave polarization anisotropy (AVs), and polarization directions of the fast shear wave ( $V_{s1}$ ) are shown.

## 4.5. Conclusion

Seismic velocity and anisotropy of the glaucophane and epidote in experimentally deformed epidote blueschist were calculated to understand the seismic properties of the subducting slab. The seismic velocity and anisotropy of epidote blueschist is affected by the magnitude of shear strain and fabric strength of deformed minerals. In addition, the volume proportion and LPO types of glaucophane and epidote, and the subducting angle of the slab can influence the delay time of S-wave and  $V_p/V_s$  ratio observed in the subduction zone. The seismic P- and S-wave velocity calculated from experimentally deformed epidote blueschist were reduced about 8–9 % and 6–7 %, respectively, compared to the seismic velocity of the lithospheric mantle surrounding the subducting slab. This result indicates that deformed epidote blueschist can contribute to the seismic low velocity layer observed on the top of the subducting slab. The trench-normal seismic anisotropy in the forearc region of the subduction zone can be attributed to the type-1 LPO of glaucophane and type-1 LPO of epidote, regardless of the subducting angle of the slab. The type-2 LPO of epidote can contribute to the trench-parallel seismic anisotropy in the forearc region of the subduction zone when the volume proportion of epidote exceeds 50 % in the oceanic crust with low subducting angle. This trench-parallel seismic anisotropy can be attributed to the type-2 LPO of glaucophane in the forearc region of the subduction zone when the volume proportion of glaucophane is more than 50 % in the oceanic crust with high subducting angle. Although the LPO of glaucophane contributes to the  $V_s1$  polarization direction more than the LPO of

epidote, the delay time in subduction zone is likely to be affected by the volume proportion of epidote more than that of glaucophane. These results suggest that seismic anisotropy of S-wave induced by the LPOs of epidote can offset the seismic anisotropy induced by the type-2 glaucophane LPO.

## **CHAPTER 5**

**Deformation microstructures of epidote blueschist from Río San Juan metamorphic complex, Dominican Republic, and implications for seismic anisotropy in the northeastern margin of the Caribbean plate**

## Abstract

To understand deformation mechanisms and LPO developments of minerals in the subducted oceanic crust and seismic anisotropy observed in the northeastern margin of the Caribbean plate, deformation microstructures of naturally deformed epidote blueschists (high pressure metabasites) from Río San Juan metamorphic complex in Dominican Republic were studied. LPOs of minerals were determined using the electron backscattered diffraction (EBSD) technique, and intracrystalline deformation microstructures were observed by high-resolution EBSD mapping. The LPOs of amphiboles mostly showed that the [001] axes were aligned subparallel to the lineation and the [100] axes were aligned subnormal to the foliation. The LPOs of zoisites showed that the [010] axes were aligned parallel to the lineation and both [100] and [001] axes were distributed in a weak girdle shape perpendicular to the lineation with clusters aligned normal to the foliation. The LPOs of epidotes mostly showed that the (010) poles were aligned subparallel to the lineation with girdle distribution parallel to the foliation and the [100] axes and/or [001] axes were aligned subnormal to the foliation. The misorientation line less than  $1^\circ$  along the chemical composition boundary between sodic to sodic-calcic amphibole in a single grain suggests that the transition of the chemical composition can moderately affect the tilting of the crystal lattice. However, the dominant misorientation lines, independent of the chemical transition boundary, suggest that the main mechanism of the LPO development of amphibole is likely to be a deformation in dislocation creep. The high density of subgrain boundaries and high orientation deviation angles in zoisite

porphyroclast suggest that they were deformed by dislocation creep and developed LPO with strong fabric strength. The small amount of misorientation lines, weak fabric strength, and low grain orientation spread values of epidote aggregates which are regarded as the lawsonite pseudomorph suggest that LPO of epidote in aggregates might not be developed by recrystallization of epidote porphyroclast in dislocation creep but developed by the metamorphic transition from lawsonite to epidote following the pre-existing subgrain boundary of the lawsonite porphyroclast. The average P- and S-wave velocity of whole rock samples were in the range of 7.17–7.69 km/s and 4.13–4.48 km/s, respectively, and the anisotropy of P-wave and maximum anisotropy of S-wave were in the range of 8.1–18.2 % and 5.27–11.41 %, respectively. Considering the transition of tectonic setting from subduction to oblique underthrust and/or lateral shear, the delay time of the oceanic crust can contribute 0.09–0.18 s to the delay time of the study area when the 7 km thick oceanic crust underthrust tilted  $\sim 20^\circ$  beneath the Caribbean plate is deformed in lateral shear by strike-slip Septentrional Fault Zone. When the break-off subducted slab exists beneath the study area and is deformed in lateral shear by sub-slab mantle flow and/or strike-slip fault, the thickness of the anisotropic layer composed of blueschist-facies metamorphic rocks is required to be  $\sim 55$ – $108$  km to derive the delay time of  $\sim 1.3$  s observed in the study area. These results suggest that the subducted oceanic crust metamorphosed in blueschist-facies condition can highly contribute to the seismic anisotropy of the northeastern margin of the Caribbean plate depending on the LPO of the constituent minerals.

## 5.1. Introduction

Blueschist-facies rocks metamorphosed under high-pressure/low-temperature (HP/LT) conditions are dominantly distributed in the subduction zone. As they have undergone a subduction to mantle depth and exhumed to the crustal surface, these rocks provide various information about the processes of paleo-subduction zones in space and time. As a result, the thermal, mechanical, microstructural, geochronological, and petrological studies of blueschist and eclogite facies rocks have been conducted to demonstrate the evolution of subducting processes. The HP/LT rocks exhumed in the Río San Juan metamorphic complex of Dominican Republic are dominated in highly sheared serpentinite bodies that contain the metabasite blocks. The protoliths of the serpentinite mélanges are considered as abyssal peridotites of oceanic lithosphere and/or hydrated mantle wedge (Krebs et al., 2008; 2011; Escuder-Viruete et al., 2011). The mechanisms for the initiation of the tectonic evolution in this area have been debated between two suggested models: one is for a subduction of the Pacific plate beneath the Caribbean plate, and the other is for an originally beginning between the North and South American plates (Krebs et al., 2011). In addition, the Caribbean plate is relatively young (~160 Ma), and age of exhumation is also recent (~70 Ma). Therefore, many studies were conducted to reveal the mechanism for an initiation of subduction and an exhumation of HP/LT and/or ultramafic rocks (Abbott Jr. et al., 2006; Draper et al., 1991; Escuder-Viruete et al., 2011; 2013b; Hattori et al., 2010; Krebs et al., 2008; 2011). However, after the Middle Miocene, the tectonic setting of the northeastern margin of the Caribbean

plate have been changed to the oblique collision domain within the transpressive tectonic regime (Mann et al., 1995; 2002). Recently, the tectonic setting in this region has been more clearly redefined through the geometric and kinematic investigations of Neotectonic geological structures (Escuder-Viruete and Pérez, 2020), as well as analysis of the 3D seismicity distribution, focal mechanisms, and geodetic data (Rodríguez-Zurrunero et al., 2020).

In the northeastern Caribbean plate, strong trench-parallel seismic anisotropy with long delay time ( $\delta t = 0.5\text{--}2.0$  s) was observed following the forearc region in subduction zone (Hodges and Miller, 2015; Lynner and Long, 2013; Meighan and Pulliam, 2013; Possee et al., 2020). They hypothesized the trench-parallel flow of sub-slab mantle in North American plate which was inhibited by thick South American plate, and suggested this sub-slab mantle flow as the source of strong trench-parallel  $V_{s1}$  polarization direction from Lesser Antilles to Hispaniola (Hodges and Miller, 2015; Lynner and Long, 2013; Meighan and Pulliam, 2013; Possee et al., 2020). Meighan and Pulliam (2013) suggested the slab tear or gap near the British Virgin Island can cause the relatively small trench-normal  $V_{s1}$  polarization direction, and Possee *et al.* (2020) suggested multiple anisotropic structures that can be source of seismic anisotropy beneath Hispaniola at Haiti regions. Although the data is relatively less, the trench-parallel  $V_{s1}$  polarization direction with delay time of  $\delta t = 1.36 \pm 0.35$  s was also reported beside the Río San Juan complex, Dominican Republic (Meighan and Pulliam, 2013). The seismic anisotropy in this area is also likely to be caused by trench-parallel sub-slab mantle flow as previously suggested, but the existence of an older subducted North American oceanic slab has been raised beneath the Hispaniola (Corbeau et al., 2019;

Núñez et al., 2019; Rodríguez-Zurrunero et al., 2020). There is also a left-lateral strike-slip fault zone which is almost parallel to the trench across the northern Hispaniola (Escuder-Viruete and Pérez, 2020). As a result, these tectonic-scale geological structures are likely to influence the Vs1 polarization direction in this region.

In this chapter, deformation microstructures and seismic properties of epidote blueschist-facies rock from Río San Juan metamorphic complex, in Dominican Republic were studied to understand deformation mechanisms and LPO development of constituent minerals, and their contribution to the strong trench-parallel seismic anisotropy in the northeastern margin of the Caribbean plate.

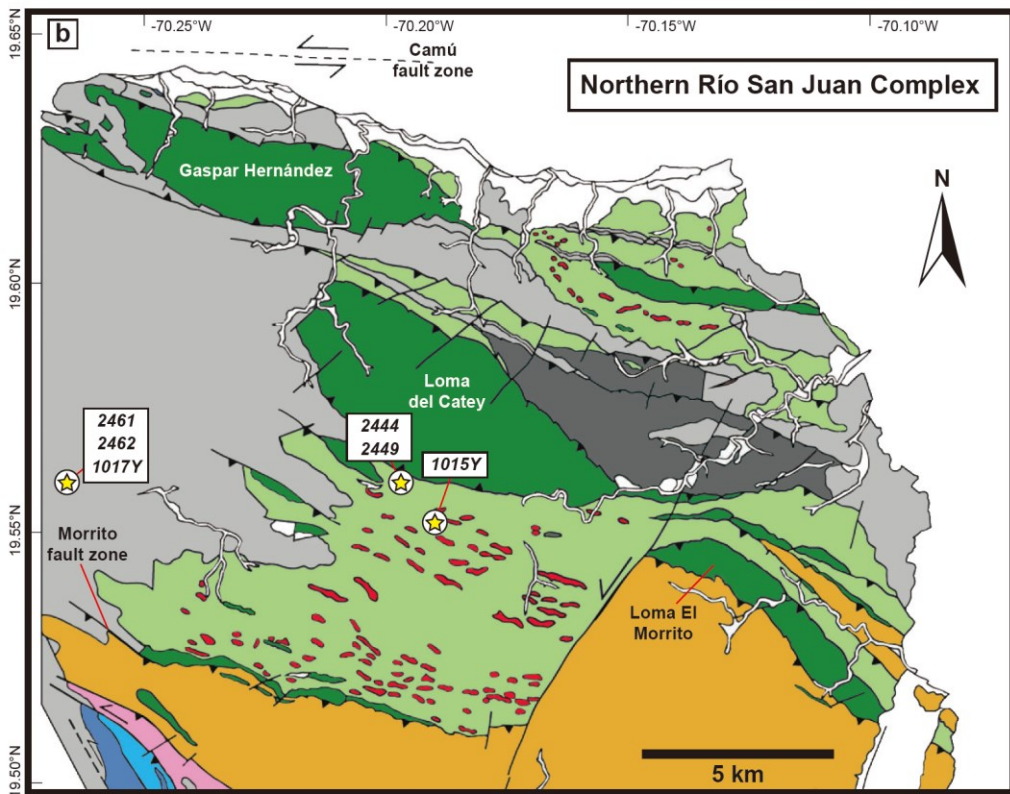
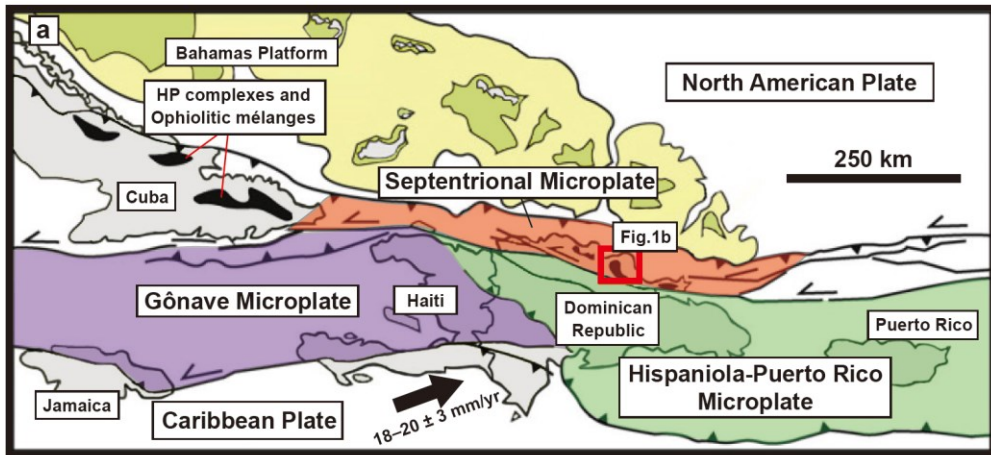
## 5.2. Geological background

Río San Juan metamorphic complex is located on the northeastern margin of the Caribbean plate (Fig. 5.1). This complex was produced by the oblique convergence to collision with North American plate (Draper et al., 1994; Escuder-Viruete and Pérez-Estaún, 2013). The complex is distinguished into three parts with increasing metamorphic grade from northern to southern areas (Draper et al., 1991; Escuder-Viruete, 2009; Escuder-Viruete and Pérez-Estaún, 2013). The Gaspar Hernández serpentinites, the northern part of Río San Juan complex, was considered to have been metamorphosed under the greenschist- to lower amphibolite-facies, and Jagua Clara mélangé was metamorphosed under mafic blueschist- to eclogite-facies followed by retrograde blueschist- to greenschist-facies metamorphism. Cuaba mafic-ultramafic unit, the southern part of the complex, is composed of the amphibolite- to retrograded eclogite-facies metamorphic rocks and mafic gneisses (Escuder-Viruete and Pérez-Estaún, 2013; Abbott Jr. et al., 2006; Hattori et al., 2010; Krebs et al., 2008; 2011).

The protolith of eclogite in Jagua Clara mélangé was known as high-P metabasites originated from the N-MORB (Escuder-Viruete et al., 2011). The age of protolith was reported as  $139.1 \pm 3.6$  Ma from U-Pb isotope dating of zircon in eclogite (Krebs et al., 2008; 2011),  $136.4 \pm 0.3$  Ma from U-Pb isotope dating of zircon in Cpx-Pl gabbro (Escuder-Viruete et al., 2011), and  $117.1 \pm 0.9$  Ma to  $113.4 \pm 1.3$  Ma from U-Pb isotope dating of zircon in jadeite-rich rocks (Hertwig et al.,

2016). The metamorphic peak age was estimated to be  $103.6 \pm 2.7$  Ma using Lu-Hf garnet-whole rock isochron age analyses (Krebs et al., 2008; 2011), and the metamorphic peak condition was suggested at the  $P = 23\text{--}26$  kbar and  $T = 750\text{--}800$  °C (Krebs et al., 2008; 2011) and  $P = 22\text{--}23$  kbar and  $T = 550\text{--}600$  °C (Escuder-Viruete and Pérez-Estaún, 2013). Exhumation time was estimated to be  $73.4 \pm 0.7$  Ma for eclogite and  $73.9 \pm 0.8$  Ma for omphacite-blueschist using  $^{40}\text{Ar}/^{39}\text{Ar}$  analyses of phengite with the cooling age below  $\sim 350\text{--}400$  °C (Krebs et al., 2008; 2011),  $71.3 \pm 0.7$  Ma for tonalite sill intruded the mélange using U-Pb dating of zircon (Escuder-Viruete et al., 2013a), and  $77.6 \pm 1.3$  Ma for jadeitite using U-Pb zircon with the metasomatic replacement that formed jadeitite (Hertwig et al., 2016).

Recently, the geometric and kinematic investigations of Neotectonic geological structures constrained the WNW-trending, left-lateral strike-slip Septentrional Fault Zone (SFZ) developed by active oblique collision (Escuder-Viruete and Pérez, 2020). In addition, recent study on the analysis of seismic and geodetic data have divided the oblique convergence tectonic setting in northern Caribbean plate boundary into five tectonic domains from east to west: oblique subduction in northwest Puerto Rico; oblique collision in north-east Hispaniola, Dominican Republic; oblique underthrusting in north-central Hispaniola, Dominican Republic and Haiti; left-lateral strike-slip in north-west Hispaniola, Haiti; and northern collision in northeast Cuba (Rodríguez-Zurrunero et al., 2020). From this division, the study area is located between oblique collision and oblique underthrusting domains.



- |                                      |  |   |
|--------------------------------------|--|---|
| <b>Jagua Clara mélangé</b>           | <b>Gaspar Hernández Serpentinities</b>         | <b>Morrito Unit</b>                               |
| ■ Hicotea mafic schists              | ■ Massive and serpentinized harzburgites       | ■ El Guineal felsic schists                       |
| ■ Eclogite and blueschist blocks     | <b>Río Boda Metaplutonic complex</b>           | ■ Puerca Gorda mafic schists                      |
| ■ Serpentinitic-schists and gouge    | ■ Hbl-gabbros, diorites and tonalites          | <b>Cenozoic cover</b>                             |
| — Thrust or high-angle reverse fault | ■ Metagabbrogranites (two-pyroxene granulites) | ■ Undifferentiated sedimentary rocks and deposits |
| — Strike-slip shear zone or fault    |  |   |

**Figure 5.1. (a)** Simplified geotectonic map of the northeastern margin of the Caribbean plate showing the major tectonic setting between North American plate and Caribbean plate (modified after Escuder-Viruete et al., 2013a; Escuder-Viruete and Pérez, 2020). Black arrow: the plate motion direction of Caribbean plate (Mann et al., 2002); **(b)** Geological map of the northern Río San Juan metamorphic complex, Dominican Republic (modified after Escuder-Viruete et al., 2011; Escuder-Viruete and Pérez-Estaún, 2013). Sample locations are indicated by yellow stars in white circles.

## 5.3. Methods

### 5.3.1. Sample description

In this study, six metamorphic rocks were collected from Jagua-Clara serpentinite mélange of the Rio San Juan metamorphic complex, Dominican Republic (Fig. 5.1). Because the high pressure metabasite blocks were exhumed from different depths and through different path with different times, there are various metamorphic rocks in the mélange which have undergone various P-T-t conditions during subduction and exhumation. To define the mineral assemblage of the samples, the composition of minerals was measured with a JEOL JXA-8530F field emission electron probe microanalyzer at the National Center for Inter-university Research Facilities (NCIRF) in Seoul National University (SNU), South Korea. The measurement conditions included an accelerating voltage of 15 kV, a beam current of 20 nA, and a beam size of 3  $\mu\text{m}$  diameter. The amphibole group minerals were classified into glaucophane, barroisite, actinolite and actinolitic hornblende, and were included in each sample with different volume ratios depending on the degree of retrograde metamorphism. The epidote group minerals were classified into epidote and zoisite/clinozoisite according to their mineral composition, but the latter was defined as a zoisite by lattice information which was obtained by electron backscattered diffraction (EBSD) technique. According to the mineral assemblage of the rocks, samples were classified as five groups. The modal composition of samples was summarized in Table 5.1, and the chemical compositions of minerals in each sample were summarized in Tables 5.2–5.7.

**Table 5.1.** Modal composition (in volume %) of the area analyzed by EBSD and whole area of samples.

Sample	Analyzed area <sup>1</sup>	Amphibole group				Epidote group				Other minerals					
		Gln <sup>2</sup>	Brs	Act	Act-Hbl	Ep	Zo	Phg	Grt	Omp	Qtz	Chl	Ttn	Ab	Lws
2449	ZPR area	45.4	11.4	-	-	11.1	16.4	1.9	0.1	4.4	-	1.0	3.3	4.9	-
	ZR area	44.9	11.2	-	-	7.2	24.4	1.4	0.003	3.9	-	1.3	2.7	3.1	-
	EZ area	47.4	11.8	-	-	14.5	12.4	1.1	0.6	4.4	-	1.1	3.1	3.7	-
	Whole <sup>3</sup>	45.8	11.5	-	-	10.9	17.6	1.5	0.2	4.3	-	1.1	3.1	4.1	-
2461	GR layer	32.1	16.0	5.3	-	36.8	0.04	0.2	3.9	-	4.0	0.2	0.5	1.0	-
	EPR area	31.0	15.5	5.2	-	42.4	0.2	0.3	0.6	-	3.6	0.2	0.7	0.5	-
	Whole	31.4	15.7	5.2	-	40.1	0.1	0.3	1.9	-	3.7	0.2	0.6	0.7	-
1017Y	GOR area	29.5	12.6	-	-	13.3	-	4.8	13.8	16.2	0.04	0.9	5.7	3.1	-
	GOP area	48.1	20.6	-	-	15.7	-	3.2	1.8	1.8	0.02	0.6	5.6	2.6	-
	Whole	38.9	16.6	-	-	14.5	-	4.0	7.9	9.1	0.03	0.8	5.6	2.9	-
2462	CR area	18.3	36.5	6.1	-	15.0	-	0.1	1.5	-	6.3	6.1	1.5	8.5	0.004
	CP area	21.1	42.2	7.0	-	19.3	-	0.1	0.4	-	2.4	1.1	2.0	4.5	0.001
	Whole	19.3	38.5	6.4	-	16.5	-	0.1	1.1	-	2.9	4.4	1.7	7.1	0.003
2444	MD layer	84.5	-	-	-	-	-	8.2	-	-	-	0.4	6.8	-	-
	WD layer	80.0	-	-	-	-	-	12.8	-	-	-	0.3	6.9	-	-
	Whole	82.2	-	-	-	-	-	10.5	-	-	-	0.4	6.9	-	-
1015Y	GR layer	3.5	17.5	7.0	7.0	26.4	-	0.5	6.0	-	0.004	3.5	3.9	24.8	-
	GP area	3.8	18.8	7.5	7.5	27.3	-	1.0	0.1	-	0.005	3.7	2.9	27.2	-
	Whole	3.7	18.3	7.3	7.3	27.0	-	0.9	2.2	-	0.005	3.6	3.3	26.4	-

<sup>1</sup> Abbreviation of area in this table: ZPR: zoisite porphyroblast rich, ZR: zoisite rich, and EZ: epidote-zoisite, GR: garnet rich, EPR: epidote porphyroblast rich, GOR: garnet-omphacite rich, GOP: garnet-omphacite poor, CR: chlorite rich, CP: chlorite poor, MD: moderately deformed, WD: weakly deformed, GR: garnet rich, GP: garnet poor.

<sup>2</sup> Abbreviation of mineral in this table: Gln: glaucophane, Brs: barroisite, Act: actinolite, Act-Hbl: actinolitic hornblende, Ep: epidote, Zo: zoisite, Phg: phengite, Grt: garnet, Omp: omphacite, Qtz: quartz, Chl: chlorite, Ttn: titanite, Ab: albite, and Lws: lawsonite.

<sup>3</sup> The modal composition of whole area was calculated by multiplying the dimensional ratio of the analyzed area.

### 5.3.1.1. *Zoisite eclogite–epidote blueschist facies metamorphic rocks*

Sample 2449 consists mainly of sodic to sodic-calcic amphibole (glauco-phane and barroisite), epidote, zoisite, omphacite, titanite and albite with minor garnet, phengite and chlorite (Table 5.2, and Fig. 5.2a–b). The matrix is composed mainly of amphibole (~56–59 %), zoisite (~12–24 %) and epidote (~7–14 %). The sample area was divided into the zoisite porphyroclast rich (ZPR) area (the maximum equivalent radius, Max.  $r_e$ , is ~560  $\mu\text{m}$  and average  $r_e \approx 35 \mu\text{m}$ ), zoisite rich (ZR) area (the volume ratio of epidote and zoisite is 0.23:0.77), and epidote-zoisite mixed (EZ) area (the volume ratio of epidote and zoisite is 0.54:0.46). Most of amphiboles were glaucophane (the volume ratio of glaucophane and barroisite is about 0.8:0.2) which were well oriented parallel to the lineation. However, omphacites were scattered showing un-hedral grain shape in the matrix. Garnet was the smallest grain size among other samples (Max.  $r_e \approx 125 \mu\text{m}$  in EZ area and average  $r_e = 18\text{--}28 \mu\text{m}$ ) showing a compositional zoning (from dark core to bright rim). Zoisite porphyroclasts well exhibited the  $\sigma$ -type mantled structures, but relatively fine-grained zoisites and epidotes were euhedral shapes (Fig. 5.2a–b).

In contrast, sample 2461 consists mainly of sodic to sodic-calcic amphibole (glaucophane and barroisite), epidote and quartz with minor zoisite, garnet, albite, phengite, titanite, calcic amphibole (actinolite) and chlorite (Table 5.3, and Fig. 5.2c–d). Most of amphiboles were glaucophane and barroisite, but some grains retrograded to the actinolite (the volume ratio of glaucophane, barroisite and actinolite is about 0.6:0.3:0.1). This sample was divided into garnet rich (GR) layer (~4 % garnet) and epidote porphyroclast rich (EPR) area (~42 % epidote). Garnet

was an intermediate grain size among other samples (Max.  $r_e \approx 240 \mu\text{m}$  and average  $r_e \approx 100\text{--}200 \mu\text{m}$ ) and showed compositional zoning (bright core–dark intermediate area–bright rim). Epidotes were well oriented parallel to the lineation, and porphyroclasts of epidote (Max.  $r_e \approx 280 \mu\text{m}$  and average  $r_e \approx 50 \mu\text{m}$ ) showed compositional zoning and included remnant zoisite. These mineral assemblages indicate the zoisite eclogite facies metamorphic rock overprinted by the epidote blueschist facies metamorphism.

### *5.3.1.2. Epidote eclogite–epidote blueschist facies metamorphic rock*

Sample 1017Y consists mainly of sodic to sodic-calcic amphibole (glaucophane and barroisite), omphacite, garnet, epidote, phengite, titanite and albite with minor chlorite and quartz (Table 5.4, and Fig. 5.2e–f). The matrix is composed mainly of amphibole (~42–69 %) and epidote (~13–17 %). The sample area was divided into the eclogite facies mineral (garnet and omphacite) rich (GOR) area (~16 % omphacite and ~14 % garnet) and eclogite facies mineral poor (GOP) area (~2 % omphacite and ~2 % garnet). Most of amphiboles were glaucophane (the volume ratio of glaucophane and barroisite is about 0.7:0.3). Omphacites were well oriented parallel to the lineation showing euhedral shape. However, epidotes were scattered showing unhedral grain shape in the matrix. Garnet was the largest grain size among other samples (Max.  $r_e \approx 580 \mu\text{m}$  in the GOR area and average  $r_e \approx 120\text{--}230 \mu\text{m}$ ) showing a compositional zoning (from bright core to dark rim) with lots of inclusions such as epidote and titanite. This mineral assemblage indicates the epidote blueschist facies metamorphism overprinting to the epidote eclogite facies metamorphic rock.

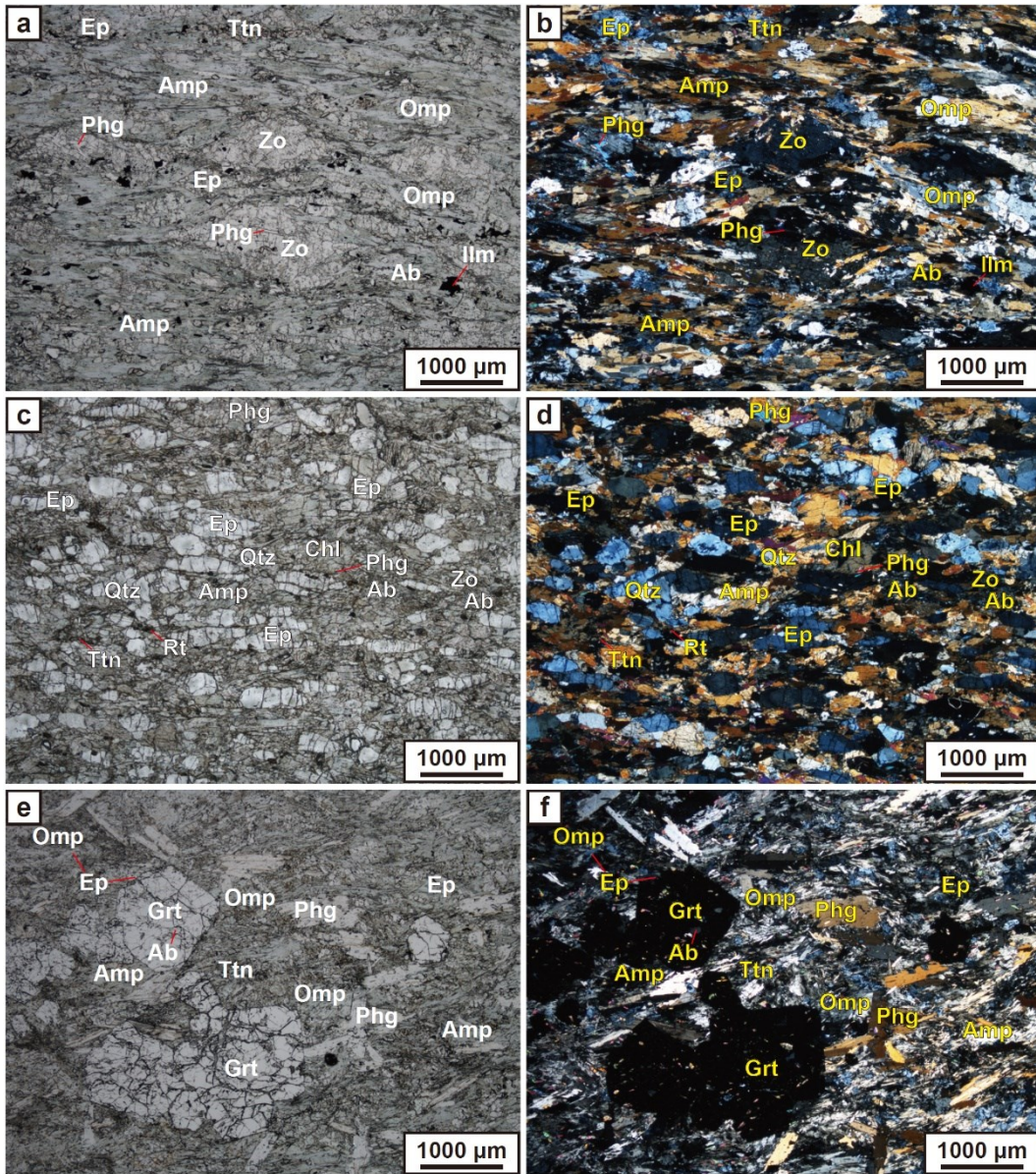


**Figure 5.2.** Plane-polarized and cross-polarized optical photomicrographs of eclogite-blueschist facies metamorphic rocks. **(a) and (b)** Zoisite eclogite-epidote blueschist facies rock (sample 2449); **(c) and (d)** zoisite bearing epidote blueschist facies rock (sample 2461); **(e) and (f)** epidote eclogite-epidote blueschist facies rock (sample 1017Y). Amp: Na/NaCa-amphibole, Ep: epidote, Zo: zoisite, Grt: garnet, Omp: omphacite, Ilm: ilmenite, Phg: phengite, Ttn: titanite, Rt: rutile, and Ab: albite.

**Table 5.2.** Representative mineral compositions of zoisite eclogite-epidote blueschist facies rock (sample 2449).

Lo.	Amphibole group		Epidote group		Garnet		Omphacite		Mica (Phengite)		Chlorite matrix		
	matrix	matrix	matrix	matrix	core	rim	matrix	beside Grt	beside Grt	inner Grt inc. in Zo			
SiO <sub>2</sub>	57.36	49.50	39.07	39.70	38.69	37.94	55.65	56.18	50.57	50.51	51.36	27.22	
TiO <sub>2</sub>	0.02	0.17	0.29	0.13	0.15	0.05	0.00	0.07	0.13	0.03	0.11	0.07	
Al <sub>2</sub> O <sub>3</sub>	11.03	9.61	28.76	32.72	21.62	21.30	6.46	9.91	27.32	27.10	26.47	19.49	
Cr <sub>2</sub> O <sub>3</sub>	0.02	0.02	0.00	0.01	0.06	0.04	0.00	0.06	0.08	0.02	0.02	0.07	
FeO	10.73	12.83	5.91	1.32	22.26	22.05	6.06	5.89	2.40	3.03	2.22	21.88	
MgO	10.33	12.42	0.05	0.00	4.10	1.32	9.92	7.75	3.61	3.37	3.81	17.48	
CaO	2.18	10.09	24.11	24.84	12.73	13.44	17.33	13.81	0.02	0.36	0.17	0.04	
MnO	0.08	0.13	0.12	0.07	1.30	3.95	0.18	0.15	0.00	0.19	0.00	0.22	
Na <sub>2</sub> O	6.46	2.81	0.00	0.02	0.02	0.00	4.70	6.80	0.50	0.26	0.54	0.01	
K <sub>2</sub> O	0.05	0.37	0.00	0.00	0.00	0.01	0.00	0.00	11.34	11.33	11.23	0.00	
Total	98.25	97.94	98.31	98.80	100.94	100.09	100.30	100.62	95.98	96.20	95.93	86.49	
F.St.	23 ox	23 ox	12.5 ox	12.5 ox	12 ox	12 ox	6 ox	6 ox	11 ox	11 ox	11 ox	14 ox	
Si	7.88	7.14	3.05	3.00	2.99	3.00	2.01	2.01	3.37	3.38	3.42	2.85	
Ti	0.00	0.02	0.02	0.01	0.01	0.00	0.00	0.00	0.01	0.00	0.01	0.01	
Al	1.79	1.63	2.64	2.92	1.97	1.98	0.28	0.42	2.15	2.13	2.08	2.41	
Cr	0.00	0.00	0.00	0.00	0.00	0.00	0.00	0.00	0.00	0.00	0.00	0.01	
Fe	1.23	1.55	0.39	0.08	1.44	1.46	0.18	0.18	0.13	0.17	0.12	1.92	
Mg	2.12	2.67	0.01	0.00	0.47	0.16	0.54	0.41	0.36	0.34	0.38	2.73	
Ca	0.32	1.56	2.01	2.01	1.05	1.14	0.67	0.53	0.00	0.03	0.01	0.00	
Mn	0.01	0.02	0.01	0.00	0.09	0.26	0.01	0.00	0.00	0.01	0.00	0.02	
Na	1.72	0.79	0.00	0.00	0.00	0.00	0.33	0.47	0.06	0.03	0.07	0.00	
K	0.01	0.07	0.00	0.00	0.00	0.00	0.00	0.00	0.97	0.97	0.95	0.00	
Sum	15.09	15.45	8.12	8.03	8.02	8.01	4.01	4.02	7.06	7.05	7.04	9.94	
Name	Gln	Brs	Ep	Zo	X <sub>Alm</sub>	X <sub>Q</sub>	X <sub>Q</sub>	0.672	0.530	Al <sup>IV</sup>	0.640	0.583	Pyc
					X <sub>Bpp</sub>	0.156	X <sub>Id</sub>	0.285	0.415	Al <sup>VI</sup>	1.498	1.484	1.492
					X <sub>Grs</sub>	0.349	X <sub>Ae</sub>	0.043	0.055				
					X <sub>Sps</sub>	0.028	0.088						
					Mg/Fe	0.336	0.107						

Lo.: location in sample, inc.: inclusion, Gln: glaucophane, Brs: barroisite, Ep: epidote, Zo: zoisite, Pyc: pycnochlorite

**Table 5.3.** Representative mineral compositions of zoisite bearing epidote blueschist facies rock (sample 2461).

Lo.	Amphibole group			Epidote group			Garnet			Mica (Phengite)	
	matrix	matrix	matrix	matrix	matrix	matrix	inner core	core-rim	rim	matrix	beside Grt
SiO <sub>2</sub>	58.03	49.23	55.71	38.76	38.25	39.30	38.69	38.96	38.53	52.19	50.70
TiO <sub>2</sub>	0.04	0.28	0.04	0.17	0.12	0.08	0.10	0.10	0.10	0.12	0.11
Al <sub>2</sub> O <sub>3</sub>	10.66	10.82	2.49	29.06	26.75	32.40	21.61	21.61	21.58	26.39	29.20
Cr <sub>2</sub> O <sub>3</sub>	0.03	0.00	0.08	0.00	0.04	0.01	0.05	0.05	0.07	0.27	0.05
FeO	9.45	10.02	9.51	5.94	8.19	1.81	22.73	22.78	25.36	2.23	2.47
MgO	11.00	13.69	16.89	0.12	0.01	0.00	4.00	3.83	3.88	3.82	3.18
CaO	1.95	9.38	11.27	23.88	23.83	24.78	9.59	10.52	9.12	0.02	0.07
MnO	0.07	0.19	0.15	0.10	0.10	0.02	4.08	2.99	2.24	0.00	0.05
Na <sub>2</sub> O	6.42	3.19	1.07	0.00	0.00	0.00	0.02	0.04	0.03	0.35	0.61
K <sub>2</sub> O	0.02	0.25	0.06	0.00	0.00	0.00	0.00	0.00	0.00	11.97	11.10
Total	97.68	97.05	97.27	98.03	97.29	98.40	100.87	100.88	100.90	97.36	97.54
F.St.	23 ox	23 ox	23 ox	12.5 ox	12.5 ox	12.5 ox	12 ox	12 ox	12 ox	11 ox	11 ox
Si	7.96	7.06	7.89	3.03	3.06	2.99	3.00	3.02	3.00	3.44	3.32
Ti	0.00	0.03	0.00	0.01	0.01	0.00	0.01	0.01	0.01	0.01	0.01
Al	1.72	1.83	0.42	2.68	2.52	2.91	1.98	1.97	1.98	2.05	2.26
Cr	0.00	0.00	0.01	0.00	0.00	0.00	0.00	0.00	0.00	0.01	0.00
Fe	1.08	1.20	1.13	0.39	0.55	0.12	1.48	1.48	1.65	0.12	0.14
Mg	2.25	2.93	3.57	0.01	0.00	0.00	0.46	0.44	0.45	0.37	0.31
Ca	0.29	1.44	1.71	2.00	2.04	2.02	0.80	0.87	0.76	0.00	0.00
Mn	0.01	0.02	0.02	0.01	0.01	0.00	0.27	0.20	0.15	0.00	0.00
Na	1.71	0.89	0.29	0.00	0.00	0.00	0.00	0.01	0.00	0.05	0.08
K	0.00	0.04	0.01	0.00	0.00	0.00	0.00	0.00	0.00	1.01	0.93
Sum	15.03	15.46	15.05	8.12	8.18	8.05	8.00	7.99	8.00	7.05	7.05
Name	Gln	Brs	Act	Ep_rim	Ep_rim	Zo	X <sub>Alm</sub>	0.489	0.493	Al <sup>IV</sup>	0.565
							X <sub>Frp</sub>	0.155	0.148	Al <sup>VI</sup>	1.483
							X <sub>Grs</sub>	0.266	0.293		1.546
							X <sub>Sps</sub>	0.090	0.066		
							Mg/Fe	0.316	0.301		

Lo.: location in sample, core-rim: between core and rim, Gln: glaucophane, Brs: barroisite, Act: actinolite, Ep: epidote, Zo: zoisite

**Table 5.4.** Representative mineral compositions of epidote eclogite-epidote blueschist facies rock (sample 1017Y).

Lo.	Amphibole group			Epidote group			Garnet		Omphacite			Mica (Phengite)			Chlorite	
	matrix	matrix	inc. in Grt	core	rim	inc. in Grt	core	rim	matrix	beside Grt	inc. in Grt	core	rim	inc. in Grt	matrix	matrix
SiO <sub>2</sub>	56.55	48.02	38.19	38.58	38.19	38.40	38.08	38.03	54.96	55.65	55.71	49.44	53.03	51.70	26.97	26.97
TiO <sub>2</sub>	0.02	0.23	0.19	0.18	0.19	0.12	0.13	0.14	0.14	0.17	0.32	0.33	0.01	0.05	0.00	0.00
Al <sub>2</sub> O <sub>3</sub>	11.18	10.69	29.73	29.73	27.47	27.61	21.17	21.38	8.43	9.73	8.83	31.19	24.84	24.31	18.45	18.45
Cr <sub>2</sub> O <sub>3</sub>	0.00	0.00	0.07	0.07	0.06	0.01	0.01	0.03	0.00	0.02	0.01	0.01	0.03	0.00	0.02	0.02
FeO	13.15	14.22	4.60	4.60	7.74	7.58	26.24	25.23	9.04	7.17	9.10	1.87	3.49	4.69	26.61	26.61
MgO	8.20	11.16	0.04	0.04	0.02	0.01	1.75	2.34	6.63	7.04	6.36	2.35	3.81	3.91	14.74	14.74
CaO	1.23	9.56	24.01	24.01	23.69	23.78	10.26	11.57	14.27	12.92	13.69	0.00	0.03	0.02	0.03	0.03
MnO	0.08	0.16	0.09	0.09	0.33	0.25	3.16	1.73	0.12	0.09	0.16	0.03	0.03	0.05	0.19	0.19
Na <sub>2</sub> O	6.80	3.02	0.01	0.01	0.00	0.00	0.01	0.03	6.32	6.72	6.66	1.02	0.14	0.12	0.00	0.00
K <sub>2</sub> O	0.01	0.31	0.00	0.00	0.00	0.00	0.00	0.00	0.00	0.01	0.02	10.63	12.01	11.75	0.00	0.00
Total	97.23	97.37	97.31	97.31	97.70	97.76	100.82	100.48	99.91	99.52	100.85	96.87	97.43	96.59	87.01	87.01
F.St.	23 ox	23 ox	12.5 ox	12.5 ox	12.5 ox	12.5 ox	12 ox	12 ox	6 ox	6 ox	6 ox	11 ox	11 ox	11 ox	14 ox	14 ox
Si	7.93	7.02	3.02	3.02	3.03	3.04	3.01	2.99	2.01	2.01	2.02	3.25	3.50	3.47	2.88	2.88
Ti	0.00	0.03	0.01	0.01	0.01	0.01	0.01	0.01	0.00	0.00	0.01	0.02	0.00	0.00	0.00	0.00
Al	1.85	1.84	2.74	2.74	2.57	2.58	1.97	1.98	0.36	0.42	0.38	2.42	1.93	1.92	2.32	2.32
Cr	0.00	0.00	0.00	0.00	0.00	0.00	0.00	0.00	0.00	0.00	0.00	0.00	0.00	0.00	0.00	0.00
Fe	1.54	1.74	0.30	0.30	0.51	0.50	1.73	1.66	0.28	0.22	0.28	0.10	0.19	0.26	2.38	2.38
Mg	1.71	2.43	0.00	0.00	0.00	0.00	0.21	0.27	0.36	0.38	0.34	0.23	0.38	0.39	2.35	2.35
Ca	0.19	1.50	2.01	2.01	2.02	2.02	0.87	0.97	0.56	0.50	0.53	0.00	0.00	0.00	0.00	0.00
Mn	0.01	0.02	0.01	0.01	0.02	0.02	0.21	0.12	0.00	0.00	0.00	0.00	0.00	0.00	0.02	0.02
Na	1.85	0.86	0.00	0.00	0.00	0.00	0.00	0.01	0.45	0.47	0.47	0.13	0.02	0.02	0.00	0.00
K	0.00	0.06	0.00	0.00	0.00	0.00	0.00	0.00	0.00	0.00	0.00	0.89	1.01	1.01	0.00	0.00
Sum	15.07	15.49	8.10	8.10	8.17	8.16	8.00	8.01	4.03	4.01	4.02	7.04	7.04	7.08	9.96	9.96
Name	Gln	Brs	Ep	Ep	Ep	Zo	X <sub>Alm</sub>	0.571	X <sub>Q</sub>	0.554	0.532	Al <sup>IV</sup>	0.760	0.502	0.560	Pyc
							X <sub>Ppp</sub>	0.069	X <sub>Id</sub>	0.362	0.441	Al <sup>VI</sup>	1.650	1.429	1.346	
							X <sub>Grs</sub>	0.290	X <sub>Ae</sub>	0.084	0.027					
							X <sub>Sps</sub>	0.070								
							Mg/Fe	0.120	0.167							

Lo.: location in sample, inc.: inclusion, Gln: glaucophane, Brs: barroisite, Ep: epidote, Zo: zoisite, Pyc: pycnochlorite

### *5.3.1.3. Lawsonite–epidote blueschist facies metamorphic rocks*

Sample 2462 consists mainly of sodic to sodic-calcic amphibole (glaucophane and barroisite), epidote, albite, quartz, chlorite, titanite and garnet with minor calcic amphibole (actinolite), phengite and lawsonite (Table 5.5, and Fig. 5.3a–b). The matrix is composed mainly of amphibole (~70 %) and epidote (~15–19 %). The sample area was divided into chlorite rich (CR) area (~6 %) and chlorite poor (CP) area (~1 %). Most of amphiboles were barroisite and glaucophane, but some grains retrograded to the actinolite (the volume ratio of glaucophane, barroisite and actinolite is about 0.3:0.6:0.1). This sample has fine-grained epidote (Max.  $r_e \approx 160 \mu\text{m}$  in CR area and average  $r_e \approx 20\text{--}26 \mu\text{m}$ ) aggregates showing a diamond shape pseudomorph. Garnet showed syn- to post-kinematic growth texture with lawsonite and epidote (clinozoisite) inclusions. This mineral assemblage indicates the lawsonite blueschist facies metamorphism overprinted by the epidote blueschist facies metamorphic rock.

### *5.3.1.4. Felsic blueschist facies metamorphic rocks*

Sample 2444 consists mainly of sodic amphibole (glaucophane), phengite and titanite with minor chlorite, Fe-oxide, apatite, and rutile (Table 5.6, and Fig. 5.3c–d). The matrix is composed mainly of amphibole (~80–85 %) and phengite (~8–13 %). This sample was relatively less deformed compared to the other samples. There was

~3 mm thick phengite vein across the matrix. The sample was divided into the weakly deformed (WD) layer and the moderately deformed (MD) layer based on the degree of alignment of amphiboles and phengites in a direction parallel to the lineation. This mineral assemblage indicates the blueschist facies metamorphism of the felsic rock.

#### *5.3.1.5. Epidote blueschist–upper greenschist facies metamorphic rocks*

Sample 1015Y consists mainly of sodic-calcic to calcic amphibole (barroisite, actinolitic hornblende, and actinolite), epidote, albite, chlorite, titanite and garnet with minor sodic amphibole (glaucophane), apatite and phengite (Table 5.7, and Fig. 5.3e–f). Most of amphiboles were barroisite, actinolitic hornblende and actinolite with remnant glaucophane (the volume ratio of glaucophane, barroisite, actinolitic hornblende and actinolite is about 0.1:0.5:0.2:0.2). These amphiboles were strongly oriented parallel to the lineation. This sample had the most abundant albite (~25–27 %) and the finest grain size of amphibole (~35–38 %; Max.  $r_e \approx 120 \mu\text{m}$  and average  $r_e \approx 12 \mu\text{m}$ ) and epidote (~26–27 %; Max.  $r_e \approx 110 \mu\text{m}$  and average  $r_e \approx 17 \mu\text{m}$ ) among the samples. The sample area was divided into the garnet rich (GR) layer (~6 %) and garnet poor (GP) area (~0.1 %). Garnet rim retrograded to the chlorite and albite with inclusions of epidote. This mineral assemblage indicates the greenschist facies metamorphism overprinting to the epidote blueschist facies metamorphic rock.



**Figure 5.3.** Plane-polarized and cross-polarized optical photomicrographs of blueschist-upper greenschist facies metamorphic rocks. **(a) and (b)** Lawsonite bearing epidote blueschist facies rock (sample 2462); **(c) and (d)** felsic blueschist facies rock (sample 2444); **(e) and (f)** epidote blueschist-upper greenschist facies rock (sample 1015Y). Amp: Na/NaCa-amphibole, Ep: epidote, Qtz: quartz, Chl: chlorite, Ilm: ilmenite, Ttn: titanite, Phg: phengite, Grt: garnet, and Ab: albite.

**Table 5.5.** Representative mineral compositions of lawsonite bearing epidote blueschist facies rock (sample 2462).

Lo.	Amphibole group		Epidote group		Garnet			Mica (Phengite)		Chlorite		Lawsonite			
	matrix	inc. in Grt	matrix	inc. in Grt	core	rim	fine	Matrix	beside Grt	matrix	matrix	inc. in Grt			
SiO <sub>2</sub>	56.09	44.42	53.91	39.48	38.55	39.48	37.79	37.49	37.55	51.71	50.72	26.05	27.18	38.99	
TiO <sub>2</sub>	0.02	1.10	0.03	0.07	0.12	0.62	0.25	0.14	0.21	0.07	0.15	0.04	0.05	0.00	
Al <sub>2</sub> O <sub>3</sub>	11.53	11.15	1.49	31.45	26.36	31.45	20.86	20.70	20.78	24.37	27.26	19.91	18.85	32.19	
Cr <sub>2</sub> O <sub>3</sub>	0.01	0.03	0.05	0.00	0.02	0.01	0.00	0.00	0.00	0.04	0.01	0.03	0.03	0.00	
FeO	13.58	16.05	15.51	2.65	8.58	2.27	18.06	18.40	18.91	4.36	2.58	24.84	22.98	0.91	
MgO	7.21	9.78	12.74	0.03	0.02	0.06	0.34	0.50	0.38	3.42	3.16	15.51	15.74	0.00	
CaO	0.45	11.11	11.55	24.12	23.18	23.47	12.57	11.92	11.46	0.02	0.06	0.00	0.41	17.66	
MnO	0.14	0.35	0.95	0.18	0.38	0.93	10.72	10.44	10.75	0.08	0.05	0.31	0.31	0.19	
Na <sub>2</sub> O	7.05	2.58	0.42	0.02	0.00	0.03	0.01	0.00	0.00	0.09	0.42	0.00	0.07	0.00	
K <sub>2</sub> O	0.00	0.27	0.06	0.00	0.01	0.00	0.00	0.00	0.02	11.57	11.41	0.00	0.00	0.00	
Total	96.07	96.83	96.70	98.00	97.22	98.32	100.60	99.58	100.07	95.72	95.81	86.70	85.61	89.94	
F.St.	23 ox	23 ox	23 ox	12.5 ox	12.5 ox	12.5 ox	12 ox	12 ox	12 ox	11 ox	11 ox	14 ox	14 ox	8 ox	
Si	7.96	6.67	7.94	3.03	3.08	3.02	3.00	3.01	3.01	3.49	3.39	2.77	2.90	2.02	
Ti	0.00	0.12	0.00	0.00	0.01	0.04	0.02	0.01	0.01	0.00	0.01	0.00	0.00	0.00	
Al	1.93	1.97	0.26	2.84	2.49	2.83	1.95	1.96	1.96	1.94	2.15	2.50	2.37	1.96	
Cr	0.00	0.00	0.01	0.00	0.00	0.00	0.00	0.00	0.00	0.00	0.00	0.00	0.00	0.00	
Fe	1.61	2.02	1.91	0.17	0.57	0.15	1.20	1.24	1.27	0.25	0.14	2.21	2.05	0.04	
Mg	1.52	2.19	2.80	0.00	0.00	0.01	0.04	0.06	0.05	0.34	0.31	2.46	2.50	0.00	
Ca	0.07	1.79	1.82	1.98	1.99	1.92	1.07	1.03	0.98	0.00	0.00	0.00	0.05	0.98	
Mn	0.02	0.04	0.12	0.01	0.03	0.06	0.72	0.71	0.73	0.00	0.00	0.03	0.03	0.01	
Na	1.94	0.75	0.12	0.00	0.00	0.00	0.00	0.00	0.00	0.01	0.05	0.00	0.01	0.00	
K	0.00	0.05	0.01	0.00	0.00	0.00	0.00	0.00	0.00	1.00	0.97	0.00	0.00	0.00	
Sum	15.05	15.62	14.99	8.05	8.17	8.03	8.01	8.00	8.00	7.04	7.04	9.98	9.92	5.00	
Name	Gln	Brs	Act	Ep	Ep	Czo	X <sub>Alm</sub>	0.389	0.401	0.414	Al <sup>IV</sup>	0.527	0.614	Rip	Pyc
							X <sub>Prp</sub>	0.014	0.020	0.015	Al <sup>VI</sup>	1.403	1.531		
							X <sub>Grs</sub>	0.357	0.342	0.328					
							X <sub>Sps</sub>	0.240	0.237	0.243					
							Mg/Fe	0.035	0.049	0.037					

Lo.: location in sample, inc.: inclusion, Gln: glaucophane, Brs: barroisite, Act: actinolite, Ep: epidote, Czo: clinzoisite, Rip: ripidolite, Pyc: pycnochlorite

**Table 5.6.** Representative mineral compositions of felsic blueschist facies rock (sample 2444).

Lo.	Amphibole		Mica (Phengite)		Chlorite		Titanite
	matrix	vein	matrix	vein	near Phg vein	near Phg vein	matrix
SiO <sub>2</sub>	57.79	51.84	48.70	51.84	26.80	27.55	30.84
TiO <sub>2</sub>	0.04	0.13	0.61	0.13	0.02	0.00	38.45
Al <sub>2</sub> O <sub>3</sub>	10.97	26.49	29.37	26.49	18.24	18.29	1.28
Cr <sub>2</sub> O <sub>3</sub>	0.04	0.01	0.02	0.01	0.00	0.00	0.01
FeO	11.76	2.82	2.47	2.82	28.99	22.61	0.29
MgO	8.80	3.89	2.73	3.89	13.44	17.15	0.00
CaO	0.27	0.00	0.00	0.00	0.00	0.00	28.54
MnO	0.16	0.04	0.00	0.04	0.41	0.37	0.07
Na <sub>2</sub> O	7.24	0.29	0.72	0.29	0.00	0.00	0.02
K <sub>2</sub> O	0.00	11.68	10.91	11.68	0.00	0.01	0.01
Total	97.08	97.20	95.53	97.20	87.90	85.99	99.52
F.St.	23 ox	11 ox	11 ox	11 ox	14 ox	14 ox	5 ox
Si	8.03	3.42	3.27	3.42	2.87	2.92	1.01
Ti	0.00	0.01	0.03	0.01	0.00	0.00	0.95
Al	1.80	2.06	2.32	2.06	2.31	2.28	0.05
Cr	0.00	0.00	0.00	0.00	0.00	0.00	0.00
Fe	1.37	0.16	0.14	0.16	2.60	2.00	0.01
Mg	1.82	0.38	0.27	0.38	2.15	2.71	0.00
Ca	0.04	0.00	0.00	0.00	0.00	0.00	1.00
Mn	0.02	0.00	0.00	0.00	0.04	0.03	0.00
Na	1.95	0.04	0.09	0.04	0.00	0.00	0.00
K	0.00	0.98	0.93	0.98	0.00	0.00	0.00
Sum	15.04	7.06	7.06	7.05	9.97	9.94	3.02
Name	Gln	Al <sup>IV</sup>	Al <sup>IV</sup>	Al <sup>IV</sup>	Bru	Pyc	
		Al <sup>VI</sup>	Al <sup>VI</sup>	Al <sup>VI</sup>			

Lo.: location in sample, Gln: glaucophane, Phg: phengite, Bru: brunsvigite, Pyc: pycnochlorite

**Table 5.7.** Representative mineral compositions of epidote blueschist-upper greenschist facies rock (sample 1015Y).

Lo.	Amphibole group			Epidote group		Garnet		Mica (Phengite)		Chlorite		Albite		Titanite	
	matrix	matrix	matrix	matrix	inc. in Grt	core	rim	coarse	fine	reacted Grt	Matrix	matrix	matrix	matrix	
SiO <sub>2</sub>	58.02	50.81	50.47	54.89	39.03	38.35	37.84	37.98	50.95	51.47	26.34	27.87	68.05	30.45	
TiO <sub>2</sub>	0.04	0.18	0.05	0.05	0.11	0.21	0.15	0.13	0.21	0.18	0.02	0.01	0.02	39.22	
Al <sub>2</sub> O <sub>3</sub>	11.83	9.06	5.68	3.59	29.08	28.25	21.29	21.16	28.04	26.76	19.30	18.95	19.62	0.94	
Cr <sub>2</sub> O <sub>3</sub>	0.05	0.07	0.04	0.04	0.06	0.10	0.05	0.06	0.05	0.11	0.06	0.03	0.00	0.00	
FeO	8.86	10.82	12.76	9.32	5.63	6.52	23.98	26.58	1.89	1.92	23.30	21.20	0.13	0.27	
MgO	10.75	13.75	14.02	17.00	0.01	0.03	4.64	2.22	3.34	3.75	17.09	18.56	0.01	0.00	
CaO	1.39	9.15	11.18	11.04	24.02	23.79	1.61	2.23	0.00	0.02	0.01	0.09	0.18	28.94	
MnO	0.03	0.03	0.14	0.05	0.20	0.33	11.39	10.27	0.03	0.07	0.22	0.21	0.00	0.02	
Na <sub>2</sub> O	6.87	3.01	1.71	1.32	0.00	0.00	0.00	0.00	0.63	0.39	0.02	0.01	11.96	0.02	
K <sub>2</sub> O	0.02	0.21	0.19	0.06	0.00	0.00	0.03	0.03	11.36	11.79	0.01	0.02	0.02	0.00	
Total	97.85	97.09	96.24	97.36	98.14	97.59	100.98	100.67	96.50	96.47	86.36	86.94	100.00	99.85	
F.St.	23 ox	23 ox	23 ox	23 ox	12.5 ox	12.5 ox	12 ox	12 ox	11 ox	11 ox	14 ox	14 ox	14 ox	14 ox	
Si	7.91	7.28	7.41	7.77	3.04	3.03	2.98	3.00	3.37	3.41	2.79	2.89	2.98	1.00	
Ti	0.00	0.02	0.01	0.01	0.01	0.01	0.01	0.01	0.01	0.01	0.00	0.00	0.00	0.97	
Al	1.90	1.53	0.98	0.60	2.67	2.63	1.98	1.97	2.19	2.09	2.41	2.32	1.01	0.04	
Cr	0.01	0.01	0.01	0.00	0.00	0.01	0.00	0.00	0.00	0.01	0.01	0.00	0.00	0.00	
Fe	1.01	1.30	1.57	1.10	0.37	0.43	1.58	1.75	0.10	0.11	2.07	1.84	0.00	0.01	
Mg	2.19	2.94	3.07	3.59	0.00	0.00	0.31	0.15	0.33	0.37	2.70	2.87	0.00	0.00	
Ca	0.20	1.41	1.76	1.67	2.01	2.01	0.19	0.26	0.00	0.00	0.00	0.01	0.01	1.01	
Mn	0.00	0.00	0.02	0.01	0.01	0.02	0.96	0.87	0.00	0.00	0.02	0.02	0.00	0.00	
Na	1.82	0.84	0.49	0.36	0.00	0.00	0.00	0.00	0.08	0.05	0.00	0.00	1.02	0.00	
K	0.00	0.04	0.04	0.01	0.00	0.00	0.00	0.01	0.96	1.00	0.00	0.00	0.00	0.00	
Sum	15.04	15.36	15.35	15.11	8.11	8.14	8.02	8.01	7.04	7.05	10.00	9.95	5.02	3.02	
Name	Gln	Brs	Act-Hbl	Act	Ep	Ep	X <sub>Alm</sub>	X <sub>Ann</sub>	Al <sup>IV</sup>	0.633	Rip	Pyc			
							X <sub>Pp</sub>	X <sub>Pp</sub>	Al <sup>VI</sup>	1.552					
							X <sub>Grs</sub>	X <sub>Grs</sub>							
							X <sub>Sps</sub>	X <sub>Sps</sub>							
							Mg/Fe	Mg/Fe							
							0.122	0.152							

Lo.: location in sample, inc.: inclusion, Gln: glaucophane, Brs: barroisite, Act-Hbl: actinolitic hornblende, Act: actinolite, Ep: epidote, Rip: ripidolite, Pyc: pycnochlorite

### 5.3.2. Determination of LPOs of minerals

Electron backscattered diffraction (EBSD) technique (Prior et al., 1999) was used to determine the LPOs of minerals in the blueschist facies metamorphic rocks. The EBSD mapping of the samples was conducted by using the Oxford Instruments' EBSD system (AZtec v.4.3 software) with a Symmetry detector attached to the FE-SEM (JEOL JSM-7100F) housed at the SEES in SNU, South Korea. Foliation of the samples was determined by both the compositional layering and/or the shape-preferred orientation of deformed grains (Passchier and Trouw, 1996), and lineation of the samples was determined by grain shape analysis of digitized lines from the elongated grain boundaries in the foliation plane, using the method of Panozzo (1983; 1984) (the detail of the method was described in Chapter 2.3.2). The LPOs of minerals were measured in the XZ plane thin sections, where the X- and Z-directions represent the lineation and direction normal to the foliation, respectively. Thin sections were polished using alumina powders, diamond paste of 1  $\mu\text{m}$ , and Syton (0.06  $\mu\text{m}$  colloidal silica slurry) because the accuracy of the LPO measurement using SEM is involved with removing the mechanical surface damage using a chemical-mechanical polishing technique (Lloyd, 1987). The polished plane was coated with a  $\sim 3$  nm thick carbon to prevent charging in the SEM, and the surface was tilted  $70^\circ$  to the incident electronic beam in the chamber. EBSD analysis was conducted under a 20 kV accelerating voltage, 25 mm working distance, a  $\sim 20$  nA probe current, and a 5.0  $\mu\text{m}$  step size. After EBSD analysis, the data was processed using MTEX (v.5.4.0), a MATLAB toolbox (Bachmann et al., 2011).

To quantify the fabric strength of minerals, the uncorrelated grain pairs and the orientations of grains as triplet of Euler angle determined from EBSD data were used to calculate the M-index (Skemer et al., 2005) and the J-index (Bunge, 1982), respectively. The M-index is defined by Equation 2.1 as:

$$M = 0.5 \int |R^T(\varphi) - R^0(\varphi)| d\varphi \quad (2.1)$$

where  $R^T(\varphi)$  is the theoretical distribution of uncorrelated misorientation angles for a random fabric,  $R^0(\varphi)$  is the observed distribution of uncorrelated misorientation angles for a real fabric from EBSD data, and  $\varphi$  is the misorientation angle of uncorrelated grain pair (Skemer et al., 2005). This M-index ranges from 0 (random fabric) to 1 (single crystal fabric). The J-index is defined by Equation 4.1 as:

$$J = \int [f(\mathbf{g})]^2 d\mathbf{g} \quad (4.1)$$

where  $f(\mathbf{g})$  is the orientation distribution function (ODF),  $\mathbf{g} = (\phi_1, \psi, \phi_2)$  is the orientation data as the Euler angle triplet, and  $d\mathbf{g}$  is a volume element in Euler angle space (Bunge, 1982). This J-index theoretically ranges from 1 (completely random fabric) to infinity (single crystal fabric).

### 5.3.3. Calculation of seismic velocity and anisotropy

The seismic velocity and anisotropy of minerals and whole rocks were calculated using both the macroscopic elastic tensor  $\langle C_{ij} \rangle$  and the density by solving the Christoffel equation with the Voigt-Reuss-Hill (VRH) averaging scheme using the MTEX with MSAT toolkits (version 1.1.1) (Walker and Wookey, 2012). The macroscopic elastic tensor was calculated by integrating elastic stiffness coefficients ( $c_{ij}$ ) of all single-crystal minerals for all orientations of grains obtained as triplet of Euler angle in the EBSD analysis. The elastic coefficients of single-crystal glaucophane as amphibole (Bezacier et al., 2010a), epidote (Aleksandrov et al., 1974), zoisite (Mao et al., 2007), muscovite as phengite (Vaughan and Guggenheim, 1986), almandine-rich garnet (Jiang et al., 2004), omphacite (Bhagat et al., 1992), quartz (Heyliger et al., 2003), chlorite (Mookherjee and Mainprice, 2014), titanite (Das et al., 2021), and albite (Brown et al., 2006) were taken from literature. The density of whole rock was calculated as the average of the densities of constituent minerals weighted by the volume proportion of each sample. The azimuthal anisotropy of P-wave ( $AV_p$ ) was calculated by Equation 2.2 as:

$$AV_p = 200 \times [(V_{p_{\max}} - V_{p_{\min}}) / (V_{p_{\max}} + V_{p_{\min}})] (\%) \quad (2.2)$$

where  $V_{p_{\max}}$  and  $V_{p_{\min}}$  are the maximum and minimum P-wave velocity, respectively.

The polarization anisotropy of shear wave ( $AV_s$ ) was calculated by Equation 2.3 as:

$$AV_s = 200 \times [(V_{s1} - V_{s2}) / (V_{s1} + V_{s2})] (\%) \quad (2.3)$$

where  $V_{s1}$  and  $V_{s2}$  are the fast and slow S-wave velocity, respectively. The average velocity of P-wave ( $V_{p_{aver}}$ ) was calculated by Equation 4.4 as:

$$V_{p_{aver}} = (V_{p_{max}} + V_{p_{min}}) / 2 \text{ (km/s)} \quad (4.4)$$

and the average velocity of S-wave ( $V_{s_{aver}}$ ) was calculated by Equation 4.5 as:

$$V_{s_{aver}} = (V_{s1_{max}} + V_{s2_{max}} + V_{s1_{min}} + V_{s2_{min}}) / 4 \text{ (km/s)} \quad (4.5)$$

where  $V_{s1_{max}}$  and  $V_{s1_{min}}$  are the maximum and minimum velocity of the fast S-wave ( $V_{s1}$ ), and  $V_{s2_{max}}$  and  $V_{s2_{min}}$  are the maximum and minimum velocity of the slow S-wave ( $V_{s2}$ ), respectively.

## 5.4. Results

### 5.4.1. LPOs of minerals

The areas analyzed by the EBSD technique are shown in the phase color map (Fig. 5.4), and LPOs of minerals in the samples are plotted as pole figures of each mineral (Figs. 5.5–5.14).

#### *5.4.1.1. LPOs of amphibole group minerals*

In the sample 2449, the crystallographic [001] axes of amphiboles were in parallel alignment with the lineation with a weak girdle distribution subparallel to the foliation, and the [100] axes were aligned normal to the foliation. (Fig. 5.5a–c). In contrast, in the sample 2461, the crystallographic [001] axes of amphiboles were aligned subnormal to the lineation showing a girdle distribution parallel to the foliation, and the (010) poles were in subparallel alignment with the lineation. The [100] axes of amphiboles in the sample 2461 were subnormally aligned with the foliation showing more scattered distribution than those in the sample 2449 (Fig. 5.5d–e). In the sample 1017Y, the crystallographic [001] axes of amphiboles were aligned subparallel to the lineation and the [100] axes were aligned subnormal to the foliation showing the weakest fabric strength among the samples (Fig. 5.5f–g). In the samples 2462 and 1015Y, the crystallographic [001] axes of amphiboles were aligned parallel to the lineation and the [100] axes were aligned normal to the

foliation showing a strong fabric strength (Fig. 5.5h–i and 5.5l–m). These samples showed the stronger fabric strengths of the amphiboles in the CR area and GR layer than those in the CP area and GP area (Fig. 5.5h–i and 5.5l–m), respectively. In the MD layer of the sample 2444, the crystallographic [001] axes of amphiboles were aligned subparallel to the lineation showing a weak girdle distribution subparallel to the foliation, and the [100] axes were aligned subnormal to the foliation (Fig. 5.5j). In the WD layer of the sample 2444, the [001] axes of amphiboles were aligned subparallel to the lineation and the [100] axes and the (010) poles were distributed in girdle shape subnormal to the lineation with clusters aligned subnormal to the foliation (Fig. 5.5k).

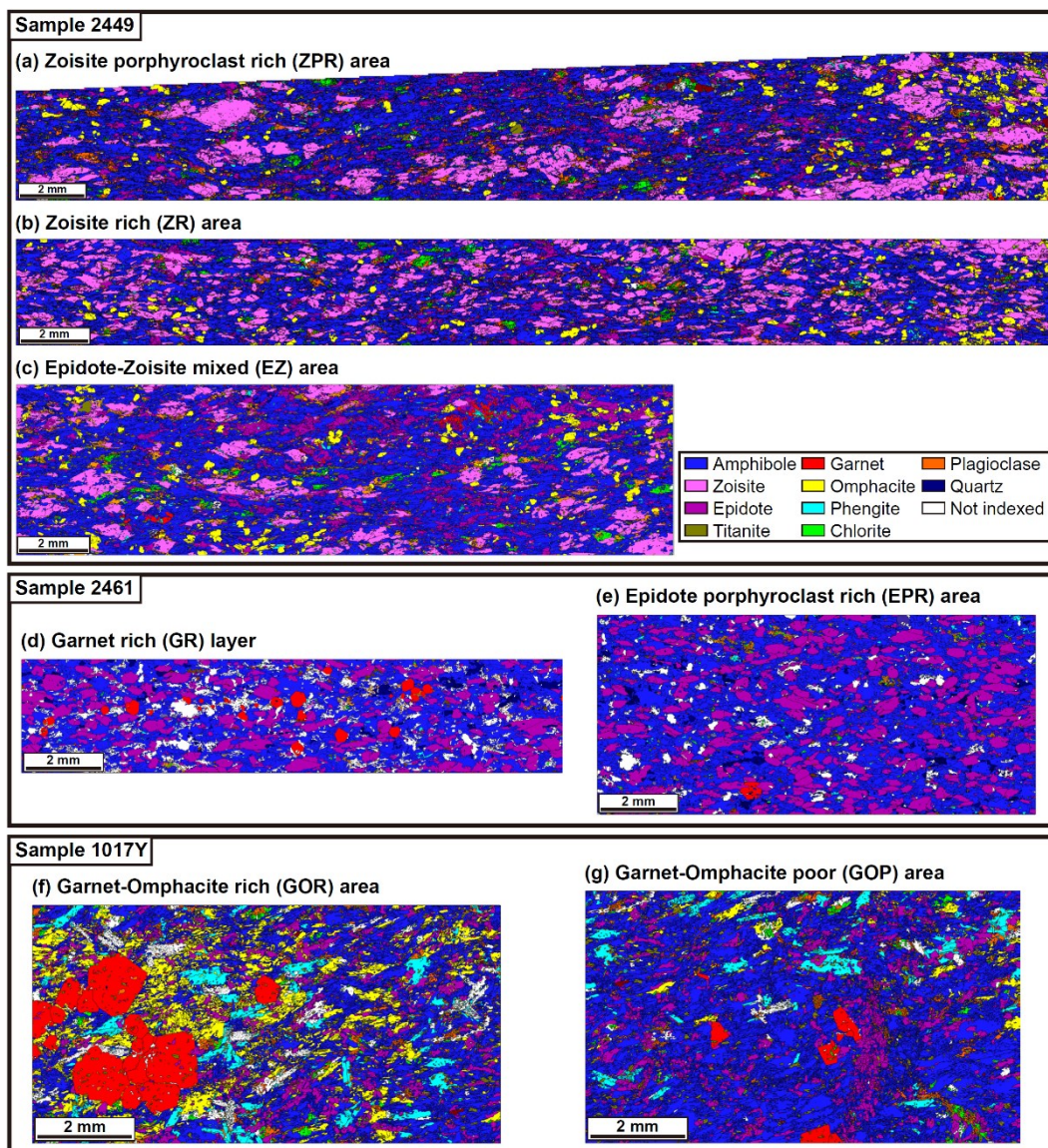


**Figure 5.4.** EBSD phase color maps of analyzed areas in each sample. **(a)–(c)** Zoisite eclogite-epidote blueschist facies rock (sample 2449); **(d)–(e)** zoisite bearing epidote blueschist facies rock (sample 2461); **(f)–(g)** epidote eclogite-epidote blueschist facies rock (sample 1017Y); **(h)–(i)** lawsonite bearing epidote blueschist facies rock (sample 2462); **(j)–(k)** felsic blueschist facies rock (sample 2444); **(l)–(m)** epidote blueschist-upper greenschist facies rock (sample 1015Y).

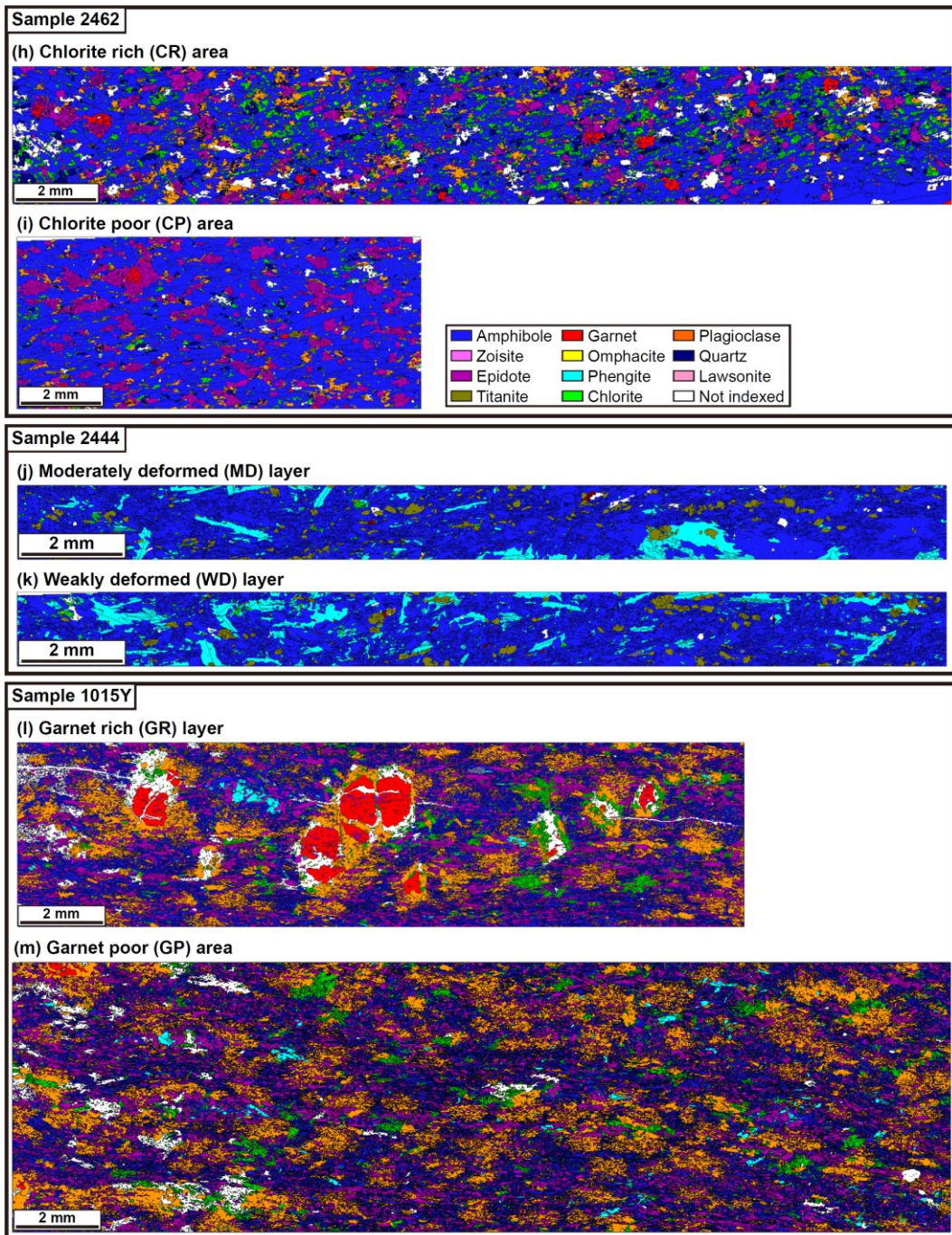
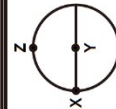


**Figure 5.4.** (continued).

Sample	Amphibole			
2449 (a) ZPR area				
	N = 26156, J = 4.7665, M = 0.1788			
(b) ZR area				
	N = 18012, J = 4.7543, M = 0.1730			
(c) EZ area				
	N = 20589, J = 4.3309, M = 0.1618			
2461 (d) GR layer				
	N = 8109, J = 4.8610, M = 0.1520			
(e) EPR area				
	N = 7371, J = 4.5756, M = 0.1591			
1017Y (f) GOR area				
	N = 15838, J = 3.0393, M = 0.1062			
(g) GOP area				
	N = 20633, J = 2.0804, M = 0.0590			
Sample	Amphibole			
2462 (h) CR area				
	N = 4406, J = 7.3760, M = 0.2225			
(i) CP area				
	N = 1888, J = 5.4470, M = 0.1780			
2444 (j) MD layer				
	N = 10271, J = 4.2535, M = 0.1333			
(k) WD layer				
	N = 9294, J = 3.1789, M = 0.0923			
1015Y (l) GR layer				
	N = 58527, J = 10.0809, M = 0.3015			
(m) GP area				
	N = 120782, J = 8.7121, M = 0.2680			



X: The lineation  
Y: The direction normal to the lineation within the foliation  
Z: The direction normal to the foliation

**Figure 5.5.** Pole figures of amphibole group minerals in **(a)–(c)** zoisite eclogite-epidote blueschist facies rock (sample 2449); **(d)–(e)** zoisite bearing epidote blueschist facies rock (sample 2461); **(f)–(g)** epidote eclogite-epidote blueschist facies rock (sample 1017Y); **(h)–(i)** lawsonite bearing epidote blueschist facies rock (sample 2462); **(j)–(k)** felsic blueschist facies rock (sample 2444); and **(l)–(m)** epidote blueschist-upper greenschist facies rock (sample 1015Y). The pole figures were presented as one point per grain in the lower hemisphere using an equal-area projection. The X-direction corresponds to the lineation of sample, and Z-direction corresponds to the direction normal to the foliation. N: the number of grains, J: the J-index value, and M: the M-index value.

#### 5.4.1.2. LPOs of epidote group minerals

There were two different epidote group minerals in this study: one is a zoisite, which is the orthorhombic crystal symmetry and Fe<sup>3+</sup>-poor chemical composition, and the other is an epidote, which is the monoclinic crystal symmetry and Fe<sup>3+</sup>-rich chemical composition. In the sample 2449, zoisite and epidote exhibited similar LPOs but different fabric strength according to the area (Figs. 5.6a–c and 5.7a–c). In the ZPR area, the fabric strength of zoisite was stronger than that of epidote. The crystallographic [010] axes of zoisites were in parallel alignment with the lineation and the [100] and [001] axes were subnormally aligned with the foliation showing a girdle distribution subnormal to the lineation (Fig. 5.6a). The epidotes were also aligned in a similar direction in which the zoisites were aligned, but the (010) poles of epidotes showed a weak girdle distribution subparallel to the foliation unlike the zoisite (Fig. 5.7a). In the ZR area, the fabric strength of zoisite was similar with that of epidote. The [010] axes of zoisites and the (010) poles of epidotes were in parallel alignment with the lineation (Figs. 5.6b and 5.7b). The [100] axes of zoisites and epidotes were subnormally aligned with the foliation showing a weak girdle distribution normal to the lineation (Figs. 5.6b and 5.7b). The [001] axes of zoisites and epidotes also showed a girdle distribution normal to the lineation, but the maximum clusters were subnormal to the lineation within the foliation (Figs. 5.6b and 5.7b). In the EZ area, the fabric strength of zoisite was much stronger than that of epidote. The [010] axes of zoisites were in parallel alignment with the lineation (Fig. 5.6c). The [100] and [001] axes of zoisites were subnormally aligned with the

foliation showing a girdle distribution subnormal to the lineation, but the cluster of the [001] axes was more strongly aligned than that of the [100] axes (Fig. 5.6c). The epidotes were also aligned in a similar direction in which the zoisites were aligned, but unlike the zoisite, the (010) poles of epidotes showed a weak girdle distribution subparallel to the foliation (Fig. 5.7c). Although the zoisite is also present in the sample 2461, it is difficult to see the LPO since this sample has very few zoisites (Figs. 5.4d–e and 5.6d–e). In the sample 2461, the (010) poles of epidotes were in subparallel alignment with the lineation showing a girdle distribution subparallel to the foliation and the [001] axes were subnormally aligned with the foliation (Fig. 5.7d–e).

In the samples 1017Y and 2462, the fabric strength of epidotes was much weaker than that of epidotes in other samples (Fig. 5.7f–i). In the GOR area of the sample 1017Y, the crystallographic (010) poles of epidotes were in parallel alignment with the lineation showing a girdle distribution subparallel to the foliation, and the [100] and [001] axes were subnormally aligned with the foliation (Fig. 5.7f). The maximum cluster of the [001] axes was more strongly aligned than that of the [100] axes (Fig. 5.7f). In the GOP area of the sample 1017Y, however, the (010) poles of epidotes were subnormally aligned with the lineation within the foliation showing girdle distribution subparallel to the foliation, and the [001] axes were subnormally aligned with the foliation (Fig. 5.7g). In the CR area of the sample 2462, the (010) poles of epidotes were in subparallel alignment with the lineation showing a girdle distribution subparallel to the foliation, and the [100] and [001] axes were subnormally aligned with the foliation (Fig. 5.7h). In the CP area of the sample 2462, the (010) poles of epidotes showed girdle distribution subparallel to the foliation and

the [001] axes were subnormally aligned with the foliation showing a girdle distribution subnormal to the lineation (Fig. 5.7i). In the sample 1015Y, the (010) poles of epidotes were in subparallel alignment with the lineation showing a weak girdle distribution subparallel to the foliation, and the [100] and [001] axes were subnormally aligned with the foliation showing a girdle distribution subnormal to the lineation (Fig. 5.7l–m). The maximum cluster of the [001] axes was more strongly aligned than that of the [100] axes (Fig. 5.7l–m).

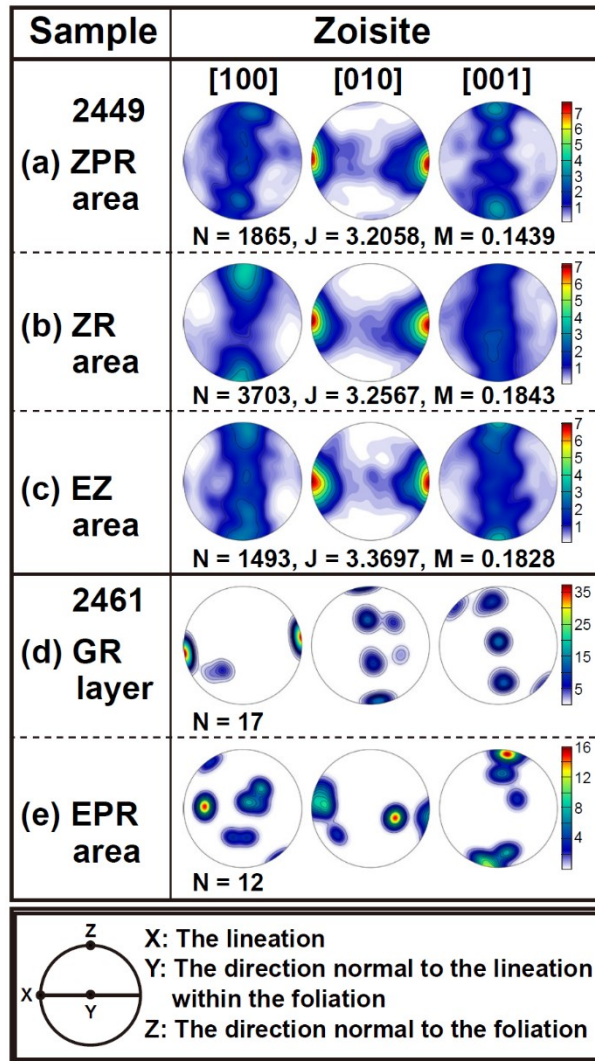


**Figure 5.6.** Pole figures of zoisite in (a)–(c) zoisite eclogite-epidote blueschist facies rock (sample 2449); and (d)–(e) zoisite bearing epidote blueschist facies rock (sample 2461). The pole figures were presented as one point per grain in the lower hemisphere using an equal-area projection. The X-direction corresponds to the lineation of sample, and Z-direction corresponds to the direction normal to the foliation. N: the number of grains, J: the J-index value, and M: the M-index value.

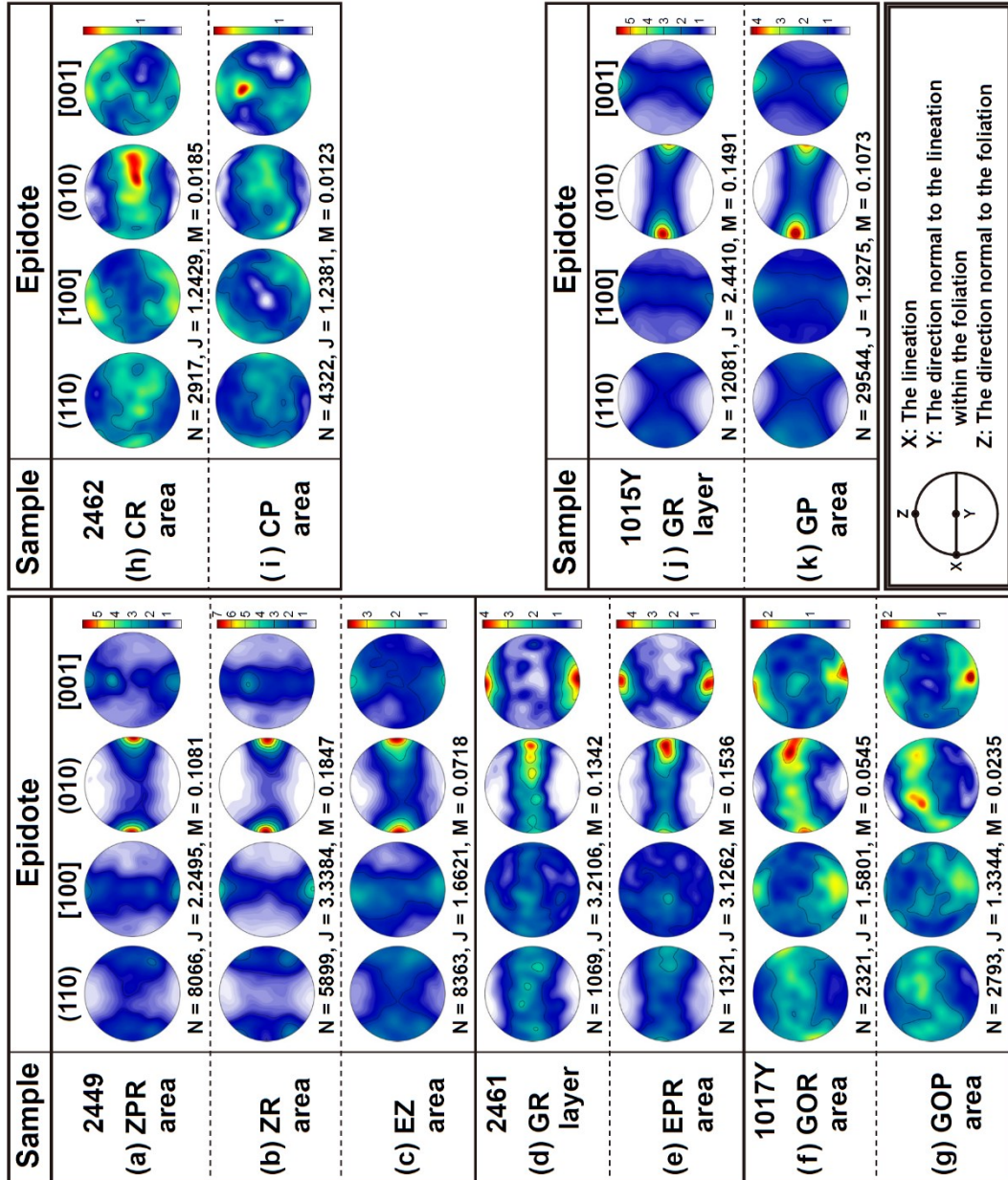


**Figure 5.7.** Pole figures of epidote in **(a)–(c)** zoisite eclogite-epidote blueschist facies rock (sample 2449); **(d)–(e)** zoisite bearing epidote blueschist facies rock (sample 2461); **(f)–(g)** epidote eclogite-epidote blueschist facies rock (sample 1017Y); **(h)–(i)** lawsonite bearing epidote blueschist facies rock (sample 2462); and **(j)–(k)** epidote blueschist-upper greenschist facies rock (sample 1015Y). The pole figures were presented as one point per grain in the lower hemisphere using an equal-area projection. The X-direction corresponds to the lineation of sample, and Z-direction corresponds to the direction normal to the foliation. N: the number of grains, J: the J-index value, and M: the M-index value.

#### 5.4.1.3. *LPOs of omphacite*

Omphacite minerals existed only in two eclogite facies metamorphic rocks overprinted by epidote blueschist facies metamorphism (samples 2449 and 1017Y). They had relatively weak fabric strength but showed obvious fabric trends (Fig. 5.8). In the sample 2449, the crystallographic [001] axes of omphacites were in subparallel alignment with the lineation, and the [100] axes were subnormally aligned with the foliation (Fig. 5.8a–c). The omphacite in ZPR area exhibited the weakest fabric strength (Fig. 5.8a), and that in EZ area showed the strongest fabric strength (Fig. 5.8c). In the sample 1017Y, the [001] axes of omphacites were in subparallel alignment with the lineation like those in the sample 2449, but the crystallographic axes aligned subnormal to the foliation was not [100] axes but (010) poles (Fig. 5.8d–e). The (010) poles of omphacite in GOR area also showed a girdle distribution subnormal to the lineation (Fig. 5.8d). In the GOP area, the J-index of omphacite was larger than that in the GOR area, whereas in the GOR area, the M-index of omphacite was larger than that in the GOP area (Fig. 5.8d–e).

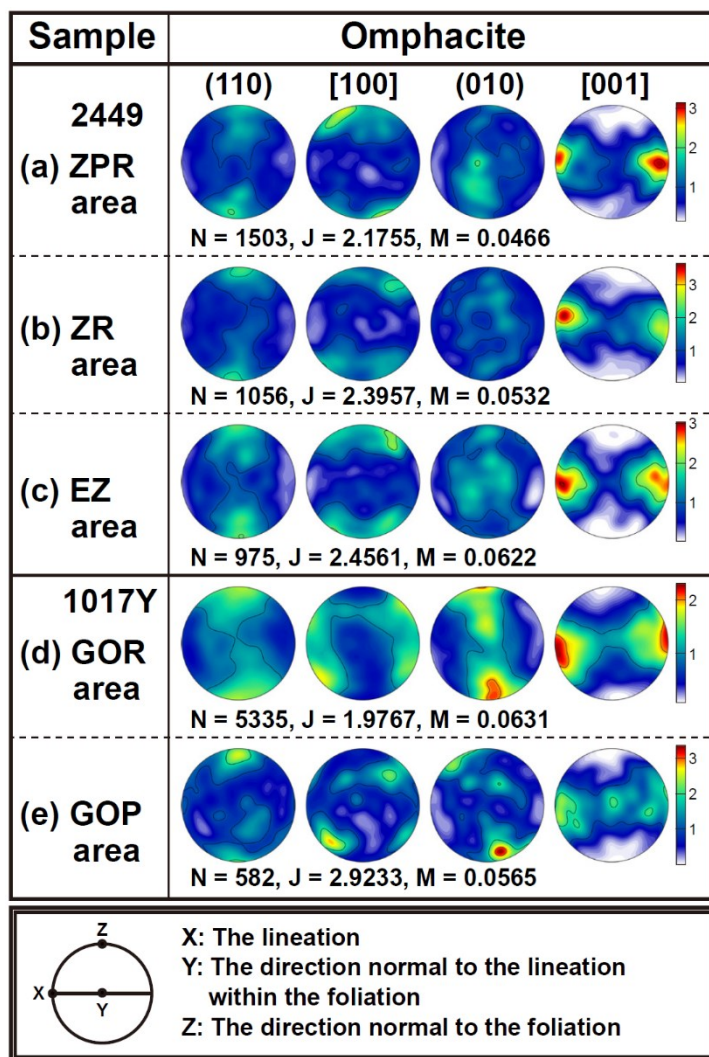


**Figure 5.8.** Pole figures of omphacite in (a)–(c) zoisite eclogite-epidote blueschist facies rock (sample 2449); and (d)–(e) epidote eclogite-epidote blueschist facies rock (sample 1017Y). The pole figures were presented as one point per grain in the lower hemisphere using an equal-area projection. The X-direction corresponds to the lineation of sample, and Z-direction corresponds to the direction normal to the foliation. N: the number of grains, J: the J-index value, and M: the M-index value.

#### 5.4.1.4. LPOs of phengite

In most samples, the crystallographic [001] axes of phengites were subnormally aligned with the foliation showing high concentration to that direction, but the [100] axes and the (110) and (010) poles were differently aligned according to the samples (Fig. 5.9). In the sample 2449, the [100] axes and the (110) and (010) poles of phengites were aligned subparallel to the foliation showing a girdle distribution, and the clusters of these axes and poles were in subparallel alignment with the lineation (Fig. 5.9a–c). In the sample 2461, on the other hand, the [100] axes and the (110) and (010) poles of phengites were in subparallel alignment with the foliation showing scattered patterns (Fig. 5.9d–e). However, the clusters of these axes and poles were in both subparallel and subnormal alignments with the lineation within the foliation (Fig. 5.9d–e). In the sample 1017Y, the [100] axes and the (110) and (010) poles of phengites were also in subparallel alignments with the foliation showing scattered pattern (Fig. 5.9f–g). The maximum cluster of the [100] axes was aligned more subparallel to the lineation than that of the (010) poles in the GOR area, but vice versa in the GOP area (Fig. 5.9f–g).

In the sample 2462, the number of phengite grains was insufficient to construct the LPO and the [100] axes and the (110) and (010) poles of phengites were scattered to all direction (Fig. 5.9h–i). However, the [001] axes were aligned subnormal to the lineation showing a girdle distribution and the large clusters were in both subnormal and subparallel alignments with the foliation (Fig. 5.9h–i). In the sample 2444, the

[100] axes and the (110) and (010) poles of phengites were aligned subparallel to the foliation showing a girdle distribution, and the maximum clusters of the [100] axes and the (010) poles were aligned subparallel and subnormal to the lineation within the foliation, respectively (Fig. 5.9j–k). In the sample 1015Y, the [100] axes and the (110) and (010) poles of phengites were in subparallel alignments with the foliation showing a weak girdle distribution (Fig. 5.9l–m). However, the maximum clusters of the [100] axes in the GR layer and the (010) poles in the GP area were aligned more subparallel to the lineation than the others in each area (Fig. 5.8l–m).

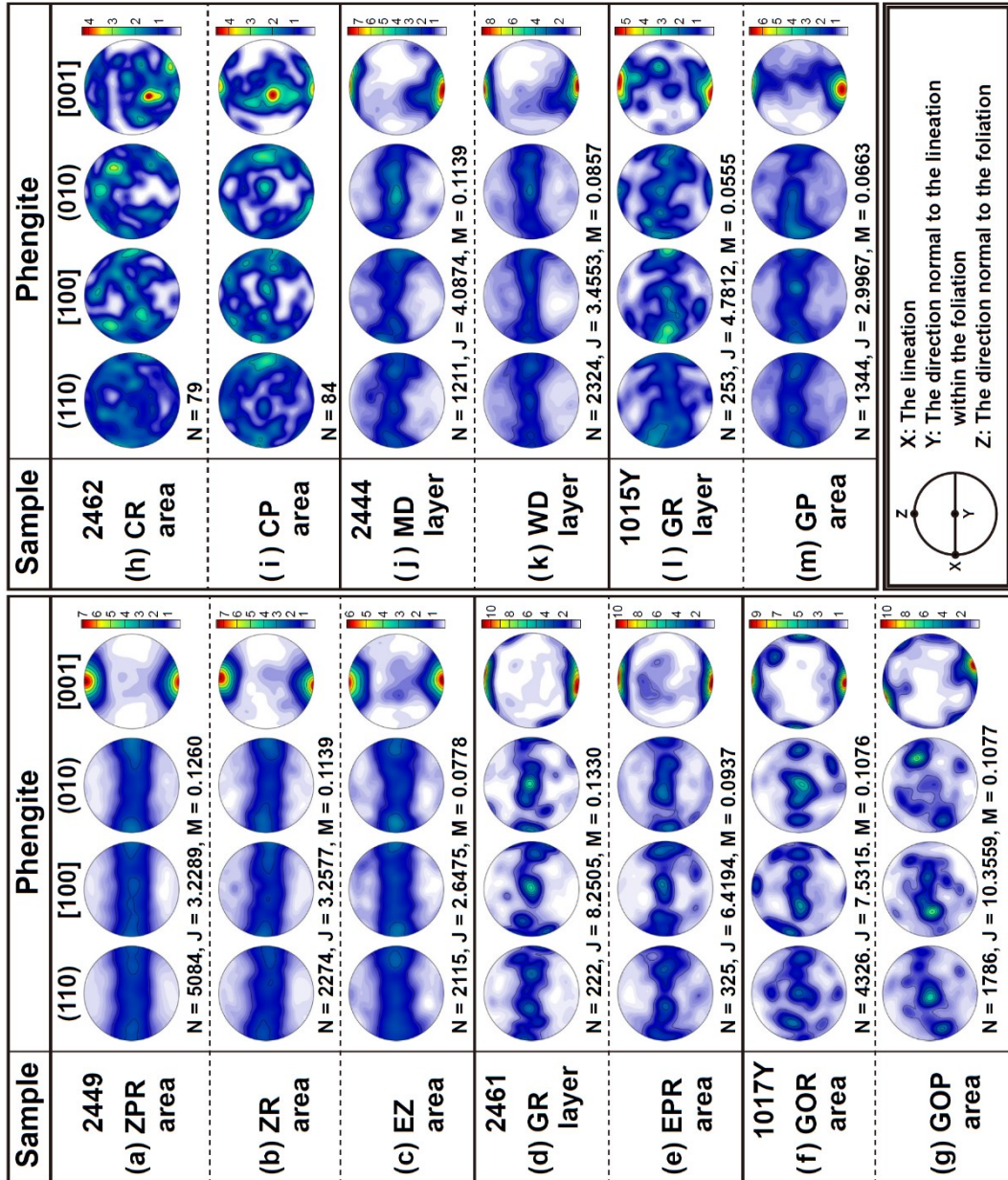


**Figure 5.9.** Pole figures of phengite in **(a)–(c)** zoisite eclogite-epidote blueschist facies rock (sample 2449); **(d)–(e)** zoisite bearing epidote blueschist facies rock (sample 2461); **(f)–(g)** epidote eclogite-epidote blueschist facies rock (sample 1017Y); **(h)–(i)** lawsonite bearing epidote blueschist facies rock (sample 2462); **(j)–(k)** felsic blueschist facies rock (sample 2444); and **(l)–(m)** epidote blueschist-upper greenschist facies rock (sample 1015Y). The pole figures were presented as one point per grain in the lower hemisphere using an equal-area projection. The X-direction corresponds to the lineation of sample, and Z-direction corresponds to the direction normal to the foliation. N: the number of grains, J: the J-index value, and M: the M-index value.

#### 5.4.1.5. LPOs of garnet

All samples contained several grains of garnet except for the sample 2444. In these samples, the number of garnet grains was mostly insufficient to construct the LPO (Fig. 5.10). However, the number of fine-grained garnets in the EZ area of the sample 2449 was sufficient to make up the LPO and exhibited some trends (Fig. 5.10c). In this area, the [100] axes of garnet were obliquely aligned to the lineation and foliation showing orthogonal pattern, and the [110] and [111] axes were in subparallel and subnormal alignments with lineation and foliation (Fig. 5.10c). However, the cluster of [110] axes showed more subparallel alignment with the lineation than that of the [111] axes, and the cluster of [111] axes showed more subnormal alignment with the foliation than that of the [110] axes (Fig. 5.10c).



#### 5.4.1.6. LPOs of quartz, chlorite, titanite, and albite

##### ***Quartz***

Although quartz minerals are present in four samples, but only two samples have enough number of quartz grains to construct the LPO (Samples 2461 and 2462). In the sample 2461, the (0001) poles (or, c-axes) of quartzes showed a weak crossed girdle distribution with multiple point maxima between the lineation and the direction normal to the foliation (Fig. 5.11a–b). The opening angle of the c-axis maxima is  $\sim 70^\circ$  (Fig. 5.11a–b). In the sample 2462, on the other hand, the c-axes of quartzes were in subparallel alignment with the lineation and the (11-20) and (10-10) poles were subnormally aligned with the lineation showing a girdle distribution (Fig. 5.11c–d).

##### ***Chlorite***

In most samples, the [001] axes of chlorites were subnormally aligned with the foliation showing high concentration to that direction, but there were some clusters of the [001] axes aligned subnormal to the lineation within the foliation (Fig. 5.12). In these samples, the [100] axes and the (110) and (010) poles of chlorites were aligned subparallel to the foliation showing a weak girdle distribution, and the clusters of these axes and poles were in both subparallel and subnormal alignment with the lineation within the foliation (Fig. 5.12). In the sample 1017Y, however, the crystallographic axes of chlorites were scattered, and some clusters of the [100] and [001] axes were aligned subnormal to the lineation within the foliation (Fig. 5.12f–

g). In the sample 1015Y, on the other hand, the [001] axes of chlorites exhibited a strong girdle distribution subnormal to the lineation, with strong cluster aligned subnormal to the foliation and moderate cluster aligned subnormal to the lineation within the foliation (Fig. 5.12l–m).

### ***Titanite***

In most samples, the (010) poles and [001] axes of titanites were in subparallel alignment with the foliation showing a girdle distribution, and the (110) poles and [100] axes were subnormally aligned with the foliation (Fig. 5.13). In three samples (2449, 2444, and 1015Y), the maximum cluster of the (010) poles were aligned subparallel to the lineation (Fig. 5.13a–c and 5.13j–m). In other samples (2461, 1017Y, and 2462), the maximum cluster of the [001] axes were aligned subparallel to the lineation (Fig. 5.13d–i). In the sample 2449 and 1015Y, fabric strength of titanite was strong (Fig. 5.13a–c and 5.13l–m), but titanites in other samples exhibited a relatively weak fabric strength (Fig. 5.13d–k).

### ***Albite***

In most samples, the fabric strength of albite was relatively weak, but the (100) poles of albites were subnormally aligned with the foliation (Fig. 5.14). In the sample 2449, the (001) poles were in subparallel alignment with the lineation (Fig. 5.15a–c). In the sample 2461, the (010) poles were in subparallel alignment with the lineation (Fig. 5.14d–e). In the other samples, the (010) and (001) poles exhibited scattering distributions (Fig. 5.14f–k).

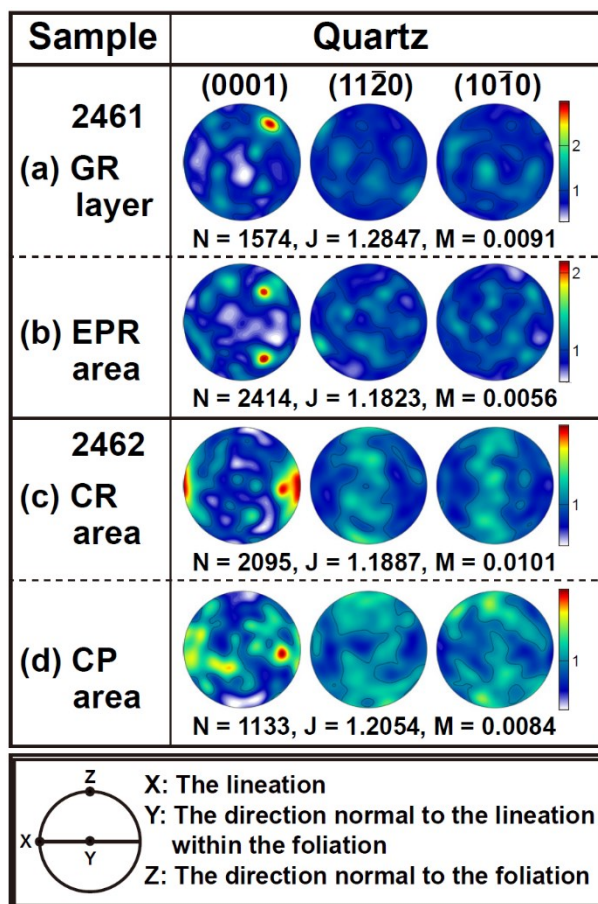


**Figure 5.11.** Pole figures of quartz in (a)–(b) zoisite bearing epidote blueschist facies rock (sample 2461); and (c)–(d) lawsonite bearing epidote blueschist facies rock (sample 2462). The pole figures were presented as one point per grain in the lower hemisphere using an equal-area projection. The X-direction corresponds to the lineation of sample, and Z-direction corresponds to the direction normal to the foliation. N: the number of grains, J: the J-index value, and M: the M-index value.

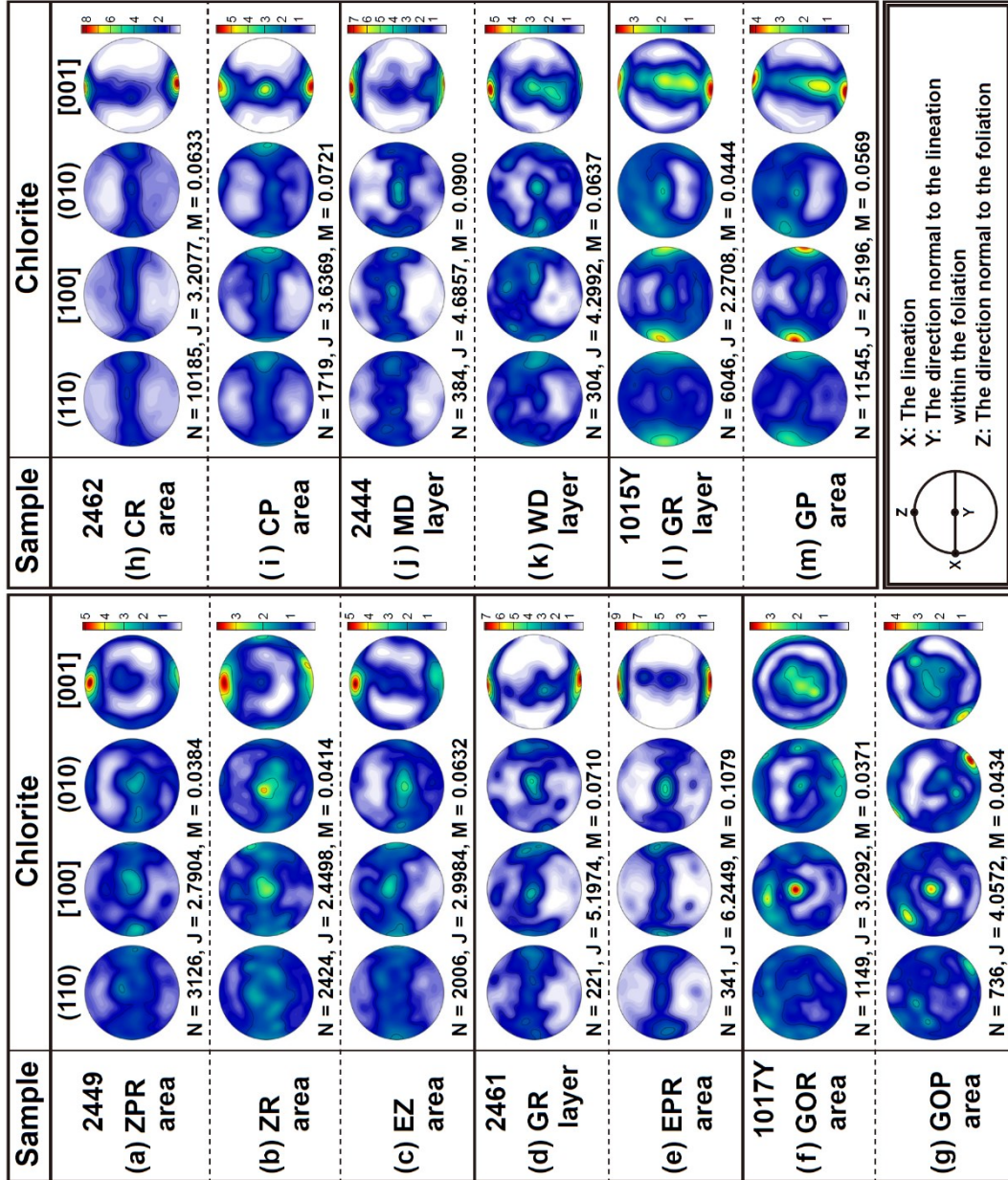


**Figure 5.12.** Pole figures of chlorite in **(a)–(c)** zoisite eclogite-epidote blueschist facies rock (sample 2449); **(d)–(e)** zoisite bearing epidote blueschist facies rock (sample 2461); **(f)–(g)** epidote eclogite-epidote blueschist facies rock (sample 1017Y); **(h)–(i)** lawsonite bearing epidote blueschist facies rock (sample 2462); **(j)–(k)** felsic blueschist facies rock (sample 2444); and **(l)–(m)** epidote blueschist-upper greenschist facies rock (sample 1015Y). The pole figures were presented as one point per grain in the lower hemisphere using an equal-area projection. The X-direction corresponds to the lineation of sample, and Z-direction corresponds to the direction normal to the foliation. N: the number of grains, J: the J-index value, and M: the M-index value.

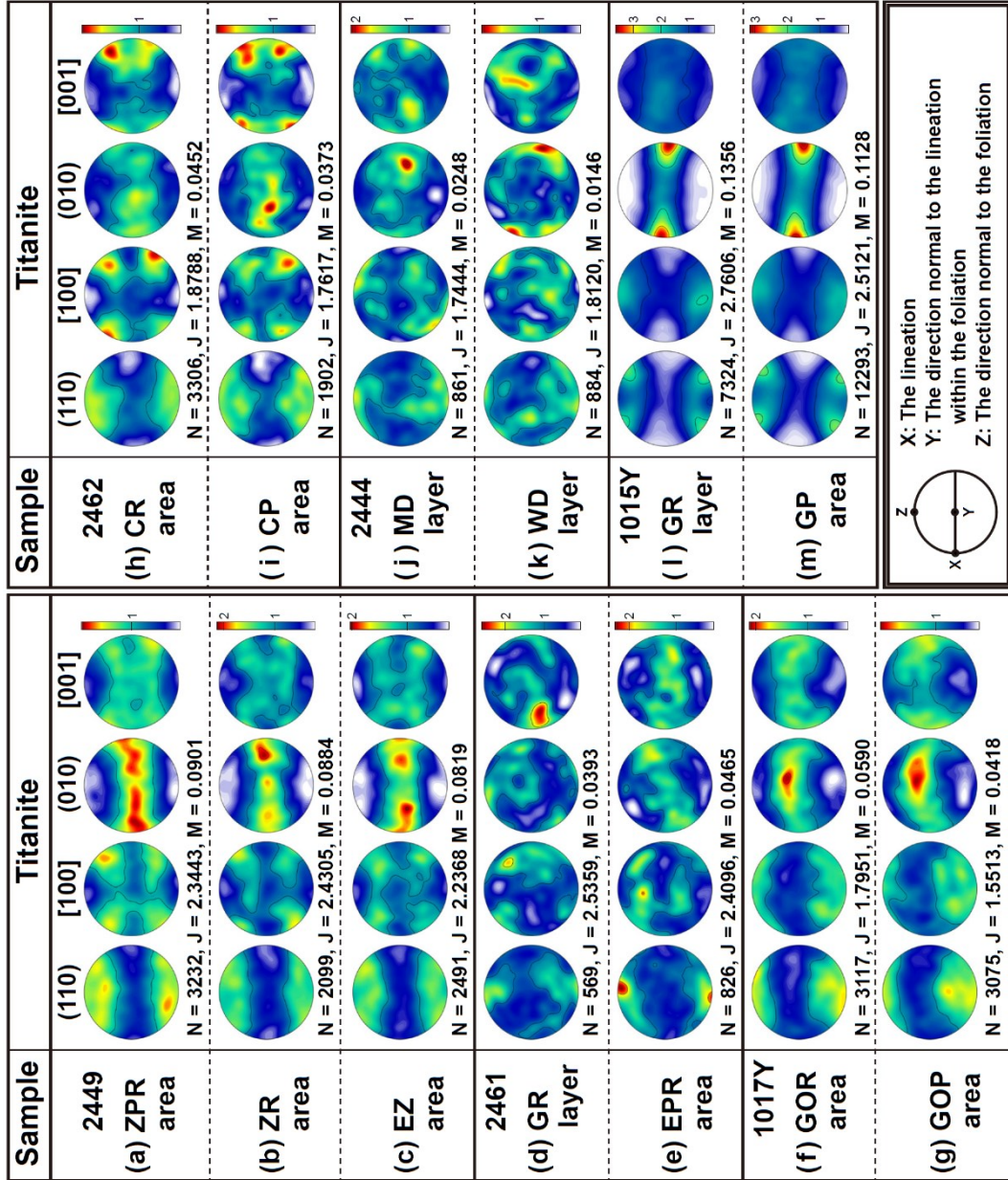


**Figure 5.13.** Pole figures of titanite in **(a)–(c)** zoisite eclogite-epidote blueschist facies rock (sample 2449); **(d)–(e)** zoisite bearing epidote blueschist facies rock (sample 2461); **(f)–(g)** epidote eclogite-epidote blueschist facies rock (sample 1017Y); **(h)–(i)** lawsonite bearing epidote blueschist facies rock (sample 2462); **(j)–(k)** felsic blueschist facies rock (sample 2444); and **(l)–(m)** epidote blueschist-upper greenschist facies rock (sample 1015Y). The pole figures were presented as one point per grain in the lower hemisphere using an equal-area projection. The X-direction corresponds to the lineation of sample, and Z-direction corresponds to the direction normal to the foliation. N: the number of grains, J: the J-index value, and M: the M-index value.

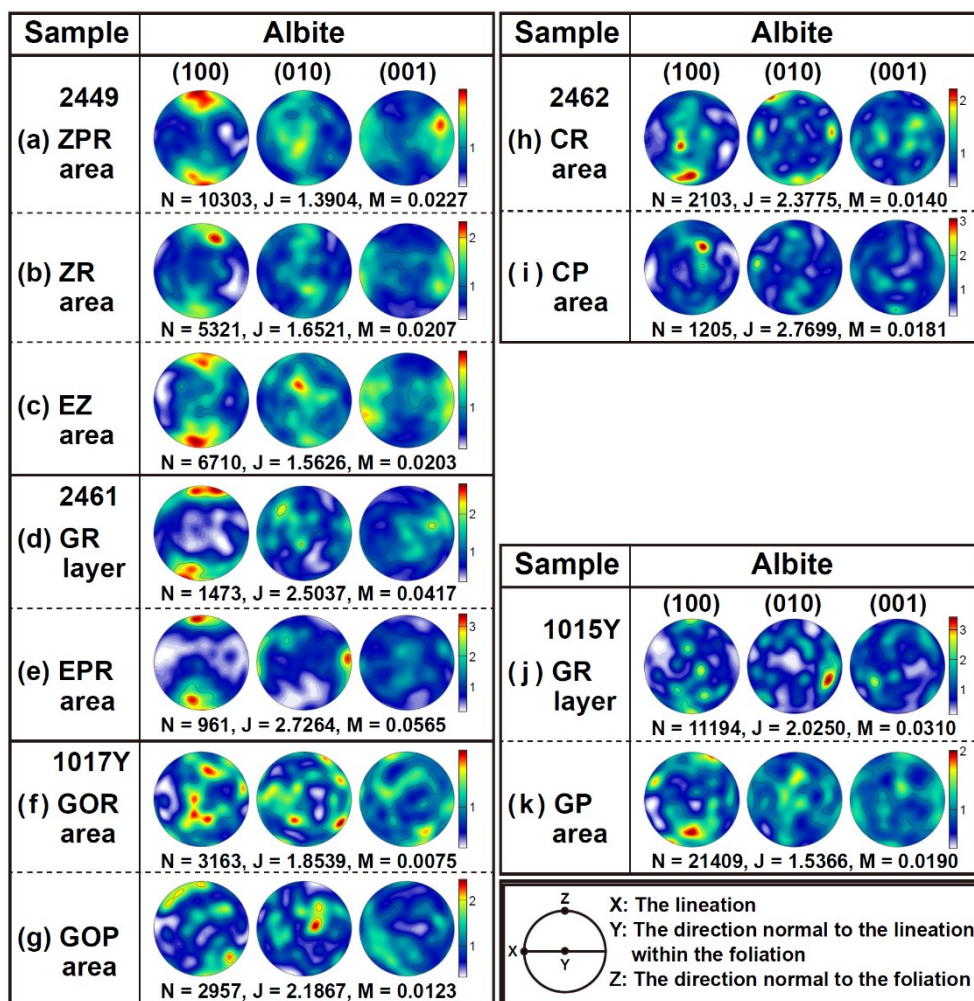


**Figure 5.14.** Pole figures of albite in (a)–(c) zoisite eclogite-epidote blueschist facies rock (sample 2449); (d)–(e) zoisite bearing epidote blueschist facies rock (sample 2461); (f)–(g) epidote eclogite-epidote blueschist facies rock (sample 1017Y); (h)–(i) lawsonite bearing epidote blueschist facies rock (sample 2462); and (j)–(k) epidote blueschist-upper greenschist facies rock (sample 1015Y). The pole figures were presented as one point per grain in the lower hemisphere using an equal-area projection. The X-direction corresponds to the lineation of sample, and Z-direction corresponds to the direction normal to the foliation. N: the number of grains, J: the J-index value, and M: the M-index value.

## 5.4.2. Seismic velocity and anisotropy of minerals

Seismic velocity and anisotropy of constituent minerals of the samples are shown in Figures 5.15–5.24. The average seismic velocity of P-wave ( $V_{p_{aver}}$ ) and S-wave ( $V_{s_{aver}}$ ) of minerals and whole rocks are summarized in Tables 5.8 and 5.9, respectively. The azimuthal anisotropy of P-wave (AVp) and maximum polarization anisotropy of S-wave (Max. AVs) of minerals and whole rocks were also summarized in Tables 5.10 and 5.11, respectively.

### 5.4.2.1. Polycrystalline amphibole group minerals

In most samples, the direction of the  $V_{p_{max}}$  of amphibole group minerals was subparallel to the lineation, and the direction of the  $V_{p_{min}}$  was subnormal to the foliation (Fig. 5.15). The low AVs region in AVs contour of amphiboles was placed in the direction subnormal to the foliation, but direction of the minimum AVs was subparallel to lineation except for amphiboles in the sample 2461 (Fig. 5.15). The  $V_{p_{aver}}$  and  $V_{s_{aver}}$  of polycrystalline amphiboles were in the range of 7.56–7.78 km/s and 4.51–4.56 km/s, respectively (Tables 5.8 and 5.9). The AVp and Max. AVs were 12.7–25.7 % and 7.10–14.27 %, respectively (Tables 5.10 and 5.11). The Vs1 polarization direction for polycrystalline amphiboles was subparallel to the lineation for the vertically propagating S-wave at the direction normal to the foliation.

**Table 5.8.** Average P-wave velocity (km/s) of the constituent minerals of the area analyzed in the samples.

Sample	Analyzed area	Amp	Ep	Zo	Phg	Grt	Omp	Qtz	Chl	Ttn	Ab	Lws	Whole rock
2449	ZPR area	7.67	7.39	8.15	6.07	8.54	8.46	-	7.56	7.17	6.40	-	7.60
	ZR area	7.66	7.42	8.22	6.13	8.54	8.46	-	7.59	7.17	6.41	-	7.69
	EZ area	7.69	7.36	8.15	6.14	8.54	8.44	-	7.57	7.20	6.41	-	7.62
2461	GR layer	7.59	7.35	8.21	6.09	8.54	-	6.08	7.66	7.27	6.41	-	7.43
	EPR area	7.56	7.39	8.15	6.17	8.54	-	6.07	7.71	7.23	6.38	-	7.41
1017Y	GOR area	7.67	7.35	-	6.12	8.54	8.38	-	7.57	7.23	6.39	-	7.64
	GOP area	7.70	7.34	-	6.11	8.54	8.39	-	7.63	7.23	6.38	-	7.51
2462	CR area	7.76	7.34	-	6.08	8.54	-	6.07	7.73	7.23	6.41	-	7.41
	CP area	7.73	7.35	-	6.20	8.54	-	6.05	7.75	7.24	6.39	-	7.49
2444	MD layer	7.70	-	-	6.10	-	-	-	7.66	7.29	-	-	7.50
	WD layer	7.78	-	-	6.15	-	-	-	7.68	7.30	-	-	7.48
1015Y	GR layer	7.75	7.44	-	5.98	8.54	-	-	7.66	7.21	6.37	-	7.25
	GP area	7.75	7.41	-	6.18	8.54	-	-	7.67	7.21	6.39	-	7.17

**Table 5.9.** Average S-wave velocity (km/s) of the constituent minerals of the area analyzed in the samples.

Sample	Analyzed area	Amp	Ep	Zo	Phg	Grt	Omp	Qtz	Chl	Ttn	Ab	Lws	Whole rock
2449	ZPR area	4.53	4.21	4.65	3.45	4.80	4.88	-	4.25	4.23	3.68	-	4.43
	ZR area	4.52	4.22	4.65	3.45	4.80	4.88	-	4.23	4.23	3.68	-	4.48
	EZ area	4.53	4.22	4.65	3.48	4.79	4.88	-	4.23	4.23	3.68	-	4.44
2461	GR layer	4.52	4.19	4.68	3.47	4.80	-	4.12	4.22	4.24	3.68	-	4.37
	EPR area	4.51	4.20	4.68	3.48	4.80	-	4.10	4.26	4.23	3.69	-	4.35
1017Y	GOR area	4.54	4.22	-	3.49	4.80	4.88	-	4.18	4.23	3.68	-	4.44
	GOP area	4.55	4.22	-	3.48	4.80	4.89	-	4.22	4.23	3.69	-	4.41
2462	CR area	4.54	4.22	-	3.52	4.80	-	4.10	4.22	4.24	3.68	-	4.33
	CP area	4.54	4.22	-	3.51	4.80	-	4.10	4.25	4.24	3.68	-	4.40
2444	MD layer	4.54	-	-	3.45	-	-	-	4.19	4.25	-	-	4.40
	WD layer	4.56	-	-	3.46	-	-	-	4.23	4.25	-	-	4.34
1015Y	GR layer	4.54	4.21	-	3.47	4.80	-	-	4.23	4.23	3.67	-	4.17
	GP area	4.54	4.22	-	3.51	4.79	-	-	4.24	4.23	3.67	-	4.13

**Table 5.10.** The azimuthal anisotropy of P-wave (%) of the constituent minerals of the area analyzed in the samples.

Sample	Analyzed area	Amp	Ep	Zo	Phg	Grt	Omp	Qtz	Chl	Ttn	Ab	Lws	Whole rock
2449	ZPR area	24.7	5.0	6.6	31.8	0.2	3.6	-	10.5	10.4	5.4	-	15.4
	ZR area	24.9	5.9	5.8	34.0	0.3	5.8	-	10.0	10.6	5.4	-	14.0
	EZ area	23.0	4.0	4.2	25.7	0.2	5.4	-	12.4	9.4	7.4	-	14.6
2461	GR layer	19.9	10.9	18.6	26.2	0.1	-	3.9	15.0	3.2	11.0	-	14.5
	EPR area	21.3	11.8	17.4	22.4	0.2	-	3.6	15.7	7.2	14.3	-	15.8
1017Y	GOR area	18.4	3.2	-	19.6	0.1	5.7	-	11.5	10.1	4.1	-	8.1
	GOP area	15.7	2.4	-	29.0	0.2	6.9	-	12.0	10.0	8.0	-	12.3
2462	CR area	24.2	2.2	-	16.9	0.1	-	3.5	14.1	5.9	6.9	-	15.8
	CP area	23.5	2.3	-	24.7	0.2	-	2.4	16.1	6.7	5.0	-	16.8
2444	MD layer	18.6	-	-	30.8	-	-	-	14.2	4.6	-	-	18.2
	WD layer	12.7	-	-	31.7	-	-	-	14.8	4.6	-	-	14.5
1015Y	GR layer	25.7	7.7	-	25.8	0.2	-	-	13.4	15.2	8.3	-	13.3
	GP area	24.7	6.4	-	20.0	0.3	-	-	13.3	13.3	5.0	-	12.6

**Table 5.11.** The maximum polarization anisotropy of S-wave (%) of the constituent minerals of the area analyzed in the samples.

Sample	Analyzed area	Amp	Ep	Zo	Phg	Grt	Omp	Qtz	Chl	Ttn	Ab	Lws	Whole rock
2449	ZPR area	13.36	4.64	5.83	28.89	0.35	2.06	-	16.04	5.17	5.46	-	9.58
	ZR area	14.00	4.90	5.11	32.01	0.76	1.75	-	13.77	5.24	5.44	-	9.75
	EZ area	12.61	3.35	6.04	22.30	0.51	1.90	-	17.37	4.69	6.24	-	8.87
2461	GR layer	11.87	11.30	15.64	29.62	0.19	-	5.27	16.88	2.18	8.98	-	10.32
	EPR area	12.67	12.14	18.68	26.00	0.54	-	4.48	22.61	3.54	12.22	-	11.41
1017Y	GOR area	10.62	4.32	-	14.83	0.21	2.89	-	18.59	4.99	6.03	-	5.27
	GOP area	9.25	2.82	-	20.06	0.41	3.84	-	17.48	5.20	8.88	-	7.51
2462	CR area	13.74	2.17	-	13.84	0.27	-	4.08	17.65	3.22	7.36	-	9.64
	CP area	13.33	2.56	-	21.05	0.42	-	3.12	19.02	3.48	5.70	-	9.41
2444	MD layer	10.34	-	-	21.30	-	-	-	20.61	3.34	-	-	10.23
	WD layer	7.10	-	-	24.36	-	-	-	16.17	3.69	-	-	9.22
1015Y	GR layer	14.27	6.68	-	18.06	0.43	-	-	14.90	7.23	6.00	-	7.19
	GP area	13.53	4.62	-	19.63	0.64	-	-	14.69	6.19	5.15	-	7.83

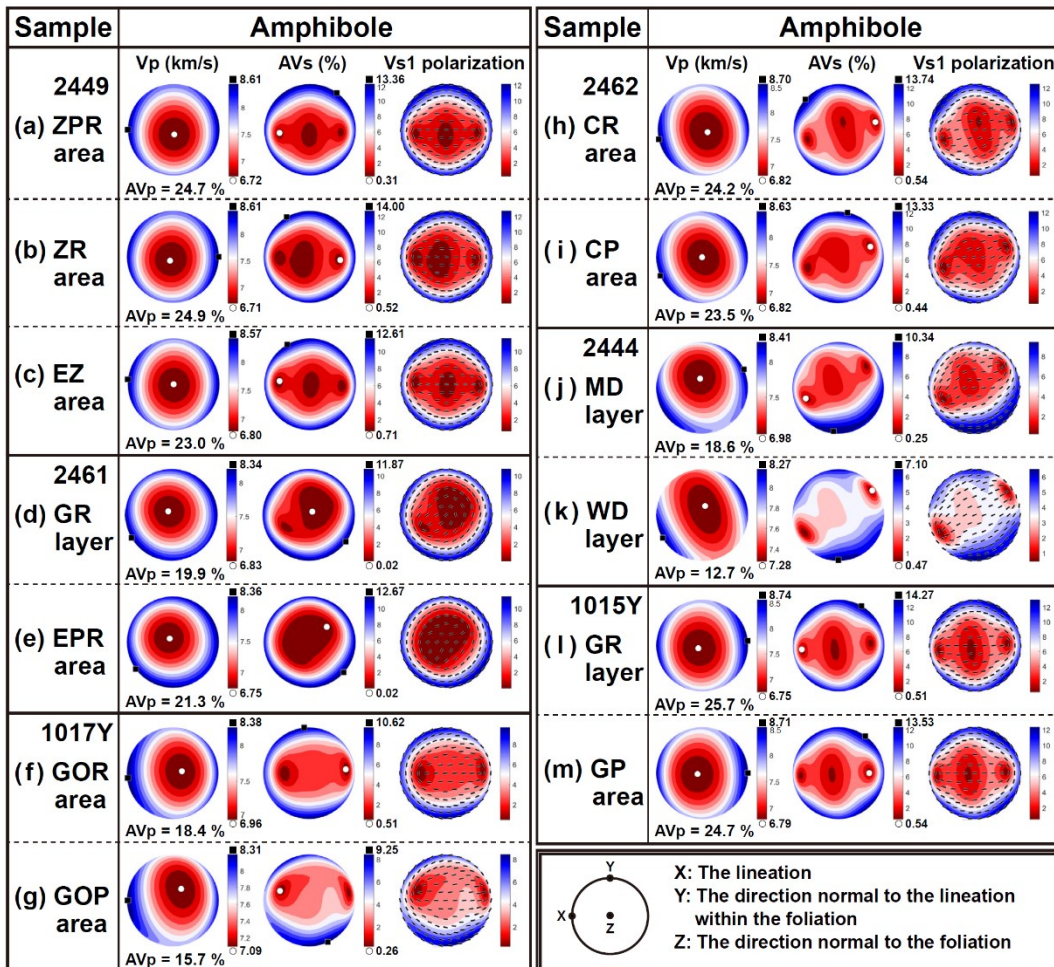


**Figure 5.15.** Seismic velocity and anisotropy of polycrystalline amphiboles calculated using crystallographic orientation data from EBSD analysis and the elastic stiffness coefficients of glaucophane (Bezacier et al., 2010a). The E-W direction corresponds to the lineation (X), and the center of a stereographic projection circle is the direction normal to the foliation (Z). The contours of P-wave velocity (Vp), the contours of S-wave polarization anisotropy (AVs), and polarization directions of the fast shear wave (Vs1) are shown.

#### 5.4.2.2. Polycrystalline epidote group minerals

There are two epidote group minerals, zoisite and epidote. The  $V_{p_{\max}}$  direction of zoisites was subnormal to the lineation within the foliation, and the  $V_{p_{\min}}$  direction was subparallel to the lineation (Fig. 5.16). In contrast, the  $V_{p_{\max}}$  direction of epidotes was subparallel to the lineation, and the  $V_{p_{\min}}$  direction was subnormal to the foliation, except for epidotes in the CP area of the sample 2462 (Fig. 5.17). The high AVs region in AVs contour of zoisites was placed in the direction subnormal to the foliation (Fig. 5.16). On the other hand, the low AVs region in AVs contour of epidotes was placed in the direction subnormal to the foliation, except for epidote in the sample 2462 (Fig. 5.17). The  $V_{p_{\text{aver}}}$  and  $V_{s_{\text{aver}}}$  of polycrystalline zoisites were 8.15–8.22 km/s and 4.65 km/s, respectively, and those of epidotes were in the range of 7.34–7.44 km/s and 4.19–4.22 km/s, respectively (Tables 5.8 and 5.9). The AVp and Max. AVs of zoisites were 4.2–6.6 % and 5.11–6.04 %, respectively, and those of epidotes were 2.2–11.8 % and 2.17–12.14 %, respectively (Tables 5.10 and 5.11). The  $V_{s1}$  polarization direction of polycrystalline zoisites and epidotes in the samples 2449 and 2461 was subnormal to the lineation, but that of epidotes in the other samples (1015Y, 1017Y, and 2462) was subparallel to the lineation for the vertically propagating S-wave at the direction normal to the foliation (Figs. 5.16 and 5.17).

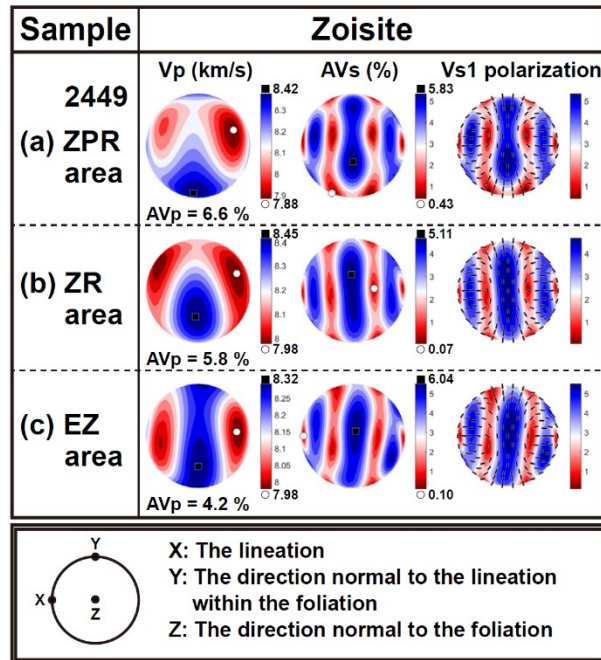


**Figure 5.16.** Seismic velocity and anisotropy of polycrystalline zoisites calculated using crystallographic orientation data from EBSD analysis and the elastic stiffness coefficients of zoisite (Mao et al., 2007). The E-W direction corresponds to the lineation (X), and the center of a stereographic projection circle is the direction normal to the foliation (Z). The contours of P-wave velocity ( $V_p$ ), the contours of S-wave polarization anisotropy (AVs), and polarization directions of the fast shear wave ( $V_{s1}$ ) are shown.

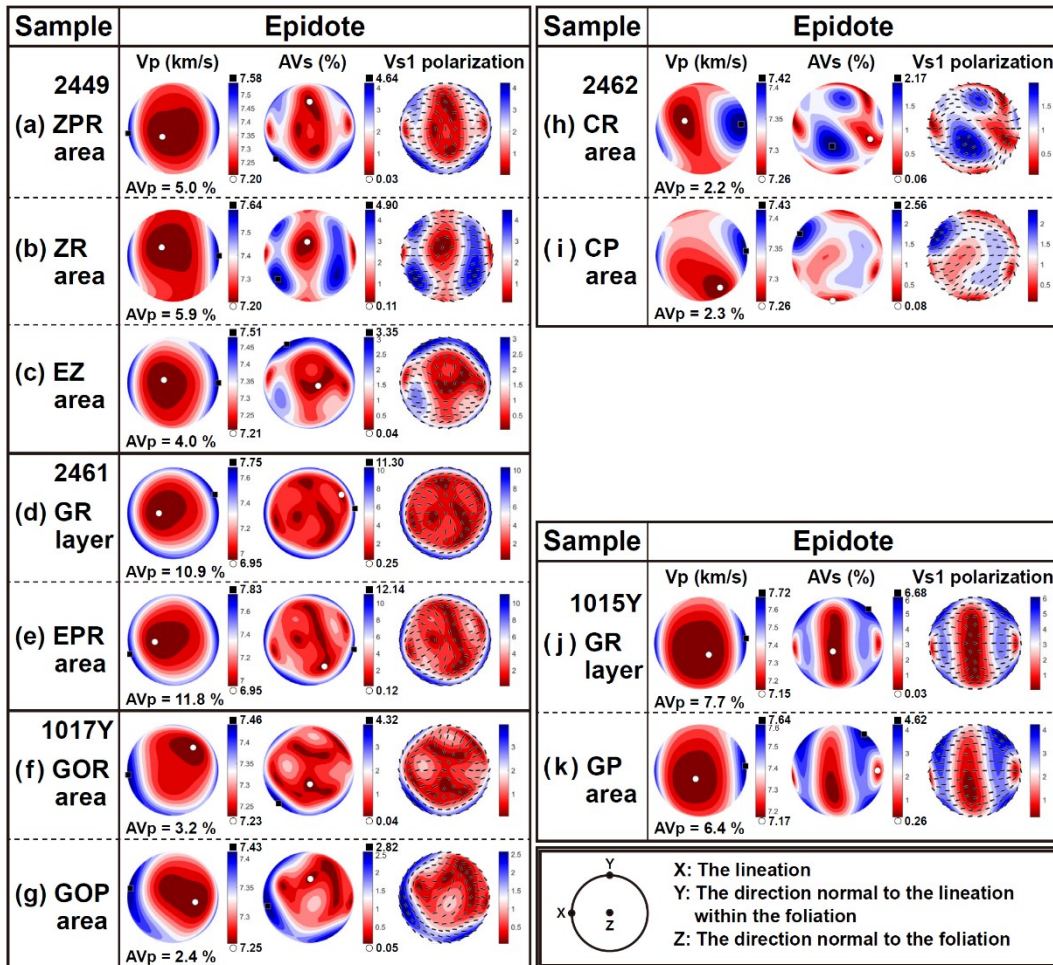


**Figure 5.17.** Seismic velocity and anisotropy of polycrystalline epidotes calculated using crystallographic orientation data from EBSD analysis and the elastic stiffness coefficients of epidote (Aleksandrov et al., 1974). The E-W direction corresponds to the lineation (X), and the center of a stereographic projection circle is the direction normal to the foliation (Z). The contours of P-wave velocity (Vp), the contours of S-wave polarization anisotropy (AVs), and polarization directions of the fast shear wave (Vs1) are shown.

#### 5.4.2.3. *Polycrystalline omphacites*

The  $V_{p_{\max}}$  direction of polycrystalline omphacites was subnormal to the foliation, and the  $V_{p_{\min}}$  direction was subparallel to the lineation of the samples (Fig. 5.18). The AVs contour of omphacites was complex, but the low AVs region was mostly placed in the direction subnormal to the foliation (Fig. 5.18). The  $V_{p_{\text{aver}}}$  and  $V_{s_{\text{aver}}}$  of polycrystalline omphacites were in the range of 8.38–8.46 km/s and 4.88–4.89 km/s, respectively (Tables 5.8 and 5.9). The AVp and Max. AVs were 3.6–6.9 % and 1.75–3.84 %, respectively (Tables 5.10 and 5.11). The Vs1 polarization direction for polycrystalline omphacites was subnormal to the lineation for the vertically propagating S-wave at the direction normal to the foliation (Fig. 5.18).

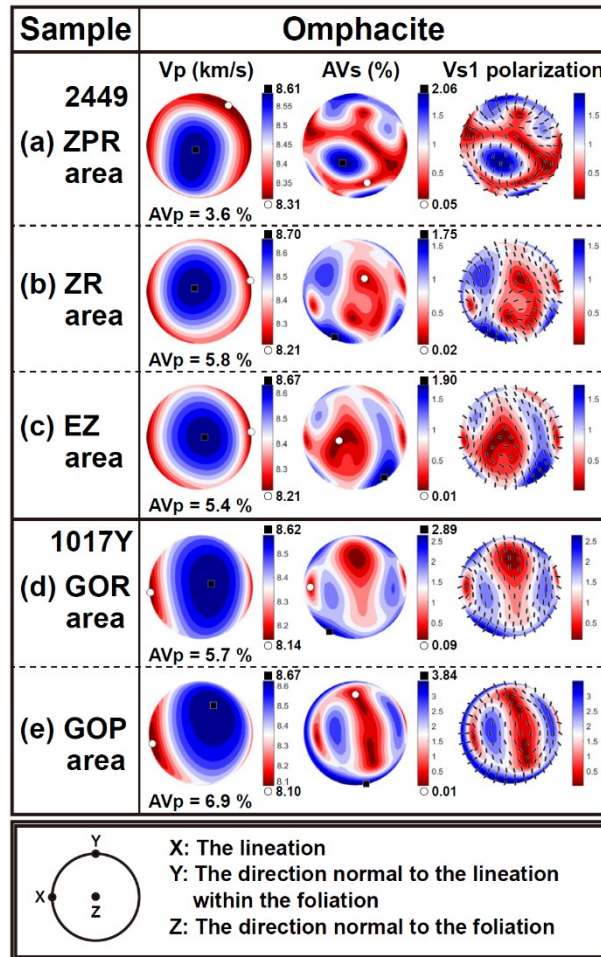


**Figure 5.18.** Seismic velocity and anisotropy of polycrystalline omphacites calculated using crystallographic orientation data from EBSD analysis and the elastic stiffness coefficients of omphacite (Bhagat et al., 1992). The E-W direction corresponds to the lineation (X), and the center of a stereographic projection circle is the direction normal to the foliation (Z). The contours of P-wave velocity ( $V_p$ ), the contours of S-wave polarization anisotropy (AVs), and polarization directions of the fast shear wave ( $V_{s1}$ ) are shown.

#### 5.4.2.4. Polycrystalline phengites

In most samples, the direction of the  $V_{p_{\max}}$  of polycrystalline phengites was subparallel to the lineation, and the direction of the  $V_{p_{\min}}$  was subnormal to the foliation (Fig. 5.19a–e, j–k and m). However, phengites in the samples 1017Y and 2462, and the GR layer of the sample 1015Y showed the  $V_{p_{\min}}$  direction placed between the direction subnormal to the lineation within the foliation and the direction normal to the foliation (Fig. 5.19f–i and l). The low AVs region in AVs contour of phengites was placed in the direction subnormal to the foliation in most samples (Fig. 5.19a–e, j–k and m), but that of phengites in the sample 1017Y and 2462, and the GR layer of the sample 1015Y was placed in the direction subnormal to the lineation within the foliation (Fig. 5.19f–i and l). The  $V_{p_{\text{aver}}}$  and  $V_{s_{\text{aver}}}$  of polycrystalline phengites were in the range of 5.98–6.20 km/s and 3.45–3.52 km/s, respectively (Tables 5.8 and 5.9). The AVp and Max. AVs were 16.9–34.0 % and 13.84–32.01 %, respectively (Tables 5.10 and 5.11). The Vs1 polarization direction for polycrystalline phengites was subparallel to the lineation for the vertically propagating S-wave at the direction normal to the foliation (Fig. 5.19).

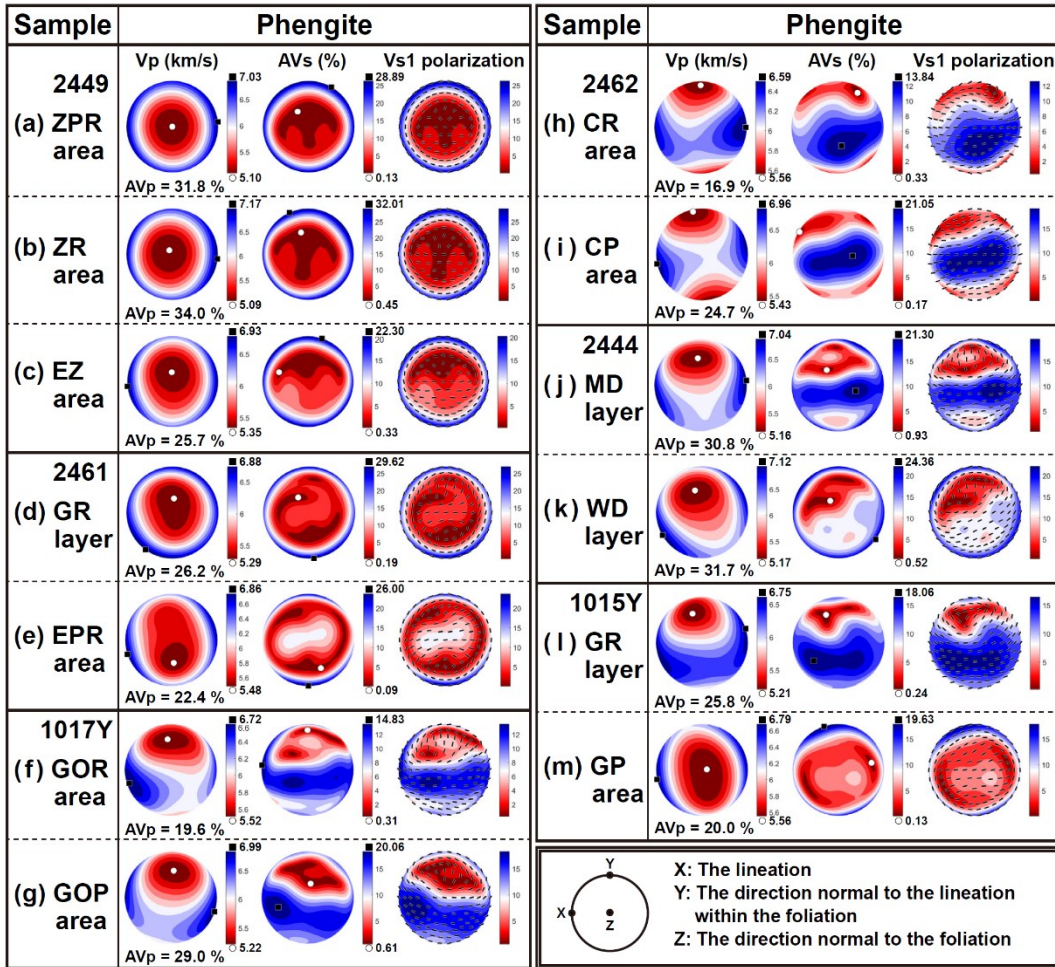


**Figure 5.19.** Seismic velocity and anisotropy of polycrystalline phengites calculated using crystallographic orientation data from EBSD analysis and the elastic stiffness coefficients of muscovite (Vaughan and Guggenheim, 1986). The E-W direction corresponds to the lineation (X), and the center of a stereographic projection circle is the direction normal to the foliation (Z). The contours of P-wave velocity (Vp), the contours of S-wave polarization anisotropy (AVs), and polarization directions of the fast shear wave (Vs1) are shown.

#### 5.4.2.5. Polycrystalline garnets

Since the garnet has a weak elastic anisotropy, the seismic anisotropy of polycrystalline garnets is rarely calculated in all samples (Fig. 5.20). The  $V_p$  and AVs contours also showed orthogonal patterns like the LPO of garnet, but it was difficult to find the correlation between the seismic properties and the LPO due to the limited number of grains. In the EZ area of the sample 2449, however, the direction of the  $V_{p_{\max}}$  of polycrystalline garnets is similar with the direction aligned the [100] axes. The  $V_{p_{\text{aver}}}$  and  $V_{s_{\text{aver}}}$  of polycrystalline garnets were 8.54 km/s and 4.79–4.80 km/s, respectively (Tables 5.8 and 5.9). The AVp and Max. AVs were 0.1–0.3 % and 0.19–0.64 %, respectively (Tables 5.10 and 5.11). The  $V_{s1}$  polarization direction for polycrystalline garnets was also hardly correlated with the LPO data (Fig. 5.20).

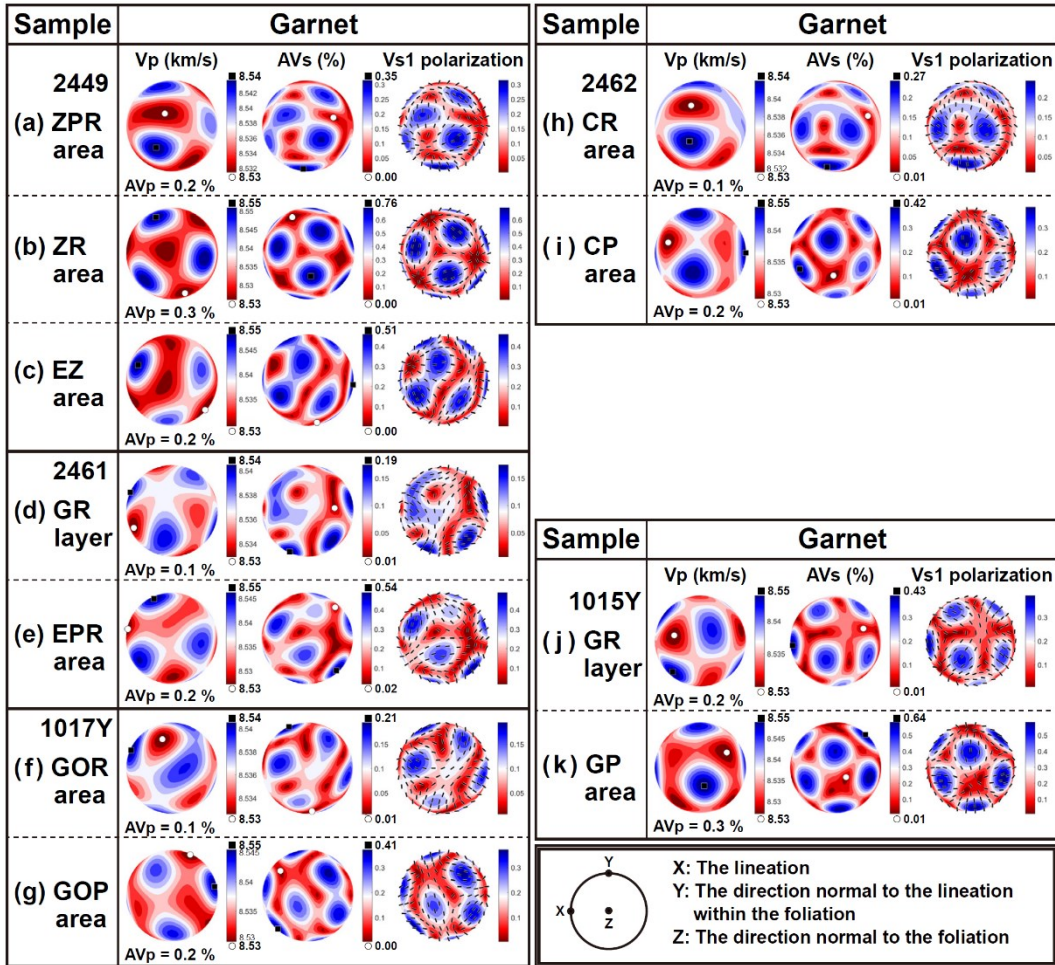


**Figure 5.20.** Seismic velocity and anisotropy of polycrystalline garnets calculated using crystallographic orientation data from EBSD analysis and the elastic stiffness coefficients of almandine-rich garnet (Jiang et al., 2004). The E-W direction corresponds to the lineation (X), and the center of a stereographic projection circle is the direction normal to the foliation (Z). The contours of P-wave velocity (Vp), the contours of S-wave polarization anisotropy (AVs), and polarization directions of the fast shear wave (Vs1) are shown.

#### 5.4.2.6. *Polycrystalline quartzes, chlorites, titanites, and albites*

##### ***Polycrystalline quartzes***

In the sample 2461, the  $V_{p_{\max}}$  direction of polycrystalline quartzes was subnormal to the foliation, and the  $V_{p_{\min}}$  direction was subnormal to the lineation within the foliation (Fig. 5.21a–b). In the sample 2462, the  $V_{p_{\max}}$  direction of quartzes was subparallel to the lineation (Fig. 5.21c–d), and the  $V_{p_{\min}}$  direction was subnormal to the lineation within the foliation at the CR area (Fig. 5.21c). In the CP area of the sample 2462, however, the  $V_{p_{\min}}$  direction of quartzes was subparallel to the lineation which was opposite side to the  $V_{p_{\max}}$  direction (Fig. 5.21d). The AVs contour of quartzes was also complex, but the low AVs region was mostly placed in the direction subnormal to the foliation (Fig. 5.21). The  $V_{p_{\text{aver}}}$  and  $V_{s_{\text{aver}}}$  of polycrystalline quartzes were 6.05–6.08 km/s and 4.10–4.12 km/s, respectively (Tables 5.8 and 5.9). The AVp and Max. AVs were 2.4–3.9 % and 3.12–5.27 %, respectively (Tables 5.10 and 5.11). The Vs1 polarization direction for polycrystalline quartzes in the sample 2461 was subnormal to the lineation, but that for quartzes in the sample 2462 was subparallel to the lineation for the vertically propagating S-wave at the direction normal to the foliation (Fig. 5.21).

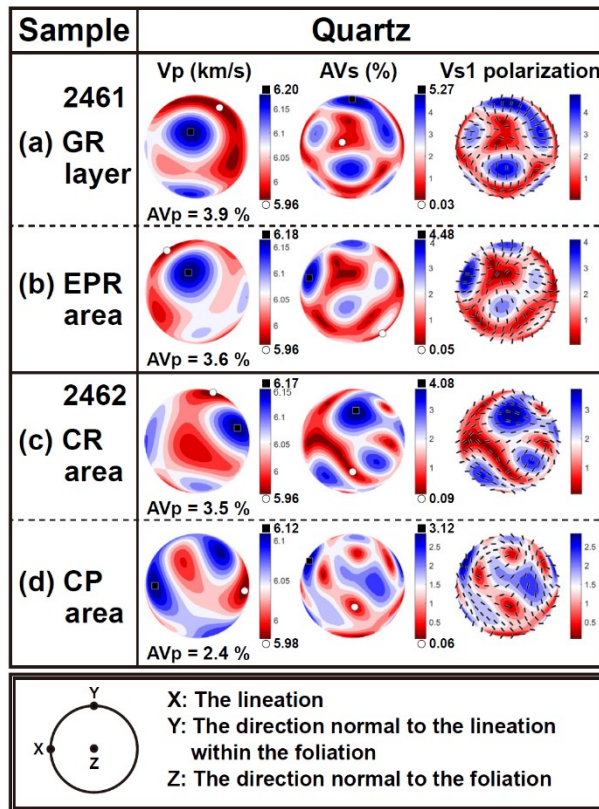


**Figure 5.21.** Seismic velocity and anisotropy of polycrystalline quartzes calculated using crystallographic orientation data from EBSD analysis and the elastic stiffness coefficients of quartz (Heyliger et al., 2003). The E-W direction corresponds to the lineation (X), and the center of a stereographic projection circle is the direction normal to the foliation (Z). The contours of P-wave velocity ( $V_p$ ), the contours of S-wave polarization anisotropy (AVs), and polarization directions of the fast shear wave ( $V_{s1}$ ) are shown.

### *Polycrystalline chlorites*

In most samples, the  $V_{p_{\max}}$  direction of polycrystalline chlorites was subparallel to the lineation, and the  $V_{p_{\min}}$  direction was subnormal to the foliation (Fig. 5.22). However, chlorites in the ZR area of the sample 2449 showed the  $V_{p_{\max}}$  direction aligned subnormal to the lineation within the foliation (Fig. 5.22c), and chlorites in the samples 1017Y and 1015Y showed the  $V_{p_{\min}}$  direction aligned subnormal to the lineation within the foliation (Fig. 5.22f–g and l–m). In the sample 2449 and the MD layer of the sample 2444, the AVs contours of chlorites showed the low AVs region at the direction subnormal to the foliation (Fig. 5.22a–c and j), but those in other samples showed the high AVs region at the direction subnormal to the foliation (Fig. 5.22d–i and k–m). The  $V_{p_{\text{aver}}}$  and  $V_{s_{\text{aver}}}$  of polycrystalline chlorites were 7.56–7.75 km/s and 4.18–4.26 km/s, respectively (Tables 5.8 and 5.9). The AVp and Max. AVs were 10.0–16.1 % and 13.77–22.61 %, respectively (Tables 5.10 and 5.11). The Vs1 polarization direction of polycrystalline chlorites in most samples was subparallel to the lineation, but that of chlorites in the ZR area of the sample 2449 was subnormal to the lineation for the vertically propagating S-wave at the direction normal to the foliation (Fig. 5.22).

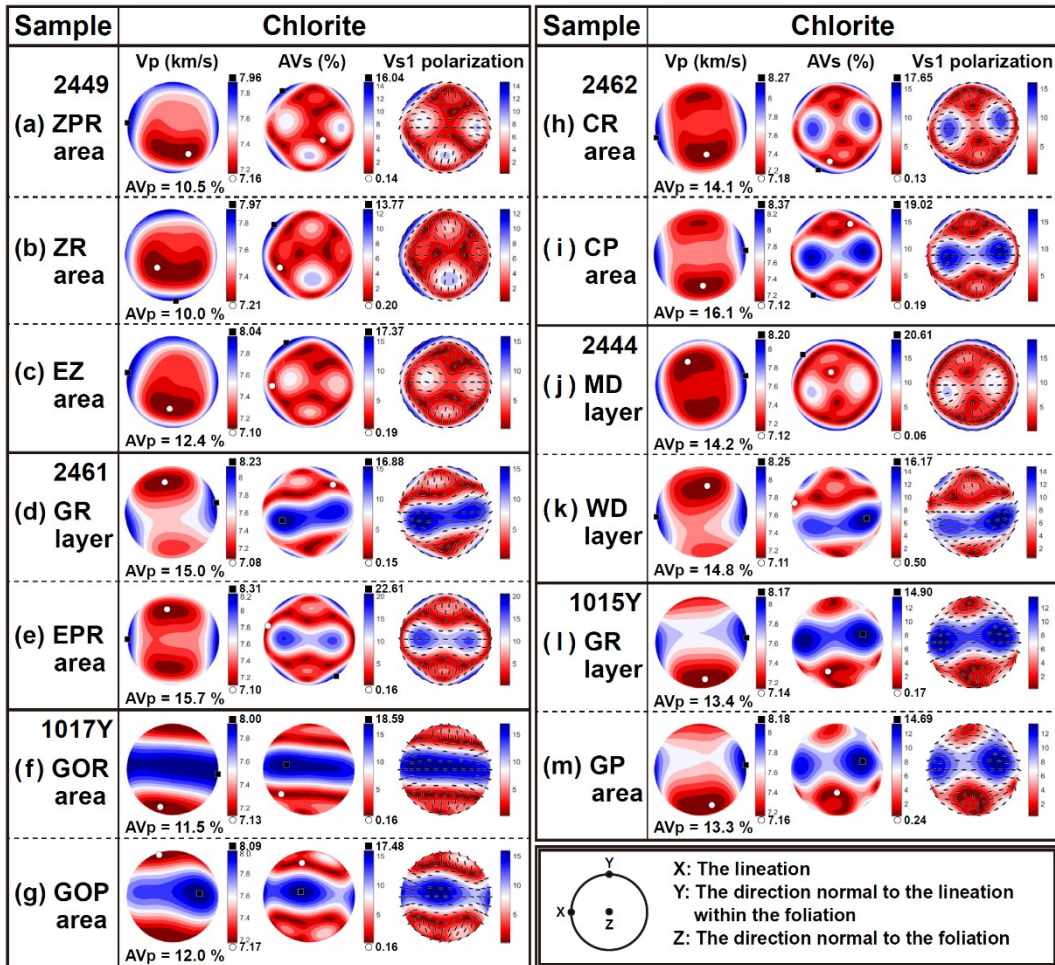


**Figure 5.22.** Seismic velocity and anisotropy of polycrystalline chlorites calculated using crystallographic orientation data from EBSD analysis and the elastic stiffness coefficients of chlorite (Mookherjee and Mainprice, 2014). The E-W direction corresponds to the lineation (X), and the center of a stereographic projection circle is the direction normal to the foliation (Z). The contours of P-wave velocity ( $V_p$ ), the contours of S-wave polarization anisotropy (AVs), and polarization directions of the fast shear wave ( $V_{s1}$ ) are shown.

### ***Polycrystalline titanites***

The seismic anisotropy of titanite (sphene) was calculated for the first time in naturally deformed sample as the elastic coefficient of titanite was reported in this year. In most samples, the  $V_{p_{\max}}$  direction of polycrystalline titanites was subparallel to the lineation, and the  $V_{p_{\min}}$  direction was subnormal to the foliation (Fig. 5.23). However, titanites in the ZPR area of the sample 2449 (Fig. 5.23a), sample 1017Y (Fig. 5.23f–g), and the CP area of the sample 2462 (Fig. 5.23i) showed the  $V_{p_{\max}}$  direction aligned subnormal to the lineation within the foliation. In the ZPR area of the sample 2449 and sample 1017Y, the AVs contours of titanites showed the high AVs region at the direction subparallel to the lineation (Fig. 5.23a and f–g), and those in the samples 2444 and 1015Y showed the high AVs region at the direction subnormal to the lineation within the foliation (Fig. 5.23j–m). In the ZR and EZ areas of the sample 2449 and the samples 2461 and 2462, the high AVs region in AVs contour of titanites was placed between the direction subparallel to the lineation and the direction subnormal to the lineation within the foliation (Fig. 5.23b–e and h–i). The  $V_{p_{\text{aver}}}$  and  $V_{s_{\text{aver}}}$  of polycrystalline titanites were 7.17–7.30 km/s and 4.23–4.25 km/s, respectively (Tables 5.8 and 5.9). The AVp and Max. AVs were 3.2–15.2 % and 2.18–7.23 %, respectively (Tables 5.10 and 5.11). The Vs1 polarization direction of polycrystalline titanites in most samples was subparallel to the lineation, but that of titanites in the sample 1017Y and the CP area of the sample 2462 was subnormal to the lineation for the vertically propagating S-wave at the direction normal to the foliation (Fig. 5.23).



### ***Polycrystalline albites***

In most samples, the  $V_{p_{\max}}$  direction of polycrystalline albites was subparallel to the lineation, and the  $V_{p_{\min}}$  direction was subnormal to the foliation (Fig. 5.24). However, the albites in the GR layer of the sample 2461 and the GP area of the sample 1015Y showed the  $V_{p_{\max}}$  direction aligned subnormal to the lineation within the foliation (Fig. 5.24d and k). The AVs contours of albites showed complex patterns, but the low AVs region was mostly placed in the direction subnormal to the foliation (Fig. 5.24). The  $V_{p_{\text{aver}}}$  and  $V_{s_{\text{aver}}}$  of polycrystalline albites were 6.37–6.41 km/s and 3.67–3.69 km/s, respectively (Tables 5.8 and 5.9). The AV<sub>p</sub> and Max. AVs were 4.1–14.3 % and 5.15–12.22 %, respectively (Tables 5.10 and 5.11). The Vs1 polarization direction of polycrystalline albites for the vertically propagating S-wave at the direction normal to the foliation was subparallel to the lineation in the EZ area of the sample 2449, the samples 2461 and 2462, and the GR layer of the sample 1015Y (Fig. 5.24c–e and h–j), but that was subnormal to the lineation in the ZPR and ZR areas of the sample 2449, sample 1017Y, and the GP area of the sample 1015Y (Fig. 5.24a–b, f–g, and k).

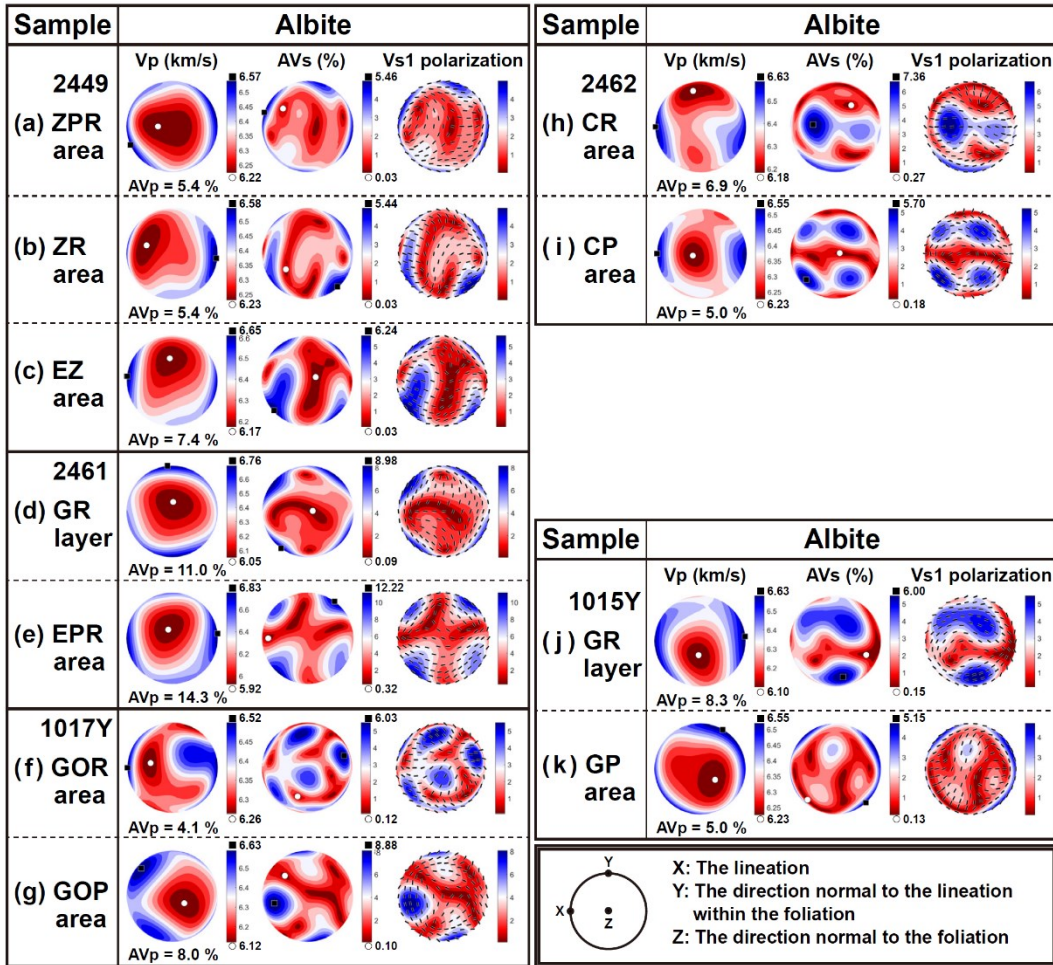


**Figure 5.24.** Seismic velocity and anisotropy of polycrystalline albites calculated using crystallographic orientation data from EBSD analysis and the elastic stiffness coefficients of albite (Brown et al., 2006). The E-W direction corresponds to the lineation (X), and the center of a stereographic projection circle is the direction normal to the foliation (Z). The contours of P-wave velocity (Vp), the contours of S-wave polarization anisotropy (AVs), and polarization directions of the fast shear wave (Vs1) are shown.

### 5.4.3. Seismic velocity and anisotropy of whole rocks

Seismic velocity and anisotropy of whole rocks are shown in Figures 5.25. All samples showed the direction of the  $V_{p_{max}}$  aligned subparallel to the lineation and the direction of the  $V_{p_{min}}$  aligned subnormal to the foliation (Fig. 5.25). These patterns mostly followed the  $V_{p_{max}}$  and  $V_{p_{min}}$  direction of the polycrystalline amphibole group minerals. The low AVs region in AVs contour of whole rock was placed in the direction subnormal to the foliation as following the patterns of the polycrystalline amphiboles. However, the direction of the minimum AVs placed in the direction subnormal to the foliation in the sample 2449 was affected by the pattern of the polycrystalline epidotes (Fig. 5.25a–c). The  $V_{p_{aver}}$  and  $V_{s_{aver}}$  of whole rocks were 7.17–7.69 km/s and 4.13–4.48 km/s, respectively (Tables 5.8 and 5.9). These average velocities of whole rock were slower than those of the polycrystalline amphiboles, except for the  $V_{p_{aver}}$  of the ZR area in the sample 2449. This fast  $V_{p_{aver}}$  of whole rock is regarded as the influence of the fast  $V_{p_{aver}}$  of the polycrystalline zoisites in this area (Table 5.8). These average velocities of whole rock were also increased with increasing modal compositions of garnet, omphacite and zoisite in the sample.

The AVp and Max. AVs of whole rocks were 8.1–18.2 % and 5.27–11.41 %, respectively (Tables 5.10 and 5.11). These anisotropies of whole rocks were lower than those of the polycrystalline amphiboles, except for the AVp and Max. AVs of the WD layer in the sample 2444. These high anisotropies of whole rock are regarded

as the influence of the high AVp and Max. AVs of the polycrystalline phengites (Tables 5.10 and 5.11). The Vs1 polarization direction of two whole rock samples (2449 and 2461) was subnormal to the lineation for the vertically propagating S-wave at the direction normal to the foliation, and that of other samples was subparallel to the lineation (Fig. 5.25). The Vs1 polarization directions subnormal to the lineation in two samples indicated that the Vs1 polarization direction of whole rock was more affected by the epidote group minerals, zoisite and epidote, which showed the Vs1 polarization direction subnormal to the lineation (Figs 5.16 and 5.17).

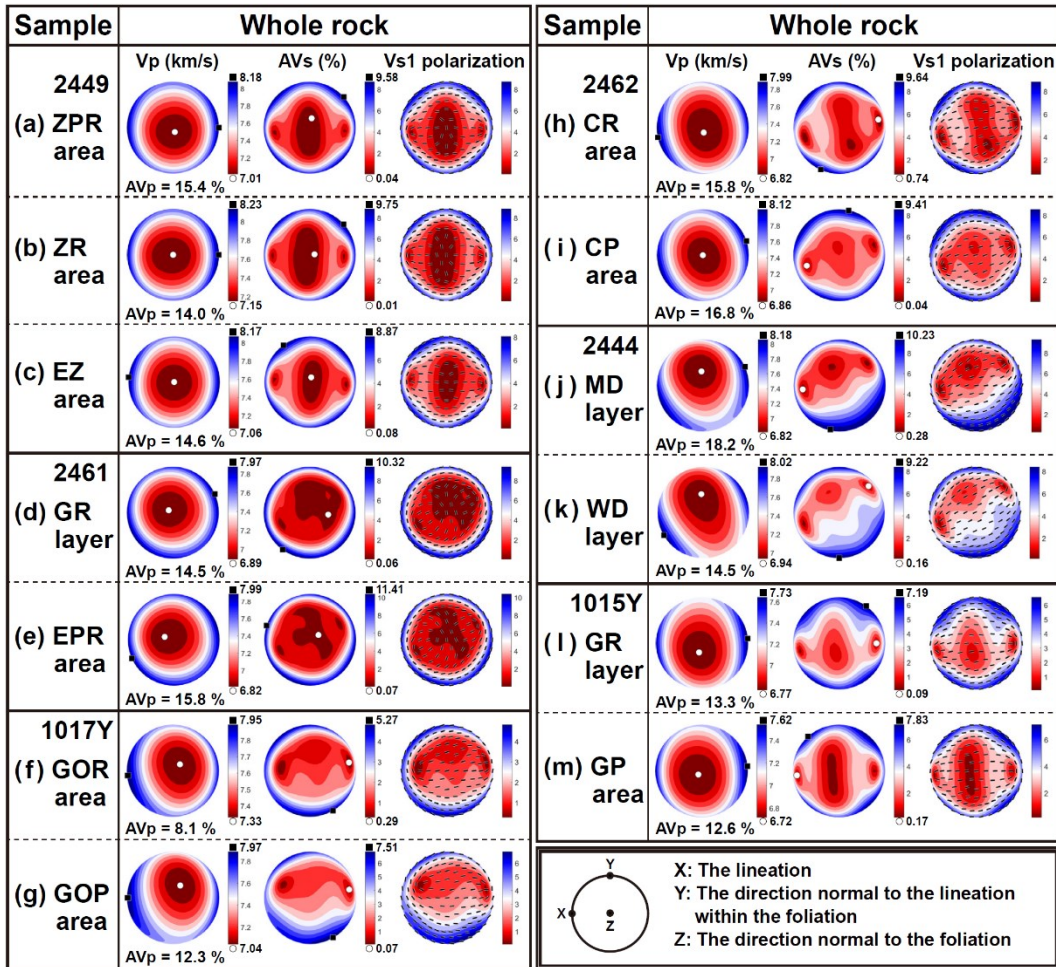


**Figure 5.25.** Seismic velocity and anisotropy of whole rocks calculated by using whole orientation data and elastic stiffness coefficients of the constituent minerals and the average density weighted by the modal composition of each sample. The E-W direction corresponds to the shear direction (X), and the center of a stereographic projection circle is the direction normal to the shear plane (Z). The contours of P-wave velocity (Vp), the contours of S-wave polarization anisotropy (AVs), and polarization directions of the fast shear wave (Vs1) are shown.

## 5.5. Discussions

### 5.5.1. The development of LPOs of minerals in high pressure metabasites

Since the high pressure metabasite blocks in the serpentinite mélange were exhumed from different depths and through different path, the deformation microstructures and fabric strength were affected by different P-T conditions in which the strain occurred. To understand the dominant deformation mechanism of LPO developments, the high-resolution EBSD mapping was performed on the representative minerals in each sample (Figs. 5.26–5.30).

#### 5.5.1.1. LPO development of amphiboles

Most LPOs of amphiboles showed the type-2 LPO indicating the (100)[001] slip system of glaucophane classified in Chapter 3 (Bezacier et al., 2010a; Cao and Jung, 2016; Cao et al., 2013; 2014; Choi et al., 2021; Fujimoto et al., 2010; Ha et al., 2018; Kim et al., 2013b; 2013a; Park et al., 2020a; Teyssier et al., 2010). Since the amphibole groups were different depending on the chemical compositions in all samples, the EBSD mapping of single glaucophane representing the chemical composition boundary was performed to determine the effect of chemical compositions on the lattice orientation in epidote eclogite-epidote blueschist facies rock (sample 1017Y; Fig. 5.26). The BSE image showed chemical boundary between

sodic amphibole composition (glaucofane, dark gray area in Fig. 5.26a) and sodic-calcic amphibole composition (barroisite, bright gray area in Fig. 5.26a). The kernel angle misorientation (KAM) map (Fig. 5.26c) and the grain reference orientation deviation (GROD) angle map (Fig. 5.26d) exhibited a misorientation line less than  $1^\circ$  along this boundary (the definition of the KAM map and GROD angle map was referred to Chapter 3.2.4). This intracrystalline microstructure of sodic to sodic-calcic amphibole suggests that the transition of the chemical composition can moderately affect the tilting of the crystal lattice (Fig. 5.26c–d). However, the misorientation lines which are irrelevant to the chemical transition boundary are dominant in KAM map and GROD map (Fig. 5.26c–d). In addition, the color maps of inverse pole figure to the X-direction (IPFX; corresponding to the lineation) and to the Z-direction (IPFZ; corresponding to the direction normal to the foliation) indicated a minor lattice transition along the chemical transition boundary (Fig. 5.26e–f). These observations suggest that the orientation transferred by the chemical change in a single grain was minor, and that the main mechanism of the LPO development in amphiboles is likely to be a deformation in dislocation creep under eclogite- to blueschist-facies conditions. Strong fabric strength of amphiboles (M-index = 0.06–0.30, and J-index = 2.08–10.08) can also support the deformation of amphibole group minerals in dislocation creep (Fig. 5.5). These results and suggestions are well consistent with previously proposed deformation mechanisms of glaucofane as a sodic amphibole (Cao et al., 2014; Kim et al., 2013a; Park et al., 2020a; Reynard et al., 1989).

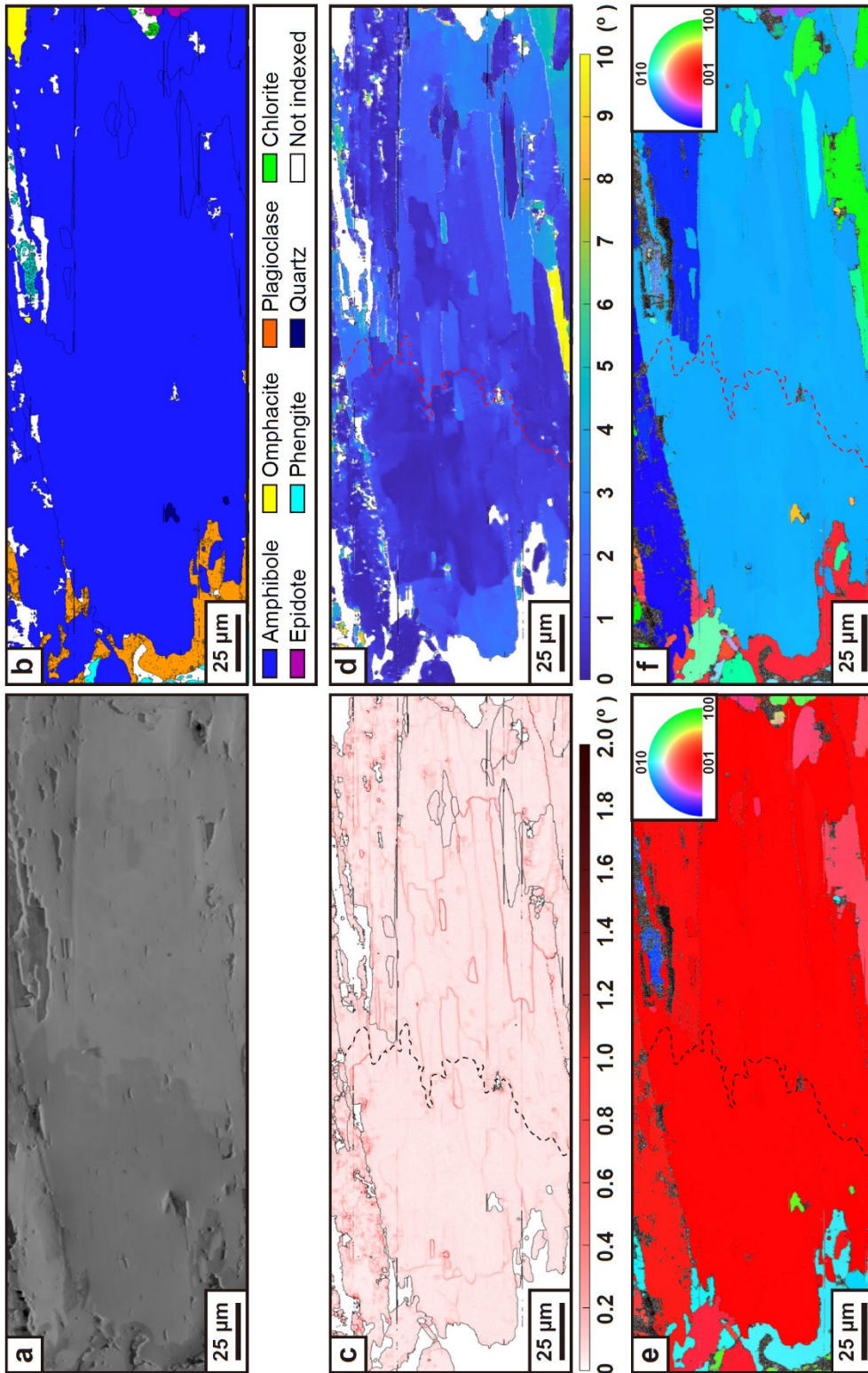


**Figure 5.26.** (a) BSE image, (b) phase color map, (c) KAM map, (d) GROD angle map (mis2mean), (e) inverse pole figure (IPF) color map of X-direction (parallel to the lineation), and (f) IPF color map of Z-direction (normal to the foliation) presenting the intracrystalline deformation microstructure of glaucophane in epidote eclogite-epidote blueschist rock (sample 1017Y). Step size of mapping: 0.1  $\mu\text{m}$ . Black and red dashed lines indicate the chemical composition boundary between sodic amphibole (glaucophane) and sodic-calcic amphibole (barroisite).

On the other hand, two sample showed different LPOs of amphibole group minerals. In the WD layer of the sample 2444, the [001] axes of amphibole (glaucophane) were aligned subparallel to the lineation and the [100] axes and the (010) poles were aligned subnormal to the foliation with girdle distribution subnormal to the lineation (Fig. 5.5k). Comparing with the LPO of amphiboles in the MD layer of the sample 2444, the maximum cluster of (010) poles were newly aligned subnormal to the foliation in the WD layer. In previous experimental study, the type-1 LPO of glaucophane deformed under low shear strain was characterized as the [001] axes aligned subparallel to the shear direction and the (010) poles aligned subnormal to the shear plane (Fig. 3.7b–e in Chapter 3.3.2; Park et al., 2020a). This suggests that the (010) poles of amphiboles (glaucophanes) in the WD layer of the sample 2444 could be possible to align subnormal to the foliation by (010)[001] dominant slip system under weak shear deformation. However, further study on the intracrystalline microstructures of amphibole in this sample is needed to determine the dominant slip system of amphibole.

In the sample 2461, the LPO of amphiboles was characterized as the [100] axes aligned subnormal to the foliation, the (010) poles aligned subparallel to the lineation, and the [001] axes distributed in girdle shape subparallel to the foliation with maximum cluster aligned subnormal to the lineation within the foliation (Fig. 5.5d–e). This LPO is similar with the type-II hornblende LPO developed under high-stress in the temperature of 590–700 °C (Ko and Jung, 2015). However, this LPO has not been reported in sodic amphibole so far. To understand how this LPO type is also developed in sodic amphibole, further research is required.

### 5.5.1.2. LPO development of epidote group minerals

The LPOs of epidote group minerals showed different fabrics according to the samples. As a result, the high-resolution EBSD mapping of epidote grains was performed to determine the dominant development mechanisms of these epidote LPOs. In the zoisite eclogite-epidote blueschist facies rock (sample 2449), the epidote LPO is similar with the zoisite LPO. In the ZPR and EZ areas, LPO of epidote showed one of the previously reported epidote fabrics indicating the  $\{101\}[010]$  slip system (Cao et al., 2011; 2013; Cossette et al., 2015; Fujimoto et al., 2010), and in the ZR area, the epidote LPO showed the type-1 LPO indicating the  $(100)[010]$  slip system of epidote classified in Chapter 3 (Park et al., 2020a). The KAM map and GROD angle map of zoisite porphyroclast in this zoisite eclogite-epidote blueschist rock (sample 2449) showed numerous misorientation lines and high orientation deviation angles (Fig. 5.27c–d). The IPFX and IPFZ color maps also exhibited lattice shifts along these subgrain boundaries in zoisite porphyroclast grains (Fig. 5.27e–f). These intracrystalline microstructures of zoisite porphyroclast suggest that they were deformed in dislocation creep and developed the LPO with strong fabric strength (M-index = 0.14–0.18, and J-index = 3.21–3.37). This suggestion is consistent with the previous suggestion that LPO of epidote/zoisite was developed by dislocation creep (Müller and Franz, 2004; 2008; Park et al., 2020a; Ray et al., 1986).

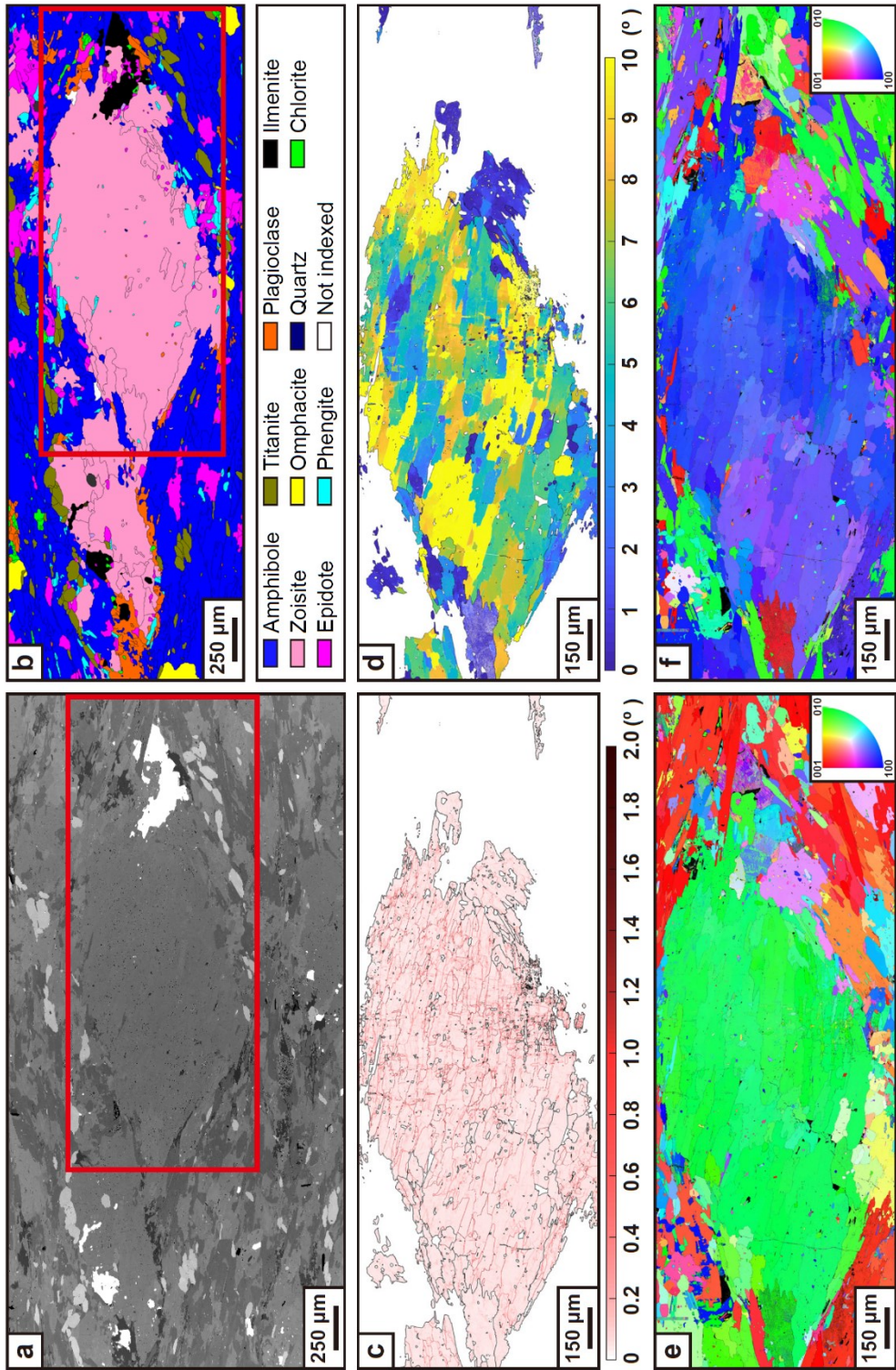


**Figure 5.27.** (a) BSE image, (b) phase color map, (c) KAM map, (d) GROD angle map (mis2mean), (e) inverse pole figure (IPF) color map of X-direction (parallel to the lineation), and (f) IPF color map of Z-direction (normal to the foliation) presenting the intracrystalline deformation microstructure of zoisite porphyroclast in zoisite eclogite-epidote blueschist rock (sample 2449). Step size of mapping: 0.4  $\mu\text{m}$ .

In the zoisite bearing epidote blueschist facies rock (sample 2461), the LPO of epidote showed another previously reported epidote fabric indicating the (001)[010] slip system (Bezacier et al., 2010a; Cao et al., 2011; 2013; Ha et al., 2018; Kim et al., 2013a). In this sample, zoisite inclusion within epidote grain suggests that epidote-zoisite transition occur in single crystal (Fig. 5.28a–b). The subgrain boundary beside the zoisite inclusion within epidote grain is likely to explain the mineral transition from zoisite to epidote, or vice versa (Fig. 5.28c–d). In addition, remnant zoisite grain in the matrix contains epidote inclusion at the grain boundary (Fig. 5.28e–f). The KAM map and GROD map showed that the intracrystalline microstructures in the zoisite grains were more than those in epidote (Fig. 5.28g–h). Since the main epidote group mineral in the matrix is epidote, these results may suggest a mineral transition from zoisite to epidote. As a result, because the main difference between epidote and zoisite is the  $\text{Fe}^{3+}$  composition, it is suggested that the zoisite-epidote transition occurred by the supply of  $\text{Fe}^{3+}$  cation during their subduction or exhumation processes. However, further study is needed to understand how  $\text{Fe}^{3+}$  cations are supplied in these processes, and whether the zoisite-epidote transition affects the development of epidote LPO indicating the (001)[010] slip system.

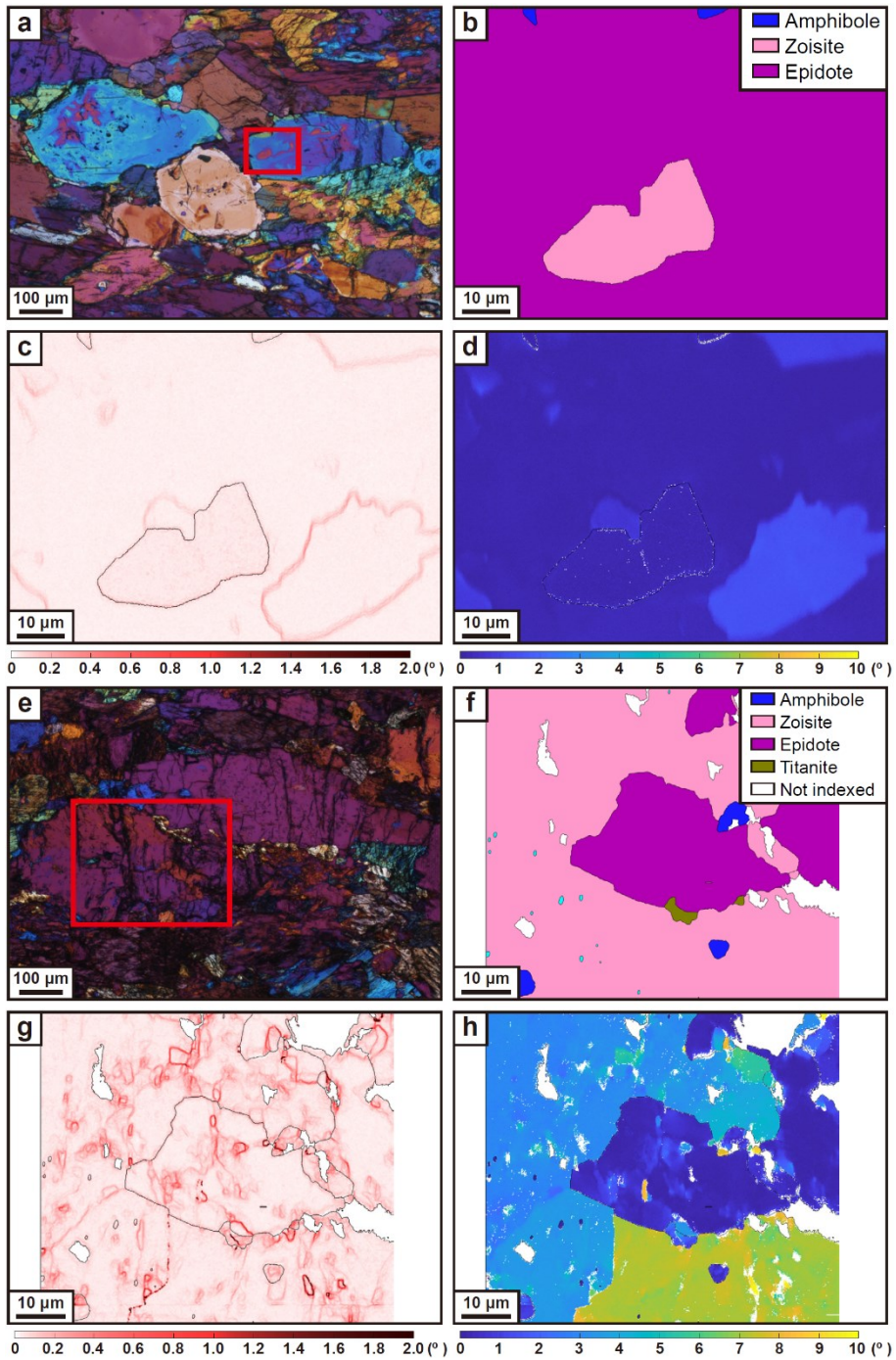


**Figure 5.28.** (a) and (e) Optical photomicrographs, (b) and (f) phase color maps, (c) and (g) KAM maps, and (d) and (h) GROD angle maps (mis2mean) presenting the intracrystalline deformation microstructure of zoisite-epidote in zoisite bearing epidote blueschist rock (sample 2461). Step size of mapping: 0.15 μm.

In the epidote eclogite-epidote blueschist facies rock (sample 1017Y) and lawsonite bearing epidote blueschist facies rock (sample 2462), the LPO of epidote looks like a mixture of the LPO indicating (100)[010] slip system (Park et al., 2020a) and the LPO indicating (001)[010] slip system (Bezacier et al., 2010a; Cao et al., 2011; 2013; Ha et al., 2018; Kim et al., 2013a). The LPO of epidote in these samples showed the weakest fabric strength among the samples (M-index = 0.02–0.05 and J-index = 1.33–1.58 in the sample 1017Y; and M-index = 0.01–0.02 and J-index = 1.24 in the sample 2462). In the sample 2462, epidote aggregates exhibited a scattered distribution in the matrix (Fig. 5.4h–i), and some aggregates had rhombic-shaped aggregate boundaries. In addition, they contained unhexagonal shaped garnet grains that captured many inclusions of epidote, amphibole, and lawsonite within the aggregates. These structures indicate that the epidote aggregates in the sample 2462 are lawsonite porphyroblast pseudomorphs formed during exhumation process (similar with lawsonite pseudomorph-bearing blueschist in Syros island, Cyclades, Greece; Philippon et al., 2013). In addition, previous study also reported the epidote and lawsonite inclusions in garnet and the epidote rim around lawsonite porphyroblast in the lawsonite eclogite from Samana Peninsular, Dominican Republic (Zack et al., 2004). There may be two possibilities to explain these structures: one is that epidotes replaced the lawsonite porphyroblast along the pre-existing subgrain boundaries and formed new grain boundaries during the breakdown of lawsonite; the other is that the lawsonite porphyroblast underwent a strong deformation simultaneously with the metamorphic reaction from lawsonite into epidote, and the epidote grains were recrystallized forming aggregates of fine grains. According to the high-resolution EBSD mapping results, the KAM map and grain orientation spread (GOS) map of

epidotes showed that the amount of intracrystalline microstructures was small (Fig. 5.29c–d). In addition, the IPFX and IPFZ color maps represented the spread alignments of epidote grains in aggregates (Fig. 5.29e–f). These intracrystalline microstructures and the weakest fabric strength of epidote among the samples suggest that LPO of epidote aggregates might not be developed by recrystallization of epidote porphyroclast in dislocation creep, but by the metamorphic transition from lawsonite to epidote along the pre-existing subgrain boundary in the lawsonite porphyroclast.

In the epidote blueschist-upper greenschist facies rock (sample 1015Y), epidote LPO exhibited the previously reported LPO indicating  $\{101\}[010]$  slip system (Cao et al., 2011; 2013; Cossette et al., 2015; Fujimoto et al., 2010). These epidotes showed the finest grain size (Max.  $r_e \approx 110 \mu\text{m}$  and average  $r_e \approx 17 \mu\text{m}$ ) among the samples, but the fabric strength is relatively strong (M-index = 0.11–0.14, and J-index = 1.93–2.44). To understand the relationship between the grain size and fabric strength of epidote, further study is required.

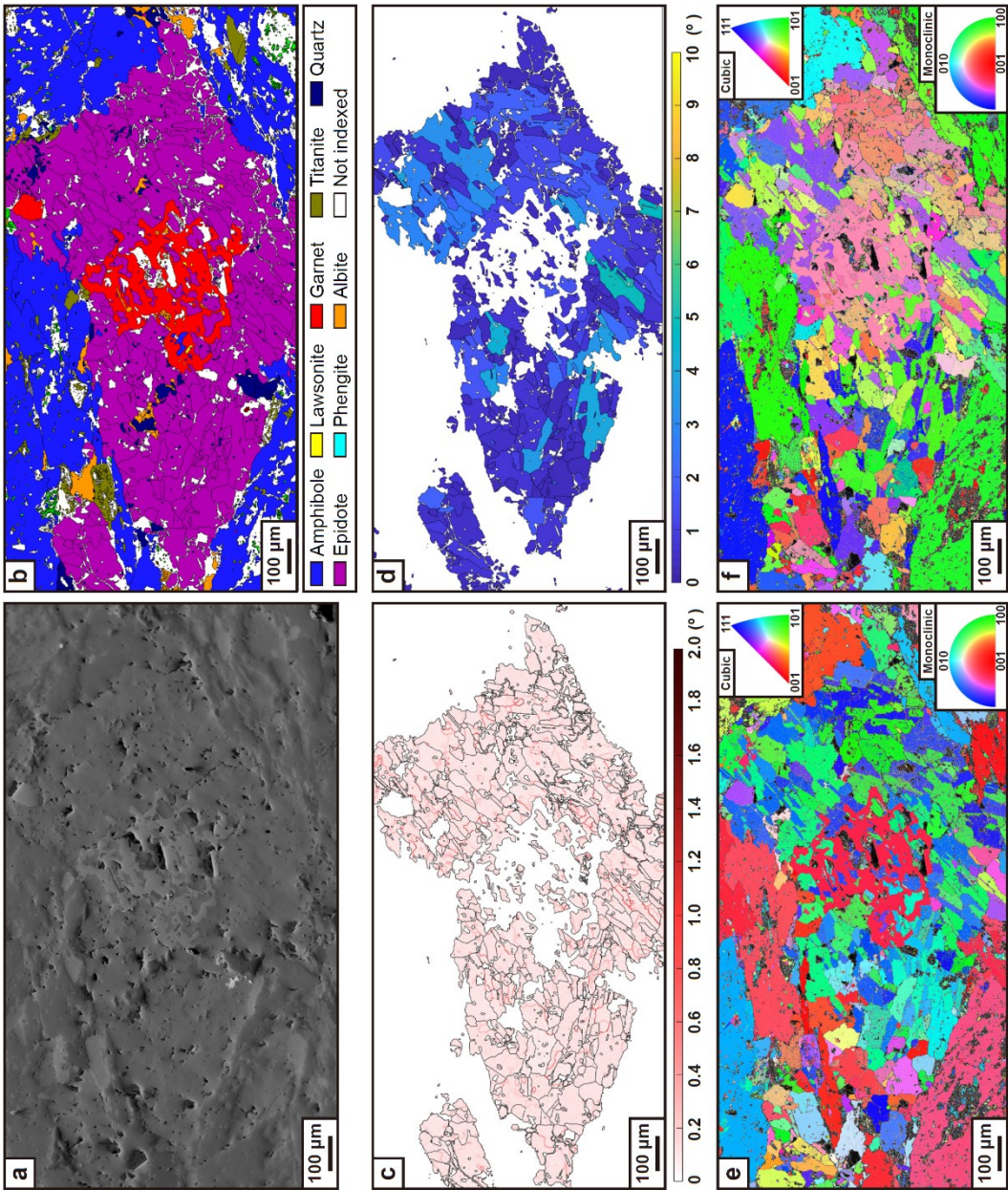


**Figure 5.29.** (a) BSE image, (b) phase color map, (c) KAM map, (d) grain orientation spread (GOS) map, (e) inverse pole figure (IPF) color map of X-direction (parallel to the lineation), and (f) IPF color map of Z-direction (normal to the foliation) showing the intracrystalline deformation microstructure of epidote aggregate (lawsonite pseudomorph) in lawsonite bearing epidote blueschist rock (sample 2462). Step size of mapping: 0.5  $\mu\text{m}$ .

### 5.5.1.3. LPO development of omphacites

The LPO of omphacite in epidote eclogite-epidote blueschist facies rock (sample 1017Y) showed L-type fabric in the GOR area and S-type fabric in the GOP area (Zhang et al., 2006). On the other hand, the Omphacite LPO in zoisite eclogite-epidote blueschist facies rock (sample 2449) was characterized as [100] axes aligned subnormal to the foliation and [001] axes aligned subparallel to the lineation, which was not previously reported with omphacite fabric. To understand the omphacite LPO development, the high-resolution EBSD mapping was performed in single crystal of omphacite in epidote eclogite-epidote blueschist rock (sample 1017Y; Fig. 5.30). As a result, numerous misorientation lines were determined by the KAM map (Fig. 5.30c) and high orientation deviation angles were observed in the GROD angle map (Fig. 5.30d), suggesting that many subgrain boundaries of omphacite grains occurred in dislocation creep. In addition, the IPFX and IPFZ color maps exhibited lattice shifts along these subgrain boundaries in omphacite grains (Fig. 5.30e–f). These intracrystalline microstructures suggest that the omphacite LPO was also developed by dislocation creep, which is consistent with previously proposed mechanisms (Zhang et al., 2006; Van Roermund and Boland, 1981). However, their relatively weak fabric strength (M-index = 0.05–0.06, and J-index = 1.98–2.92) may be due to the large number of subgrain boundaries in single grain. These results suggest a possibility that these subgrain boundaries were not consumed by dominant slip direction and plane in dislocation creep after formation. Two hypotheses can be presented to explain these structures: one is that there was not enough time to form

new grain boundaries to develop LPO since the degree of strain received by omphacite was weak under the eclogite facies metamorphic condition; the other is that the dislocations in omphacite were captured after subgrain boundary formation because the dislocation slip system of omphacite was not activated under the blueschist facies metamorphic condition. However, further research is needed to verify these hypotheses. In addition, further study is required to observe intracrystalline microstructures of omphacite in the sample 2449.

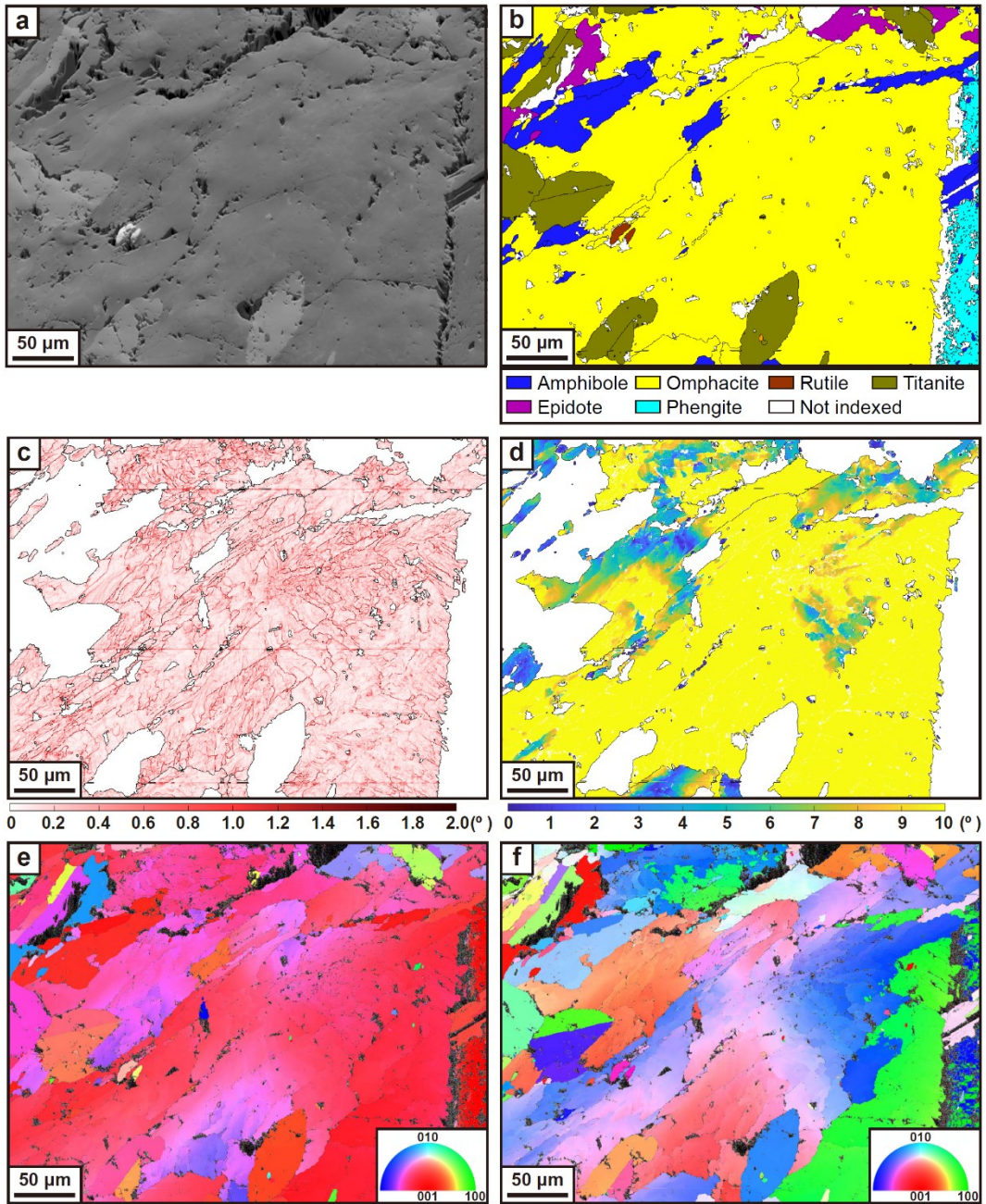


**Figure 5.30.** (a) BSE image, (b) phase color map, (c) KAM map, (d) GROD angle map (mis2mean), (e) inverse pole figure (IPF) color map of X-direction (parallel to the lineation), and (f) IPF color map of Z-direction (normal to the foliation) showing the intracrystalline deformation microstructure of omphacite in epidote eclogite-epidote blueschist rock (sample 1017Y). Step size of mapping: 0.2  $\mu\text{m}$ .

### **5.5.2. Estimation of metamorphic pressure (P) and temperature (T) of epidote blueschist facies rocks**

The high pressure metabasite blocks in Río San Juan metamorphic complex are petrologically different and represent diverse mineral assemblage. Kreb et al. (2011) calculated P-T pseudosections of these blocks using 14 samples classified into 8 groups: jadeite-lawsonite blueschist, jadeite blueschist, garnet blueschist, omphacite blueschist, garnet-omphacite blueschist, sodic amphibole-bearing eclogite, sodic amphibole-free eclogite, and granitic orthogneiss. According to their classification, the three samples in this study may belong to garnet-omphacite blueschist (sample 2449), garnet blueschist (sample 2461), and sodic amphibole-bearing eclogite (sample 1017Y). However, other three samples showed different mineral assemblage. They suggested that garnet-omphacite blueschist underwent peak metamorphism at  $P \sim 18$  kbar and  $T = 550$  °C and retrograded at  $P \sim 12$  kbar and  $T = 500$  °C, and sodic amphibole-bearing eclogite underwent peak metamorphism at  $P \sim 23$  kbar and  $T = 650$  °C and retrograded at  $P \sim 17$  kbar and  $T = 600$  °C showing clockwise paths (Krebs et al., 2011). Escuder-Viruete and Pérez-Estaún (2013) calculated P-T pseudosection using eclogite in Río San Juan metamorphic complex and suggested peak metamorphic condition at  $P \sim 23$  kbar and  $T = 580$  °C and retrograde condition at  $P \sim 6.5$  kbar and  $T = 410$  °C showing counterclockwise path (Escuder-Viruete and Pérez-Estaún, 2013). In this study, peak metamorphic conditions for two samples (sample 2449 and 1017Y) were estimated by using garnet-clinopyroxene-phengite geothermobarometry (Ravna and Terry, 2004), and retrograde conditions except for

one (sample 2444) were estimated for sodic-calcic and calcic amphiboles by using amphibole-plagioclase geobarometry (Molina et al., 2015) and garnet-amphibole geothermometry (Ravna, 2000a). The amount of ferric- ( $\text{Fe}^{3+}$ ) and ferrous-iron ( $\text{Fe}^{2+}$ ) in amphibole was calculated using mineral formula calculation step (Schumacher, 1991). As a result, peak metamorphic condition of sample 2449 was estimated to be  $P = 21\text{--}22$  kbar and  $T = 515\text{--}560$  °C, and retrograde condition was estimated to be  $P \sim 8$  kbar and  $T = 340\text{--}385$  °C. On the other hand, peak metamorphic condition of sample 1017Y was estimated to be  $P = 25\text{--}26$  kbar and  $T = 600\text{--}620$  °C, and retrograde condition was estimated to be  $P = 12\text{--}13$  kbar and  $T = 505\text{--}550$  °C. Compared with the previous study (Krebs et al., 2011), estimated peak metamorphic pressures are higher than previously reported peak metamorphic pressures, and retrograde pressures are lower than previously reported retrograde pressures. However, multi-equilibrium calculations are needed to constrain the exact P-T paths for these samples. In case of other samples, retrograde conditions were estimated to be  $P = 8\text{--}10$  kbar and  $T = 360\text{--}420$  °C for the sample 2461,  $P = 2\text{--}3$  kbar and  $T = 330\text{--}365$  °C for the sample 2462, and  $P = 1\text{--}3$  kbar and  $T = 250\text{--}350$  °C for the sample 1015Y. These conditions relatively well correspond to the degree of retrograde metamorphism of the samples. However, further studies are required to determine the precise P-T conditions that samples underwent.

### **5.5.3. Implications for seismic anisotropy in the northeastern margin of the Caribbean plate**

Previous study reported the trench-parallel  $V_{s1}$  polarization direction with delay time of  $\delta t = 1.36 \pm 0.35$  s beside the Río San Juan complex, Dominican Republic (Meighan and Pulliam, 2013). The seismic anisotropy in this area was regarded from trench-parallel sub-slab mantle flow as previously suggested (Hodges and Miller, 2015; Lynner and Long, 2013; Meighan and Pulliam, 2013; Possee et al., 2020). However, the study area is located between oblique collision and oblique underthrusting domains (Rodríguez-Zurrunero et al., 2020) near the WNW-trending, left-lateral strike-slip Septentrional Fault Zone (Escuder-Viruete and Pérez, 2020). In addition, the existence of an older subducted North American oceanic slab was suggested beneath the Hispaniola (Corbeau et al., 2019; Núñez et al., 2019; Rodríguez-Zurrunero et al., 2020).

Therefore, to understand the influence of these tectonic-scale geological structures on the seismic anisotropy in this region, the delay time from subducting oceanic crust was calculated by considering the transition of the tectonic setting from subduction to oblique underthrust and/or lateral shear in the study area. In addition, the thickness of subducted oceanic crust, which was detached from subducting slab, was calculated by assuming that the crust was composed of blueschist-facies metamorphic rocks and deformed in lateral shear by sub-slab mantle flow and/or strike-slip fault. The delay time ( $\delta t$ ) of the subducting oceanic crust and the thickness

(T) of detached oceanic crust as an anisotropic layer were calculated by Equations 4.6 and 2.6, respectively, as:

$$\delta t = (T \times AVs) / (100 \times \langle Vs \rangle) \text{ (s)} \quad (4.6)$$

$$T = (100 \times \delta t \times \langle Vs \rangle) / AVs \text{ (km)} \quad (2.6)$$

where  $\langle Vs \rangle$  is the average velocity of fast and slow shear wave velocities ( $Vs1$  and  $Vs2$ ), and  $AVs$  is the seismic anisotropy of the S-wave expressed as a percentage (Pera et al., 2003).

As a result, when the 7 km thick oceanic crust underthrust tilted  $\sim 20^\circ$  beneath the Caribbean plate is deformed in lateral shear by strike-slip Septentrional Fault Zone, they can contribute to the delay time of 0.09–0.17 s in the study area (Fig. 5.31). When the detached oceanic slab is deformed in lateral shear mode, the thickness of the anisotropic layer composed of blueschist-facies metamorphic rocks is required to be  $\sim 56$ – $114$  km to derive the delay time of  $\sim 1.3$  s observed in the study area (Fig. 5.32). These results suggest that the subducted oceanic crust metamorphosed in blueschist-facies condition can highly contribute to the seismic anisotropy of the northeastern margin of the Caribbean plate depending on the LPOs of the constituent minerals and their alignment directions according to the tectonic setting.

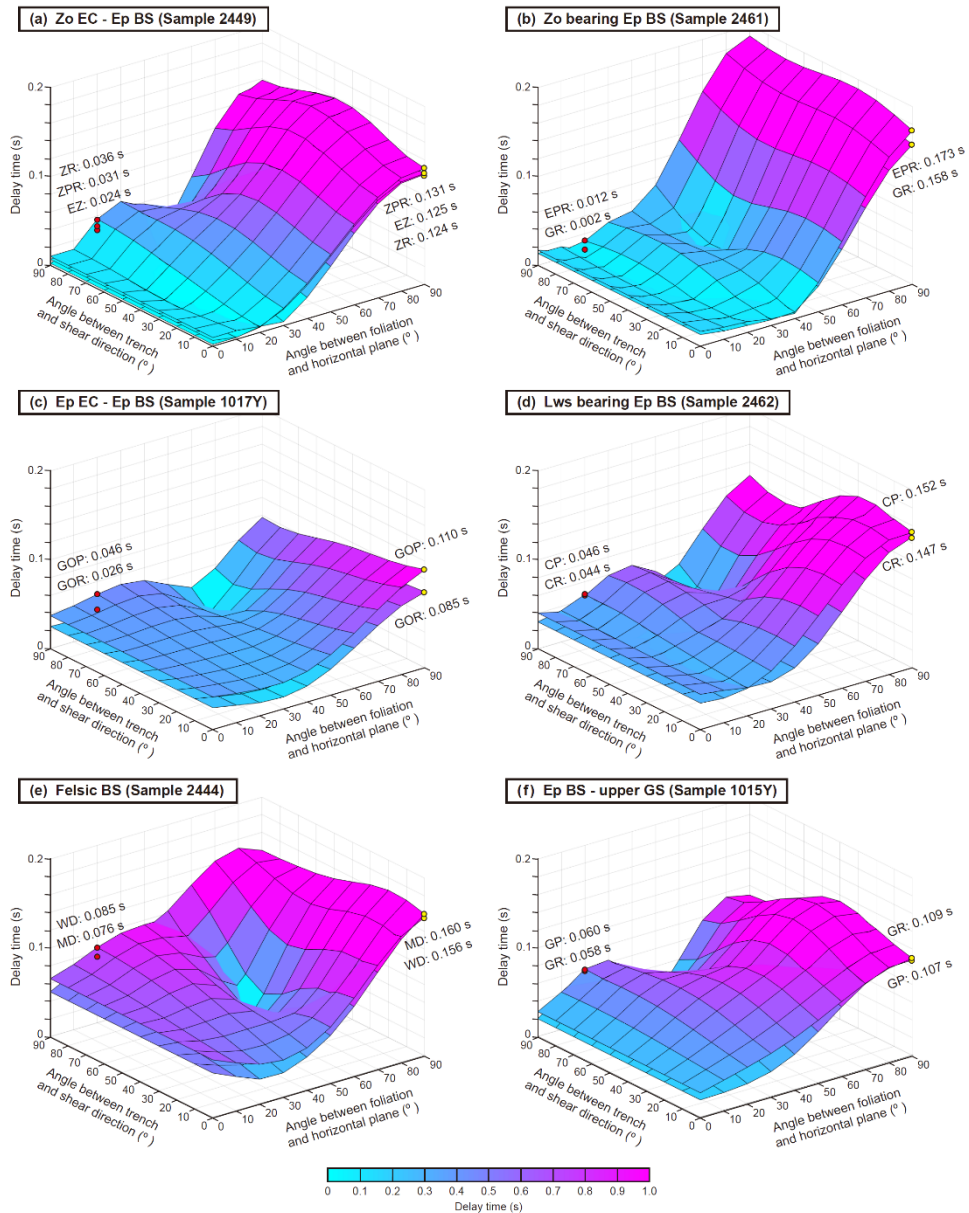


**Figure 5.31.** The delay time of S-wave for 7 km-thick oceanic crust underthrust tilted  $\sim 20^\circ$  beneath the Caribbean plate calculated by different angles between trench and shear direction from  $0^\circ$  (trench-parallel) to  $90^\circ$  (trench-normal) and different angles between foliation and horizontal plane from  $0^\circ$  (horizontal) to  $90^\circ$  (vertical). Red dots: delay times when oceanic crust is deformed in subduction by tilted slab. Yellow dots: delay time when oceanic crust is deformed in lateral shear by strike-slip fault.

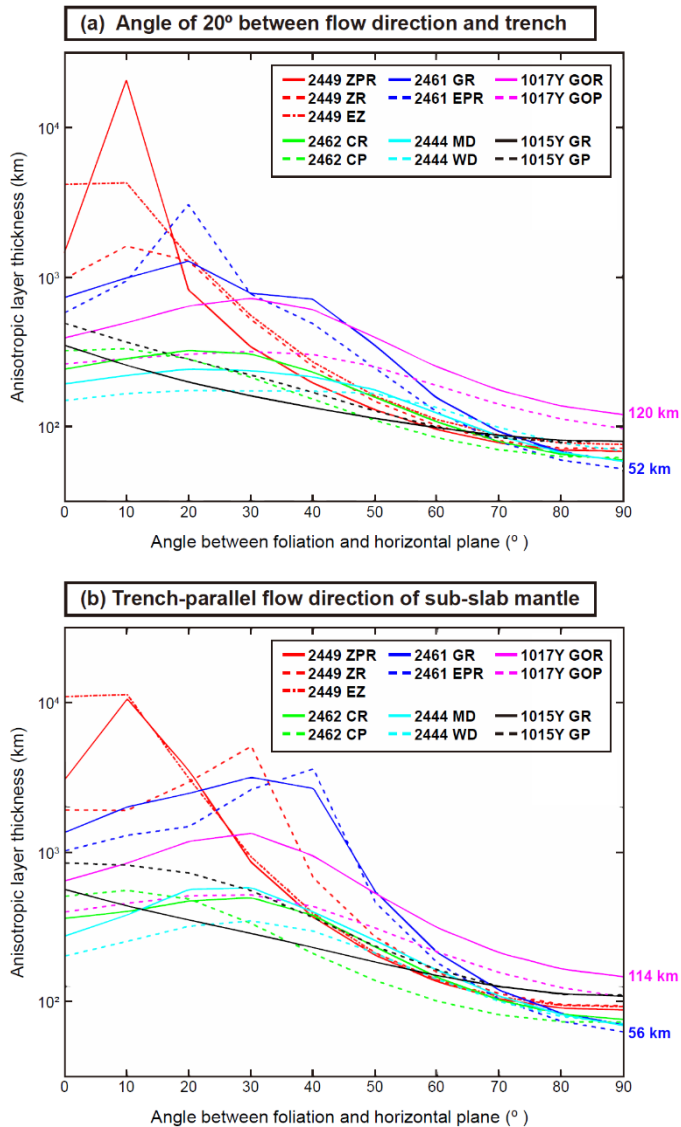


**Figure 5.32.** The required thickness of the anisotropic layer (log scale) beneath the Hispaniola to derive the delay time of  $\delta t \sim 1.3$  s observed near the study area by assuming that the oceanic crust of the subducted slab detached from North American plate was composed of blueschist-facies metamorphic rocks and was deformed by **(a)** mantle flow parallel to the plate motion ( $\sim 20^\circ$  to the trench) or by **(b)** sub-slab mantle flow parallel to the trench.

## 5.6. Conclusion

In this chapter, deformation microstructures of naturally deformed epidote blueschists (high pressure metabasites) from Río San Juan metamorphic complex in Dominican Republic were studied to understand deformation mechanisms and LPO developments of minerals in the subducted oceanic crust, and seismic anisotropy observed in the northeastern margin of the Caribbean plate. Since the high pressure metabasite blocks in the serpentinite mélangé were exhumed from different depths and through different path, the deformation microstructures and fabric strength were different depending on the P-T-t condition in which the strain occurred. The misorientation line less than  $1^\circ$  along the chemical composition boundary between sodic to sodic-calcic amphibole within a single grain in epidote eclogite-epidote blueschist facies rock (sample 1017Y) suggests that the transition of the chemical composition can moderately affect the tilting of the crystal lattice. However, the dominant misorientation lines, irrelevant to the chemical transition boundary, suggest that the main mechanism of the LPO development of amphibole is likely to be a deformation in dislocation creep. The high density of subgrain boundaries and high orientation deviation angles of zoisite porphyroclast in zoisite eclogite-epidote blueschist facies rock (sample 2449) suggest that they were deformed by dislocation creep and developed LPO with strong fabric strength. The remnant of zoisite inclusion within epidote grain and epidote at the zoisite grain boundary in zoisite bearing epidote blueschist facies rock (sample 2461) suggest a possibility of the transition from zoisite to epidote due to the supply of  $\text{Fe}^{3+}$  cation during their

subduction or exhumation processes. The small amount of misorientation lines, weak fabric strength, and low grain orientation spread values of epidote aggregates which are regarded as the lawsonite pseudomorph in lawsonite bearing epidote blueschist facies rock (sample 2462) suggest that LPO of epidote in aggregates might not be developed by recrystallization of epidote porphyroclast in dislocation creep but by the metamorphic transition from lawsonite to epidote following the pre-existing subgrain boundary of the lawsonite porphyroclast. The numerous misorientation lines, high orientation deviation angles, and lattice shifts along these subgrain boundaries of omphacite in epidote eclogite-epidote blueschist facies rock (sample 1017Y) suggest that the omphacite LPO was developed by dislocation creep, but their weak fabric strength might be due to the slip system of omphacite not being activated and capturing many subgrain boundaries under the blueschist-facies metamorphic conditions. Considering the transition of tectonic setting from subduction to oblique underthrust and/or lateral shear, the delay time of the oceanic crust can contribute 0.09–0.18 s to the delay time of the study area when the 7 km thick oceanic crust underthrust tilted  $\sim 20^\circ$  beneath the Caribbean plate is deformed in lateral shear by strike-slip Septentrional Fault Zone. When the break-offed subducted slab exists beneath the study area and is deformed in lateral shear by sub-slab mantle flow and/or strike-slip fault, the thickness of the anisotropic layer composed of blueschist-facies metamorphic rocks is required to be  $\sim 55$ – $108$  km to derive the delay time of  $\sim 1.3$  s observed in the study area. These results suggest that the subducted oceanic crust metamorphosed in blueschist-facies condition can highly contribute to the seismic anisotropy of the northeastern margin of the Caribbean plate depending on the LPO of the constituent minerals and their alignment directions according to the tectonic setting.

# CHAPTER 6

## Summary & Conclusion

To understand the deformation environments and mechanisms of rocks and seismic properties in the lithospheric mantle and the convergent plate margins, this dissertation presents detailed analysis of naturally deformed rocks derived from lithospheric mantle and subducted oceanic crust, as well as the results of the first deformation experiments of epidote blueschist under the conditions prevailing over the subducting slab in a warm subduction zone. This dissertation presents deformation microstructures and seismic properties of naturally deformed rocks in paleo- and active convergent plate margins: the former is the mantle peridotite xenolith derived from the lithospheric mantle within the strike-slip fault zone in eastern China (Chapter 2); the latter is the high pressure metamorphic rocks (from eclogite- to epidote blueschist-facies) derived from subducted oceanic crust in serpentinite mélange of northern Dominican Republic (Chapter 5). This dissertation also presents deformation microstructures developed by the first deformation experiments of epidote blueschist-facies rocks in simple shear (Chapter 3) and their resultant seismic properties of minerals and whole rocks (Chapter 4).

In Chapter 2, it is found that there are different types of olivine LPOs in mantle peridotite xenoliths from Shanwang in eastern China: one is the type-B LPO of olivine in spinel lherzolite samples, the other is the type-E LPO of olivine in spinel wehrlite samples. The strong fabric strength ( $M$ -index = 0.12–0.17 for type-B LPO of olivine, and 0.04–0.16 for type-E LPO of olivine) and the numerous dislocation microstructures (free dislocation density  $\rho = 0.270 \times 10^{12}$ – $0.384 \times 10^{12} \text{ m}^{-2}$ ) in olivine suggest that these mantle peridotite samples were deformed in dislocation creep. Paleostress estimation of olivine ( $\sim 50$  MPa) and measurement of water content in pyroxenes (120–760 $\pm$ 100 ppm H/Si in Opx, and 1320–7690 $\pm$ 100 ppm H/Si in Cpx) of spinel lherzolites suggest that the type-B olivine LPO is most likely developed in the presence of water at high stress. In contrast, paleostress of olivine ( $\sim 20$  MPa) and water content in olivine (50–200 $\pm$ 30 ppm H/Si) and pyroxene (1060–3970 $\pm$ 30 ppm H/Si in Cpx) of spinel wehrlites suggest that the type-E olivine LPO is most likely developed in the presence of water at relatively low stress. This result suggests the possibility that their microstructures may have developed in different deformation environments. The thickness of the anisotropic layer, estimated for four geodynamic end models, suggests that two different types of olivine LPOs could explain the seismic anisotropy under the study area by two deformation modes. During/after the Mesozoic continental collision between the Sino-Korean and South China cratons, spinel lherzolites mantle wedge might be deformed by lateral shear mode developing a type-B olivine LPO due to the syn-orogenic strike-slip fault (Tan-Lu fault zone). During the period of change in plate motion in relation to the westward-subducting Pacific plate, spinel wehrlites mantle might be deformed by horizontal extension mode developing a type-E olivine LPO as the Tan-Lu fault zone has changed from strike-slip to extensional fault related to the trench roll-back of Pacific plate.

In Chapter 3, deformation experiments of epidote blueschist were conducted for the first time in simple shear using a high-pressure, high-temperature solid medium apparatus (modified Griggs apparatus) under the epidote blueschist-facies condition at pressures of  $P = 0.9\text{--}1.5$  GPa and temperatures of  $T = 400\text{--}500$  °C. After the experiments, two types of glaucophane LPO were developed by similar mechanisms bounded by the shear strain of  $1 < \gamma \leq 2$ , while two types of epidote LPO were developed by different mechanisms bounded by the shear strain of  $3 < \gamma < 4$ . The numerous dislocation microstructures observed by TEM and intracrystalline microstructures determined through high-resolution EBSD mapping of glaucophane suggest that the LPO of glaucophane was developed by dislocation creep under a shear strain of  $0.4 \leq \gamma \leq 4.5$ , somewhat affected by cataclastic/granular flow at a shear strain of  $\gamma > 2$  in large grains. Thin ductile shear bands observed at a high shear strain of  $\gamma = 4.5$  in small grains suggests that the brittle–ductile transition of glaucophane likely occurs at epidote blueschist-facies metamorphic conditions depending on the magnitude of shear strain and grain size. The dislocation microstructures in epidote such as subgrain boundaries and twins revealed by TEM observations suggest that the LPO of epidote was developed by dislocation creep under a shear strain of  $2 < \gamma < 4$ . However, because the epidote is more rigid than other minerals in the matrix, the LPO development of epidote is considered to be affected by cataclastic flow with rigid body rotation under a high shear strain ( $\gamma > 4$ ). These experimental results suggest that the magnitude of shear strain, grain size, and rheological contrast between constituent minerals are important factors affecting the deformation mechanisms that mainly developed the LPO of glaucophane and epidote at the top of a subducting slab in a warm subduction zone.

In Chapter 4, the seismic velocity and anisotropy of the glaucophane and epidote in experimentally deformed epidote blueschist in Chapter 3 were calculated to understand the seismic low velocity layer and seismic anisotropy induced by LPOs of glaucophane and epidote of the subducting slab. The seismic velocity and anisotropy of glaucophane was increased with increasing shear strain, whereas those of epidote was decreased with increasing shear strain. The seismic velocity and anisotropy of whole rock (epidote blueschist) was increased with increasing shear strain, following the trends of glaucophane. These data suggest that the magnitude of shear strain can affect the seismic velocity and anisotropy of the upper subducting slab within the epidote blueschist-facies metamorphic condition. The calculation of delay time and  $V_p/V_s$  ratio for the oceanic crust composed of epidote blueschist suggests that the subducting angle of the slab and the volume proportion of glaucophane and epidote with different LPO types can influence the delay time of S-wave and  $V_p/V_s$  ratio observed in the subduction zone. The 8–9 % reduction of  $V_p$  and 6–7 % reduction of  $V_s$  of experimentally deformed epidote blueschist, compared to the seismic velocity of the lithospheric mantle surrounding the subducting slab, indicate that deformed epidote blueschist can contribute to the seismic low velocity layer observed on the top of the subducting slab. The calculation of seismic anisotropy for the oceanic crust composed of epidote blueschist suggests that the trench-normal  $V_s1$  polarization direction in the forearc region of the subduction zone can be caused by the type-1 LPO of glaucophane and the type-1 LPO of epidote, regardless of the subducting angle of the slab. On the other hand, the calculation data suggest that the trench-parallel  $V_s1$  polarization direction can be caused by the type-2 LPO of epidote with low subducting angle and the type-2 LPO of glaucophane with high subducting angle, when the volume proportion of each other exceeds 50 %

in the oceanic crust. These results suggest that the volume proportion and LPO types of glaucophane and epidote, and the subducting angle of the slab can be important factors to control seismic velocity and anisotropy observed in subduction zones.

In chapter 5, deformation microstructures of naturally deformed epidote blueschists (high pressure metabasites) from serpentinite mélangé of Río San Juan metamorphic complex in Dominican Republic were different depending on the P-T conditions in which the strain occurred. The misorientation line less than  $1^\circ$  along the chemical composition boundary between sodic to sodic-calcic amphibole within a single grain suggests that the transition of the chemical composition can moderately affect the tilting of the crystal lattice. However, the dominant misorientation lines, irrelevant to the chemical transition boundary, suggest that the main mechanism of the LPO development of amphibole is likely to be a deformation in dislocation creep. The high density of subgrain boundaries and high orientation deviation angles of zoisite porphyroclast suggest that they were deformed by dislocation creep and developed the LPO with strong fabric strength. In addition, the remnant of zoisite inclusion within epidote grain and epidote at the zoisite grain boundary suggest a possibility of the zoisite-epidote transition due to the supply of  $\text{Fe}^{3+}$  cation during their subduction or exhumation processes. The small amount of misorientation lines, weak fabric strength, and low grain orientation spread values of epidote aggregates which are regarded as the lawsonite pseudomorph suggest that LPO of epidote in aggregates might not be developed by recrystallization of epidote porphyroclast in dislocation creep, but by the metamorphic transition from lawsonite to epidote following the pre-existing subgrain boundary of the lawsonite porphyroclast. The numerous misorientation lines, high orientation deviation angles,

and lattice shifts along these subgrain boundaries of omphacite suggest that the omphacite LPO was developed by dislocation creep, but their weak fabric strength may be due to the slip system of omphacite not being activated and capturing many subgrain boundaries under the blueschist-facies metamorphic conditions. Considering the transition of tectonic setting from subduction to oblique underthrust and/or lateral shear in the study area, the delay time of the oceanic crust can contribute 0.09–0.18 s to the delay time of the northeastern margin of the Caribbean plate when the 7 km thick oceanic crust underthrust tilted  $\sim 20^\circ$  beneath the Caribbean plate is deformed in lateral shear by strike-slip Septentrional Fault Zone. Considering the existence of the break-offed oceanic slab detached from older subducted North American oceanic plate beneath the Hispaniola, the thickness of the anisotropic layer composed of blueschist-facies metamorphic rocks is required to be  $\sim 55$ – $108$  km to derive the delay time of  $\sim 1.3$  s observed in the study area when it is deformed in lateral shear mode by sub-slab mantle flow and/or strike-slip fault zone. These results suggest that the subducted oceanic crust metamorphosed in blueschist-facies condition can highly contribute to the seismic anisotropy of the northeastern margin of the Caribbean plate depending on the LPO of the constituent minerals and their alignment directions according to the tectonic setting.

These studies are expected to provide further interpretations of the mantle dynamics in the lithospheric mantle and the deformation processes of the subducting oceanic crust at the convergent plate margins.

## REFERENCES

- Abbott Jr., R.N., Draper, G., Broman, B.N., 2006. P-T Path for Ultrahigh-Pressure Garnet Ultramafic Rocks of the Cuaba Gneiss, Rio San Juan Complex, Dominican Republic. *International Geology Review* 48, 778-790.
- Abers, G.A., 2000. Hydrated subducted crust at 100–250 km depth. *Earth and Planetary Science Letters* 176, 323-330.
- Abers, G.A., Nakajima, J., van Keken, P.E., Kita, S., Hacker, B.R., 2013. Thermal–petrological controls on the location of earthquakes within subducting plates. *Earth and Planetary Science Letters* 369-370, 178-187.
- Abramson, E.H., Brown, J.M., Slutsky, L.J., Zaug, J., 1997. The elastic constants of San Carlos olivine to 17 GPa. *Journal of Geophysical Research: Solid Earth* (1978–2012) 102, 12253-12263.
- Abt, D.L., Fischer, K.M., Abers, G.A., Strauch, W., Protti, J.M., González, V., 2009. Shear wave anisotropy beneath Nicaragua and Costa Rica: Implications for flow in the mantle wedge. *Geochemistry, Geophysics, Geosystems* 10, Q05S15, 01-26.
- Agard, P., Yamato, P., Jolivet, L., Burov, E., 2009. Exhumation of oceanic blueschists and eclogites in subduction zones: Timing and mechanisms. *Earth-Science Reviews* 92, 53-79.
- Ai, Y., Zheng, T., 2003. The upper mantle discontinuity structure beneath eastern China. *Geophysical research letters* 30, 1-5.
- Aleksandrov, K., Alchikov, U., Belikov, B., Zaslavskii, B., Krupnyi, A., 1974. Velocities of elastic waves in minerals at atmospheric pressure and increasing precision of elastic constants by means of EVM. *Izv. Acad. Sci. USSR, Geol. Ser* 10, 15-24.
- Aubaud, C., Hauri, E.H., Hirschmann, M.M., 2004. Hydrogen partition coefficients between nominally anhydrous minerals and basaltic melts. *Geophysical Research Letters* 31, 1-4.
- Audet, P., Bostock, M.G., Boyarko, D.C., Brudzinski, M.R., Allen, R.M., 2010. Slab morphology in the Cascadia fore arc and its relation to episodic tremor and slip. *Journal of Geophysical Research* 115, B00A16, 01-15.
- Audet, P., Kim, Y., 2016. Teleseismic constraints on the geological environment of deep episodic slow earthquakes in subduction zone forearcs: A review. *Tectonophysics* 670, 1-15.
- Bachmann, F., Hielscher, R., Schaeben, H., 2011. Grain detection from 2d and 3d EBSD data—Specification of the MTEX algorithm. *Ultramicroscopy* 111, 1720-1733.

- Bai, Q., Kohlstedt, D.L., 1992. High-temperature creep of olivine single crystals, 2. Dislocation structures. *Tectonophysics* 206, 1-29.
- Balestro, G., Festa, A., Tartarotti, P., 2014. Tectonic significance of different block-in-matrix structures in exhumed convergent plate margins: examples from oceanic and continental HP rocks in Inner Western Alps (northwest Italy). *International Geology Review* 57, 581-605.
- Bascou, J., Barruol, G., Vauchez, A., Mainprice, D., Egydio-Silva, M., 2001. EBSD-measured lattice-preferred orientations and seismic properties of eclogites. *Tectonophysics* 342, 61-80.
- Bascou, J., Doucet, L.S., Saumet, S., Ionov, D.A., Ashchepkov, I.V., Golovin, A.V., 2011. Seismic velocities, anisotropy and deformation in Siberian cratonic mantle: EBSD data on xenoliths from the Udachnaya kimberlite. *Earth and Planetary Science Letters* 304, 71-84.
- Bell, D.R., Rossman, G.R., Maldener, J., Endisch, D., Rauch, F., 2003. Hydroxide in olivine: A quantitative determination of the absolute amount and calibration of the IR spectrum. *Journal of Geophysical Research: Solid Earth* (1978–2012) 108, 1-9.
- Ben Ismaïl, W., Mainprice, D., 1998. An olivine fabric database: an overview of upper mantle fabrics and seismic anisotropy. *Tectonophysics* 296, 145-157.
- Bezacier, L., Reynard, B., Bass, J.D., Sanchez-Valle, C., Van de Moortèle, B., 2010b. Elasticity of antigorite, seismic detection of serpentinites, and anisotropy in subduction zones. *Earth and Planetary Science Letters* 289, 198-208.
- Bezacier, L., Reynard, B., Bass, J.D., Wang, J., Mainprice, D., 2010a. Elasticity of glaucophane, seismic velocities and anisotropy of the subducted oceanic crust. *Tectonophysics* 494, 201-210.
- Bhagat, S.S., Bass, J.D., Smyth, J.R., 1992. Single-crystal elastic properties of omphacite-C2/c by Brillouin spectroscopy. *Journal of Geophysical Research* 97.
- Birch, F., 1960. The velocity of compressional waves in rocks to 10 kilobars: 1. *Journal of Geophysical Research* 65, 1083-1102.
- Brenker, F.E., Prior, D.J., Müller, W.F., 2002. Cation ordering in omphacite and effect on deformation mechanism and lattice preferred orientation (LPO). *Journal of Structural Geology* 24, 1991-2005.
- Brey, G.P., Köhler, T., 1990. Geothermobarometry in four-phase lherzolites II. New thermobarometers, and practical assessment of existing thermobarometers. *Journal of Petrology* 31, 1353-1378.
- Browaeyns, J.T., Chevrot, S., 2004. Decomposition of the elastic tensor and geophysical applications. *Geophysical Journal International* 159, 667-678.
- Brown, J.M., Abramson, E.H., Angel, R.J., 2006. Triclinic elastic constants for low albite. *Physics and Chemistry of Minerals* 33, 256-265.

- Brunsmann, A., Franz, G., Erzinger, J., Landwehr, D., 2000. Zoisite-and clinozoisite-segregations in metabasites (Tauern Window, Austria) as evidence for high-pressure fluid-rock interaction. *Journal of Metamorphic Geology* 18, 1-22.
- Bunge, H.-J., 1982. *Texture Analysis in Materials Science: Mathematical Models*. Butterworths, London, UK.
- Bystricky, M., Kunze, K., Burlini, L., Burg, J.-P., 2000. High shear strain of olivine aggregates: rheological and seismic consequences. *Science* 290, 1564-1567.
- Cao, Y., Jung, H., 2016. Seismic properties of subducting oceanic crust: Constraints from natural lawsonite-bearing blueschist and eclogite in Sivrihisar Massif, Turkey. *Physics of the Earth and Planetary Interiors* 250, 12-30.
- Cao, Y., Jung, H., Song, S., 2013. Petro-fabrics and seismic properties of blueschist and eclogite in the North Qilian suture zone, NW China: Implications for the low-velocity upper layer in subducting slab, trench-parallel seismic anisotropy, and eclogite detectability in the subduction zone. *Journal of Geophysical Research: Solid Earth* 118, 3037-3058.
- Cao, Y., Jung, H., Song, S., 2014. Microstructures and petro-fabrics of lawsonite blueschist in the North Qilian suture zone, NW China: Implications for seismic anisotropy of subducting oceanic crust. *Tectonophysics* 628, 140-157.
- Cao, Y., Song, S., Niu, Y.L., Jung, H., Jin, Z.M., 2011. Variation of mineral composition, fabric and oxygen fugacity from massive to foliated eclogites during exhumation of subducted ocean crust in the North Qilian suture zone, NW China. *Journal of Metamorphic Geology* 29, 699-720.
- Carter, N.L., Ave'Lallemant, H.G., 1970. High temperature flow of dunite and peridotite. *Geological Society of America Bulletin* 81, 2181-2202.
- Chai, M., Brown, J.M., Slutsky, L.J., 1997. The elastic constants of an aluminous orthopyroxene to 12.5 GPa. *Journal of Geophysical Research: Solid Earth* (1978–2012) 102, 14779-14785.
- Chang, L.J., Wang, C.Y., Ding, Z.F., 2009. Seismic anisotropy of upper mantle in eastern China. *Science in China Series D: Earth Sciences* 52, 774-783.
- Chen, L., 2010. Concordant structural variations from the surface to the base of the upper mantle in the North China Craton and its tectonic implications. *Lithos* 120, 96-115.
- Chen, L., Tao, W., Zhao, L., Zheng, T., 2008. Distinct lateral variation of lithospheric thickness in the Northeastern North China Craton. *Earth and Planetary Science Letters* 267, 56-68.
- Chen, L., Zheng, T., Xu, W., 2006. A thinned lithospheric image of the Tanlu Fault Zone, eastern China: Constructed from wave equation based receiver function migration. *Journal of Geophysical Research* 111, B09312.

- Choi, S., Fabbri, O., Topuz, G., Okay, A.I., Jung, H., 2021. Twin Induced Reduction of Seismic Anisotropy in Lawsonite Blueschist. *Minerals* 11.
- Christensen, D.H., Abers, G.A., 2010. Seismic anisotropy under central Alaska from SKS splitting observations. *Journal of Geophysical Research* 115.
- Christensen, N.I., Lundquist, S.M., 1982. Pyroxene orientation within the upper mantle. *Geological Society of America Bulletin* 93, 279-288.
- Chu, Z.-Y., Wu, F.-Y., Walker, R.J., Rudnick, R.L., Pitcher, L., Puchtel, I.S., Yang, Y.-H., Wilde, S.A., 2009. Temporal evolution of the lithospheric mantle beneath the eastern North China Craton. *Journal of Petrology* 50, 1857-1898.
- Collins, M.D., Brown, J.M., 1998. Elasticity of an upper mantle clinopyroxene. *Physics and chemistry of minerals* 26, 7-13.
- Connolly, J., Kerrick, D., 2002. Metamorphic controls on seismic velocity of subducted oceanic crust at 100–250 km depth. *Earth and Planetary Science Letters* 204, 61-74.
- Corbeau, J., Gonzalez, O.L., Clouard, V., Rolandone, F., Leroy, S., Keir, D., Stuart, G., Momplaisir, R., Boisson, D., Prépetit, C., 2019. Is the local seismicity in western Hispaniola (Haiti) capable of imaging northern Caribbean subduction? *Geosphere* 15, 1738-1750.
- Cossette, É., Schneider, D., Audet, P., Grasemann, B., Habler, G., 2015. Seismic properties and mineral crystallographic preferred orientations from EBSD data: Results from a crustal-scale detachment system, Aegean region. *Tectonophysics* 651-652, 66-78.
- Das, P.K., Mondal, S.K., Mandal, N., 2021. First principles prediction of exceptional mechanical and electronic behaviour of Titanite (CaTiSiO<sub>5</sub>). *Materialia* 15.
- Deer, W.A., Howie, R.A., Zussman, J., 1986. *Rock-Forming Minerals: Disilicates and Ring Silicates*, 2nd ed. Geological Society of London, UK.
- Draper, G., Mann, P., Lewis, J.F., 1994. Hispaniola, in: Donovan, S.K., Jackson, T.A. (Eds.), *Caribbean geology: an introduction*. University of the West Indies Publishers Association, Kingston, Jamaica, pp. 129-150.
- Draper, G., Nagle, F., Renne, P.R., 1991. Geology, structure, and tectonic development of the Rio San Juan Complex, northern Dominican Republic. *Geological Society of America Special Papers* 262, 77-96.
- Drury, M.R., Urai, J.L., 1990. Deformation-related recrystallization processes. *Tectonophysics* 172, 235-253.
- Ebert, A., Herwegh, M., Pfiffner, A., 2007. Cooling induced strain localization in carbonate mylonites within a large-scale shear zone (Glarus thrust, Switzerland). *Journal of Structural Geology* 29, 1164-1184.
- Ernst, W., 1988. Tectonic history of subduction zones inferred from retrograde blueschist PT paths. *Geology* 16, 1081-1084.
- Escuder-Viruete, J., 2009. Mapa Geológica de la República Dominicana E. 1: 50.000, Río San Juan (6174-I). Dirección General de Minería, Santo Domingo, 223.

- Escuder-Viruete, J., Friedman, R., Castillo-Carrión, M., Jabites, J., Pérez-Estaún, A., 2011. Origin and significance of the ophiolitic high-P mélanges in the northern Caribbean convergent margin: Insights from the geochemistry and large-scale structure of the Río San Juan metamorphic complex. *Lithos* 127, 483-504.
- Escuder-Viruete, J., Pérez-Estaún, A., 2013. Contrasting exhumation P–T paths followed by high-P rocks in the northern Caribbean subduction–accretionary complex: Insights from the structural geology, microtextures and equilibrium assemblage diagrams. *Lithos* 160-161, 117-144.
- Escuder-Viruete, J., Pérez, Y., 2020. Neotectonic structures and stress fields associated with oblique collision and forearc sliver formation in northern Hispaniola: Implications for the seismic hazard assessment. *Tectonophysics* 784.
- Escuder-Viruete, J., Valverde-Vaquero, P., Rojas-Agramonte, Y., Gabites, J., Castillo-Carrión, M., Pérez-Estaún, A., 2013a. Timing of deformational events in the Río San Juan complex: Implications for the tectonic controls on the exhumation of high-P rocks in the northern Caribbean subduction–accretionary prism. *Lithos* 177, 416-435.
- Escuder-Viruete, J., Valverde-Vaquero, P., Rojas-Agramonte, Y., Jabites, J., Pérez-Estaún, A., 2013b. From intra-oceanic subduction to arc accretion and arc-continent collision: Insights from the structural evolution of the Río San Juan metamorphic complex, northern Hispaniola. *Journal of Structural Geology* 46, 34-56.
- Evans, B.W., 1990. Phase relations of epidote-blueschists. *Lithos* 25, 3-23.
- Faccenda, M., Burlini, L., Gerya, T.V., Mainprice, D., 2008. Fault-induced seismic anisotropy by hydration in subducting oceanic plates. *Nature* 455, 1097-1100.
- Fan, W.M., Zhang, H.F., Baker, J., Jarvis, K.E., Mason, P.R.D., Menzies, M.A., 2000. On and off the North China Craton: where is the Archaean keel? *Journal of Petrology* 41, 933-950.
- Fletcher, C.J.N., Fitches, W.R., Rundle, C.C., Evans, J.A., 1995. Geological and isotopic constraints on the timing of movement in the Tan-Lu Fault Zone, northeastern China. *Journal of Southeast Asian Earth Sciences* 11, 15-22.
- Fornieris, J.F., Holloway, J.R., 2003. Phase equilibria in subducting basaltic crust: implications for H<sub>2</sub>O release from the slab. *Earth and Planetary Science Letters* 214, 187-201.
- Franz, G., Liebscher, A., 2004. Physical and Chemical Properties of the Epidote Minerals—An Introduction—. *Reviews in mineralogy and geochemistry* 56, 1-81.
- Fujimoto, Y., Kono, Y., Hirajima, T., Kanagawa, K., Ishikawa, M., Arima, M., 2010. P-wave velocity and anisotropy of lawsonite and epidote blueschists:

- Constraints on water transportation along subducting oceanic crust. *Physics of the Earth and Planetary Interiors* 183, 219-228.
- Gao, S., Rudnick, R.L., Carlson, R.W., McDonough, W.F., Liu, Y.S., 2002. Re-Os evidence for replacement of ancient mantle lithosphere beneath the North China craton. *Earth and Planetary Science Letters* 198, 307-322.
- Gardner, R., Piazzolo, S., Evans, L., Daczko, N., 2017. Patterns of strain localization in heterogeneous, polycrystalline rocks – a numerical perspective. *Earth and Planetary Science Letters* 463, 253-265.
- Gifkins, R.C., 1970. *Optical microscopy of metals*. American Elsevier, New York.
- Gilder, S.A., Leloup, P.H., Courtillot, V., Chen, Y., Coe, R.S., Zhao, X.X., Xiao, W.J., Halim, N., Cogné, J.P., Zhu, R.X., 1999. Tectonic evolution of the Tancheng-Lujiang (Tan-Lu) fault via Middle Triassic to Early Cenozoic paleomagnetic data. *J Geophys Res-Sol Ea* 104, 15365-15390.
- Godard, G., van Roermund, H.L.M., 1995. Deformation-induced clinopyroxene fabrics from eclogites. *Journal of Structural Geology* 17, 1425-1443.
- Goetze, C., Kohlstedt, D.L., 1973. Laboratory study of dislocation climb and diffusion in olivine. *Journal of Geophysical Research* 78, 5961-5971.
- Greve, S.M., Savage, M.K., Hofmann, S.D., 2008. Strong variations in seismic anisotropy across the Hikurangi subduction zone, North Island, New Zealand. *Tectonophysics* 462, 7-21.
- Griffin, W.L., Andi, Z., O'Reilly, S.Y., Ryan, C.G., 1998a. Phanerozoic evolution of the lithosphere beneath the Sino-Korean craton, in: Flower, M.F.J., Chung, S.-L., Lo, C.-H., Lee, T.-Y. (Eds.), *Mantle Dynamics and Plate Interactions in East Asia*, Geodynamics Series. American Geophysical Union, Washington, D.C., pp. 107-126.
- Griffin, W.L., O'Reilly, S.Y., Ryan, C.G., Gaul, O., Ionov, D.A., 1998b. Secular variation in the composition of subcontinental lithospheric mantle: Geophysical and geodynamic implications, in: Braun, J., Dooley, J., Goleby, B., van der Hilst, R., Klootwijk, C. (Eds.), *Structure and Evolution of the Australian Continent*, Geodynamic Series. American Geophysical Union, Washington, D.C., pp. 1-26.
- Gripp, A.E., Gordon, R.G., 2002. Young tracks of hotspots and current plate velocities. *Geophysical Journal International* 150, 321-361.
- Ha, Y., Jung, H., Raymond, L.A., 2018. Deformation fabrics of glaucophane schists and implications for seismic anisotropy: the importance of lattice preferred orientation of phengite. *International Geology Review* 61, 720-737.
- Hacker, B.R., Abers, G.A., Peacock, S.M., 2003. Subduction factory 1. Theoretical mineralogy, densities, seismic wave speeds, and H<sub>2</sub>O contents. *Journal of Geophysical Research: Solid Earth* 108, 2029, 2021-2026.

- Harigane, Y., Michibayashi, K., Morishita, T., Tani, K., Dick, H.J., Ishizuka, O., 2013. The earliest mantle fabrics formed during subduction zone infancy. *Earth and Planetary Science Letters* 377-378, 106-113.
- Hasegawa, A., Nakajima, J., Kita, S., Okada, T., Matsuzawa, T., Kirby, S.H., 2007. Anomalous deepening of a belt of intraslab earthquakes in the Pacific slab crust under Kanto, central Japan: Possible anomalous thermal shielding, dehydration reactions, and seismicity caused by shallower cold slab material. *Geophysical Research Letters* 34.
- Hattori, K.H., Guillot, S., Saumur, B.-M., Tubrett, M.N., Vidal, O., Morfin, S., 2010. Corundum-bearing garnet peridotite from northern Dominican Republic: A metamorphic product of an arc cumulate in the Caribbean subduction zone. *Lithos* 114, 437-450.
- Hauri, E.H., Gaetani, G.A., Green, T.H., 2006. Partitioning of water during melting of the Earth's upper mantle at H<sub>2</sub>O-undersaturated conditions. *Earth and Planetary Science Letters* 248, 715-734.
- Healy, D., Reddy, S.M., Timms, N.E., Gray, E.M., Brovarone, A.V., 2009. Trench-parallel fast axes of seismic anisotropy due to fluid-filled cracks in subducting slabs. *Earth and Planetary Science Letters* 283, 75-86.
- Helmstaedt, H., Anderson, O.L., Gavasci, A.T., 1972. Petrofabric Studies of Eclogite, Spinel-Websterite, and Spinel-Lherzolite Xenoliths from Kimberlite-Bearing Breccia Pipes in Southeastern Utah and Northeastern Arizona. *Journal of Geophysical Research Solid Earth* 77, 4350-4365.
- Hertwig, A., McClelland, W.C., Kitajima, K., Schertl, H.-P., Maresch, W.V., Stanek, K., Valley, J.W., Sergeev, S.A., 2016. Inherited igneous zircons in jadeitite predate high-pressure metamorphism and jadeitite formation in the Jagua Clara serpentinite mélangé of the Rio San Juan Complex (Dominican Republic). *Contributions to Mineralogy and Petrology* 171.
- Heyliger, P., Ledbetter, H., Kim, S., 2003. Elastic constants of natural quartz. *J Acoust Soc Am* 114, 644-650.
- Hidas, K., Falus, G., Szabó, C., Szabó, P.J., Kovács, I., Földes, T., 2007. Geodynamic implications of flattened tabular equigranular textured peridotites from the Bakony-Balaton Highland Volcanic Field (Western Hungary). *Journal of Geodynamics* 43, 484-503.
- Hirose, F., Nakajima, J., Hasegawa, A., 2008. Three-dimensional seismic velocity structure and configuration of the Philippine Sea slab in southwestern Japan estimated by double-difference tomography. *Journal of Geophysical Research* 113, B09315, 09311-09326.
- Hodges, M., Miller, M.S., 2015. Mantle flow at the highly arcuate northeast corner of the Lesser Antilles subduction zone: Constraints from shear-wave splitting analyses. *Lithosphere* 7, 579-587.

- Holtzman, B.K., Kohlstedt, D.L., Zimmerman, M.E., Heidelbach, F., Hiraga, T., Hustoft, J., 2003. Melt segregation and strain partitioning: Implications for seismic anisotropy and mantle flow. *Science* 301, 1227-1230.
- Holyoke, C.W., Tullis, J., 2006. Mechanisms of weak phase interconnection and the effects of phase strength contrast on fabric development. *Journal of Structural Geology* 28, 621-640.
- Hu, S., He, L., Wang, J., 2000. Heat flow in the continental area of China: a new data set. *Earth and Planetary Science Letters* 179, 407-419.
- Huang, J., Zhao, D., 2006. High-resolution mantle tomography of China and surrounding regions. *Journal of Geophysical Research: Solid Earth* (1978–2012) 111, 1-21.
- Huang, Z., Xu, M., Wang, L., Mi, N., Yu, D., Li, H., 2008. Shear wave splitting in the southern margin of the Ordos Block, north China. *Geophysical Research Letters* 35, 1-4.
- Iidaka, T., Niu, F., 2001. Mantle and crust anisotropy in the eastern China region inferred from waveform splitting of SKS and PpSms. *Earth Planets and Space* 53, 159-168.
- Ildefonse, B., Lardeaux, J.-M., Caron, J.-M., 1990. The behavior of shape preferred orientations in metamorphic rocks: amphiboles and jadeites from the Monte Mucrone area (Sesia-Lanzo zone, Italian Western Alps). *Journal of Structural Geology* 12, 1005-1011.
- Ji, S., Xia, B., 2002. Rheology of polyphase earth materials. Presses inter Polytechnique.
- Jiang, F., Speziale, S., Duffy, T.S., 2004. Single-crystal elasticity of grossular- and almandine-rich garnets to 11 GPa by Brillouin scattering. *Journal of Geophysical Research: Solid Earth* 109.
- Jin, L.Y., 1985. Xenoliths in Cenozoic basalts from Tanlu fault. *Journal of Changchun College of Geology* 3, 21-32 (in Chinese).
- Jung, H., 2009. Deformation fabrics of olivine in Val Malenco peridotite found in Italy and implications for the seismic anisotropy in the upper mantle. *Lithos* 109, 341-349.
- Jung, H., 2011. Seismic anisotropy produced by serpentine in mantle wedge. *Earth and Planetary Science Letters* 307, 535-543.
- Jung, H., 2017. Crystal preferred orientations of olivine, orthopyroxene, serpentine, chlorite, and amphibole, and implications for seismic anisotropy in subduction zones: a review. *Geosciences Journal* 21, 985-1011.
- Jung, H., Karato, S.-I., 2001a. Effects of water on dynamically recrystallized grain-size of olivine. *Journal of Structural Geology* 23, 1337-1344.
- Jung, H., Karato, S.-I., 2001b. Water-induced fabric transitions in olivine. *Science* 293, 1460-1463.

- Jung, H., Katayama, I., Jiang, Z., Hiraga, T., Karato, S., 2006. Effect of water and stress on the lattice-preferred orientation of olivine. *Tectonophysics* 421, 1-22.
- Jung, H., Lee, J., Ko, B., Jung, S., Park, M., Cao, Y., Song, S., 2013. Natural type-C olivine fabrics in garnet peridotites in North Qaidam UHP collision belt, NW China. *Tectonophysics* 594, 91-102.
- Jung, H., Mo, W., Choi, S.H., 2009a. Deformation microstructures of olivine in peridotite from Spitsbergen, Svalbard and implications for seismic anisotropy. *Journal of Metamorphic Geology* 27, 707-720.
- Jung, H., Mo, W., Green, H.W., 2009b. Upper mantle seismic anisotropy resulting from pressure-induced slip transition in olivine. *Nature Geoscience* 2, 73-77.
- Jung, H., Park, M., Jung, S., Lee, J., 2010. Lattice preferred orientation, water content, and seismic anisotropy of orthopyroxene. *Journal of Earth Science* 21, 555-568.
- Jung, S., Jung, H., Austrheim, H., 2014. Characterization of olivine fabrics and mylonite in the presence of fluid and implications for seismic anisotropy and shear localization. *Earth, Planets and Space* 66, 46: 41-21.
- Jung, S., Jung, H., Austrheim, H., 2020. Microstructural Evolution of Amphibole Peridotites in Åheim, Norway, and the Implications for Seismic Anisotropy in the Mantle Wedge. *Minerals* 10.
- Kamei, A., Obata, M., Michibayashi, K., Hirajima, T., Svojtka, M., 2010. Two Contrasting Fabric Patterns of Olivine Observed in Garnet and Spinel Peridotite from a Mantle-derived Ultramafic Mass Enclosed in Felsic Granulite, the Moldanubian Zone, Czech Republic. *Journal of Petrology* 51, 101-123.
- Karato, S.-I., 1987. Scanning electron microscope observation of dislocations in olivine. *Physics and Chemistry of Minerals* 14, 245-248.
- Karato, S.-i., 2008. *Deformation of earth materials: an introduction to the rheology of solid earth*. Cambridge University Press, UK.
- Karato, S.-I., Jung, H., 2003. Effects of pressure on high-temperature dislocation creep in olivine. *Philosophical Magazine* 83, 401-414.
- Karato, S.-I., Jung, H., Katayama, I., Skemer, P., 2008. Geodynamic significance of seismic anisotropy of the upper mantle: new insights from laboratory studies. *Annu. Rev. Earth Planet. Sci.* 36, 59-95.
- Karato, S.-I., Lee, K.H., 1999. Stress-strain distribution in deformed olivine aggregates: inference from microstructural observations and implications for texture development, in: Szpunar, J.A. (Ed.), *Proceedings of the 12th International Conference on textures of materials*. National Research Council Press, Montreal, pp. 1546-1555.

- Karato, S.-I., Toriumi, M., Fujii, T., 1980. Dynamic recrystallization of olivine single crystals during high-temperature creep. *Geophysical Research Letters* 7, 649-652.
- Katayama, I., Jung, H., Karato, S.-I., 2004. New type of olivine fabric from deformation experiments at modest water content and low stress. *Geology* 32, 1045-1048.
- Katayama, I., Karato, S., 2006. Effect of temperature on the B-to C-type olivine fabric transition and implication for flow pattern in subduction zones. *Physics of the Earth and Planetary Interiors* 157, 33-45.
- Katayama, I., Karato, S., Brandon, M., 2005. Evidence of high water content in the deep upper mantle inferred from deformation microstructures. *Geology* 33, 613-616.
- Kawakatsu, H., Watada, S., 2007. Seismic evidence for deep-water transportation in the mantle. *Science* 316, 1468-1471.
- Kelemen, P.B., Hart, S.R., Bernstein, S., 1998. Silica enrichment in the continental upper mantle via melt/rock reaction. *Earth and Planetary Science Letters* 164, 387-406.
- Kil, Y., Wendlandt, R.F., 2004. Pressure and temperature evolution of upper mantle under the Rio Grande Rift. *Contributions to Mineralogy and Petrology* 148, 265-280.
- Kim, D., Jung, H., 2015. Deformation microstructures of olivine and chlorite in chlorite peridotites from Almklovdaalen in the Western Gneiss Region, southwest Norway, and implications for seismic anisotropy. *International Geology Review* 57, 650-668.
- Kim, D., Katayama, I., Michibayashi, K., Tsujimori, T., 2013a. Deformation fabrics of natural blueschists and implications for seismic anisotropy in subducting oceanic crust. *Physics of the Earth and Planetary Interiors* 222, 8-21.
- Kim, D., Katayama, I., Michibayashi, K., Tsujimori, T., 2013b. Rheological contrast between glaucophane and lawsonite in naturally deformed blueschist from Diablo Range, California. *Island Arc* 22, 63-73.
- Kim, D., Katayama, I., Wallis, S., Michibayashi, K., Miyake, A., Seto, Y., Azuma, S., 2015. Deformation microstructures of glaucophane and lawsonite in experimentally deformed blueschists: Implications for intermediate-depth intraplate earthquakes. *Journal of Geophysical Research: Solid Earth* 120, 1229-1242.
- Kim, D., Kim, T., Lee, J., Kim, Y., Kim, H., Lee, J.I., 2018. Microfabrics of omphacite and garnet in eclogite from the Lanterman Range, northern Victoria Land, Antarctica. *Geosciences Journal* 22, 939-953.
- Kim, D., Wallis, S., Endo, S., Ree, J.-H., 2016. Seismic properties of lawsonite eclogites from the southern Motagua fault zone, Guatemala. *Tectonophysics* 677-678, 88-98.

- Kneller, E.A., Van Keken, P.E., Karato, S.-I., Park, J., 2005. B-type olivine fabric in the mantle wedge: Insights from high-resolution non-Newtonian subduction zone models. *Earth and Planetary Science Letters* 237, 781-797.
- Ko, B., Jung, H., 2015. Crystal preferred orientation of an amphibole experimentally deformed by simple shear. *Nature communications* 6, 1-10.
- Kohlstedt, D., Evans, B., Mackwell, S., 1995. Strength of the lithosphere: Constraints imposed by laboratory experiments. *Journal of Geophysical Research: Solid Earth* 100, 17587-17602.
- Kohlstedt, D.L., Goetze, C., 1974. Low-stress high-temperature creep in olivine single crystals. *Journal of Geophysical Research* 79, 2045-2051.
- Kohlstedt, D.L., Goetze, C., Durham, W.B., 1976a. Experimental deformation of single crystal olivine with application to flow in the mantle, in: Strens, R.G.J. (Ed.), *The physics and chemistry of minerals and rocks*. John Wiley & Sons, London, pp. 35-49.
- Kohlstedt, D.L., Goetze, C., Durham, W.B., Vander Sande, J., 1976b. New technique for decorating dislocations in olivine. *Science* 191, 1045-1046.
- Krebs, M., Maresch, W.V., Schertl, H.P., Münker, C., Baumann, A., Draper, G., Idleman, B., Trapp, E., 2008. The dynamics of intra-oceanic subduction zones: A direct comparison between fossil petrological evidence (Rio San Juan Complex, Dominican Republic) and numerical simulation. *Lithos* 103, 106-137.
- Krebs, M., Schertl, H.P., Maresch, W.V., Draper, G., 2011. Mass flow in serpentinite-hosted subduction channels: P-T-t path patterns of metamorphic blocks in the Rio San Juan mélange (Dominican Republic). *Journal of Asian Earth Sciences* 42, 569-595.
- Le Maitre, R.W., 2002. *Igneous rocks: a classification and glossary of terms: recommendations of the International Union of Geological Sciences, Subcommittee on the Systematics of Igneous Rocks*. Cambridge University Press, Cambridge, New York.
- Lee, J., Jung, H., 2015. Lattice-preferred orientation of olivine found in diamond-bearing garnet peridotites in Finsch, South Africa and implications for seismic anisotropy. *Journal of Structural Geology* 70, 12-22.
- Lee, J., Jung, H., Klemd, R., Tarling, M.S., Konopelko, D., 2020. Lattice preferred orientation of talc and implications for seismic anisotropy in subduction zones. *Earth and Planetary Science Letters* 537.
- Lee, J., Mookherjee, M., Kim, T., Jung, H., Klemd, R., 2021. Seismic Anisotropy in Subduction Zones: Evaluating the Role of Chloritoid. *Frontiers in Earth Science* 9.
- Levin, V., Droznin, D., Park, J., Gordeev, E., 2004. Detailed mapping of seismic anisotropy with local shear waves in southeastern Kamchatka. *Geophysical Journal International* 158, 1009-1023.

- Li, Z.X., 1994. Collision between the North and South China blocks: a crustal-detachment model for suturing in the region east of the Tanlu fault. *Geology* 22, 739-742.
- Liu, K.H., Gao, S.S., Gao, Y., Wu, J., 2008. Shear wave splitting and mantle flow associated with the deflected Pacific slab beneath northeast Asia. *Journal of Geophysical Research: Solid Earth* (1978–2012) 113.
- Lloyd, G.E., 1987. Atomic number and crystallographic contrast images with the SEM: a review of backscattered electron techniques. *Mineralogical Magazine* 51, 3-19.
- Long, M.D., 2013. Constraints on Subduction Geodynamics from Seismic Anisotropy. *Reviews of Geophysics* 51, 76-112.
- Long, M.D., Becker, T.W., 2010. Mantle dynamics and seismic anisotropy. *Earth and Planetary Science Letters* 297, 341-354.
- Long, M.D., Silver, P.G., 2008. The subduction zone flow field from seismic anisotropy: A global view. *Science* 319, 315-318.
- Long, M.D., Silver, P.G., 2009a. Mantle flow in subduction systems: The subslab flow field and implications for mantle dynamics. *Journal of Geophysical Research: Solid Earth* (1978–2012) 114, 1-25.
- Long, M.D., Silver, P.G., 2009b. Shear wave splitting and mantle anisotropy: measurements, interpretations, and new directions. *Surveys in geophysics* 30, 407-461.
- Long, M.D., van der Hilst, R.D., 2005. Upper mantle anisotropy beneath Japan from shear wave splitting. *Physics of the Earth and Planetary Interiors* 151, 206-222.
- Long, M.D., van der Hilst, R.D., 2006. Shear wave splitting from local events beneath the Ryukyu arc: Trench-parallel anisotropy in the mantle wedge. *Physics of the Earth and Planetary Interiors* 155, 300-312.
- Lynner, C., Long, M.D., 2013. Sub-slab seismic anisotropy and mantle flow beneath the Caribbean and Scotia subduction zones: Effects of slab morphology and kinematics. *Earth and Planetary Science Letters* 361, 367-378.
- Lysak, S.V., 2009. Thermal history, geodynamics, and current thermal activity of lithosphere in China. *Russian Geology and Geophysics* 50, 815-825.
- Mainprice, D., 1990. A FORTRAN program to calculate seismic anisotropy from the lattice preferred orientation of minerals. *Computers and Geosciences* 16, 385-393.
- Mainprice, D., 2007. Seismic anisotropy of the deep Earth from a mineral and rock physics perspective, in: Schubert, G. (Ed.), *Treatise of Geophysics*. Elsevier, Amsterdam, pp. 437-491.
- Mainprice, D., Barruol, G., Ben Ismaïl, W., 2000. The seismic anisotropy of the Earth's mantle: from single crystal to polycrystal, in: Karato, S.-i., Forte, A., Liebermann, R., Masters, G., Stixrude, L. (Eds.), *Earth's Deep Interior*:

- Mineral physics and tomography from the atomic to the global scale, Geophysical Monograph Series. American Geophysical Union, Washington, D.C., pp. 237-264.
- Malatesta, C., Crispini, L., Federico, L., Capponi, G., Scambelluri, M., 2012. The exhumation of high pressure ophiolites (Voltri Massif, Western Alps): Insights from structural and petrologic data on metagabbro bodies. *Tectonophysics* 568–569, 102-123.
- Mann, P., Calais, E., Ruegg, J.-C., DeMets, C., Jansma, P.E., Mattioli, G.S., 2002. Oblique collision in the northeastern Caribbean from GPS measurements and geological observations. *Tectonics* 21, 7-1-7-26.
- Mann, P., Taylor, F., Edwards, R.L., Ku, T.-L., 1995. Actively evolving microplate formation by oblique collision and sideways motion along strike-slip faults: An example from the northeastern Caribbean plate margin. *Tectonophysics* 246, 1-69.
- Manthilake, M., Miyajima, N., Heidelbach, F., Soustelle, V., Frost, D., 2013. The effect of aluminum and water on the development of deformation fabrics of orthopyroxene. *Contributions to Mineralogy and Petrology* 165, 495-505.
- Mao, Z., Jiang, F., Duffy, T.S., 2007. Single-crystal elasticity of zoisite  $\text{Ca}_2\text{Al}_3\text{Si}_3\text{O}_{12}(\text{OH})$  by Brillouin scattering. *American Mineralogist* 92, 570-576.
- Mauler, A., Godard, G., Kunze, K., 2001. Crystallographic fabrics of omphacite, rutile and quartz in Vendée eclogites (Armorican Massif, France). Consequences for deformation mechanisms and regimes. *Tectonophysics* 342, 81-112.
- Mehl, L., Hacker, B.R., Hirth, G., Kelemen, P.B., 2003. Arc-parallel flow within the mantle wedge: Evidence from the accreted Talkeetna arc, south central Alaska. *Journal of Geophysical Research: Solid Earth* (1978–2012) 108.
- Meighan, H.E., Pulliam, J., 2013. Seismic anisotropy beneath the Northeastern Caribbean: Implications for the subducting North American lithosphere. *Bulletin de la Société Géologique de France* 184, 67-76.
- Mercier, J.C., Nicolas, A., 1975. Textures and fabrics of upper-mantle peridotites as illustrated by xenoliths from basalts. *Journal of Petrology* 16, 454-487.
- Michibayashi, K., Ina, T., Kanagawa, K., 2006. The effect of dynamic recrystallization on olivine fabric and seismic anisotropy: Insight from a ductile shear zone, Oman ophiolite. *Earth and Planetary Science Letters* 244, 695-708.
- Michibayashi, K., Kusafuka, Y., Satsukawa, T., Nasir, S.J., 2012. Seismic properties of peridotite xenoliths as a clue to imaging the lithospheric mantle beneath NE Tasmania, Australia. *Tectonophysics* 522-523, 218-223.

- Michibayashi, K., Mainprice, D., 2004. The role of pre-existing mechanical anisotropy on shear zone development within oceanic mantle lithosphere: an example from the Oman ophiolite. *Journal of Petrology* 45, 405-414.
- Michibayashi, K., Oohara, T., Satsukawa, T., Ishimaru, S., Arai, S., Okrugin, V.M., 2009. Rock seismic anisotropy of the low-velocity zone beneath the volcanic front in the mantle wedge. *Geophysical Research Letters* 36, L12305.
- Mizukami, T., Wallis, S.R., Yamamoto, J., 2004. Natural examples of olivine lattice preferred orientation patterns with a flow-normal a-axis maximum. *Nature* 427, 432-436.
- Molina, J.F., Moreno, J.A., Castro, A., Rodríguez, C., Fershtater, G.B., 2015. Calcic amphibole thermobarometry in metamorphic and igneous rocks: New calibrations based on plagioclase/amphibole Al-Si partitioning and amphibole/liquid Mg partitioning. *Lithos* 232, 286-305.
- Montagner, J.-P., Tanimoto, T., 1990. Global anisotropy in the upper mantle inferred from the regionalization of phase velocities. *Journal of Geophysical Research: Solid Earth (1978–2012)* 95, 4797-4819.
- Montagner, J.-P., Tanimoto, T., 1991. Global upper mantle tomography of seismic velocities and anisotropies. *Journal of Geophysical Research* 96, 20337-20320,20351.
- Mookherjee, M., Bezacier, L., 2012. The low velocity layer in subduction zone: Structure and elasticity of glaucophane at high pressures. *Physics of the Earth and Planetary Interiors* 208, 50-58.
- Mookherjee, M., Mainprice, D., 2014. Unusually large shear wave anisotropy for chlorite in subduction zone settings. *Geophysical Research Letters* 41, 1506-1513.
- Müller, C., 2001. Upper mantle seismic anisotropy beneath Antarctica and the Scotia Sea region. *Geophysical Journal International* 147, 105-122.
- Müller, W.F., Franz, G., 2004. Unusual deformation microstructures in garnet, titanite and clinozoisite from an eclogite of the Lower Schist Cover, Tauern Window, Austria. *European Journal of Mineralogy* 16, 939-944.
- Müller, W.F., Franz, G., 2008. TEM-microstructures in omphacite and other minerals from eclogite near to a thrust zone; the Eclogite Zone–Venediger nappe area, Tauern Window, Austria. *Neues Jahrbuch für Mineralogie-Abhandlungen: Journal of Mineralogy and Geochemistry* 184, 285-298.
- Nakajima, J., Hasegawa, A., 2004. Shear-wave polarization anisotropy and subduction-induced flow in the mantle wedge of northeastern Japan. *Earth and Planetary Science Letters* 225, 365-377.
- Nakajima, J., Shimizu, J., Hori, S., Hasegawa, A., 2006. Shear-wave splitting beneath the southwestern Kurile arc and northeastern Japan arc: A new insight into mantle return flow. *Geophysical research letters* 33, 1-4.

- Nicolas, A., Christensen, N.I., 1987. Formation of Anisotropy in Upper Mantle Peridotites-A Review, in: Fuchs, K., Froidevaux, C. (Eds.), *Composition, structure and dynamics of the lithosphere-asthenosphere system*, Geodynamics Series. American Geophysical Union, Washington, D.C., pp. 111-123.
- Nicolas, A., Poirier, J.P., 1976. *Crystalline plasticity and solid state flow in metamorphic rocks*. John Wiley & Sons.
- Núñez, D., Córdoba, D., Kissling, E., 2019. Seismic structure of the crust in the western Dominican Republic. *Tectonophysics* 773.
- O'Neill, H.S.C., Wood, B.J., 1979. An experimental study of Fe-Mg partitioning between garnet and olivine and its calibration as a geothermometer. *Contributions to Mineralogy and Petrology* 70, 59-70.
- O'Reilly, S.Y., Griffin, W.L., Poudjom, Y.H., Morgan, P., 2001. Are lithospheres forever? Tracking changes in subcontinental lithospheric mantle through time. *GSA Today* 11, 4-10.
- Ohuchi, T., Kawazoe, T., Nishihara, Y., Irifune, T., 2012. Change of olivine a-axis alignment induced by water: Origin of seismic anisotropy in subduction zones. *Earth and Planetary Science Letters* 317-318, 111-119.
- Ohuchi, T., Kawazoe, T., Nishihara, Y., Nishiyama, N., Irifune, T., 2011. High pressure and temperature fabric transitions in olivine and variations in upper mantle seismic anisotropy. *Earth and Planetary Science Letters* 304, 55-63.
- Panozzo, R.H., 1983. Two-dimensional analysis of shape-fabric using projections of digitized lines in a plane. *Tectonophysics* 95, 279-294.
- Panozzo, R.H., 1984. Two-dimensional strain from the orientation of lines in a plane. *Journal of Structural Geology* 6, 215-221.
- Park, J., Levin, V., 2002. Seismic anisotropy: tracing plate dynamics in the mantle. *Science* 296, 485-489.
- Park, M., Jung, H., 2019. Relationships Between Eclogite-Facies Mineral Assemblages, Deformation Microstructures, and Seismic Properties in the Yuka Terrane, North Qaidam Ultrahigh-Pressure Metamorphic Belt, NW China. *Journal of Geophysical Research: Solid Earth* 124, 13168-13191.
- Park, M., Jung, H., Kil, Y., 2014. Petrofabrics of olivine in a rift axis and rift shoulder and their implications for seismic anisotropy beneath the Rio Grande rift. *Island Arc* 23, 299-311.
- Park, M., Kil, Y., Jung, H., 2020b. Evolution of Deformation Fabrics Related to Petrogenesis of Upper Mantle Xenoliths Beneath the Baekdusan Volcano. *Minerals* 10.
- Park, Y., Jung, H., 2015. Deformation microstructures of olivine and pyroxene in mantle xenoliths in Shanwang, eastern China, near the convergent plate margin, and implications for seismic anisotropy. *International Geology Review* 57, 629-649.

- Park, Y., Jung, S., Jung, H., 2020a. Lattice Preferred Orientation and Deformation Microstructures of Glaucophane and Epidote in Experimentally Deformed Epidote Blueschist at High Pressure. *Minerals* 10, 803, 801-819.
- Passchier, C.W., Trouw, R.A., 1996. *Microtectonics*. Springer, Berlin and Heidelberg, Germany.
- Passchier, C.W., Trouw, R.A.J., 2005. *Microtectonics*, 2nd ed. Springer, Berlin, Germany.
- Paterson, M.S., 1982. The determination of hydroxyl by infrared absorption in quartz, silicate glasses and similar materials. *Bull. Mineral* 105, 20-29.
- Peacock, S.M., 1992. Blueschist-facies metamorphism, shear heating, and P-T-t Paths in Subduction Shear Zones. *Journal of Geophysical Research: Solid Earth* 97, 17693-17707.
- Peacock, S.M., 1993. The importance of blueschist → eclogite dehydration reactions in subducting oceanic crust. *Geological Society of America Bulletin* 105, 684-694.
- Pera, E., Mainprice, D., Burlini, L., 2003. Anisotropic seismic properties of the upper mantle beneath the Torre Alfina area (northern Apennines, central Italy). *Tectonophysics* 370, 11-30.
- Peslier, A.H., Luhr, J.F., 2006. Hydrogen loss from olivines in mantle xenoliths from Simcoe (USA) and Mexico: mafic alkalic magma ascent rates and water budget of the sub-continental lithosphere. *Earth and Planetary Science Letters* 242, 302-319.
- Philippson, M., Gueydan, F., Pitra, P., Brun, J.P., 2013. Preservation of subduction-related prograde deformation in lawsonite pseudomorph-bearing rocks. *Journal of Metamorphic Geology* 31, 571-583.
- Poli, S., Schmidt, M.W., 2002. Petrology of subducted slabs. *Annual Review of Earth and Planetary Sciences* 30, 207-235.
- Possee, D., Keir, D., Harmon, N., Rychert, C., Eakin, C., Rolandone, F., Leroy, S., Corbeau, J., Stuart, G., Boisson, D., Momplaisir, R., Prépetit, C., 2020. Spatial Variations in Crustal and Mantle Anisotropy Across the North American-Caribbean Boundary on Haiti. *Journal of Geophysical Research: Solid Earth* 125.
- Prior, D.J., Boyle, A.P., Brenker, F., Cheadle, M.C., Day, A., Lopez, G., Peruzzo, L., Potts, G.J., Reddy, S., Spiess, R., 1999. The application of electron backscatter diffraction and orientation contrast imaging in the SEM to textural problems in rocks. *American Mineralogist* 84, 1741-1759.
- Raterron, P., Chen, J., Geenen, T., Girard, J., 2011. Pressure effect on forsterite dislocation slip systems: Implications for upper-mantle LPO and low viscosity zone. *Physics of the Earth and Planetary Interiors* 188, 26-36.

- Ravna, E.J.K., 2000a. Distribution of Fe<sup>2+</sup> and Mg between coexisting garnet and hornblende in synthetic and natural systems: an empirical calibration of the garnet–hornblende Fe–Mg geothermometer. *Lithos* 53, 265-277.
- Ravna, E.J.K., 2000b. The garnet–clinopyroxene Fe<sup>2+</sup>–Mg geothermometer: an updated calibration. *Journal of Metamorphic Geology* 18, 211-219.
- Ravna, E.J.K., Terry, M.P., 2004. Geothermobarometry of UHP and HP eclogites and schists - an evaluation of equilibria among garnet-clinopyroxene-kyanite-phengite-coesite/quartz. *Journal of Metamorphic Geology* 22, 579-592.
- Ray, N.J., Putnis, A., Gillet, P., 1986. Polytypic relationship between clinozoisite and zoisite. *Bulletin De Mineralogie* 109, 667-685.
- Reynard, B., Gillet, P., Willaime, C., 1989. Deformation mechanisms in naturally deformed glaucophanes: a TEM and HREM study. *European Journal of Mineralogy* 1, 611-624.
- Robinson, P., Ross, M., Nord, G., Smyth, J., Jaffe, H., 1977. Exsolution lamellae in augite and pigeonite; fossil indicators of lattice parameters at high temperature and pressure. *American Mineralogist* 62, 857-873.
- Rodríguez-Zurrunero, A., Granja-Bruña, J.L., Muñoz-Martín, A., Leroy, S., ten Brink, U., Gorosabel-Araus, J.M., Gómez de la Peña, L., Druet, M., Carbó-Gorosabel, A., 2020. Along-strike segmentation in the northern Caribbean plate boundary zone (Hispaniola sector): Tectonic implications. *Tectonophysics* 776.
- Russ, J.C., Dehoff, R.T., 2000. *Practical stereology*, 2nd ed. Kluwer Academic/Plenum publishers, New York.
- Satsukawa, T., Michibayashi, K., Anthony, E.Y., Stern, R.J., Gao, S.S., Liu, K.H., 2011. Seismic anisotropy of the uppermost mantle beneath the Rio Grande rift: Evidence from Kilbourne Hole peridotite xenoliths, New Mexico. *Earth and Planetary Science Letters* 311, 172-181.
- Savage, M.K., 1999. Seismic anisotropy and mantle deformation: What have we learned from shear wave splitting? *Reviews of Geophysics* 37, 65-106.
- Sawaguchi, T., 2004. Deformation history and exhumation process of the Horoman Peridotite Complex, Hokkaido, Japan. *Tectonophysics* 379, 109-126.
- Schmidt, M.W., Poli, S., 1998. Experimentally based water budgets for dehydrating slabs and consequences for arc magma generation. *Earth and Planetary Science Letters* 163, 361-379.
- Schumacher, J.C., 1991. Empirical ferric iron corrections: necessity, assumptions, and effects on selected geothermobarometers. *Mineralogical Magazine* 55, 3-18.
- Silver, P.G., 1996. Seismic anisotropy beneath the continents: Probing the depths of geology. *Annual Review of Earth and Planetary Sciences* 24, 385-432.

- Skemer, P., Katayama, I., Jiang, Z., Karato, S., 2005. The misorientation index: Development of a new method for calculating the strength of lattice-preferred orientation. *Tectonophysics* 411, 157-167.
- Skemer, P., Katayama, I., Karato, S., 2006. Deformation fabrics of the Cima di Gagnone peridotite massif, Central Alps, Switzerland: evidence of deformation at low temperatures in the presence of water. *Contributions to Mineralogy and Petrology* 152, 43-51.
- Skemer, P., Warren, J.M., Hirth, G., 2012. The influence of deformation history on the interpretation of seismic anisotropy. *Geochemistry, Geophysics, Geosystems* 13, 1-10.
- Skemer, P., Warren, J.M., Kelemen, P.B., Hirth, G., 2010. Microstructural and rheological evolution of a mantle shear zone. *Journal of Petrology* 51, 43-53.
- Soudoudi, F., Yuan, X., Liu, Q., Kind, R., Chen, J., 2006. Lithospheric thickness beneath the Dabie Shan, central eastern China from S receiver functions. *Geophysical Journal International* 166, 1363-1367.
- Song, S., Cao, Y., 2021. Textures and Structures of Metamorphic Rocks, *Encyclopedia of Geology*, pp. 375-388.
- Song, T.-R.A., Kawakatsu, H., 2012. Subduction of oceanic asthenosphere: Evidence from sub-slab seismic anisotropy. *Geophysical Research Letters* 39, n/a-n/a.
- Soustelle, V., Tommasi, A., Demouchy, S., Ionov, D.A., 2010. Deformation and fluid-rock interaction in the supra-subduction mantle: microstructures and water contents in peridotite xenoliths from the Avacha Volcano, Kamchatka. *Journal of Petrology* 51, 363-394.
- Stünitz, H., Tullis, J., 2001. Weakening and strain localization produced by syn-deformational reaction of plagioclase. *Int J Earth Sci (Geol Rundsch)* 90, 136-148.
- Tasaka, M., Michibayashi, K., Mainprice, D., 2008. B-type olivine fabrics developed in the fore-arc side of the mantle wedge along a subducting slab. *Earth and Planetary Science Letters* 272, 747-757.
- Teyssier, C., Whitney, D.L., Toraman, E., Seaton, N.C.A., 2010. Lawsonite vorticity and subduction kinematics. *Geology* 38, 1123-1126.
- Tommasi, A., Vauchez, A., Ionov, D.A., 2008. Deformation, static recrystallization, and reactive melt transport in shallow subcontinental mantle xenoliths (Tok Cenozoic volcanic field, SE Siberia). *Earth and Planetary Science Letters* 272, 65-77.
- Tsuji, Y., Nakajima, J., Hasegawa, A., 2008. Tomographic evidence for hydrated oceanic crust of the Pacific slab beneath northeastern Japan: Implications for water transportation in subduction zones. *Geophysical Research Letters* 35.

- Tsujimori, T., Ernst, W.G., 2014. Lawsonite blueschists and lawsonite eclogites as proxies for palaeo-subduction zone processes: a review. *Journal of Metamorphic Geology* 32, 437-454.
- Ukar, E., Cloos, M., 2019. Cataclastic deformation and metasomatism in the subduction zone of mafic blocks-in-mélange, San Simeon, California. *Lithos* 346-347.
- Van der Wal, D., Chopra, P., Drury, M., Gerald, J.F., 1993. Relationships between dynamically recrystallized grain size and deformation conditions in experimentally deformed olivine rocks. *Geophysical Research Letters* 20, 1479-1482.
- van Duysen, J.C., Doukhan, J.C., 1984. Room temperature microplasticity of a spodumene  $\text{LiAlSi}_2\text{O}_6$ . *Physics and Chemistry of Minerals* 10, 125-132.
- Van Roermund, H., Boland, J., 1981. The dislocation substructures of naturally deformed omphacites. *Tectonophysics* 78, 403-418.
- Vauchez, A., Dineur, F., Rudnick, R., 2005. Microstructure, texture and seismic anisotropy of the lithospheric mantle above a mantle plume: insights from the Labait volcano xenoliths (Tanzania). *Earth and Planetary Science Letters* 232, 295-314.
- Vaughan, M.T., Guggenheim, S., 1986. Elasticity of muscovite and its relationship to crystal structure. *Journal of Geophysical Research* 91.
- Vignaroli, G., Rossetti, F., Bouybaouene, M., Massonne, H.J., Theye, T., Faccenna, C., Funiciello, R., 2005. A counter-clockwise P–T path for the Voltri Massif eclogites (Ligurian Alps, Italy). *Journal of Metamorphic Geology* 23, 533-555.
- Vinnik, L.P., Farra, V., Romanowicz, B., 1989. Azimuthal anisotropy in the earth from observations of SKS at GEOSCOPE and NARS broadband stations. *Bulletin of the Seismological Society of America* 79, 1542-1558.
- Walker, A.M., Wookey, J., 2012. MSAT—A new toolkit for the analysis of elastic and seismic anisotropy. *Computers & Geosciences* 49, 81-90.
- Wassmann, S., Stöckhert, B., 2013. Rheology of the plate interface — Dissolution precipitation creep in high pressure metamorphic rocks. *Tectonophysics* 608, 1-29.
- Watanabe, T., Shirasugi, Y., Michibayashi, K., 2014. A new method for calculating seismic velocities in rocks containing strongly dimensionally anisotropic mineral grains and its application to antigorite-bearing serpentinite mylonites. *Earth and Planetary Science Letters* 391, 24-35.
- Xiao, Y., Zhang, H.-F., 2011. Effects of melt percolation on platinum group elements and Re–Os systematics of peridotites from the Tan-Lu fault zone, eastern North China Craton. *Journal of the Geological Society* 168, 1201-1214.
- Xiao, Y., Zhang, H.F., Fan, W.M., Ying, J.F., Zhang, J., Zhao, X.M., Su, B.X., 2010. Evolution of lithospheric mantle beneath the Tan-Lu fault zone, eastern

- North China Craton: Evidence from petrology and geochemistry of peridotite xenoliths. *Lithos* 117, 229-246.
- Xu, J., Zhu, G., 1994. Tectonic models of the Tan-Lu fault zone, eastern China. *International Geology Review* 36, 771-784.
- Xu, X., O'Reilly, S.Y., Griffin, W., Zhou, X., 2000. Genesis of young lithospheric mantle in southeastern China: an LAM-ICPMS trace element study. *Journal of Petrology* 41, 111-148.
- Xu, X., O'Reilly, S.Y., Griffin, W., Zhou, X., Huang, X., 1998. The nature of the Cenozoic lithosphere at Nushan, eastern China, in: Flower, M.F.J., Chung, S.L., Lo, C.H., Lee, T.Y. (Eds.), *Mantle Dynamics and Plate Interactions in East Asia*, Geodynamics Series. American Geophysical Union, Washington, D.C., pp. 167-195.
- Yang, X.-Z., Xia, Q.-K., Deloule, E., Dallai, L., Fan, Q.-C., Feng, M., 2008. Water in minerals of the continental lithospheric mantle and overlying lower crust: A comparative study of peridotite and granulite xenoliths from the North China Craton. *Chemical Geology* 256, 33-45.
- Yin, A., Nie, S., 1993. An indentation model for the North and South China collision and the development of the Tan-Lu and Honam fault systems, eastern Asia. *Tectonics* 12, 801-813.
- Ying, J., Zhang, H., Kita, N., Morishita, Y., Shimoda, G., 2006. Nature and evolution of Late Cretaceous lithospheric mantle beneath the eastern North China Craton: Constraints from petrology and geochemistry of peridotitic xenoliths from Jūnan, Shandong Province, China. *Earth and Planetary Science Letters* 244, 622-638.
- Yuan, X., 1996. *Atlas of geophysics in China*. Geological Publishing House, Beijing, China.
- Zack, T., Rivers, T., Brumm, R., Kronz, A., 2004. Cold subduction of oceanic crust: Implications from a lawsonite eclogite from the Dominican Republic. *European Journal of Mineralogy* 16, 909-916.
- Zhang, H.-F., 2005. Transformation of lithospheric mantle through peridotite-melt reaction: a case of Sino-Korean craton. *Earth and Planetary Science Letters* 237, 768-780.
- Zhang, H.-F., Deloule, E., Tang, Y.-J., Ying, J.-F., 2010. Melt/rock interaction in remains of refertilized Archean lithospheric mantle in Jiaodong Peninsula, North China Craton: Li isotopic evidence. *Contributions to Mineralogy and Petrology* 160, 261-277.
- Zhang, H.-F., Goldstein, S.L., Zhou, X.-H., Sun, M., Zheng, J.-P., Cai, Y., 2008. Evolution of subcontinental lithospheric mantle beneath eastern China: Re-Os isotopic evidence from mantle xenoliths in Paleozoic kimberlites and Mesozoic basalts. *Contributions to Mineralogy and Petrology* 155, 271-293.

- Zhang, H.-F., Nakamura, E., Sun, M., Kobayashi, K., Zhang, J., Ying, J.-F., Tang, Y.-J., Niu, L.-F., 2007. Transformation of subcontinental lithospheric mantle through peridotite-melt reaction: evidence from a highly fertile mantle xenolith from the North China craton. *International Geology Review* 49, 658-679.
- Zhang, H.-F., Sun, M., 2002. Geochemistry of Mesozoic basalts and mafic dikes, southeastern North China Craton, and tectonic implications. *International Geology Review* 44, 370-382.
- Zhang, J., Green II, H.W., Bozhilov, K.N., 2006. Rheology of omphacite at high temperature and pressure and significance of its lattice preferred orientations. *Earth and Planetary Science Letters* 246, 432-443.
- Zhang, J., Yang, X., Sun, W., Wang, G., Yang, C., Liu, C., Liu, D., 2012. New data on the evolution of the Tan–Lu fault belt: constraints from geological–geophysical surveys in the southern segment. *International Geology Review* 54, 1562-1578.
- Zhang, J., Zhang, H., Kita, N., Shimoda, G., Morishita, Y., Ying, J., Tang, Y., 2011. Secular evolution of the lithospheric mantle beneath the eastern North China craton: evidence from peridotitic xenoliths from Late Cretaceous mafic rocks in the Jiaodong region, east-central China. *International Geology Review* 53, 182-211.
- Zhang, S., Karato, S.-I., 1995. Lattice preferred orientation of olivine aggregates deformed in simple shear. *Nature* 375, 774-777.
- Zhang, S., Karato, S.-I., Fitz Gerald, J., Faul, U.H., Zhou, Y., 2000. Simple shear deformation of olivine aggregates. *Tectonophysics* 316, 133-152.
- Zhao, D., Maruyama, S., Omori, S., 2007a. Mantle dynamics of Western Pacific and East Asia: Insight from seismic tomography and mineral physics. *Gondwana Research* 11, 120-131.
- Zhao, G., Cawood, P.A., Wilde, S.A., Sun, M., Lu, L., 2000. Metamorphism of basement rocks in the Central Zone of the North China Craton: implications for Paleoproterozoic tectonic evolution. *Precambrian Research* 103, 55-88.
- Zhao, G., Wilde, S.A., Cawood, P.A., Sun, M., 2001. Archean blocks and their boundaries in the North China Craton: lithological, geochemical, structural and *P–T* path constraints and tectonic evolution. *Precambrian Research* 107, 45-73.
- Zhao, L., Allen, R.M., Zheng, T., Hung, S.H., 2009. Reactivation of an Archean craton: Constraints from P- and S-wave tomography in North China. *Geophysical Research Letters* 36, 1-5.
- Zhao, L., Xue, M., 2010. Mantle flow pattern and geodynamic cause of the North China Craton reactivation: Evidence from seismic anisotropy. *Geochemistry, Geophysics, Geosystems* 11, 1-18.

- Zhao, L., Zheng, T., 2005. Using shear wave splitting measurements to investigate the upper mantle anisotropy beneath the North China Craton: Distinct variation from east to west. *Geophysical research letters* 32, 1-4.
- Zhao, L., Zheng, T., Chen, L., Tang, Q., 2007b. Shear wave splitting in eastern and central China: Implications for upper mantle deformation beneath continental margin. *Physics of the Earth and Planetary Interiors* 162, 73-84.
- Zhao, L., Zheng, T., Lü, G., 2008. Insight into craton evolution: Constraints from shear wave splitting in the North China Craton. *Physics of the Earth and Planetary Interiors* 168, 153-162.
- Zhao, L., Zheng, T., Lu, G., 2013. Distinct upper mantle deformation of cratons in response to subduction: constraints from SKS wave splitting measurements in eastern China. *Gondwana Research* 23, 39-53.
- Zhao, L., Zheng, T., Lu, G., Ai, Y., 2011. No direct correlation of mantle flow beneath the North China Craton to the India–Eurasia collision: constraints from new SKS wave splitting measurements. *Geophysical Journal International* 187, 1027-1037.
- Zheng, J., Dai, H., 2018. Subduction and retreating of the western Pacific plate resulted in lithospheric mantle replacement and coupled basin-mountain respond in the North China Craton. *Science China Earth Sciences* 61, 406-424.
- Zheng, J., Griffin, W., O'Reilly, S.Y., Liou, J., Zhang, R., Lu, F., 2005a. Late Mesozoic-Eocene mantle replacement beneath the eastern North China Craton: evidence from the Paleozoic and Cenozoic peridotite xenoliths. *International Geology Review* 47, 457-472.
- Zheng, J., Griffin, W.L., O'Reilly, S.Y., Yang, J., Li, T., Zhang, M., Zhang, R.Y., Liou, J.G., 2006. Mineral chemistry of peridotites from Paleozoic, Mesozoic and Cenozoic lithosphere: constraints on mantle evolution beneath eastern China. *Journal of Petrology* 47, 2233-2256.
- Zheng, J., Lu, F., 1999. Mantle xenoliths from kimberlites, Shandong and Liaoning: Paleozoic mantle character and its heterogeneity. *Acta Petrologica Sinica* 15, 65-74 (in Chinese).
- Zheng, J., O'Reilly, S.Y., Griffin, W.L., Lu, F., Zhang, M., 1998. Nature and evolution of Cenozoic lithospheric mantle beneath Shandong peninsula, Sino-Korean craton, eastern China. *International Geology Review* 40, 471-499.
- Zheng, J., O'Reilly, S.Y., Griffin, W.L., Lu, F., Zhang, M., Pearson, N.J., 2001. Relict refractory mantle beneath the eastern North China block: significance for lithosphere evolution. *Lithos* 57, 43-66.
- Zheng, J., Sun, M., Zhou, M.F., Robinson, P., 2005b. Trace elemental and PGE geochemical constraints of Mesozoic and Cenozoic peridotitic xenoliths on

- lithospheric evolution of the North China Craton. *Geochimica et cosmochimica acta* 69, 3401-3418.
- Zheng, J.P., Griffin, W.L., O'Reilly, S.Y., Yu, C.M., Zhang, H.F., Pearson, N., Zhang, M., 2007. Mechanism and timing of lithospheric modification and replacement beneath the eastern North China Craton: Peridotitic xenoliths from the 100 Ma Fuxin basalts and a regional synthesis. *Geochimica et Cosmochimica Acta* 71, 5203-5225.
- Zhi, X., Chen, D., Zhang, Z., Wang, J., 1994. The Neodymium and Strontium Isotopic Compositions of Cenozoic Alkalic Basalts from Penglai and Lingqu, Shandong Province. *Geological Review* 40, 526-533 (in Chinese).
- Zhu, G., Liu, G., Dunlap, W.J., Teyssier, C., Wang, Y., Niu, M., 2004.  $^{40}\text{Ar}/^{39}\text{Ar}$  geochronological constraints on syn-orogenic strike-slip movement of Tan-Lu fault zone. *Chinese Science Bulletin* 49, 499-508.
- Zhu, R.-X., Zheng, T.-Y., 2009. Destruction geodynamics of the North China Craton and its Paleoproterozoic plate tectonics. *Chinese Science Bulletin* 54, 3354-3366.
- Zhu, R., Xu, Y., 2019. The subduction of the west Pacific plate and the destruction of the North China Craton. *Science China Earth Sciences* 62, 1340-1350.
- Zucali, M., Chateigner, D., Dugnani, M., Lutterotti, L., Ouladdiaf, B., 2002. Quantitative texture analysis of glaucophanite deformed under eclogite facies conditions (Sesia-Lanzo Zone, Western Alps): comparison between X-ray and neutron diffraction analysis. *Geological Society, London, Special Publications* 200, 239-253.

## 국 문 초 록

### 맨틀 포획암과 녹렴석 청색편암의 변형미구조 진화: 암석권 및 섭입대에서의 지진과 특성에 대한 의의

본 학위논문에서는 암석권 맨틀과 수렴판 경계에서의 암석의 변형 환경 및 메커니즘, 그리고 지진과 특성을 이해하기 위하여, 맨틀 감람암 포획암과 녹렴석 청색편암의 변형미구조를 연구하였다. 첫번째로는 중국 동부 산왕(Shanwang)지역의 암석권 맨틀에서 산출된 맨틀 감람암 포획암 내의 감람석의 변형 환경과 격자선호방향(LPO)을 연구하였다. 연구 결과, 침정석 레졸라이트(spinel lherzolite)에서는 감람석의 B타입 격자선호방향이, 침정석 웰라이트(spinel wehrlite)에서는 감람석의 E타입 격자선호방향이 각각 측정되었다. 시료들이 받은 응력(stress)은 자유 전위 밀도와 감람석의 재결정 입자 크기 응력계를 사용하여 약 18-74 MPa로 추정되었다. 광물들이 포함한 물의 함량은 푸리에 변환 적외선 분광법을 사용하여 감람석에서 50-200 ppm H/Si, 사방휘석에서 120-760 ppm H/Si, 단사휘석에서 1060-7690 ppm H/Si로 각각 측정되었다. 이러한 데이터들은 감람석의 B타입 격자선호방향이 높은 응력과 물의 존재 하에 형성되었고, 감람석의 E타입 격자선호방향이 상대적으로 낮은 응력과 물이 존재하는 경우에 형성되었을 것임을 시사하였다. 이러한 두 가지 유형의 감람석 격자선호방향을 사용하여, 본 연구에서는 중국 동부 산왕지역에서 관측되는 지진과 이방성이 서로 다른 시기의 두 가지 변형 양식으로 설명될 수 있음을 제안하였다. 두번째로는 따뜻한 섭입대에서 섭입하는 판의 상부에 존재하는 남섬석과 녹렴석의 변형미구조와 격자선호방향을 이해하기 위하여, 0.9-1.5 GPa의 압력과 400-500 °C의 온도에서 녹렴석 청색편암의 단순전단 변형실험을 최초로 수행하였다. 실험 결과, 전단 변형 정도가 증가함에 따라 남섬석과 녹렴석의 1형 및 2형 격자선호방향이 각각 형성되었다. 이들의 변형미구조 및 결정 내 미세구조 관찰을 통하여, 본 연구에서는 따뜻한 섭입대의 섭입하는 판 상부에서 남섬석과 녹렴석의 격자선호방향

형성에 영향을 미치는 중요한 요인들로서 암석의 전단 변형 정도와 광물들의 입자 크기, 그리고 구성 광물들 사이의 유변학적 대비를 제안하였다. 이렇게 실험적으로 변형된 녹립석 청색편암에서 계산한 지진파 속도를 섭입하는 판을 둘러싼 암석권 맨틀의 지진파 속도와 비교하였을 때, P파 속도는 약 8-9 %가 감소하였고, S파 속도는 약 6-7 %가 감소하였다. 이러한 결과는 변형된 녹립석 청색편암이 섭입하는 판 상부에서 관측되는 지진파 저속도층에 기여할 수 있음을 시사하였다. 또한 녹립석 청색편암으로 구성된 해양 지각에 대한 지진파 이방성의 계산 결과는 남섬석과 녹립석의 부피 비율과 격자선호방향의 유형, 그리고 섭입하는 판의 섭입각이 섭입대에서 관측되는 지진파 속도와 이방성을 결정하는 중요한 요소들이 될 수 있음을 시사하였다. 마지막으로, 자연상에서 변형된 암석 상에서의 광물들의 변형 메커니즘과 격자선호방향 형성을 이해하기 위하여, 도미니카 공화국 리오 산 후안(Río San Juan) 변성 복합체의 사문암 벨란지에서 섭입된 해양지각으로부터 산출된 청색 편암의 변형미구조를 연구하였다. 연구결과, 대부분의 시료에서 측정된 각섬석의 격자선호방향은 변형실험에서 형성된 각섬석의 2형 격자선호방향에 해당하였고, 유립석과 녹립석의 격자선호방향은 변형실험에서 형성된 녹립석의 1형 격자선호방향에 해당하였다. 각섬석과 유립석 반상쇄정에서 관찰된 높은 밀도의 아결정경계들과 강한 격자 세기는 이들의 격자선호방향이 전위크리프에 의해 형성되었음을 시사하였다. 그리고 연구지역에서의 S파 지연 시간과 이방성층의 두께를 계산한 결과들은 청색편암상 변성작용을 겪은 섭입된 해양지각이 구성 광물의 격자선호방향과 이들이 지구조운동에 의해 배열된 방향에 따라 카리브판 북동경계부에서의 지진파 이방성에 크게 기여할 수 있음을 시사하였다.

**주요어:** 변형미구조, 격자선호방향, 녹립석 청색편암, 맨틀 포획암, 암석변형실험, 지진파 이방성

**학번:** 2012-20341